

Hitting the right target : noninvasive localization of the subthalamic nucleus motor part for specific deep brain stimulation

Citation for published version (APA):

Brunenberg, E. J. L. (2011). *Hitting the right target : noninvasive localization of the subthalamic nucleus motor part for specific deep brain stimulation*. [Phd Thesis 1 (Research TU/e / Graduation TU/e), Biomedical Engineering]. Technische Universiteit Eindhoven. <https://doi.org/10.6100/IR715250>

DOI:

[10.6100/IR715250](https://doi.org/10.6100/IR715250)

Document status and date:

Published: 01/01/2011

Document Version:

Publisher's PDF, also known as Version of Record (includes final page, issue and volume numbers)

Please check the document version of this publication:

- A submitted manuscript is the version of the article upon submission and before peer-review. There can be important differences between the submitted version and the official published version of record. People interested in the research are advised to contact the author for the final version of the publication, or visit the DOI to the publisher's website.
- The final author version and the galley proof are versions of the publication after peer review.
- The final published version features the final layout of the paper including the volume, issue and page numbers.

[Link to publication](#)

General rights

Copyright and moral rights for the publications made accessible in the public portal are retained by the authors and/or other copyright owners and it is a condition of accessing publications that users recognise and abide by the legal requirements associated with these rights.

- Users may download and print one copy of any publication from the public portal for the purpose of private study or research.
- You may not further distribute the material or use it for any profit-making activity or commercial gain
- You may freely distribute the URL identifying the publication in the public portal.

If the publication is distributed under the terms of Article 25fa of the Dutch Copyright Act, indicated by the "Taverne" license above, please follow below link for the End User Agreement:

www.tue.nl/taverne

Take down policy

If you believe that this document breaches copyright please contact us at:

openaccess@tue.nl

providing details and we will investigate your claim.



HITTING THE RIGHT TARGET

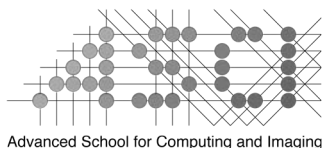
Noninvasive localization of the
subthalamic nucleus motor part
for specific deep brain stimulation

Ellen Brunenberg

Hitting the right target

Noninvasive localization of the subthalamic nucleus
motor part for specific deep brain stimulation

Colophon



This work was carried out in the ASCI graduate school. ASCI dissertation series number 232.



Netherlands Organisation for Scientific Research

This project was financially supported by a Top talent grant (number 021.001.055) from NWO, the Netherlands Organisation for Scientific Research.

Financial support for the publication of this thesis was kindly provided by the ASCI graduate school and Eindhoven University of Technology.

Travel grants were awarded by the International Society for Magnetic Resonance in Medicine (ISMRM) and the Medical Image Computing and Computer Assisted Intervention Society (MICCAI).

The cover of this thesis was designed by the author (Ellen Brunenberg).

The contents were typeset by the author using $\text{\LaTeX}2_{\epsilon}$. The main body of the text was set using a 10-point Computer Modern Bright font.

Printed by Off Page, Amsterdam, the Netherlands.

A catalogue record is available from the Eindhoven University of Technology Library. ISBN: 978-90-386-2526-3

© 2011 Ellen J.L. Brunenberg, Tilburg, the Netherlands, unless stated otherwise at the beginning of chapters. All rights reserved. No part of this publication may be reproduced or transmitted in any form or by any means, electronic or mechanical, including photocopying, recording, or any information storage and retrieval system, without permission in writing from the copyright owner.

Hitting the right target

Noninvasive localization of the subthalamic nucleus
motor part for specific deep brain stimulation

PROEFSCHRIFT

ter verkrijging van de graad van doctor aan de
Technische Universiteit Eindhoven, op gezag van de
rector magnificus, prof.dr.ir. C.J. van Duijn, voor een
commissie aangewezen door het College voor
Promoties in het openbaar te verdedigen
op donderdag 8 september 2011 om 16.00 uur

door

Ellen Johanna Leonarda Brunenberg

geboren te Weert

Dit proefschrift is goedgekeurd door de promotoren:

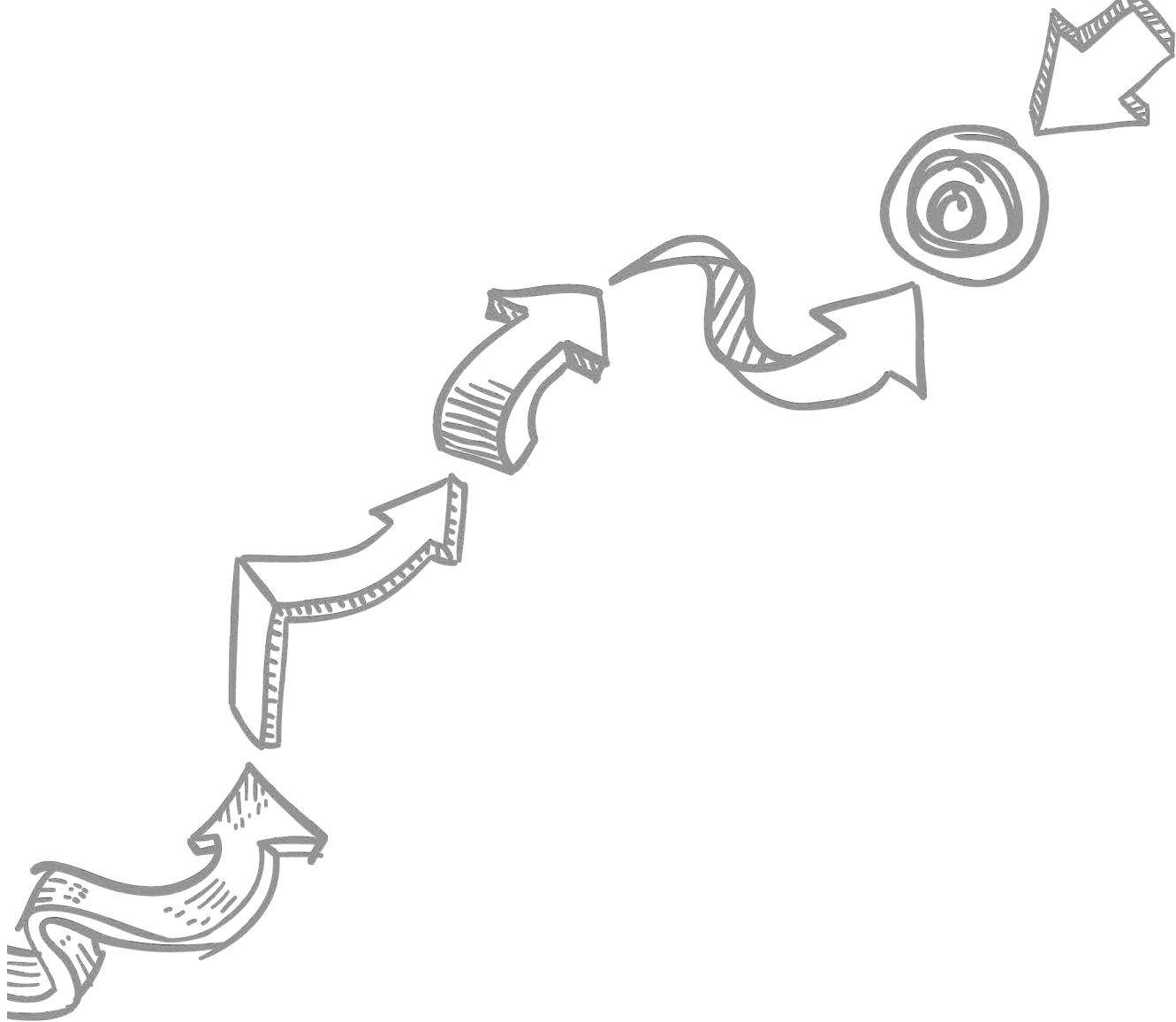
prof.dr.ir. B.M. ter Haar Romeny

en

prof.dr. V.E.R.M. Visser-Vandewalle

Copromotor:

dr.ir. B. Platel



What seems astonishing is that a mere three-pound object, made of the same atoms that constitute everything else under the sun, is capable of directing virtually everything that humans have done: flying to the moon and hitting seventy home runs, writing Hamlet and building the Taj Mahal - even unlocking the secrets of the brain itself.

Joel Havemann

Contents

Colophon	ii
Contents	vii
Summary	xi
Samenvatting	xiii
1 General introduction	1
1.1 Preface	2
1.2 Context of this research	3
1.3 Outline	4
2 Clinical background	7
2.1 A history of electrical stimulation	8
2.2 The basal ganglia	9
2.3 Parkinson's disease	10
2.4 Evolution of therapy for Parkinson's disease	12
2.5 The subthalamic nucleus	13
2.6 Deep brain stimulation of the STN	15
3 Technical background	19
3.1 Magnetic resonance imaging	20
3.1.1 Spin physics	20
3.1.2 Imaging protocols	20
3.2 Diffusion MRI	22
3.2.1 Diffusion	22
3.2.2 Magnetic resonance and diffusion	23
3.2.3 Models applied to diffusion MRI	24
3.2.4 Fiber tracking	29
3.3 Functional MRI	31
3.3.1 The BOLD effect	31
3.3.2 fMRI EPI acquisition	31
3.3.3 Experiment design and analysis	32
3.4 Brain connectivity	34
3.4.1 Introduction	34
3.4.2 Structural brain connectivity	37
3.4.3 Functional and effective brain connectivity	38
3.4.4 Connectivity-based parcellation	38

4	The STN on MRI	39
4.1	Introduction	40
4.2	Summary of targeting methods	40
4.2.1	Indirect targeting	40
4.2.2	Direct targeting	41
4.3	Systematic review	41
4.3.1	Search strategy	41
4.3.2	Indirect targeting	42
4.3.3	Direct targeting	46
4.3.4	Comparative studies	49
4.4	Discussion	50
5	Clustering	57
5.1	Introduction	58
5.1.1	Background	58
5.1.2	Related work	58
5.1.3	Aim	59
5.2	Exploration of the rat STN	60
5.2.1	Methods	60
5.2.2	Results	62
5.3	Preliminary clustering experiments	63
5.3.1	Methods	63
5.3.2	Results	66
5.4	A specialized distance measure: the Sobolev norm	68
5.4.1	Theory	68
5.4.2	Methods	73
5.4.3	Results	76
5.5	Discussion	77
5.5.1	Current findings	77
5.5.2	Future work	77
5.5.3	Conclusion	81
5.6	Acknowledgments	81
6	Structural connectivity	83
6.1	Introduction	84
6.1.1	Background	84
6.1.2	Related work	84
6.1.3	Aim	85
6.2	Methods	85
6.2.1	Data acquisition	85
6.2.2	Data preprocessing	86
6.2.3	Identification of the subthalamic nucleus ROIs	88

6.2.4	Probabilistic tractography	89
6.2.5	Connectivity measures	90
6.2.6	Segregation of motor and non-motor regions of the STN . .	92
6.3	Results	93
6.3.1	Probabilistic tractography	93
6.3.2	STN connectivity	93
6.3.3	Segregation of motor and non-motor regions of the STN . .	96
6.4	Discussion	96
6.4.1	Current findings	96
6.4.2	Correspondence of findings with existing literature	97
6.4.3	Clinical perspective	100
6.4.4	Future work	101
6.4.5	Conclusions	102
6.5	Acknowledgments	102
7	Functional connectivity	107
7.1	Introduction	108
7.1.1	Background	108
7.1.2	Related work	108
7.1.3	Aim	109
7.2	Methods	110
7.2.1	Data acquisition	110
7.2.2	Data preprocessing	112
7.2.3	Identification of the subthalamic nucleus ROIs	112
7.2.4	Linear regression analysis	113
7.2.5	Statistical analysis	113
7.2.6	Reverse regression for segregation of STN regions	115
7.3	Results	115
7.3.1	Whole-brain STN connectivity	115
7.3.2	Segregation of STN regions	118
7.4	Discussion	119
7.4.1	Current findings	119
7.4.2	Correspondence of findings with existing literature	120
7.4.3	Clinical perspective	121
7.4.4	Future work	121
7.4.5	Conclusions	122
7.5	Acknowledgments	122
8	General discussion	123
8.1	Contributions	124
8.2	Methodological considerations	126
8.2.1	Localization and registration	126

8.2.2	Diffusion MRI and structural connectivity	127
8.2.3	Functional MRI and functional connectivity	128
8.2.4	Ethical considerations	128
8.3	Future work	129
8.3.1	Imaging for deep brain stimulation	129
8.3.2	Deep brain stimulation and other therapies for Parkinson's .	131
8.4	Conclusion	132
A	Appendix to Chapter 6	133
B	Appendix to Chapter 7	141
	References	147
	List of figures	175
	List of tables	177
	List of abbreviations	177
	List of symbols	181
	Dankwoord	184
	Curriculum vitae	187
	List of publications	189
	PhD portfolio	193

Summary

Hitting the right target

Noninvasive localization of the subthalamic nucleus motor part for specific deep brain stimulation

Deep brain stimulation of the subthalamic nucleus (STN) has gained momentum as a therapy for advanced Parkinson's disease. The stimulation effectively alleviates the patients' typical motor symptoms on a long term, but can give rise to cognitive and psychiatric adverse effects as well. Based on primate studies, the STN has been divided into three functionally different parts, which were distinguished by their afferent and efferent connections. The largest part is the motor area, followed by an associative and a limbic area.

The serious adverse effects on cognition and behavior occurring after deep brain stimulation are assumed to be caused by electrical current spread to the associative and limbic areas of the STN. Therefore, selective stimulation of the motor part of the STN seems crucial, both to obtain the best possible therapeutic effect on the motor symptoms and to minimize the debilitating effects on cognition and behavior. However, current medical imaging techniques do not yet facilitate the required accurate identification of the STN itself, let alone its different functional areas. The final target for DBS is still often adjusted using intraoperative electrophysiology.

Therefore, in this thesis we aimed to improve imaging for deep brain stimulation using noninvasive MRI protocols, in order to identify the STN and its motor part. We studied the benefits and drawbacks of already available noninvasive methods to target the STN. This review did not lead to a straightforward conclusion; identification of the STN motor part remained an open question. In follow-up on this question, we investigated the possibility to distinguish the different functional STN parts based on their connectivity information. Three types of information were carefully analyzed in this thesis.

First, we looked into the clustering of local diffusion information within the STN region. We visually inspected the complex diffusion profiles, derived from postmortem rat brain data with high angular resolution, and augmented this manual segmentation method using k-means and graph cuts clustering. Because the weighing of different orders of diffusion information in the traditionally used \mathbb{L}_2 norm on the orientation distribution functions (ODFs) remained an open issue, we developed a specialized distance measure, the so-called Sobolev norm. This norm does not only take into account the amplitudes of the diffusion profiles, but also their extrema. We showed that the Sobolev norm performs better than the \mathbb{L}_2 norm on synthetic

.....

phantom data and real brain (thalamus) data. The research done on this topic facilitates better classification by clustering of gray matter structures in the (deep) brain.

Secondly, we were the first to analyze the STN's full structural connectivity, based on probabilistic fiber tracking in diffusion MRI data of healthy volunteers. The results correspond well to topical literature on STN projections. Furthermore, we assessed the structural connectivity per voxel of the STN seed region, and discovered a gradient in connectivity to the motor cortical areas within the STN. While going from the medial to the lateral part of the STN, the connectivity increases, confirming the expected lateral location of the STN motor part. Finally, the connectivity analysis produced evidence for the existence of a "hyperdirect" pathway between the motor cortex and the STN in humans, which is very useful for future research into stimulation targets. The results of these experiments indicate that it is possible to find the motor part of the STN as specific target for deep brain stimulation using structural connectivity information acquired in a noninvasive way.

Third and last, we studied functional connectivity using resting state functional MRI data of healthy volunteers. The resulting statistically significant clusters provided us with the first complete description of the STN's resting state functional connectivity, corresponding to the expectations based on available literature. Moreover, we performed a reverse-regression procedure with the average time-series signals in motor and limbic areas as principal regressors. The results were analyzed for each STN voxel separately and also showed mediolateral gradients in functional connectivity within the STN. The lateral STN part exhibited more motor connectivity, while the medial part seemed to be more functionally connected to limbic brain areas, as described in neuronal tracer studies. These results show that functional connectivity analysis also is a viable noninvasive method to find the motor part of the STN.

The work on noninvasive MRI methods for identification of the STN and its functional parts, as presented in this thesis, thus contributes to future specific stimulation of the motor part of the STN for deep brain stimulation in patients with Parkinson's disease. This may help to maximize the motor effects and minimize severe cognitive and psychiatric side effects.

Samenvatting

Diepe hersenstimulatie van de nucleus subthalamicus (STN) is een populaire therapie geworden voor de ziekte van Parkinson in een gevorderd stadium. De stimulatie verlicht de typische motorische symptomen van de patiënten op effectieve wijze en op lange termijn, maar kan ook cognitieve en psychiatrische bijwerkingen veroorzaken. Op basis van experimenten met primaten is de STN onderverdeeld in drie verschillende functionele gebieden, die onderscheiden konden worden door hun afferente en efferente verbindingen. Het motorisch gebied is het grootste deel, gevolgd door een associatief en een limbisch gebied.

De serieuze bijwerkingen op het gebied van cognitie en gedrag die optreden na diepe hersenstimulatie worden vermoedelijk veroorzaakt door een spreiding van elektrische stroom naar de associatieve en limbische gebieden van de STN. Het lijkt daarom essentieel om selectief het motorisch deel van de STN te stimuleren, zowel om het best mogelijke therapeutische effect op de motorische symptomen te bereiken, als om de invaliderende effecten op cognitie en gedrag te minimaliseren. Echter, met de huidige technieken voor medische beeldvorming is het nog niet mogelijk om de STN zelf precies te identificeren, laat staan de verschillende functionele gebieden. Het uiteindelijke doel bij diepe hersenstimulatie wordt daarom nog vaak bijgesteld met behulp van intraoperatief elektrofysiologisch onderzoek.

De doelstelling van dit proefschrift was dan ook het verbeteren van de beeldvorming voor diepe hersenstimulatie door middel van niet-invasieve MRI protocollen, om zo de STN en zijn motorisch deel te identificeren. We hebben de voor- en nadelen van reeds beschikbare niet-invasieve methoden om de STN te vinden bestudeerd. Dit overzicht heeft niet geleid tot een duidelijke conclusie; de vraag naar identificatie van het motorisch deel van de STN bleef open. Als vervolg hierop hebben we onderzocht of het mogelijk is om de verschillende functionele delen van de STN te onderscheiden op basis van hun connectiviteit. In dit proefschrift zijn drie soorten informatie met betrekking tot connectiviteit nauwkeurig onderzocht.

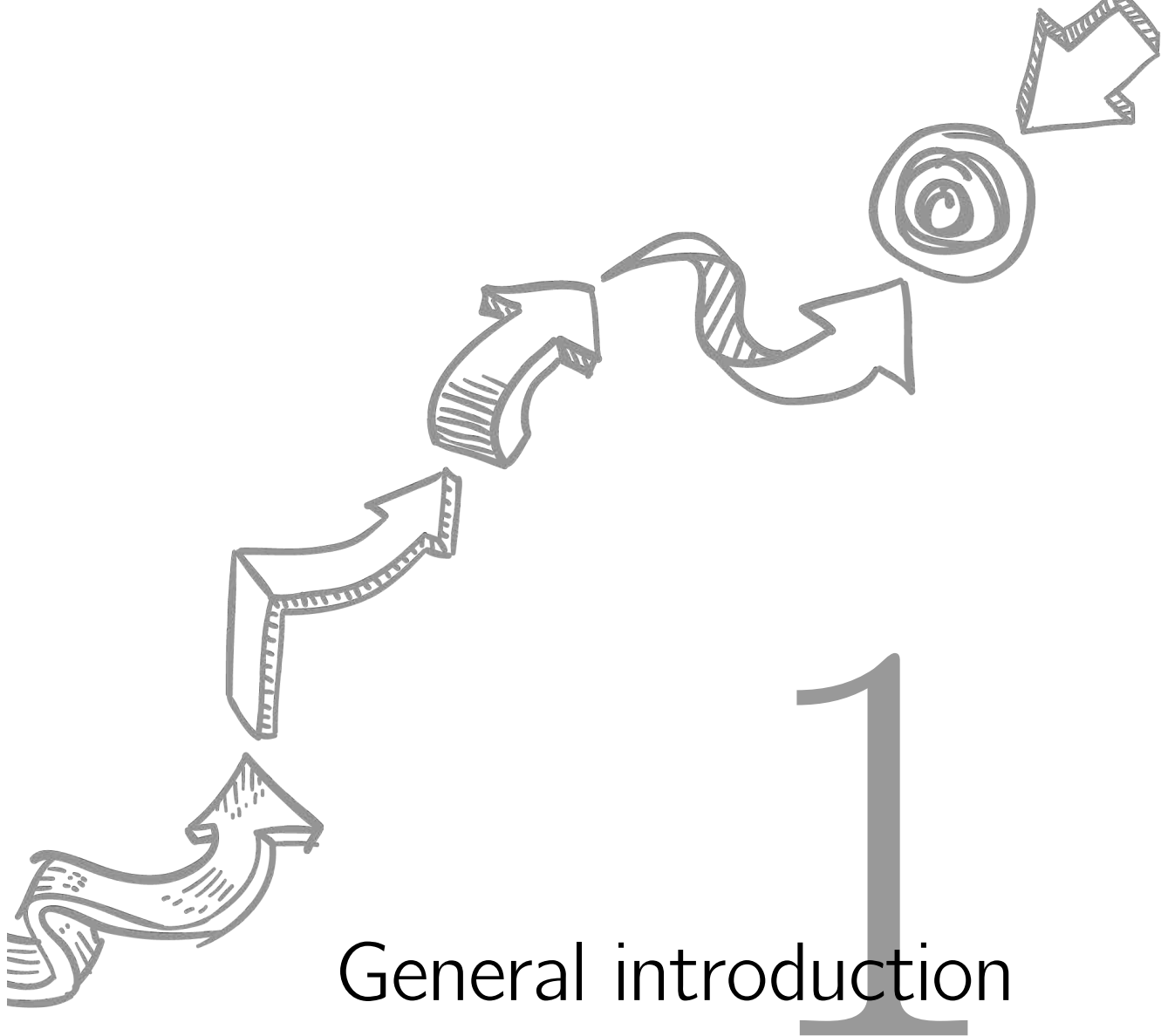
Als eerste hebben we gekeken naar het clusteren van lokale diffusie-informatie in het STN gebied. We hebben de complexe diffusieprofielen, afgeleid van data met een hoge hoekresolutie, gemaakt van postmortem rattenhersenen, eerst visueel geïnspecteerd. Deze handmatige segmentatiemethode is vervolgens uitgebreid met k-means en graph cuts clustering. Omdat het wegen van verschillende ordes van diffusie-informatie in de traditionele \mathbb{L}_2 norm op de oriëntatie-distributiefuncties (ODF's) een belemmering vormde, hebben we een speciale afstandsmaat ontwikkeld, de zogenaamde Sobolev norm. Deze norm houdt niet alleen rekening met de amplitudes van de diffusieprofielen, maar ook met hun extrema. We hebben laten zien dat de Sobolev norm beter presteert dan de \mathbb{L}_2 norm op synthetische fantoomdata

en echte data van de thalamus in de hersenen. Dit onderzoek maakt het mogelijk om kernen van grijze stof (diep) in de hersenen beter te classificeren door middel van clustering.

Ten tweede hebben we als eerste de volledige structurele connectiviteit van de STN geanalyseerd, gebaseerd op probabilistische fiber-tracking in diffusie-gewogen MRI data van gezonde vrijwilligers. De resultaten komen goed overeen met de projecties van de STN zoals beschreven in de literatuur. Bovendien hebben we de structurele connectiviteit van elk voxel in de STN regio bepaald, waarbij we ontdekten dat de connectiviteit met de premotorische cortex een verloop vertoont binnen de STN. Deze connectiviteit neemt toe als we van het mediale naar het laterale deel van de STN gaan en bevestigt daarmee de verwachte laterale lokatie van het motorische deel van de STN. Tenslotte vonden we op basis van onze analyse ook bewijs voor het bestaan van een “hyperdirecte” baan tussen de motorische cortex en de STN in de mens, wat heel nuttig is voor toekomstig onderzoek naar mogelijke gebieden voor stimulatie. De resultaten van deze experimenten geven aan dat het mogelijk is om op basis van structurele connectiviteit, informatie verkregen op een niet-invasieve manier, het motorisch deel van de STN te vinden als specifiek doel voor diepe hersenstimulatie.

Als derde en laatste hebben we functionele connectiviteit bestudeerd, gebaseerd op functionele MRI data van gezonde vrijwilligers in rust. De resulterende significante clusters geven ons de eerste complete omschrijving van de functionele connectiviteit in rust van de STN, die overeenkomt met de verwachtingen gebaseerd op de beschikbare literatuur. Bovendien hebben we ook een omgekeerde regressie uitgevoerd, met de gemiddelde signalen over tijd in motorische en limbische gebieden als belangrijkste regressor variabelen. De resultaten zijn voor elk voxel van de STN apart geanalyseerd en vertoonden ook een mediolateraal verloop in functionele connectiviteit in de STN. Het laterale deel van de STN liet meer motorische connectiviteit zien, terwijl het mediale deel meer functioneel verbonden leek met limbische hersengebieden, zoals beschreven in experimenten met neuronale tracers. Deze resultaten laten zien dat analyse van functionele connectiviteit ook een uitvoerbare niet-invasieve methode is om het motorisch deel van de STN te vinden.

Het werk op het gebied van niet-invasieve MRI methoden voor identificatie van de STN en zijn functionele gebieden, zoals gepresenteerd in dit proefschrift, draagt dus bij aan toekomstige specifieke stimulatie van het motorisch deel van de STN voor diepe hersenstimulatie in patiënten met de ziekte van Parkinson. Dit zou kunnen helpen om de motorische effecten te maximaliseren en de ernstige cognitieve en psychiatrische bijwerkingen te minimaliseren.



General introduction

*Alice laughed. "There's no use trying," she said "one can't believe impossible things."
"I daresay you haven't had much practice," said the Queen. "When I was your age,
I always did it for half-an-hour a day. Why, sometimes I've believed
as many as six impossible things before breakfast."*

Lewis Carroll - Alice in Wonderland

1.1 Preface

ser·en·dip·i·ty | ,serən'dipitē | (noun)

the occurrence and development of events by chance in a happy or beneficial way:
a fortunate stroke of serendipity | a series of small serendipities

Throughout the history of science, serendipity has played an important role in many discoveries. Famous examples include the “Eureka” that Archimedes exclaimed while bathing, and the epiphany that Newton experienced under his apple tree. In modern medicine, the discovery of new therapies is still often serendipitous. The lucky stroke that provided us with penicillin is well-known, but other widespread drugs such as chlorpromazine (an antipsychotic drug [199]) and cisplatin (a chemotherapy agent [4]) were also discovered while looking for something different.

The same holds for the series of events that enabled high-frequency stimulation of a small part in the brain, the subthalamic nucleus, in patients with Parkinson’s disease. The idea of “switching off” brain areas in order to cure these patients stems from a serendipitous discovery by Irving Cooper, one of the pioneers in functional neurosurgery [147, 291, 319]. In 1952, he wanted to perform a pedunculotomy, i.e., lesion the motor pathway at the level of the midbrain, to paralyze the patient and stop his tremor. During the intervention, Cooper ruptured an artery in the brain, forcing him to ligate (tie off) the artery and abort the pedunculotomy. To everyone’s surprise, when the patient awoke, his tremor had gone and no signs of paralysis were present. Consequently, people investigated how to mimic the lesion that was caused by the ligation of the artery and the subsequent small brain infarct.

Another serendipity that has been very important for research on deep brain stimulation and Parkinson’s disease, is the discovery of parkinsonism induced by MPTP (1-methyl-4-phenyl-1,2,3,6-tetrahydropyridine) in the early 1980s [176]. This happened by means of a dramatic outbreak of parkinsonism among young drug-abusers in California, caused by a contaminated batch of drugs. Analysis of the drugs that were used, the symptoms, and autopsy data of an earlier case in 1976, pointed towards degeneration of a brain part called the substantia nigra caused by the toxic MPTP. The biggest breakthrough came when MPTP appeared to induce Parkinson’s disease in primates, as research on Parkinson’s was until then restricted by the lack of an animal model on which to test possible therapies.

Even Alim-Louis Benabid (see Figure 2.1), the man who developed deep brain stimulation for Parkinson’s disease with his Grenoble group in the late 1980s, rather modestly put his discovery down to luck [327].

During the research done for this thesis, no serendipitous findings were done. Fortunately, we did find answers to the research questions that we had started with. The

context of our research and the rationale and outline of this thesis will be discussed in the next sections.

1.2 Context of this research

Deep brain stimulation (DBS) involves a chronic implantation of electrodes into a specific part deep in the brain, in order to deliver continuous high-frequency stimulation to this area. Soon after its introduction in 1993 [246], deep brain stimulation of the subthalamic nucleus (STN), a gray matter nucleus of 240 mm³ in humans, became a widely recognized therapy for advanced Parkinson's disease (PD). With respect to typical PD motor symptoms, it has been proven that DBS of the STN is an effective treatment, which has a significant long-term beneficial impact on these symptoms [34, 259, 321].

However, stimulation-induced adverse effects such as cognitive alterations and psychiatric side effects occur in a substantial number of patients [41, 245, 258, 277, 300, 318]. Although dopaminergic withdrawal, premorbid neuropsychiatric vulnerability, and psychosocial factors play a role as well, it is believed that these behavioral side effects can be accounted for by a spread of current beyond the functional target in the STN. Primate studies have shown that the STN can be divided into three functionally different parts, namely a motor, an associative, and a limbic part, from large to small [136, 233, 298]. Hence, it is assumed that the side effects are caused by a spread of current induced by the stimulator beyond the STN motor part, to the associative and limbic pathways running through the STN [298].

Therefore, accurate targeting and subsequent selective stimulation of the motor part of the STN is of utmost importance: not only to achieve the best possible effect on the PD motor symptoms [123, 308], but also to minimize the undesirable adverse effects on cognition and behavior. Yet, current medical imaging techniques do not facilitate such an accurate planning procedure. The method for primary targeting of the STN before DBS still varies greatly between centers [185]. In addition, most DBS procedures involve a secondary targeting step using intraoperative assessments, such as microelectrode recordings (MER) or macrostimulation, to adapt the position of the electrodes to the clinical aim of stimulation of the STN motor part [55, 87].

Unfortunately, noninvasive methods to stimulate the motor part of the STN specifically do not yet exist. Furthermore, it is still unknown to what extent the functionally different subregions actually overlap in the human STN. The effect of a more accurate stimulation of the motor part is related to this level of segregation. Current literature describes that the different parts of the STN play a role in different functional pathways, and as such can be distinguished by their afferent and efferent projections [136, 233, 298]. These projections can be mapped by noninvasive MRI

techniques that provide information on brain connectivity. On the one hand, the MRI acquisition can be sensitized to diffusion, which enables estimation of the nerve fibers between different regions of the brain and the so-called structural connectivity. On the other hand, neural activity can be measured with functional MRI, in order to visualize correlations in brain activity (the so-called functional connectivity).

We hypothesize that it is possible to distinguish the different functional parts of the STN using noninvasive MRI protocols. From this hypothesis, we have derived some research questions that we would like to answer in this thesis:

1. Can the local fiber structure within the STN region be assessed using diffusion MRI?
2. Is it possible to map the projections of the STN and thus structural connectivity of the STN based on diffusion MRI?
3. Can the brain regions that display correlation in activity, and as such are functionally connected to the STN, be identified using functional MRI?
4. Given the answers to questions 1 to 3, to what extent do the different STN parts overlap and is it possible to stimulate the motor part specifically?

If segmentation and subsequent specific stimulation of the STN motor part would be feasible, motor results of deep brain stimulation in Parkinson's disease could be enhanced and the serious side effects reduced.

1.3 Outline

The aim of this thesis is to investigate whether the structural and functional connectivity of the STN can be mapped using noninvasive MRI protocols. Moreover, we would like to determine the level of segregation of the motor and non-motor parts of the STN based on these connectivity results, possibly combined with local diffusion information.

In **Chapter 2**, we will elucidate the clinical background of this research. In addition to discussing historical forms of electrical stimulation therapy, we will also show how the typical symptoms of Parkinson's disease are caused by a disbalance in the so-called basal ganglia system. Subsequently, we will explain how therapy for Parkinson's disease has evolved into contemporary deep brain stimulation.

The technical background of this research will be elaborated on in **Chapter 3**. This chapter will discuss principles that have been used for our data acquisition, ranging from MR physics to specific diffusion and functional MRI sequences. In addition,

we will explain fiber tracking in diffusion MRI data and different modes of brain connectivity, based on both diffusion and functional MRI.

We have reviewed the noninvasive methods already available to identify the STN and we will present the results in **Chapter 4**. This chapter will give a systematic overview of techniques for primary targeting of the (dorsolateral part of the) STN, discussing both indirect and direct targeting studies, as well as comparative papers. Finally, the advantages and disadvantages of the targeting techniques will be discussed. The overall focus of this review will lie on MRI, because this modality is most widely used, and has also proven to be more effective than ventriculography and CT.

Since anatomical MRI did not seem to be sufficient to segment the STN parts, we proceeded with diffusion MRI. We started with a feasibility study, locally investigating the added value of noninvasive diffusion MRI and specifically HARDI (high angular resolution diffusion imaging), by visual inspection of the rat STN region. The results of this experiment will be presented in **Chapter 5**. In addition to the visual inspection, we have also performed automatic clustering experiments on the rat data, using k-means and graph cuts algorithms. Lastly, we will introduce a new norm for clustering of diffusion MRI, the so-called Sobolev norm. This norm does not only take into account the amplitudes of the diffusion profiles, but also the coincidence of extrema, and performs well on synthetic and real data.

We have also used diffusion MRI beyond the STN region, of which we will present the results in **Chapter 6**. We will give a full description of the structural connectivity of the STN in human volunteers based on diffusion MRI and probabilistic fiber tracking. Furthermore, we have investigated the level of separation between the motor and non-motor parts of the STN based on local differences in structural connectivity. Apart from these results, we will also show the evidence for the existence of the so-called “hyperdirect” pathway. This pathway is important because it could be used to target the STN motor part using electrophysiology and might also be a new stimulation target in itself.

In addition to the structural connectivity analysis, we have followed a similar approach to determine the functional connectivity of the STN, based on resting state BOLD functional MRI. The results of this analysis will be presented in **Chapter 7**. In this chapter, we will first present a complete account of the functional connectivity of the STN, based on a seed correlation approach. Afterwards, we will proceed with the local functional connectivity per voxel of the STN, in order to investigate the overlap between the motor and other parts of the STN.

Finally, in **Chapter 8** we will provide a general discussion, including conclusions and implications for future research.



Clinical background

When prescribing one of the drugs I take, my doctor warned me of a common side effect: exaggerated, intensely vivid dreams. To be honest, I've never really noticed the difference. I've always dreamt big.

Michael J. Fox

2.1 A history of electrical stimulation

Since antiquity, humans have used electrical stimulation to modulate the nervous system [260, 270]. Apparently, the ancient Egyptians already used Nile catfish to treat headaches and neuralgia (nerve pain) [163]. However, the first written record stems from the Roman era, when the physician Scribonius Largus suggested the use of electric rays as therapy for headaches and gout in 46 A.D. [164]. Fortunately, electrical stimulation as a therapy has progressed since then, although the so-called electro-ichthyotherapy continued to be applied in Europe until the middle of the nineteenth century, and even longer among American and African tribes [164].

In the late 1800s, the invention of the voltaic cell and the electrical generator facilitated the application of electric currents for a variety of disorders. The patient response (e.g., contralateral movement) occurring during such procedures induced pioneering experiments on cortical excitability in dogs by Fritsch and Hitzig [114], and seriously ill patients by Bartholow [23] and Horsley [148] (see Figure 2.1). However, the technology back then was not yet advanced enough to consider stimulation electrodes that did not hinder patient motility. For decades, ablations were performed instead, for example cortical ablations [149] and ablations of the basal ganglia [207]. In addition, the operating microscope did not yet exist, so ablation procedures were open interventions with significant morbidity and mortality rates. The latter issue was reduced upon the introduction of the stereotactic frame [281]. Unfortunately, there were still cases of inaccurate stereotactic targeting, possibly due to patient-specific anatomy or brain shift.

Electrical stimulation and recording therefore became of great help in stereotactic lesioning procedures. These techniques were used during the intervention to probe the location of vital structures and consequently avoid them [142], and for several days before a thalamotomy [98]. The development of the stereotactic frame and electrophysiological recordings boosted the use of stereotactic functional neurosurgery

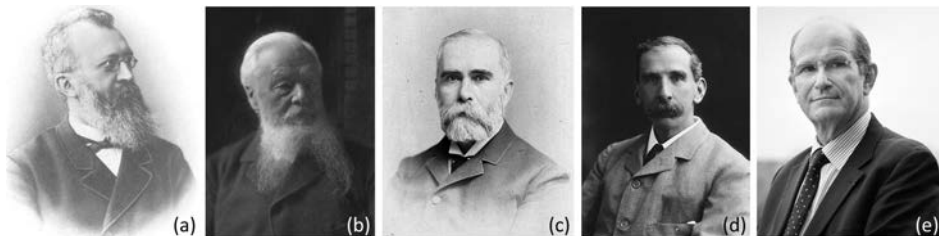


Figure 2.1 Pioneers of deep brain stimulation. (a) Eduard Hitzig (1838–1907). (b) Gustav Fritsch (1838–1927). (c) Robert Bartholow (1831–1904). (d) Victor Horsley (1857–1916). (e) Alim-Louis Benabid (1942). Images (a)–(d) from Wikipedia, image (e) from www.inserm.fr.

in the late 1950s. To treat pain and psychiatric disease, cingulotomy, anterior capsulotomy and subcaudate tractotomy replaced the ice-pick frontal leukotomies by Freeman [297]. For Parkinson's disease and dystonia, pallidotomy and thalamotomy were introduced. In addition, the 1960s brought the first implantable pacemaker [59] and radiofrequency-driven spinal cord stimulator [260].

A decade later, stereotactic functional neurosurgery for psychiatric diseases ground to a halt due to the introduction of chlorpromazine medication [168]. For Parkinson's disease, something similar happened, as we will see in Section 2.4. However, before discussing Parkinson's disease, it is convenient to explore the anatomy and functionality of the basal ganglia, the brain area where this disorder originates.

2.2 The basal ganglia

The basal ganglia are a group of subcortical structures (see Figure 2.2), which have a critical influence on movement planning and cognitive behaviors [122]. The group comprises two input nuclei, namely the striatum (consisting of the caudate nucleus and putamen) and the subthalamic nucleus (STN). These input nuclei receive excitatory signals from the cerebral cortex, many parts of the brainstem (via the thalamus), and the limbic system. The main output nuclei are the substantia nigra pars reticulata (SNr) and the medial globus pallidus (GPi). They provide mostly inhibitory efferents to nuclei of the thalamus (which then project back to the cerebral cortex) and to premotor areas of the midbrain and brainstem. The external globus pallidus (GPe) has only an intrinsic function. This also holds for the substantia nigra pars compacta (SNc), that provides the striatum with important modulatory signals [248].

The projections that are received and emitted by the basal ganglia are organized in several so-called cortico-basal ganglia-thalamocortical circuits. Each of these circuits originates from specific parts of the cortex, travels via specific thalamic nuclei, and projects back to at least one of the cortical input areas. Five different circuits are distinguished, namely the motor, oculomotor, limbic, and two prefrontal (dorsolateral and lateral orbitofrontal) circuits [5, 298], of which the motor circuit is most relevant to the pathophysiology of movement and thus Parkinson's disease.

In Figure 2.3(a) the functional motor circuit for the basal ganglia is shown. Two circuits can be distinguished: a direct pathway, from the cortex via the putamen, GPi/SNr complex, and the thalamus back to the cortex; and an indirect pathway, that includes the GPe and the STN in this loop. The existence of a hyperdirect pathway from the cortex to the STN has been described in primates [217, 218] and is still subject to research in humans. In Parkinson's disease (see Figure 2.3(b)), the decreased dopamine production in the SNc causes decreased inhibition of the

STN. This gives rise to hyperactivity of the STN, which in turn leads to a decreased excitation of the cortex. The direct and indirect pathway thus form a delicate dual control mechanism that is disturbed in Parkinson's disease.

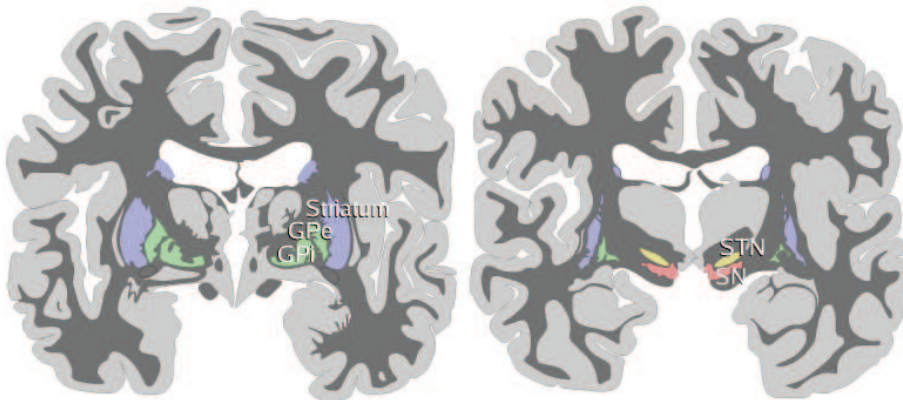


Figure 2.2 The basic anatomy of the brain showing the major regions within the basal ganglia: the striatum (blue), the globus pallidus (green, consisting of a medial and a lateral part, abbreviated as GPi and GPe, respectively), the subthalamic nucleus (yellow, abbreviated as STN), and the substantia nigra (red, abbreviated as SN). Image from Wikipedia.

2.3 Parkinson's disease

Parkinson's disease (PD) is a common, progressive neurological condition, estimated to affect 100–180 per 100,000 of the population [219]. This prevalence will grow as populations shift in age, and is expected to be doubled in Western Europe's five and the world's ten most populous nations by 2030 [88]. The disease is named after James Parkinson, who vividly described it in his 1817 essay [236].

PD is a progressive neurodegenerative disorder, caused by the preferential cell death of dopaminergic neurons in the SNc. This degeneration leads to a marked deficit of the neurotransmitter dopamine, which normally modulates the striatal output in the direct as well as in the indirect pathway. The shortage causes neurons in the direct pathway (see Section 2.2 and Figure 2.3(b)) to be activated less easily, reducing their inhibitory influence on GPi and SNr and contributing to the excessive output activity. The neurons in the indirect pathway experience reduced inhibition due to the dopamine decrease. This leads to overinhibition of GPe, disinhibition (and thus hyperactivity) of STN, and also to increased excitation of GPi and SNr. In short, PD can be said to involve a pathological non-equilibrium between the direct and indirect pathway of the motor circuit [122, 290].

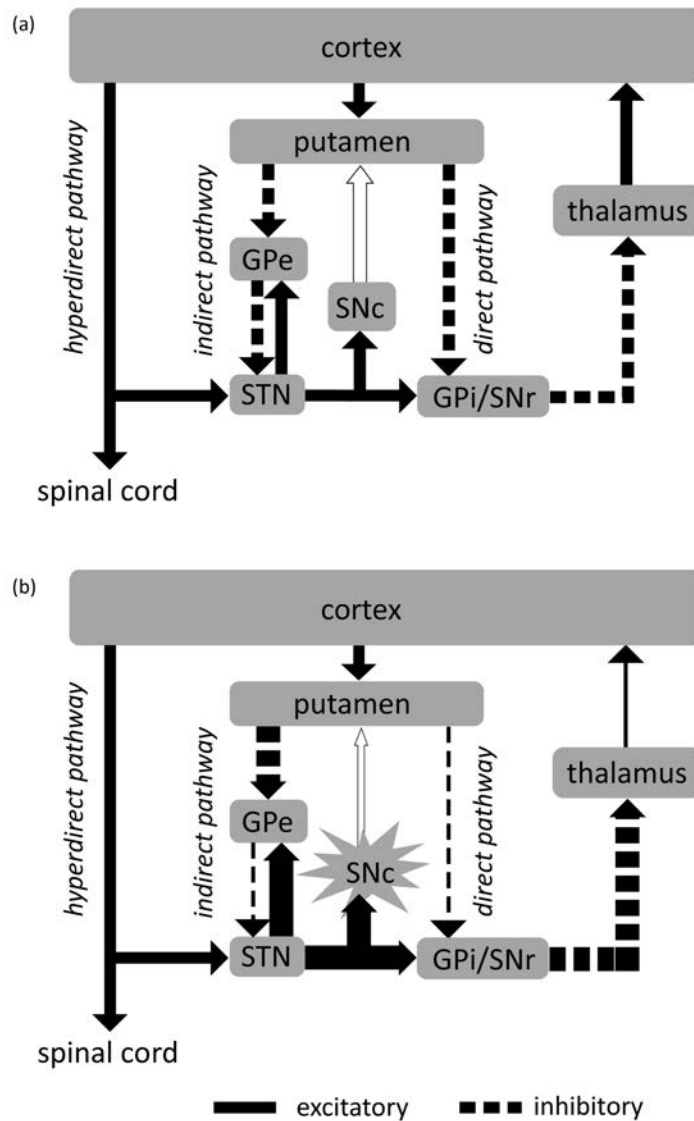


Figure 2.3 A simplified representation of the motor cortico-basal ganglia-thalamocortical circuit in normal state (a) and Parkinson's disease (b). GPe = lateral globus pallidus; GPi = medial globus pallidus; SNr = substantia nigra pars reticulata; SNc = substantia nigra pars compacta; STN = subthalamic nucleus. Adapted from [225] and [290].

People with PD present classical symptoms associated with parkinsonism, such as rigidity, bradykinesia, hypokinesia, akinesia, and rest tremor, declining people's ability to complete even simple motor tasks [70]. Rigidity refers to the increased stiffness of a patient's limbs. Bradykinesia (i.e., slowness of movement), hypokinesia (i.e., poverty of movement), and akinesia (i.e., absence of normal unconscious movements, such as arm swing in walking) can manifest themselves as a variety of symptoms, for example a decreased size and speed of handwriting, a decreased stride length, and drooling [77]. Although PD is predominantly a movement disorder, patients frequently suffer from other impairments, including psychiatric problems such as depression and dementia [219].

Unfortunately, there is no preventive therapy for PD, as the underlying mechanism of the dopaminergic cell degeneration remains elusive. About 85–90% of PD cases are idiopathic, i.e., without known cause, while the remainder are familial, caused by gene mutations. Previous research has suggested that PD is a multi-factorial disease, that can be attributed to several factors working in conjunction, such as intracellular toxic aggregates, formed through oxidative modification, mitochondrial dysfunction, or genetic alterations, and the susceptibility of the dopaminergic neurons to these conditions [165]. Parkinsonism can also be caused by drugs and less common conditions such as cerebral infarction, progressive supranuclear palsy and multiple system atrophy [219].

2.4 Evolution of therapy for Parkinson's disease

As discussed in Section 2.1, lesioning of the thalamus (thalamotomy, reducing tremor) and of the globus pallidus (pallidotomy, reducing both tremor and rigidity) were used to treat Parkinson's disease from the 1950s onward [270]. However, this development was soon replaced by another revolution: the introduction of oral levodopa (L-dopa) therapy in 1968 [116, 117]. Levodopa is a precursor of dopamine, which proved to exert a positive influence on akinesia as well as the other symptoms. However, after a few years, people came to realize that levodopa was not the magic cure it had initially seemed to be [116]. Side effects of chronic levodopa treatment such as dyskinesias (diminished voluntary movements and increased involuntary movements) and motor "on-off" fluctuations, caused by the continuing progress of PD and a decreasing levodopa response, became apparent [288, 315].

These issues revived the interest in stereotactic functional neurosurgical procedures. Although the thalamus had been the preferred target before the uprise of medication, new studies were focusing on pallidotomy [170, 171], because of growing insights in outcome measures [297] and basal ganglia circuitry [80]. Given the experience with stimulation of the thalamus for chronic pain [254] and tremor [36, 43], which

showed that high-frequency stimulation has the same clinical effect as lesioning, and the reduced safety risks of this procedure in comparison to thalamotomy [271], it did not take long to adapt deep brain stimulation (DBS) of the pallidum as alternative to pallidotomy [275].

At the same time, another line of research focused on a new target for DBS: the subthalamic nucleus [246]. Although the STN and zona incerta target had been investigated in the 1960s [13], most surgeons chose to avoid this region for fear of causing ballism (involuntary movements). However, primate experiments [80] nursed the idea of an important role for the STN in brain circuitry in PD. This idea could be put to the test when a primate model of PD was developed by means of the MPTP ((1-methyl-4-phenyl-1,2,3,6-tetrahydropyridine) monkey [53]. The outcome was positive: lesioning or stimulation of the STN in MPTP monkeys alleviated tremor, rigidity, and bradykinesia, without causing ballism [19, 38, 40].

2.5 The subthalamic nucleus

As described in Section 2.2, the STN, the most recent target for DBS in PD, is a very important input nucleus of the basal ganglia. The STN displays a hyperactivity that causes inhibition of the motor circuit target structures in a patient with Parkinson's disease. Anatomically, the STN can be described as a biconvex or peanut-shaped structure that is surrounded by white matter bundles, as is shown in Figure 2.4. In humans, it contains about 560,000 neurons and has a volume of 240 mm³. Anteriorly and laterally, the STN is enveloped by the internal capsule that separates the nucleus from the globus pallidus. Rostromedially, the STN borders the Fields of Forel and the posterior lateral hypothalamic area, while it is adjacent to the red nucleus on its posteromedial side. The STN is limited ventrally by the cerebral peduncle and the substantia nigra, while dorsally the fasciculus lenticularis and the zona incerta separate it from the ventral thalamus.

Similar to the rest of the basal ganglia, the STN plays a role in multiple circuits. Tracer studies in primates have reported that within the motor circuit, the STN is connected with the primary motor cortex, premotor and supplementary motor cortex, and the somatosensory cortex [140, 216, 218, 232]. With respect to the deep brain nuclei, the STN exhibits connectivity with the striatum, the central and ventrolateral part of the lateral globus pallidus (GPe), the ventrolateral part of the medial globus pallidus (GPi), and the thalamus [57, 158, 233, 262, 274]. Concerning the associative loop, the STN is connected to the orbitofrontal and dorsolateral prefrontal cortex, as well as the centromedian-parafascicular nuclei of the thalamus, the nucleus accumbens, the ventral part of the putamen and caudate nucleus, the ventral pallidum, the ventral tegmental area, and the medial part of the substantia

2.5. The subthalamic nucleus

nigra reticulata [5, 6, 7, 57, 140, 215, 233]. For the limbic circuit, tracer studies have presented connections with the (para)limbic cortical areas such as the anterior cingulate and the medial orbitofrontal cortex [6]. Subcortically, the limbic loop comprises the nucleus accumbens, ventral pallidum, ventral tegmental area, substantia nigra pars reticulata, globus pallidus, thalamus, hippocampus and amygdala [6, 129].

The different afferent and efferent connections per circuit in primates have led to a tripartite functional subdivision of the STN in current literature [136, 233, 298]. With respect to this subdivision, the medial tip of the nucleus is devoted to the limbic circuit and the associative part is situated ventrolaterally. The motor subterritory, which is the largest part, comprising two-thirds of the nucleus, is located at the dorsolateral side of the STN. Though schematic figures such as Figure 2.5 exist that show the three functional parts of the STN, it is still not obvious to what extent these functional areas are segregated within the human STN.

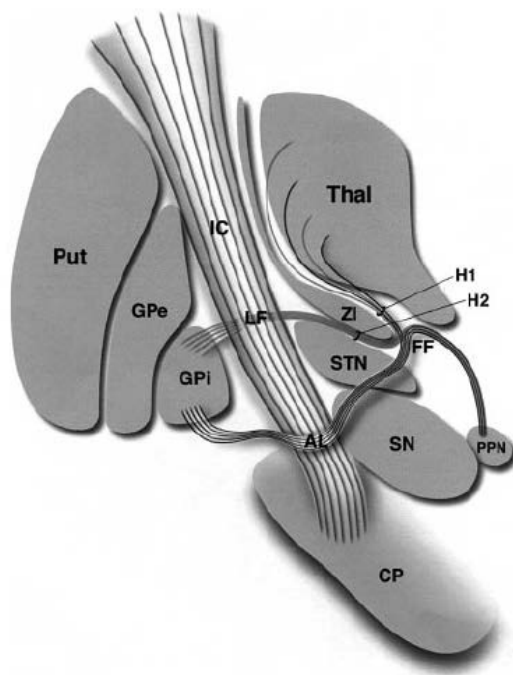


Figure 2.4 Representation of the major anatomical structures and fiber tracts associated with the subthalamic nucleus. AL = ansa lenticularis; CP = cerebral peduncle; FF = Fields of Forel; GPe = lateral globus pallidus; GPi = medial globus pallidus; H1 = H1 Field of Forel (thalamic fasciculus); IC = internal capsule; LF = lenticular fasciculus (H2); PPN = pedunculopontine nucleus; Put = putamen; SN = substantia nigra; STN = subthalamic nucleus; Thal = thalamus; ZI = zona incerta. Image taken from Hamani et al. [136].

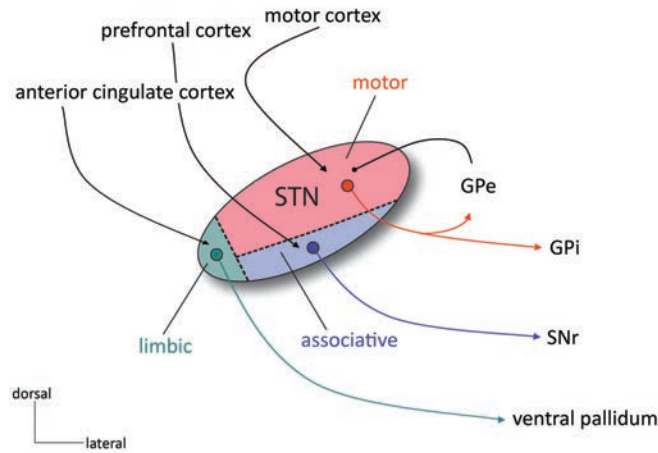


Figure 2.5 The functional subdivision of the STN into different parts and circuits is illustrated here. The STN is divided in the somatomotor part (red) located dorsolaterally, the associative part (blue) located ventromedially and the limbic part (green) on the medial tip. Image adapted from Benarroch [37].

2.6 Deep brain stimulation of the STN

Soon after its introduction in a case report in 1993 [246], DBS of the STN became a widely recognized therapy for advanced PD. STN DBS has a significant long-term beneficial impact on PD motor symptoms [34, 259, 321]. It involves the implantation of one or two quadripolar electrodes into the STN. These electrodes are connected to an internal pulse generator, a battery-powered neurostimulator that is placed subcutaneously below the clavicle (see Figure 2.6) and sends electrical currents to the brain to interfere with neural activity at the target site. The inhibitory effect is reached by high-frequency stimulation, most often monopolar at 130 or 185 Hz, with a typical pulse width of 60 μ s and a voltage around 3 V [134].

There is still no complete theory regarding the mechanism of these electrical currents working on deep brain structures. As has been described by Temel et al. [298], a popular hypothesis is that DBS causes a reduction of neuronal activity through a depolarization block, leading to an interruption of spontaneous activity within the neurons [42]. Another idea is that the silencing of target nuclei is achieved by the stimulation of inhibitory afferents and the consequent release of inhibitory neurotransmitters [213]. Even more complex is the statement that DBS can have opposing effects on structures being stimulated, depending on the cellular architecture. The similarity in clinical outcomes between DBS and lesions led to the proposition

2.6. Deep brain stimulation of the STN

that DBS inhibits the target being stimulated. Recordings of the stimulated nucleus show inhibition during and after the stimulus train [39, 103, 292]. However, electrical recordings in efferent nuclei indicate that DBS increases the output of the stimulated nucleus [141, 328].

Patients are only eligible for a DBS operation when they meet a list of requirements. In the first place, the clinical findings have to be consistent with idiopathic Parkinson's disease. Second, the patient should suffer from severe fluctuations in the pharmacological response and/or dyskinesias, despite optimal pharmacological treatment. Finally, a good initial levodopa response is necessary (except for patients who suffer from levodopa-resistant resting tremor) [33, 83, 315]. Exclusion criteria are significant brain atrophy, multiple white matter lesions, other focal anomalies in the brain (as visible on MRI), parkinsonism with known causative factors, classification in phase 5 of the Hoehn and Yahr scale at the best moment of the day (the patient is then completely invalidated), psychoses, significant cognitive disfunction, and severe affective disorders. Naturally, the general contra-indications for surgery, like severe hypertension or coagulation diseases, are also applicable [315].

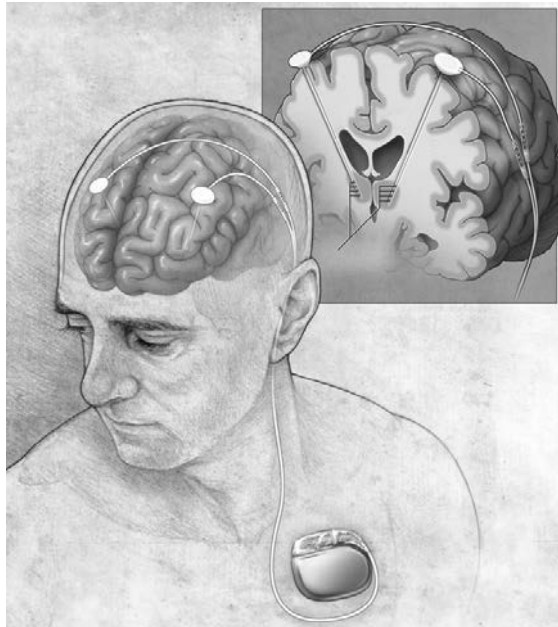


Figure 2.6 The deep brain stimulation system includes quadripolar electrodes inserted into the brain, that are connected with the internal pulse generator via inline extensions running behind the ear. Image adapted from Thevathasan and Gregory [302].

As described in the beginning of this section, STN DBS induces a distinct long-term improvement in motor function [34, 259, 321]. On the other hand, the procedure can be accompanied by a set of complications and side effects, which may occur at any time from surgery to several years postoperatively. The rate of surgical complications in DBS is usually low and their severity mild and reversible. These complications can be infections (most often superficial and manageable), or related to the hardware, such as lead fracture and dislocation. In addition, problems can occur due to electrode insertion, e.g., hemorrhages, a rare but severe complication, or epileptic attacks. Some patients experience confusion immediately postoperatively, from which they recover within 2–3 days on average [33, 300, 315].

However, on the long run, stimulation-induced adverse effects such as cognitive alterations and psychiatric side effects occur in a substantial number of patients [41, 245, 258, 277, 300, 318]. Psychiatric side effects can include depression and (hypo)mania, or scarcer complications such as anxiety disorders, personality changes, hypersexuality, apathy, and aggressiveness. It is believed that these behavioral side effects can be accounted for by a spread of current to the associative and limbic pathways running through the STN [298], although dopaminergic withdrawal, pre-morbid neuropsychiatric vulnerability, and psychosocial factors play a role as well. Hence, accurate targeting and subsequent selective stimulation of the motor part of the STN is of great importance: to achieve the best possible effect on the PD motor symptoms [123, 308], but also to minimize the undesirable adverse effects on cognition and behavior.



Technical background

When something's dark, let me shed a little light on it

Pearl Jam - The Fixer

3.1 Magnetic resonance imaging

3.1.1 Spin physics

Without taking all the workup into account, an MRI scan typically starts with the excitation of the nuclei under investigation [159, 204, 316, 323]. Before the excitation, the net magnetization vector \mathbf{M}_0 of these nuclei is aligned with the main magnetic field \mathbf{B}_0 . After excitation with a 90-degree radiofrequency (RF) pulse, the net magnetization vector is flipped into the plane perpendicular to the main magnetic field. As a result, the longitudinal component of the magnetization M_{\parallel} , lying along \mathbf{B}_0 , will diminish, while the transverse magnetization M_{\perp} , lying in the perpendicular plane, will increase.

Immediately afterwards, different processes will begin. The longitudinal component M_{\parallel} will gradually return to its steady-state magnitude. This so-called longitudinal relaxation takes places with time constant T_1 . The transverse component M_{\perp} also experiences relaxation: the spins will dephase and the transverse magnetization will be restored to equilibrium (i.e., zero magnitude), with time constant T_2 . If the magnetic field is inhomogeneous, the dephasing will speed up, causing the transverse relaxation constant to be shorter than T_2 , then defined as T_2^* .

Simultaneously, the direction of M_{\perp} rotates around the axis of \mathbf{B}_0 , a process called Larmor precession. The frequency of this precession is determined by the experienced magnetic field (in this case \mathbf{B}_0) and the gyromagnetic ratio, a constant specific to the nucleus under examination. Protons in a field strength of 3.0 T rotate with a Larmor frequency of 128 MHz. This precession enables detection of transverse magnetization through the emission of electromagnetic radiation. In the next section we will see how the emitted signals are exploited during MR imaging.

3.1.2 Imaging protocols

Anatomical MR images can be constructed by detecting emitted radiation from a given location. The amount of radiation is proportional to the proton density and thus the amount of water molecules at that location. However, if equal proton density occurs at different locations, these locations cannot be resolved using the main magnetic field \mathbf{M}_0 only. To this end, we can add a gradient field to the main field, resulting in a spatially varying magnetic field strength. Consequently, precession at different locations now occurs at distinct frequencies. The now inhomogeneous magnetic field will cause faster transverse relaxation with time constant T_2^* .

The dephasing results in accelerated signal loss, which can be partially recovered by the application of a second RF pulse that tilts the magnetization by 180 degrees.

This flip in the perpendicular plane will transform all the “fast” spins, with a phase lead, into “slow” spins, with a phase lag, and the other way around. This event in turn will lead to rephasing of the spins, until all spins assemble and emit a burst of electromagnetic radiation, the so-called spin-echo [133]. This echo, occurring at echo time TE after the initial 90-degree flip, can be detected by an MR receiver coil. The spin-echo sequence is depicted in Figure 3.1.

A multitude of variations on this basic spin-echo scheme have been developed in order to acquire different kinds of MR images. Examples are inversion recovery (IR) and turbo spin-echo (TSE), which have been used in this thesis for the generation of anatomical (structural) MR images of the brain. In addition, pulsed gradient spin-echo (PGSE) and echo-planar imaging (EPI) have been used for diffusion-weighted and functional MRI acquisition, respectively. These protocols will be explained in the appropriate sections.

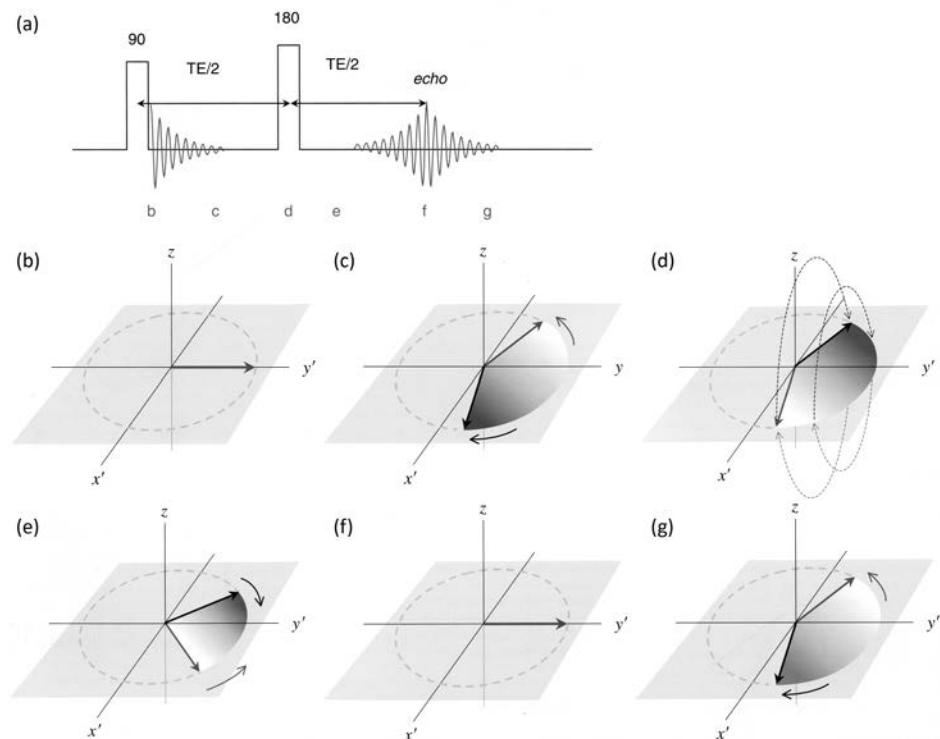


Figure 3.1 Spin-echo MRI protocol. (a) Spin-echo pulse sequence ($TE = \text{echo time}$). Spins initially in phase (b) dephase naturally (c) until the 180-degree RF pulse is applied (d). Immediately after the pulse the phases are reversed, but they continue to dephase in the same direction (e) forming an echo (f) and then dephasing again (g). Figure adapted from [204].

3.2 Diffusion MRI

3.2.1 Diffusion

Diffusion is a mixing process that occurs without the need for stirring or other ways of bulk motion. This phenomenon is described by Fick's first law [102], stating that the net particle flux is proportional to any difference in concentration, by means of the diffusion coefficient D :

$$\mathbf{J} = -D\nabla C, \quad (3.1)$$

with \mathbf{J} the net particle flux and C the particle concentration. D , which relates the flux to the difference in concentration, is called the diffusion coefficient. This coefficient is an intrinsic property of the medium, dependent on the size of the diffusing molecules, the temperature, and the microstructure of the environment. Although the net flux vanishes in a thermodynamic equilibrium, microscopic motions of molecules still exist. This process is called Brownian motion, after its discoverer Robert Brown, who reported on the random motions of pollen grains under a microscope [46]. Independently, Einstein came to the same conclusion [96] and, using a probabilistic framework for the description of diffusion, united the theories of Fick and Brown with the following formula:

$$\langle \mathbf{R}^T \mathbf{R} \rangle(\tau) = 6D\tau, \quad (3.2)$$

where $\langle \mathbf{R}^T \mathbf{R} \rangle(\tau)$ is the mean-squared displacement of particles during a diffusion time τ , and D again the classical diffusion coefficient from Fick's law.

The random motion of water molecules within neural tissue such as the brain is very much influenced by the environment. The presence of cell membranes, elements of the cytoskeleton, and macromolecules restricts the otherwise free motion of water. In gray matter, no macroscopic preferred directions in tissue structure can be distinguished. The measured diffusion in gray matter is therefore often rather isotropic and its properties can be represented by a single (scalar) apparent diffusion coefficient (ADC). On the other hand, in white matter, but also in skeletal and cardiac muscle for example, water molecules can move more freely along the direction of the axonal (or muscle) fiber bundles than perpendicular to it. In these environments, anisotropic diffusion takes place. Estimation of the principal directions of diffusion within neural tissue could therefore be related to orientations in tissue structure.

3.2.2 Magnetic resonance and diffusion

MRI can be used to probe the orientations in tissue structure noninvasively, by sensitizing the MR acquisition to diffusion of water molecules in different directions. The principle of such a diffusion-sensitive protocol was devised by Carr and Purcell [58] and improved upon by Stejskal and Tanner [286]. The so-called pulsed gradient spin-echo (PGSE) sequence involves the addition of a pair of opposing (one positive and one negative) pulsed magnetic field gradients to the normal spin-echo MRI sequence, as represented in Figure 3.2 [209, 211]. After the excitation RF pulse, protons at different locations within a pixel start to emit electromagnetic signals at the same frequency, as they all experience the same magnetic field \mathbf{B}_0 . During the application of the first gradient, protons experience a different magnetic field, dependent on their locations. After the gradient application, the system returns to the homogeneous \mathbf{B}_0 and thus one frequency for all protons, but the phases of the different water molecules are no longer equal. This dephasing leads to a loss of overall signal. The second gradient has opposite polarity but identical strength and length, and therefore enables the protons to rephase, i.e., all return to the same phase at the end of this gradient.

The MR signal is now diffusion-weighted, because perfect refocusing of the spins happens only when there is no diffusion of water molecules between the two gradients. When diffusion has occurred, this will be detected by the signal attenuation due to imperfect rephasing. Note that this experiment only measures water diffusion along a given axis. In Figure 3.2, it can be seen that for this case, only molecules moving in the horizontal direction (the direction in which the gradient was applied) can be detected, and diffusion along the vertical axis goes unnoticed. Besides on the gradient direction, the sensitivity to diffusion and thus the resulting signal is also dependent on several other factors, such as the duration and amplitude of the gradients and the time during which diffusion takes place.

The MR signal attenuation or normalized MR signal can be expressed as

$$E(\mathbf{q}, \tau) = \frac{S(\mathbf{q}, \tau)}{S_0}, \quad (3.3)$$

with $S(\mathbf{q}, \tau)$ the signal in the presence of diffusion gradients and S_0 the baseline (unweighted) signal. E and S are dependent on \mathbf{q} , a 3D vector $\mathbf{q} = \gamma\delta\mathbf{G}$ with γ the gyromagnetic ratio, and δ and \mathbf{G} the duration and magnitude of the gradients, respectively, and on the effective diffusion time $\tau = \Delta - \delta/3$, with Δ the time between two complementary diffusion gradients [159].

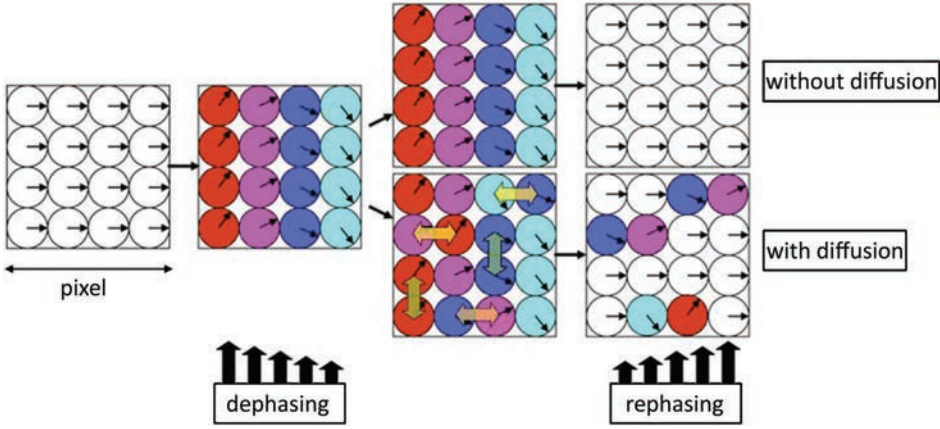


Figure 3.2 Effect of diffusion in an MRI experiment with a pair of opposing gradients. Each circle represents a water molecule at a different location within a pixel. The vectors in the circles indicate phases of the signal at each location. If water molecules move between the two gradient applications, the second gradient cannot perfectly refocus the spins, which leads to signal loss. Note that in this example, horizontal motion leads to signal attenuation, but vertical motion does not affect the signal intensity. Figure adapted from [211].

Stejskal and Tanner [286] showed that the signal attenuation is related to the probability density function (PDF) of the displacement of the water molecules (i.e., the averaged diffusion propagator) p , if the gradient pulses are short enough:

$$E(\mathbf{q}, \tau) = \frac{S(\mathbf{q}, \tau)}{S_0} = \int_{\mathbb{R}^3} p(\mathbf{R}|\tau) e^{-i\mathbf{q}^T \mathbf{R}} d\mathbf{R}, \quad (3.4)$$

where \mathbf{R} is the net displacement vector of the water molecule. Intuitively we understand that to reconstruct the diffusion PDF, we need to sample the diffusion along many \mathbf{q} vectors [187]. In clinical practice the b -value, a quantity proportional to the squared gradient strength, is often used to characterize the level of sensitivity to diffusion. This parameter is given by $b = \mathbf{q}^2 \tau$, where $\mathbf{q} = \gamma \delta \mathbf{G}$ and $\tau = \Delta - \delta/3$.

3.2.3 Models applied to diffusion MRI

The acquired diffusion MR signal can be modeled to resolve the underlying structure of the measured tissue. These models come in different levels of complexity.

The simplest model approximates the apparent diffusion coefficient (ADC) in a voxel. When the displacement of the water molecules is Gaussian and behaves according to the Einstein equation (3.2), the attenuation is given by

$$E(\mathbf{q}, \tau) = \frac{S(\mathbf{q}, \tau)}{S_0} = e^{-\mathbf{q}^2 \tau D} = e^{-bD}, \quad (3.5)$$

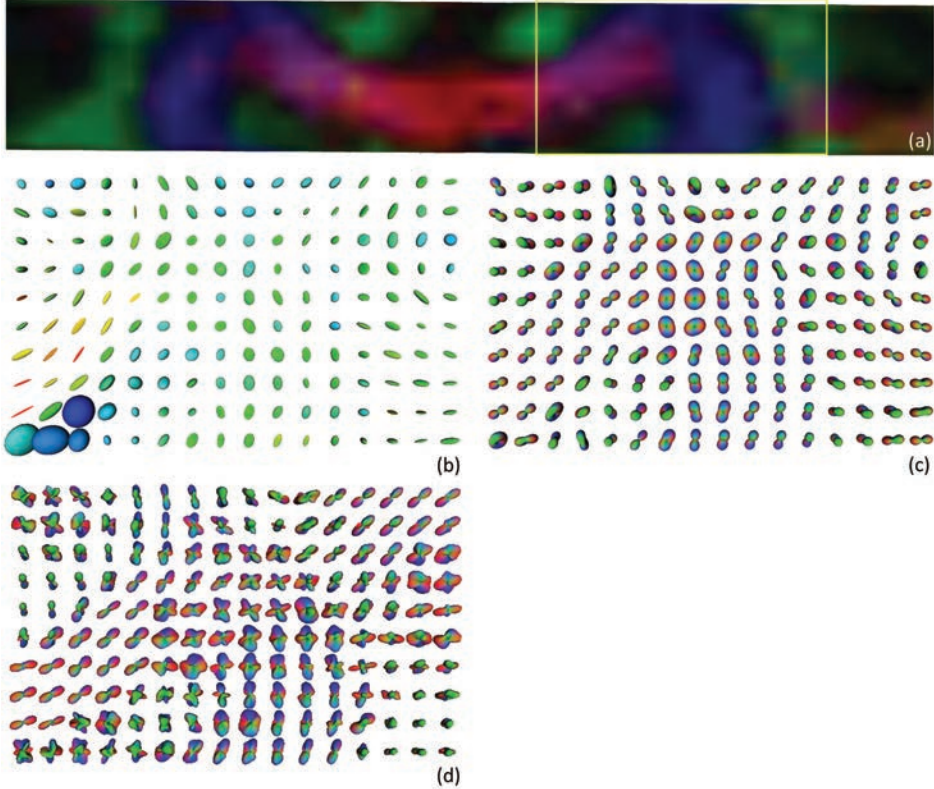


Figure 3.3 Different DTI and HARDI glyphs in the centrum semiovale. (a) FA map of a coronal brain slice, with the ROI indicated by the yellow rectangle. (b) DTI ellipsoids within the ROI, derived from diffusion tensor \mathbf{D} , color-coded by FA. (c) ODFs derived from DTI data according to Equation (3.9), RGB color-coded by orientation and min-max normalized. (d) Regularized Q-ball ODFs of order 6, based on diffusion MRI data with b -value 3000 s/mm² and 121 unique gradient directions. Figure adapted from [249].

dependent on the b -value and the diffusion coefficient D . So, to obtain quantitative maps of the diffusion per voxel, we need at least two measurements, typically one diffusion-weighted and one unweighted measurement.

However, as described in Section 3.2.1, diffusion in white matter is often anisotropic. For this case, we can use an anisotropic Gaussian model using diffusion tensor imaging (DTI). This method describes the diffusion profile in a voxel as an ellipsoid. The diffusion coefficient D is thus generalized to a symmetric 3x3 diffusion tensor

\mathbf{D} with 6 unique values:

$$\begin{pmatrix} D_{xx} & D_{xy} & D_{xz} \\ D_{xy} & D_{yy} & D_{yz} \\ D_{xz} & D_{yz} & D_{zz} \end{pmatrix} \quad (3.6)$$

If we again assume the diffusion to be Gaussian, the MR signal attenuation for this case is given by:

$$E(\mathbf{q}, \tau) = \frac{S(\mathbf{q}, \tau)}{S_0} = e^{-b\mathbf{g}^T \mathbf{D} \mathbf{g}}, \quad (3.7)$$

with \mathbf{g} the unit vector $\frac{\mathbf{q}}{|\mathbf{q}|}$ and b again equal to $\mathbf{q}^2 \tau$. In order to construct this tensor \mathbf{D} , we need a minimum of six diffusion-weighted images with fixed b -value but varying \mathbf{g} , and one unweighted image [24]. Eigenanalysis of \mathbf{D} can provide us with eigenvectors $\mathbf{e}_1, \mathbf{e}_2, \mathbf{e}_3$ (the principal diffusion directions) and eigenvalues $\lambda_1 \geq \lambda_2 \geq \lambda_3 > 0$ (the corresponding diffusion coefficients).

From these parameters, scalar measures characterizing the diffusion can be derived, such as fractional anisotropy (FA) [25]:

$$\text{FA} = \frac{\sqrt{(\lambda_1 - \lambda_2)^2 + (\lambda_2 - \lambda_3)^2 + (\lambda_1 - \lambda_3)^2}}{\sqrt{2(\lambda_1^2 + \lambda_2^2 + \lambda_3^2)}}. \quad (3.8)$$

Besides an FA map, we can also visualize the ellipsoid derived from the diffusion tensor \mathbf{D} describing the diffusion profile in each voxel. The 3D anisotropic Gaussian PDF is rarely depicted in DTI. Another option that is sometimes used is the orientation distribution function (ODF). To obtain this ODF, a sphere is deformed by the values of the ADC for each direction \mathbf{u} :

$$D(\mathbf{u}) = \mathbf{u}^T \mathbf{D} \mathbf{u}, \quad (3.9)$$

which results in a peanut-shaped ODF. The different DTI visualizations are depicted in Figure 3.3 (b) and (c).

Although DTI does not require a long acquisition time and is therefore popular in clinical practice, it cannot resolve complex intravoxel diffusion patterns such as crossings. Typical diffusion MRI voxels are 2 mm in size, while white matter axons have radii in the range of 0.1–10 μm [159]. This is a serious limitation, because according to Behrens et al. [31], between one and two thirds of voxels in the human brain white matter contain multiple fiber bundle crossings, in which case the second-order model described above breaks down (see Figure 3.4). This deficiency caused the emergence of higher-order mathematical models to describe the PDF, which require denser sampling in \mathbf{q} -space and are therefore collectively called high angular resolution diffusion imaging (HARDI).

HARDI acquisition schemes do not assume anything about the form of the diffusion propagator p but just sample \mathbf{q} -space as well as possible in order to reconstruct this propagator [187]. Modeling methods that can resolve multiple diffusion directions per voxel include [159]:

- Multi-tensor models [311] are the simplest extensions of the DTI method in which the diffusion PDF is modeled as a mixture of multiple Gaussian PDFs. Though the models are simple, they involve predefined constraints such as the number of orientations to recover.
- Spherical deconvolution (SD) [9, 305] attempts to recover the fiber orientation distribution function (fODF) directly, using an inverse convolution process. The fODF quantifies the fraction of fiber pieces with different orientations within a voxel and is thus zero apart from spikes in the fiber directions, while the diffusion orientation distribution function (dODF) is a smoother function that gives the probability that a diffusing water molecule moves in a particular direction. The main drawback of the spherical deconvolution method is its sensitivity to noise.
- Diffusion spectrum imaging (DSI) [311, 322] uses sampling of the whole \mathbf{q} -space on a Cartesian grid and then estimates p as a dODF by inverse Fourier transformation. The main limitation of this method is the long acquisition time, due to the dense sampling of \mathbf{q} -space.
- Persistent angular structure (PAS) MRI [154] tries to find the persistent angular structure, which is a projection of p onto the sphere that resembles the fODF. Nonlinear optimization and numerical integration schemes make the PAS MRI algorithm rather slow.
- Q-ball imaging [309, 312] approximates the dODF estimated by DSI using a spherical measurement scheme. Q-ball imaging will be discussed further below.
- Diffusion orientation transform (DOT) [228] is related to Q-ball imaging and calculates a variant of the dODF, in this case a single contour of p at a fixed radius R_0 (while the dODF contains contributions from all contours). DOT requires some parameter tuning, but for sensible choices of τ and R_0 , the result is similar to Q-ball imaging.

For the studies described in this thesis, we mainly used Q-ball imaging [309, 312]. The spherical acquisition scheme for this technique is less time-consuming and thus more suitable in practice than the dense sampling required for DSI, although the dODF approximation might suffer from some reduction in angular resolution and precision of peak directions [159].

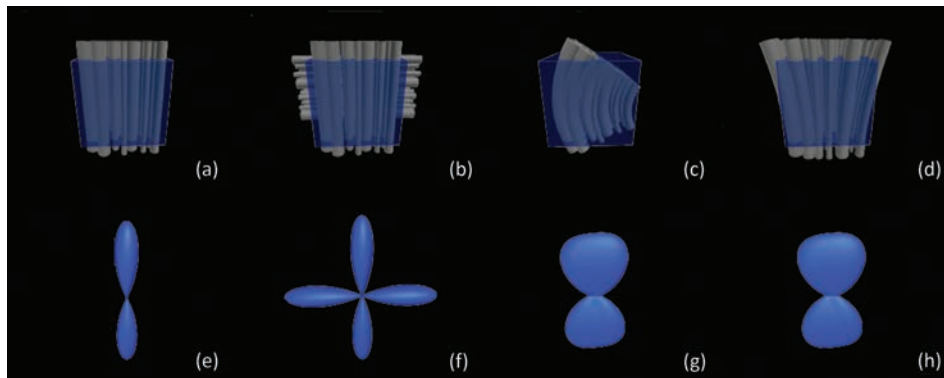


Figure 3.4 Various axon fiber configurations arising frequently in brain white matter voxels (top row: (a) parallel, (b) crossing, (c) bending, (d) fanning). The bottom row images (e) to (h) show the fODF for each configuration. DTI would only be able to resolve the parallel fibers. Figure adapted from [159].

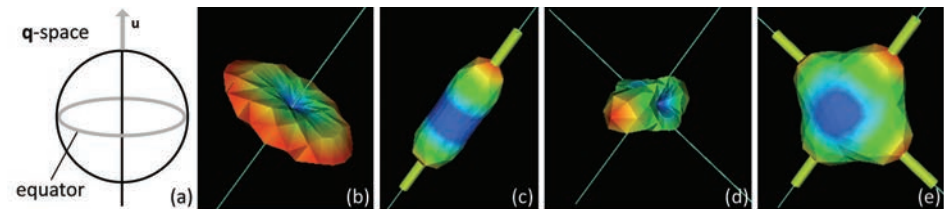


Figure 3.5 Funk-Radon transform. (a) Principle of the Funk-Radon transform. The FRT of the signal sampled on a sphere for a given orientation u (represented by the gray arrow) is equal to the integral of the signal along the equator (gray ellipse) of u . (b) HARDI signal with one fiber. (c) FRT of the signal in (b). (d) HARDI signal with two orthogonal fibers. (e) FRT of the signal in (d). The thin lines are the true underlying orientations, while the thicker tubes are the detected maxima. The radius of the spherical functions was scaled by the corresponding value on the surface. Figure (a) adapted from [244], other figures from [81].

In Q-ball imaging, the dODF is approximated using a transformation of spherical functions called the Funk-Radon transform (FRT). Intuitively, the dODF value at a given point on the sphere (corresponding to a unique orientation), resulting from the FRT, is the great circle integral of the attenuation signal on the sphere defined by the plane through the origin perpendicular to the point of evaluation (see Figure 3.5) [187].

While the original Q-ball algorithm has a numerical solution [309], people have introduced an analytical solution based on spherical harmonics that is faster, more robust to noise and less stringent in acquisition requirements [81, 82]. In this case, the HARDI signal is first represented using spherical harmonics (SH) basis functions.

Subsequently, the FRT can be solved analytically using an SH basis. For this purpose, a modified real and symmetric SH basis is defined, with Y_{lm} the SH of even order l ($l = 0, 2, \dots, \infty$) and degree m ($m = -l, \dots, l$). A single index j is defined in terms of l and m , such that $j(l, m) = (l^2 + l + 2)/2 + m$. The modified SH is then given by:

$$Y_j = \begin{cases} \sqrt{2}\text{Re}(Y_{l|m|}), & \text{if } m < 0, \\ Y_{lm}, & \text{if } m = 0, \\ \sqrt{2}(-1)^{m+1}\text{Im}(Y_{lm}), & \text{if } m > 0, \end{cases} \quad (3.10)$$

where $\text{Re}(Y_{lm})$ and $\text{Im}(Y_{lm})$ are the real and imaginary parts of Y_{lm} , respectively.

Then, the dODF Ψ can be analytically estimated by:

$$\Psi(\theta, \phi) = \sum_{j=1}^{n_{\text{SH}}} 2\pi P_{l(j)}(0) c_j Y_j(\theta, \phi), \quad (3.11)$$

with $\theta \in [0, \pi]$ and $\phi \in [0, 2\pi]$ the spherical coordinates, $n_{\text{SH}} = \frac{1}{2}(l+1)(l+2)$ the number of SH elements, c_j the SH coefficients describing the HARDI signal, and $P_{l(j)}$ the Legendre polynomial of order $l(j)^2$. An example of the resulting Q-ball glyphs can be seen in Figure 3.3 (d).

3.2.4 Fiber tracking

Fiber tracking algorithms integrate the fiber orientations derived from diffusion profiles at a voxel level. These algorithms are the only tools for noninvasive and in vivo identification of longer pathways and thus global connectivity of the brain. The fundamental aim of tractography methods is to find pathways through the diffusion MRI data along which diffusion is least hindered. Although this aim is common, the means by which to achieve it vary greatly from method to method. Often, fiber tracking algorithms are classified as either deterministic or probabilistic. In addition, the complexity of the diffusion representation is an important factor [159].

The simplest method is deterministic streamline tracking. Streamlines are reconstructed starting from a seed point and simply following the local principal direction (when working with DTI input). Multiple algorithms implementing this method exist, exploiting varying step sizes and different integration and interpolation schemes. A commonly used algorithm is fiber assignment by continuous tracking (FACT) [210], applying the measurement from each voxel over the entire voxel. However, it was shown that smooth interpolation between grid points leads to decreased error propagation in fiber tracking [178]. Other important features of the tractography algorithm are the stopping criteria. The most used constraints are a minimum FA, a maximum curvature, and a minimum length. Deterministic methods can be extended to a more complex (HARDI) diffusion profile by simply choosing which of

the multiple directions to follow at each step. One strategy is to select the direction that lies closest to the direction of the previous step [131], but it is also possible to use the shape and peak orientation of the dODFs for this purpose [243].

The error propagation that is inherent to streamline tracking can be incorporated and visualized by the use of probabilistic fiber tracking methods. These methods use a random walk method, starting a large number of particles from a seed point and counting the number of paths passing a given voxel. In this way, it is possible to determine the confidence level of the path from the seed point to the given voxel. An important feature of these probabilistic algorithms is a function that characterizes the uncertainty in the fiber orientation, which we can call the uncertainty ODF (uODF) [159, 187].

The probabilistic method used in this thesis is called probabilistic index of connectivity (PICO) [235]. This algorithm exploits the uncertainty in the orientation of the principal direction of diffusion and generates connection probability maps based on repeated streamline tracking. PICO was developed for streamline tracking using DTI data [235], using the uncertainty in the orientation of the first eigenvector \mathbf{e}_1 of the diffusion tensor \mathbf{D} in two ways. The first manner includes a simple uncertainty term based on tensor anisotropy only, thus resulting in an isotropic normal distribution, centered around the original \mathbf{e}_1 . The more complex method also exploits the skewness of the tensor based on the magnitudes of the eigenvalues λ_2 and λ_3 and the orientations of the eigenvectors \mathbf{e}_2 and \mathbf{e}_3 , which yields a more accurate distribution for oblate tensors. Based on this uncertainty information, probability distribution functions (PDFs) for the fiber orientation are generated. Subsequently, these PDFs are repeatedly sampled by the streamline propagation algorithm. Finally, a map is generated that defines the probability of a given voxel to be connected to the seed point for tracking as the ratio between the number of streamlines crossing the voxel and the total number of tracked streamlines.

This algorithm was extended to work on multi-tensor models, still using the tensor anisotropy as uODF [65, 67]. Although this improved tracking through fiber crossings, the method suffered from the limitations of multi-tensor models, such as the need to specify the number of fiber populations per voxel a priori. Incorporation of Q-ball (or PAS MRI) input was facilitated by Parker and Alexander [234]. They used peak directions as estimates of fiber orientation, and the sharpness of these peaks to predict the uncertainty: the broader the peak, the higher the uncertainty. The drawback of this approach is that it does not take into account anisotropy in the uncertainty, which occurs in regions of fanning or bending fibers, for example. Seunarine et al. [273] solved this problem by using the peak shape, particularly the anisotropy of the peak cross section, to estimate the uODF.

3.3 Functional MRI

3.3.1 The BOLD effect

Functional MRI (fMRI) is an indirect method to measure the activation of the brain and therefore brain function. The most commonly used fMRI technique is the so-called blood-oxygen-level-dependent fMRI, or BOLD fMRI [99].

In 1890 already, the regional cerebral blood flow (CBF) was found to be connected to neuronal activity [261]. Although the rate of glucose metabolism and the change in CBF appeared to be coupled closely [251], Fox et al. reported that the change in CBF exceeds the oxygen metabolic rate [109, 110]. The oxygen demand of the activated neurons increases and therefore the blood oxygen supply will have to rise. However, because of the involved vascular dilatation mechanism, the cerebral blood volume (CBV) and CBF increase as well. As a result, blood cells then have a smaller probability to deliver oxygen to the neurons, and the oxygen extraction fraction will decrease. This in turn leads to an elevated oxygenation level in the veins, as can be seen in Figure 3.6 [197, 198].

Consequently, the ratio of deoxygenated hemoglobin (de-oxy-Hb) to oxygenated hemoglobin (oxy-Hb) will diminish. Because de-oxy-Hb has different magnetic properties from oxy-Hb and the surrounding brain tissue, it locally distorts the magnetic field. The resulting inhomogeneities cause quick dephasing of the magnetic spins, so deoxygenated blood has a short T_2^* [226]. Using the BOLD mechanism, activated areas display a higher blood oxygenation level, which results in less field inhomogeneities and therefore a longer T_2^* . This response can be measured with a T_2^* -sensitive EPI sequence, which will be discussed in the next section. Typically, the signal difference is determined, by acquiring both baseline and activated measurements.

3.3.2 fMRI EPI acquisition

When acquiring an MRI image of $n \times n$ pixels with a conventional spin-echo sequence, during each repetition (lasting TR seconds), one line of n samples is measured in the so-called k -space. The sequence thus has to be repeated n times in order to fill the complete image. However, when measuring the dynamic BOLD response, we need to reconstruct the entire image volume in the shortest possible time (while still long enough for the response to develop) [99]. This can be achieved by filling the k -space in one TR (typically in the order of 2 seconds), using an echo-planar imaging (EPI) protocol.

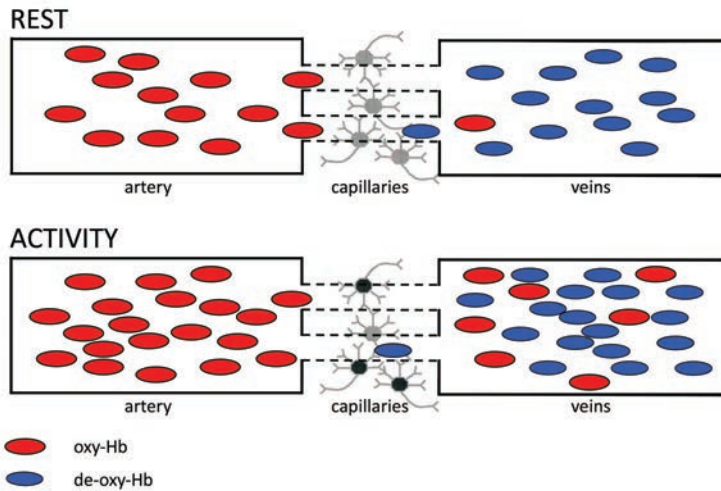


Figure 3.6 The origin of the BOLD effect. In activation (bottom), the large provision of fully oxygenated blood leads to a relative reduction in de-oxy-Hb and an increase in local T_2^* in the veins as compared with the rest condition (top). Figure adapted from [204].

In this thesis, a BOLD contrast sensitive gradient-echo echo-planar imaging protocol was used. In the case of a gradient-echo protocol, the signal echo is not generated by a 180-degree RF pulse, but by using a pair of bipolar gradient pulses. A gradient-echo sequence starts with an excitation pulse which tilts the magnetization by a flip angle α (in our case 90°). A negative pulse gradient then dephases the spins before they are rephased by an opposite gradient in order to prompt the echo. In standard gradient-echo imaging, this basic pulse sequence is repeated as many times as image lines have to be acquired, similar to the traditional spin-echo imaging. In case of a gradient-echo-based EPI sequence the initial part is very similar to a standard gradient-echo sequence. However, in EPI a train of echoes is generated, by fast and periodical reversion of the gradients. The benefits of the faster imaging come at a price: EPI is very sensitive to distortions and to image artifacts such as ghosting and chemical shift.

3.3.3 Experiment design and analysis

Using EPI acquisition, an fMRI image volume is acquired every few seconds. A typical fMRI experiment therefore yields hundreds of volumes in total. Often, some of these volumes were taken as the subject was stimulated (i.e., coerced into brain activity by a certain task), while others were acquired with the subject at rest. The images measured during stimulation should show higher signal intensity in the

activated brain regions than the images in rest, due to local changes in the blood oxygenation. Statistical analysis can identify whether there is a significant contrast between the signal intensities in voxels during the task and during rest. This analysis can be done by fitting a general linear model (GLM) to the data.

The GLM aims to describe the variation of the BOLD time course $y(t)$ in terms of a linear combination of explanatory variables and an error term. In case of a simple model with only one time-dependent explanatory variable $x(t)$, the GLM would look as follows:

$$y(t) = \beta x(t) + \epsilon(t), \quad (3.12)$$

with β the slope and $\epsilon(t)$ the error term.

If the model incorporates $p > 1$ explanatory variables (also called regressors) it is convenient to write the GLM in discrete matrix form:

$$\mathbf{y}(t) = \boldsymbol{\beta} \mathbf{X}(t) + \boldsymbol{\epsilon}(t), \quad (3.13)$$

where $\mathbf{y}(t)$ is the $n \times 1$ time course signal vector of n observed time points, $\boldsymbol{\beta}$ is the $p \times 1$ vector of coefficients, and $\boldsymbol{\epsilon}(t)$ the $n \times 1$ vector of error terms. The so-called design matrix $\mathbf{X}(t)$ now has n rows, one for every time point t in the original data, and p columns, one for every explanatory variable (or regressor) in the model. For simplicity, the time-dependency will be omitted from the notation further on.

One of the most important columns of the design matrix for a task-based fMRI experiment is the timing of the stimulation (see Figure 3.7). This column contains values corresponding to the stimulation and rest conditions. By estimating the coefficient vector $\boldsymbol{\beta}$ belonging to these values with $\hat{\boldsymbol{\beta}}$, the response of the BOLD signal to the stimulation paradigm can be assessed.

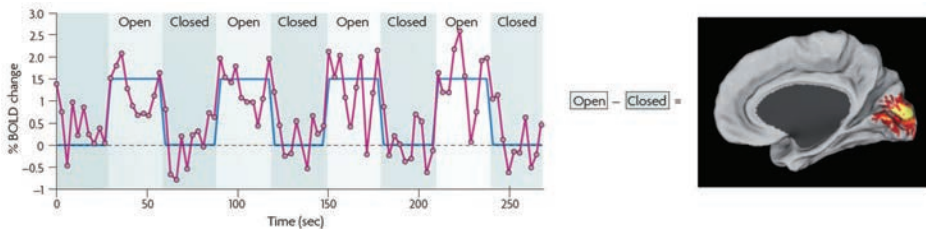


Figure 3.7 BOLD time course (magenta) from a region in the visual cortex during a simple opening and closing eyes task. The stimulus function is shown in blue (corrected for a delay in hemodynamic response). Subtraction analysis identifies a signal intensity difference in the visual cortex (as shown on the right). Figure from [107].

The vector $\hat{\beta}$ can be solved by a least squares estimation [111]:

$$\hat{\beta} = (\mathbf{X}^T \mathbf{X})^{-1} \mathbf{X}^T \mathbf{y}. \quad (3.14)$$

The stimulus function is often convolved with a hemodynamic response function to account for the delay in brain activation. Other regressors can be easily included as well; the general linear model provides a comprehensive framework for data modeling and can eliminate effects that may confound the analysis, such as drift or respiration, provided that they can be modeled. In the end, the model is fit to the fMRI data in each voxel, yielding an estimate of the “goodness of fit” of each regressor to the signal. This estimate can then be converted into a useful statistic, to see whether the coefficient is significantly different from the null hypothesis [279].

During fMRI experiments using a stimulation paradigm, spontaneous modulation of the BOLD signal that does not correlate with the stimulus function is also present. Though regarded as noise in task studies, spontaneous brain activity actually represents a specific organization of the resting human brain [107]. Therefore, resting state fMRI measurements are also done, while subjects lie still in the scanner but are not allowed to fall asleep. The resulting data can be analyzed using independent component analysis (ICA) [28, 72, 203]. This method analyzes the entire data set and decomposes it into components that are maximally independent. ICA is data-driven and very powerful, but is sensitive to the number of components chosen and interpretation of the results can be cumbersome. Another possibility, that was used for this thesis, is seed-region-based correlation analysis [68, 69, 108]. In this case, the BOLD time course is extracted from a seed region and used as a regressor in a GLM, to compare the seed region signal with the time course of all other voxels in the brain. Though a very simple technique, suitable for the analysis of a specific region of interest, it can suffer from dependency on the seed region segmentation and from the fact that the extracted waveform might not be an independent variable.

3.4 Brain connectivity

3.4.1 Introduction

In the seventeenth century, brain connectivity schematics were still pretty much determined by philosophical ideas, such as in Figure 3.8. Since then, a multitude of methods to measure and describe brain connectivity have emerged [282]. These methods include microscopic examination of histological sections, of which the ornate Brainbow technique (see Figure 3.9) is an example, electrical recordings of single nerve cells (local field potentials), and noninvasive functional imaging of the brain.

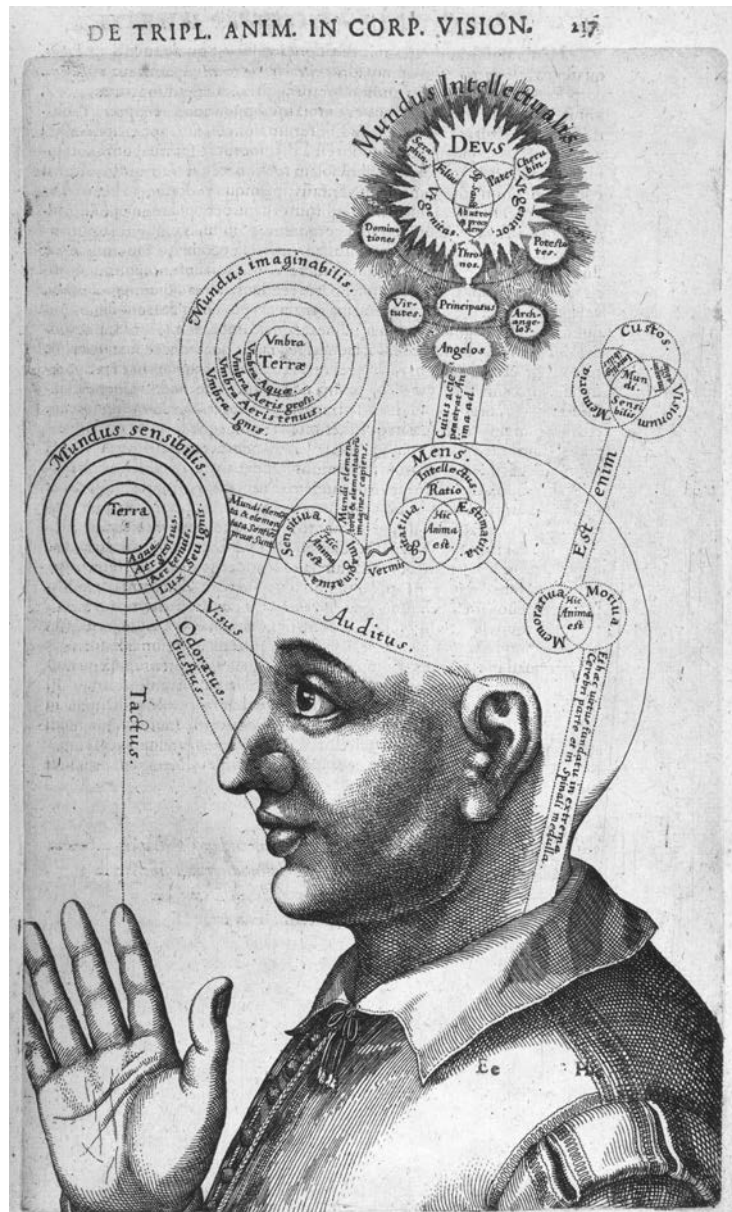


Figure 3.8 Mind and universe (Robert Fludd, ca. 1621). Seventeenth-century illustration by English physician Robert Fludd, which relates the soul's faculties to realms such as the sensible, the imaginary, and the divine. A writhing worm connects imagination (which overlaps with perception) and cognition (which is linked to judgment). Many theories were just passed along since Galen's time (1500 years earlier) because of a lack of anatomical knowledge. Empiricism would soon be reintroduced during the Renaissance. Figure from [268].

3.4. Brain connectivity

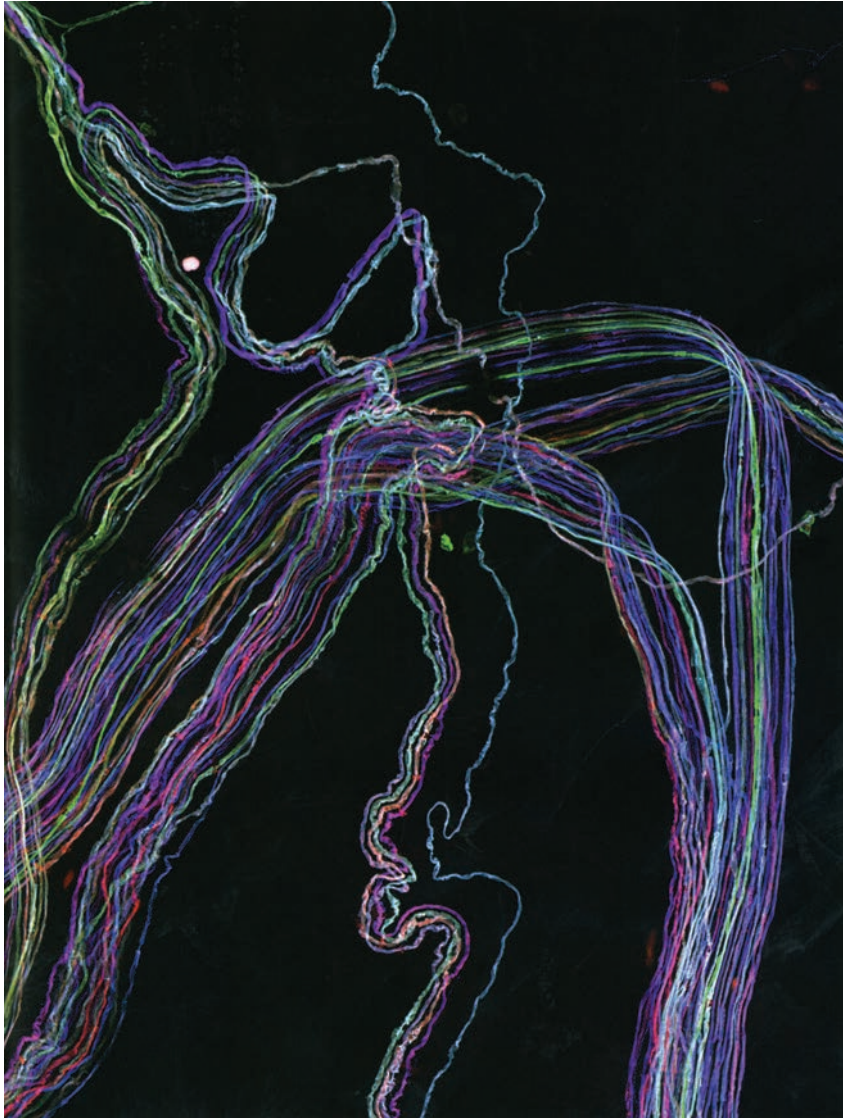


Figure 3.9 Motor neuron axons traveling side by side through a mouse brain, on their way to the ear muscle whose contraction they regulate. The axons are colored by a genetic manipulation technique called Brainbow [196]. Figure from [268].

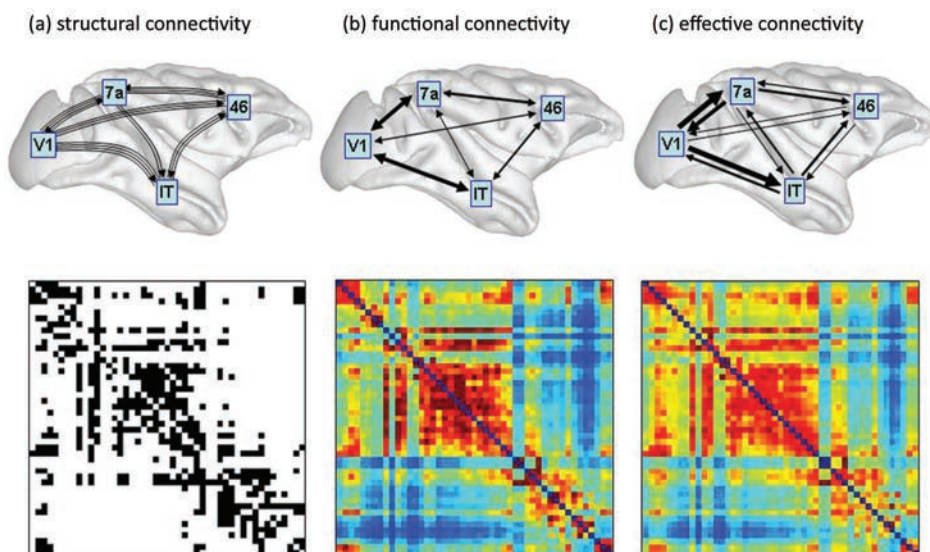


Figure 3.10 Different types of brain connectivity. Sketches at the top illustrate (a) structural connectivity (fiber pathways), (b) functional connectivity (correlations), and (c) effective connectivity (information flow) among four brain regions in macaque cortex. Matrices at the bottom show (a) binary structural connections, (b) symmetric mutual information, and (c) non-symmetric transfer entropy. Figure from [268], based on data from [146].

In this thesis, we will concentrate on the latter. Three types of brain connectivity can be distinguished, which will be discussed in the following sections, namely structural, functional, and effective connectivity (see Figure 3.10).

3.4.2 Structural brain connectivity

Structural connectivity refers to a set of structural (anatomical) connections between different areas of the brain. The scale of these connections can vary from local circuits of single cells to large networks of pathways through the whole brain. With respect to time, the connection pattern is relatively static at shorter time scales (for example during an MRI scan), but may be plastic at longer time scales including development and learning. The connection matrix resulting from structural connectivity analysis might be binary, but could also contain other values, depending on the method used. Furthermore, the matrix does not have to be symmetrical [282].

Structural connectivity can be estimated using postmortem examination of dissected tissue, histologically stained samples, and neural tract tracing. Noninvasive brain

imaging techniques that can be applied in vivo include cortical thickness correlation (based on structural MRI) and streamline counting after probabilistic fiber tracking in diffusion MRI, which is used in this thesis [159, 282].

3.4.3 Functional and effective brain connectivity

Functional connectivity captures dependency in time-series data between different areas of the brain [112, 113]. These time series can be generated by local field potential recordings, EEG, MEG, and fMRI, for example, and are analyzed by estimating measures like correlation, covariance, and spectral coherence. Brain function and functional connectivity are far from static even at short time scales. Another characteristic is that an observed statistical dependence does not infer a causal interaction between brain areas, and therefore, the resulting connection matrix will be symmetrical.

Effective connectivity describes causal effects between brain areas [113], which can be determined by statistical modeling, and experimental perturbations, amongst others. Effective connectivity is as time-dependent as functional connectivity and requires complex data processing and modeling techniques. Due to the resulting causal relationships, the connection matrix will be asymmetrical.

3.4.4 Connectivity-based parcellation

The division of the brain in anatomically segregated regions is often based on cytoarchitecture alone, for example for Brodmann's areas. However, microstructurally coherent regions can have functional subdivisions and furthermore, studying the microstructure is not feasible in vivo [282]. Brain connectivity analysis provides us with complementary information that can aid in the segmentation of brain regions, because we assume that neurons in a coherent region share the same projections. The brain connectivity information can be used in a couple of ways.

Using prior knowledge about the position of brain structures from atlases, the connectivity patterns in different brain regions can be analyzed, either for the whole brain or at least a large number of cortical and subcortical regions [120, 130, 131, 132, 152, 153], or for individual anatomical structures [29, 89, 182, 183, 184, 201].

Behrens and Johansen-Berg reviewed two other methods to parcellate brain structures using structural connectivity information, that do not use prior information about the locations of brain structures [30]. First, segmentation can be based on the clustering of local diffusion profiles [47, 320, 325]. Second, people have used changes in structural connectivity within a region of interest without any prior knowledge on anatomy [160].



The STN on MRI

You could write the entire history of science in the last 50 years in terms of papers rejected by Science or Nature.

Paul C. Lauterbur

This chapter is based on:

"Magnetic resonance imaging techniques for visualization of the subthalamic nucleus: a review."
Ellen Brunenberg, Bram Platel, Paul Hofman, Bart ter Haar Romeny, and Veerle Visser-Vandewalle.
In *Journal of Neurosurgery*, DOI:10.3171/2011.6.JNS101571, in press (accepted June 8, 2011).

4.1 Introduction

A precise targeting of the dorsolateral (motor) part of the STN for deep brain stimulation is of great importance for two reasons: first of all, to obtain the best possible effect on motor symptoms, second, to minimize undesirable side effects on cognition and behavior [123, 308]. Yet, the operative technique of STN DBS including the imaging method for primary targeting of the STN still varies greatly between centers [186]. Magnetic resonance imaging (MRI) is one of the most frequently used modalities, alone or in combination with computed tomography (CT) or ventriculography [301]. Most procedures also involve a secondary targeting step using intraoperative assessments, such as microelectrode recordings (MER) or macrostimulation, to adapt the electrode position to the clinical aims [55, 87].

The aim of this study is to review the multitude of available methods and give a systematic overview of techniques for primary targeting of the (dorsolateral part of the) STN. This review discusses both indirect and direct targeting procedures, as well as comparative studies. The overall focus of this review lies on MRI, because this modality is most widely used. The next section of this chapter will focus on a summary of indirect and direct targeting methods using MRI. Subsequently, the results of the systematic review will be presented. Finally, the advantages and disadvantages of the targeting techniques will be discussed.

4.2 Summary of targeting methods

Methods for targeting of the dorsolateral STN can be classified as either direct or indirect. Indirect methods rely on contextual information, while direct methods focus on visualizing the STN itself on preoperative images of the patient.

4.2.1 Indirect targeting

Indirect targeting can rely on two types of contextual information. On the one hand, patient-specific landmarks can be used, while on the other hand, generic atlas information can be adapted to the patient's anatomy.

The gold standard in indirect targeting using anatomical landmarks involves the anterior (AC) and posterior commissure (PC) [284]. Having localized the AC, PC, and the midcommissural point (MCP), the stereotactic coordinates of the STN follow from fixed distances based on classical atlases such as the Schaltenbrand-Wahren brain atlas, as can be seen in Figure 4.1 [266]. The second most used landmark is the red nucleus (RN, see Figure 4.2) [18, 32]. Less widespread methods include the use of the nigrocapsular angle (as explained in Figure 4.3) [118], the supramammillary commissure (SMC) [181], the postmammillary commissure (PMC) [303], and the line connecting the mammillary bodies and the PC [256].

Furthermore, regions of interest can also be determined by mapping an anatomical and/or functional atlas onto the patient's MRI (see Figure 4.4). Anatomical atlases incorporate information about the position of brain structures [227, 265]. The most popular ones are the Talairach-Tournoux atlas [293], the Schaltenbrand-Wahren atlas [266], and the MNI atlas [64]. Functional atlases consist of point sets that are collected during MER, postoperative imaging or neurological assessments [84, 124, 126, 222, 230].

4.2.2 Direct targeting

Direct targeting involves the use of specific MRI protocols that enable direct visualization of the STN, avoiding the need to employ contextual information.

An often used method is the T_2 -weighted fast spin-echo (FSE) MR imaging protocol [283, 285], on which the STN shows as a hypointense area (see Figure 4.5(a)). Another popular technique for direct visualization is the inversion recovery (IR) protocol (see Figure 4.5(b)) [166]. Still subject to more research are the use of relaxation time maps [44] and susceptibility-weighted (SWI, T_2^*) imaging [86] (see Figure 4.5(c)), together with special postprocessing methods to reduce signal loss and enhance contrast.

4.3 Systematic review

In order to present a review on different targeting methods, we performed a thorough search for papers on STN targeting. The used criteria are briefly outlined below.

4.3.1 Search strategy

First, we searched PubMed and ScienceDirect for papers published from January 1999 until January 2011, using the terms “targeting”, “magnetic resonance imaging”,

“mri”, “visualization” in combination with “subthalamic nucleus” or “STN”. Second, we explored the bibliographies of relevant publications, until no further additional studies were found. Papers were selected if they provided qualitative descriptions or quantitative results of direct or indirect MRI-based STN targeting methods. Language other than English was an exclusion criterion.

We included 70 publications, of which 33 studies contained quantitatively validated results of patient trials. The quantitative results are reported in tables in the next sections. The details extracted from the studies for this purpose included the following: number of subjects, targeting techniques used (landmark, MRI protocol, atlas, registration method), validation method, outcome, and the main conclusion.

4.3.2 Indirect targeting

Anatomical landmarks

Publications on landmark-based targeting presenting quantitative results can be found in Table 4.1. After the ventriculography-based study by Schuurman et al. in 1999 [269], one of the first MRI-based studies was presented by Starr et al. [284]. Their AC-PC-based targets differed 1–1.5 mm from directly visualized STNs. Due to the variability in manual selection of AC-PC [231], the need for automated methods became apparent. The resulting landmarks of an atlas-based method by Ardekani et al. were very close (within 1 mm) to points determined manually [14]. A similar study by Pallavaram et al. yielded more accurate targets than achieved by manual selection [229].

The first studies on RN-based targeting have been presented by Aziz et al. [18] and Bejjani et al. [32]. The latter reported selection of the central electrode in 19 out of 24 cases. However, other studies, based on best response [71] and anatomical relationships [76], have stated that the RN is not reliable enough. To solve this, Liu et al. used the RN and substantia nigra (SN), but did not report quantitative results [195]. Pollo et al. exploited the AC-PC, RN, thalamus, internal capsule (IC), SN and the midline, resulting in a mean target in the inferior STN [247].

Regarding less widespread methods, according to Giller et al. [118], the use of the nigrocapsular angle was justified by the higher visibility of the IC and SN on MRI. Lee et al. proposed the SMC [181], which lacked reliability. Toda et al. used the PMC and selected the central electrode in 81% of cases [303]. Finally, Rijkers et al. suggested the line connecting the mammillary bodies and PC [256], though this should still be validated.

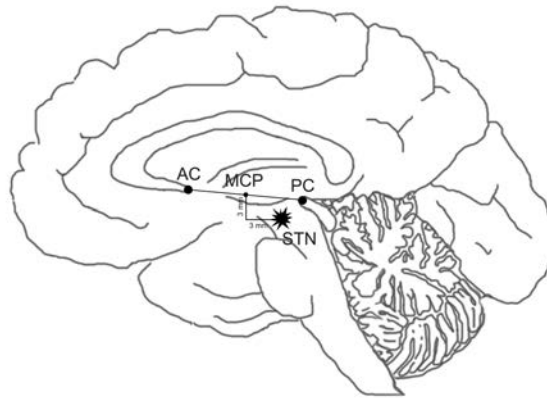


Figure 4.1 Diagram showing AC-PC-based targeting in a sagittal plane. After localizing the AC and PC, the MCP is determined. From there, the STN position can be calculated using fixed distances (often 12 mm lateral, 3 mm inferior and 3 mm posterior) that are based on an atlas.

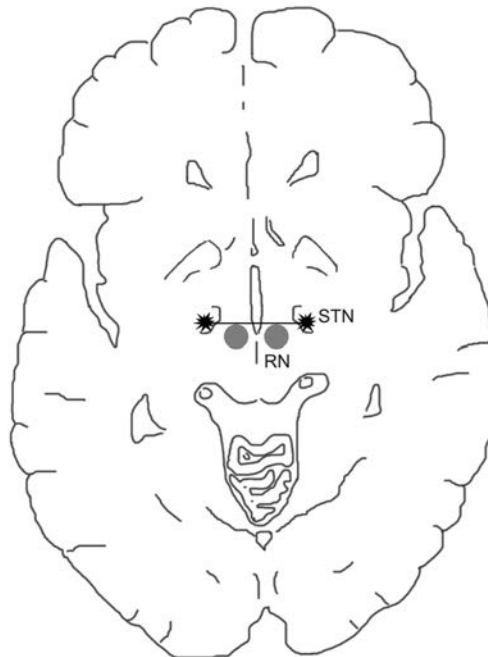


Figure 4.2 Diagram showing RN-based targeting in an axial plane. The center of the STN lies on the same line as the anterior boundary of the RN.

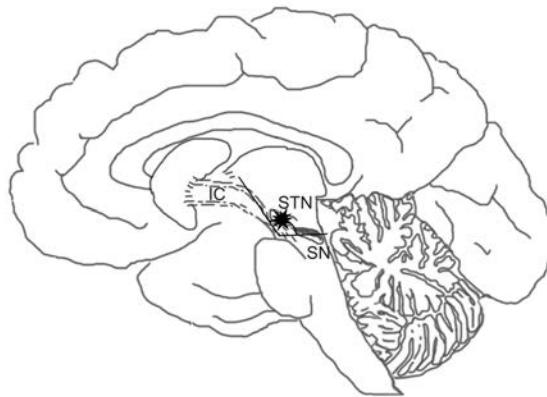


Figure 4.3 Diagram showing targeting based on the nigrocapsular angle in a sagittal plane. The STN lies in the corner that is formed by the descending IC and the SN.

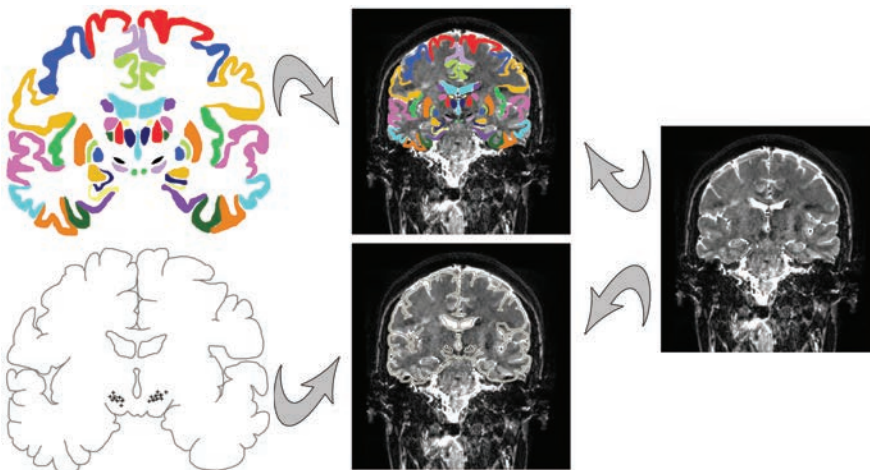


Figure 4.4 Diagram showing the idea of indirect targeting based on atlas mapping. On the left-hand side, at the top, an atlas slice with anatomical information can be seen, containing labeled structures. At the bottom, a functional atlas is represented, consisting of a cloud of target points that were used in previously performed DBS operations. On the right-hand side, the patient's MRI data can be seen. The gray arrows represent the transformation that is necessary to map the atlases to the patient's MRI data, resulting in overlaid information (as shown in the middle).

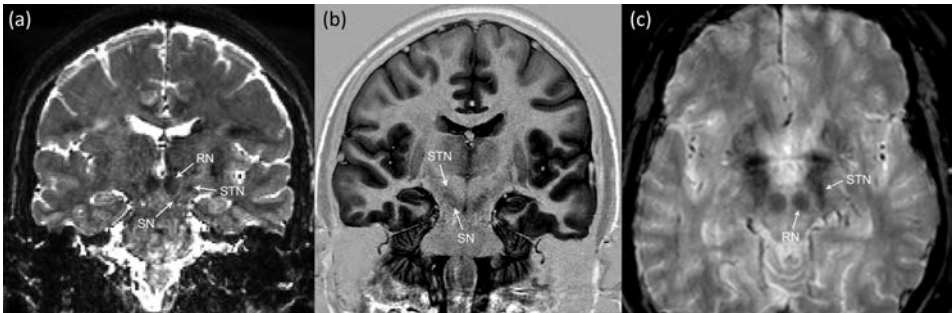


Figure 4.5 Coronal slices of (a) T_2 -weighted FSE and (b) IR MRI data sets, and an axial slice of an (c) SWI MRI data set, visualizing the STN directly.

Brain atlas registration

Table 4.2 summarizes the papers found on atlas-based STN targeting that presented quantitative results. Ortega et al. digitized the anatomical Talairach-Tournoux atlas, registered it nonlinearly, and compared the resulting targets with recorded micro-electrode positions, obtaining good results [227]. However, Nowinski et al. demonstrated inconsistency of the three planes for an anatomical atlas in the STN region, restricting the use of the atlas in 3D [223].

Sánchez Castro et al. collected MRI data with visible STNs to use as a brain atlas [264, 265]. Duay et al. [92] increased the speed of the registration algorithm and showed that the atlas targeting variability is comparable to an expert, with a registration error similar to those reported by Sánchez Castro et al. [265]. Bardin et al. [21] combined two kinds of anatomical information, namely histological and MRI data, into a human basal ganglia atlas (cf. Yelnik et al. [334]). After atlas registration, the resulting STN coordinates correlated well with MER and postoperative MRI. The authors improved the registration step, enabling a better match with individual patient anatomy (error <1 mm) [20].

With respect to functional atlases, Nowinski et al. investigated the differences in spatial position between the anatomical and functional STN [224]. The anatomical STN was derived from the Schaltenbrand-Wahren atlas [266], while the functional STN was constructed from ventriculography, MER, and X-ray data, and neurological assessment of 184 Parkinson's patients [222]. The anatomical and functional STN correlated well.

D'Haese et al. developed a targeting method using MER and optimal electrode contacts determined postoperatively, and showed that automatic target prediction

is feasible [84]. Pallavaram et al. extended this, achieving a better correlation of the electrophysiological maps with the underlying anatomy [230]. Guo et al. compared six methods using functional data, among which a brain atlas, MER data, and a collection of previous targets [124, 126]. The combination of all data performed best, followed by the previous targets and the MER data. All three methods provided a more accurate estimation than techniques solely dependent on anatomy. The authors used these results to construct probabilistic maps for STN DBS trajectory planning [125].

4.3.3 Direct targeting

T₂-weighted MRI

As can be seen in Table 4.3, a multitude of papers have reported validated results of T_2 -weighted MRI for direct STN identification. Starr et al. [285] showed that direct targeting is possible on T_2 -weighted FSE MRI, leading to consistent electrode placement in the dorsolateral STN [283]. Bejjani et al. selected the central track for implantation in 19 out of their 24 clinical cases [32]. Egidi et al. reported even slightly better results: their visualized target track was chosen in 85% of cases [95]. Dormont et al. examined postmortem tissue and showed that the hypointense signal reported by these first studies correlates with the presence of iron and corresponds anatomically to the STN [86]. They noted, however, that the most posterior part of the STN was not visible in any of the cases.

In addition, research has been done on the correspondence between MRI-based and landmark-based STN coordinates. Zhu et al. [337] and Richter et al. [255] concluded that MRI is needed, because atlas-based coordinates suffer from interpatient variability in STN size [255] and position [255, 337]. Littlechild et al. [193] and Slavin et al. [276] both reported that the STN target varies considerably in relation to the MCP, again suggesting that direct visualization on MRI enables more accurate targeting than the atlas-based method. Ashkan et al. confirmed this, finding a significant difference between this target and the STN as visualized on MRI [17]. The latter lies on average 1.7 mm more medial, 0.7 mm more anterior, and 0.7 mm more ventral than the atlas target.

A substantial interindividual variability of STN size, orientation and position and a significant difference between MRI-based and atlas-based coordinates in 66 patients was also demonstrated by Patel et al [238]. Davies and Daniluk found similar variation, based on series of 60 and 62 patients [74, 78]. In the latter, the STN's lateral coordinate varied by as much as 5.8 mm and the anteroposterior size of the STN varied by 8 mm [75], implying that the use of atlas-based targeting may result in failure to identify the STN during MER.

Patel et al. validated direct targeting on axial and coronal MRI [237]. In a first series, they used macrostimulation for target adjustment, while subsequently, target verification was based solely on preoperative MRI. The latter yielded a mean error of 0.3–0.4 mm only. Together with a follow-up study on the improvement of activities of daily living and the motor score, this led to the conclusion that T_2 -weighted-MRI-based targeting is safe and effective [239].

Inversion recovery MRI

Researchers have also investigated IR methods for direct visualization of the basal ganglia. Starr et al. [283] identified the globus pallidus internus (GPi), while Benabid et al. [35] depicted the GPi and the thalamus. The protocols they used were not suitable to visualize the STN. Though many research groups have tried to improve upon this, no quantitative studies on this subject are available yet.

Kitajima et al. proposed the short inversion time inversion recovery (STIR) method and compared this to T_2 -weighted FSE MRI [166]. FSE depicted the upper and lateral STN margins more clearly, while fast STIR was superior with respect to the visibility of the lower margin and provided a better contrast between STN and SN. In addition, Taoka et al. developed two sets of guidelines that facilitate identification of the STN on STIR images, the so-called “Sukeroku sign” and the “dent internal-capsule sign” [295]. Ishimori et al. [151] investigated phase sensitive IR and showed that the STN position on IR MRI differs at most 2 mm from the coordinates found with AC-PC-based targeting, comparable to the results obtained with T_2 -weighted images [17].

Susceptibility-weighted MRI

Apart from T_2 -weighted and IR MRI, it is also possible to acquire T_2^* -weighted (susceptibility-weighted) MR scans. T_2^* imaging is even more sensitive to local iron deposits, as occur in the STN amongst others. Dormont et al. [86] established the correlation of these iron deposits and the hypointensities on T_2^* -weighted MRI, while Slavin et al. [276] applied this to 3T data. Taoka et al. also visualized the iron content of the STN using T_2^* -weighted MRI [296]. They compared the results with STIR MRI and found that the posterior STN parts were not visible on the T_2^* -weighted images, leading to the conclusion that a combination with STIR might be more useful to target the STN.

Bonny et al. generated multiple images with increased T_2^* -weighting to maximize the contrast between the STN and surrounding structures [44]. Elolf et al. also used multiple gradient-echoes to add contrast to conventional T_1 -weighted MRI

[97]. Wu et al. used a steady-state free precession (SSFP) MRI method, facilitating the visualization of midbrain nuclei with a heavy T_2^* -weighting and relatively short TE [331]. However, none of these studies presented quantitative results on STN targeting.

To enhance T_2^* -weighted images, Volz et al. presented a method to reduce signal loss, resulting in good contrast [317]. Another applicable technique is SWI (susceptibility-weighted imaging), a method that uses the phase data. Young and Chen exploited this to produce T_2^* contrast additive to the T_1 or T_2 contrast intrinsic to the imaging protocol, in this way improving the contrast between the nuclei of interest [335]. Rauscher et al. [253] and Vertinsky et al. [314] also performed postprocessing with phase images, giving rise to a higher visibility of the STN and even of the subthalamic fasciculus. However, for these methods, the STN position as identified on MRI again has not been validated.

Relaxation time maps derived from MRI

Apart from T_1 -, T_2 - or T_2^* -weighted acquisitions, it is also possible to map the true relaxation time for each voxel by performing multiple MR acquisitions with different parameters. Bonny et al. already reconstructed T_2^* maps from their measurements in 2001 [44]. Helms et al. used T_2^* maps for improved delineation of iron rich structures, in particular the STN and SN [143]. Lebel et al. investigated T_2^* mapping of the basal ganglia at 4.7 T, in order to increase spatial resolution and sensitivity to iron content [180].

Guo et al. [127] were the first to introduce relaxation time maps, for T_1 and T_2 , into their DBS targeting application [124, 126]. This study compared the centers of basal ganglia nuclei based on the relaxation time maps with the coordinates derived from the Schaltenbrand-Wahren atlas and the actual surgical targets of 15 patients that underwent surgery. As the mean displacement was 3.21 ± 0.80 mm, these results indicated the potential of the relaxation time maps for DBS targeting.

High-field-strength MRI

Following the example of Lebel et al. [180], recently more studies have been published on direct visualization of the STN and other basal ganglia using MRI scanners with high field-strengths. Abosch et al. acquired susceptibility-weighted MRI data at 7.0 T and showed that the superior resolution and contrast at this field strength dramatically improves delineation of the STN [1]. Cho et al. also visualized the STN using T_2^* -weighted scans on 7-T MRI [61], and in addition imaged the SN in 9 healthy controls and 8 PD patients, revealing distinct morphological changes due

to PD [62].

4.3.4 Comparative studies

Much research has been done on the comparison of direct and indirect targeting. Table 4.4 summarizes the comparative papers that presented quantitative results.

Studies that favor indirect targeting

Zonenshayn et al. investigated STN targeting using four different methods, namely: 1) coronal MRI, 2) the STN center on a Schaltenbrand-Wahren atlas, 3) AC-PC-based targeting, and 4) a composite target based on all three methods [340]. The results were compared to the final target (found with help of MER). The combination of three methods appeared to be best, while only MRI gave the worst result. Cuny et al. also compared three methods [71]. The first technique was direct identification on T_2 -weighted MRI (see Table 1). The second and third method both involved indirect targeting based on the AC-PC line, determined by ventriculography or MRI, respectively. The most effective contact was taken as the gold standard. The authors concluded that indirect targeting based on MR worked best, while direct targeting gave the worst outcome.

Andrade-Souza et al. investigated direct targeting using coronal MRI, indirect targeting using the AC-PC, and a technique using the RN as a landmark [11]. The implantation was optimized using MER, while the most effective contact was identified using postoperative MRI. After comparing the mean distances between the targets and optimal contact, the authors concluded that the RN is a reliable marker for STN targeting. This is contradictory to the results of Danish et al. [76] (see Table 4.1). Breit et al. also evaluated coronal T_2 -weighted MRI, this time in comparison to AC-PC-based targeting using ventriculography [45]. The implantation was refined using MER, and the actual target was chosen to be the most effective contact. Their findings showed that targeting of the STN using AC-PC from ventriculography is more accurate than direct targeting on MRI. Sánchez Castro et al. [264] compared coronal T_2 -weighted (IR) MRI with indirect targeting using a registered atlas, which was based on MRI data with visible STNs. Their results showed an average error of 1.72 mm, according to Sánchez Castro et al. small enough to justify the use of the atlas.

In further research, Andrade-Souza et al. compared 2D T_2 -weighted axial and 3D reconstruction MRI [12]. They found that indirect and direct targets based on 3D reconstruction more closely approximate the optimal contact than targets chosen using 2D MRI. However, both indirect targets were better than the direct targets.

Studies that favor direct targeting on MRI

Starr et al. performed MRI and MER to target the STN [284]. They used a combination of indirect AC-PC-based targeting and direct targeting on T_2 -weighted MRI. The authors managed to visualize the STN directly for 92% of procedures, which supports the choice for direct imaging instead of AC-PC-based methods for STN targeting. The reliability of indirect methods as compared to direct targeting was also investigated by Schlaier et al [267]. They determined STN targets in five different ways: 1) direct targeting using axial T_2 -weighted MRI, 2) direct targeting on coronal T_2 -weighted MRI, 3) indirect targeting using an axial atlas slice, 4) indirect targeting on a coronal atlas slice, 5) indirect targeting using AC-PC references. Direct targeting seemed more reliable than atlas-based targeting, due to large inter-patient variability in the STN coordinates as derived from MRI. Ashkan et al. [17] confirmed these results on variability in STN position. Their direct target differed on average 0.7–1.7 mm in all three directions.

Although all studies described above preferred direct targeting, they did not validate this claim with intra- or postoperative information. Koike et al. did use the identified STN thickness during MER and clinical parameters, namely the effect on the disease and on the medication dose, as evaluation parameters [167]. They compared direct targeting on T_2 -weighted FSE MRI to the conventional indirect AC-PC method. The results showed a significantly larger mean STN thickness (indicating a longer electrode track through the STN and thus a better targeting) in the direct group and clinical parameters also displayed larger improvements for the direct group.

Though all studies mentioned previously in this section used 1.5-T MRI, Acar et al. investigated the benefit of direct targeting on 3.0 T over traditional AC-PC-based targeting using 1.5 T [2]. They calculated Euclidean distances between the directly and indirectly determined coordinates in three dimensions, resulting in mean differences between the two locations of 0.45 mm, 0.72 mm, and 0.98 mm in the X, Y, and Z axes, respectively. According to the authors, MRI has advanced such that direct targeting of the STN is no longer imprecise.

4.4 Discussion

In this chapter we reviewed indirect and direct STN targeting methods based on MRI. The most common indirect methods use either landmarks such as AC-PC [17, 229, 231, 284] and RN [18, 32, 71, 76] or atlases built from anatomical [20, 21, 92, 264, 265] and/or functional [84, 124, 126, 222, 230] information. These methods are applicable in all cases but are not very patient-specific. Direct methods already in use clinically comprise T_2 -weighted FSE [32, 86, 95, 285] and IR MRI

[151, 166, 295]. These techniques can account for interpatient variability [17, 75, 193, 238, 276] but often suffer from low contrast and technical issues [139], such as a long acquisition time [32, 237, 337], required reformatting of images, and the need for preparatory T_1 -weighted sequences used to plan the acquisition of T_2 -weighted planes [32, 284].

The comparative studies presented do not provide us with a straightforward conclusion on the best STN targeting protocol. Earlier publications tend to be in favor of indirect methods, mainly AC-PC-based, while more recent studies are more inclined to prefer direct visualization. Most publications report the use of 1.5-T MRI and the majority of hospitals still use this field strength, so the recent preference for direct targeting is not likely to be due to 3-T MRI. The phenomenon might be caused by advances in MR imaging at 1.5 T, with respect to contrast, noise and distortion, resulting in a targeting method that is more specific than AC-PC-based targeting. Due to continuous progress in MRI technology, direct targeting is still expected to improve in the future.

Although it seems that the future of STN targeting will be focused on patient-specific direct methods, it is still important to keep in mind the limitations of STN visualization on anatomical MRI. Often, only the anterior STN is visible as a hypointense region [86]. In addition, the contrast between the STN and surrounding structures is not optimal, hindering identification of the STN boundaries [97, 143, 166]. Furthermore, the question remains whether the visualized STN coincides with the functional target for DBS (often determined by MER) [135, 138, 193]. Promising new methods such as relaxation time maps and susceptibility-weighted imaging, as well as imaging at 7 T, have not been validated yet in large clinical studies. Besides, technical issues strongly influence the MRI procedure and quality. Examples are the MR compatibility of the stereotactic frame, image artifacts (which will be even larger at higher field strengths) due to patient movement and magnetic field distortion, although the latter can be controlled reasonably for the midbrain [75, 206]. Because of these issues, further research into STN localization methods, both direct and indirect, seems necessary.

The comparative studies that have validated the targeting with the most effective contact location also have their limitations. The conclusions of Cuny et al. [71], Andrade-Souza et al. [11, 12] and Breit et al. [45], that indirect targeting is more relevant for electrode placement, should thus be considered with care. As the primary targeting in these studies was indirect, the final contact, even after intraoperative adjustment, was close to the original indirect target by definition. In addition, analyzing indirect versus direct targeting according to the optimal contact only underlines differences between the final position and the primary targets. This bias would of course also exist if primary targeting were to be performed using a direct method. Caire et al. also compared STN localization methods based on AC-PC and 1.5-T

MRI [55], revealing significant differences in all three dimensions. Instead of drawing conclusions on which targeting method is more suitable, the authors stated that apparently, it would be better to conclude that the indirect AC-PC-based target does not coincide with the center of the STN as visualized on anatomical MRI. Moreover, various follow-up [137, 177, 185, 263] and post-mortem [289] studies state that the best clinical target is located in the dorsolateral part of the STN and the area just superior to the STN (zona incerta, field of Forel).

The results from several papers show that stimulating the dorsolateral motor part of the STN is more effective than stimulating the center [55, 137, 177, 185, 263, 289]. As conventional direct targeting on anatomical MRI cannot distinguish the dorsolateral STN part due to lack of contrast, it is useful to further investigate the use of other MRI-based methods in order to facilitate specific targeting of this part. Examples of techniques that have not yet proven their clinical usefulness but that might aid in the localization of the STN are the use of landmarks such as the nigrocapsular angle [118], the mammillary commissures [181, 303], and the line connecting the mammillary bodies [256]. In addition, a fast-developing line of research focuses on susceptibility-weighted MRI and T_2^* mapping in order to improve the contrast in the STN region [143, 180, 314, 317, 331]. However, it is improbable that this improved contrast would give rise to identification of the dorsolateral STN part specifically.

Besides trying to find the dorsolateral STN part, possibilities to divide the STN functionally and identify the motor part should also be investigated. Modalities such as functional or diffusion-weighted MRI could yield features that facilitate separation of the motor part of the STN. Diffusion-weighted MRI sensitizes the MR acquisition to water diffusion in specific directions. Afterwards, the diffusion profile in a voxel can be fitted as an ellipse (DTI [211]) or a higher-order shape (HARDI [311]). By analyzing these profiles in the STN itself, it was shown that different parts of the STN in a rat brain could be separated visually and automatically [48, 49]. Recently, Coenen et al. also published a case study on DTI-based fiber anatomy in the STN region, to help identification of the tremor suppression target [63].

Apart from the primary targeting based on (MR) imaging, there are other parts of the surgical pipeline that influence the clinical outcome of a DBS procedure and should not be ignored. The most important are the type of stereotactic frame, the selection of the trajectory (this can be done manually or automatic [52]), registration of different imaging modalities, intraoperative brain shift [150], intraoperative electrode adjustment, and postoperative parameter estimation. Whilst striving for the best possible results of deep brain stimulation, all these factors should be given appropriate attention.

Table 4.1 Table summarizing indirect studies based on anatomical landmarks as visualized on MRI.

Study	Subjects	Landmark	MRI protocol	Validation method	Outcome	Conclusion
Schuurman et al. 1999 [269]	15	AC-PC	3D gradient-echo, 1.5 T	Intraoperative ventriculography	Difference in coordinates: 1.29 mm for different targets	Correspondence between ventriculography and MR justifies the use of MR
Starr 2002 [283]	180	AC-PC	3D gradient-echo, 1.5 T	MRI: coronal FSE, 1.5 T	Direct/indirect concordant to within 1–1.5 mm	MRI-based targeting should be combined with MER and postoperative MRI
Pallavaram et al. 2008 [230]	2	AC-PC	T_1 -weighted, 1.5 T	Comparison of 38 neurosurgeons	Mean distance of >1 mm with same standard deviation	Automatic AC-PC selection or direct targeting should be used
Ardekani and Bachman 2009 [14]	42	AC-PC	T_1 - and T_2 -weighted, 1.5 and 3.0 T	Comparison of manual and automatic method	Average Euclidean distance of 1.1 mm	The authors' model-based algorithm is better than earlier automatic AC-PC methods
Bejjani et al. 2000 [32]	12	RN	Coronal spin-echo, 1.5 T	MER	The central track was selected 19 out of 24 times	MRI targeting is useful for STN stimulation but should be combined with MER
Cuny et al. 2002 [71]	14	RN	Coronal double-echo spin-echo, 1.5 T	AC-PC-based using MRI and ventriculography; best clinical response	Distances optimum-target: 2.61 mm for AC-PC MRI, 3.92 mm for RN method	Targeting of STN based on RN is less effective than AC-PC based methods
Danish et al. 2006 [76]	26	AC-PC, RN	Sagittal T_1 -weighted, FSE, 1.5T	Comparison of distances: MCP-STN, MCP-RN, STN-RN	Standard deviation of MCP-RN and STN-RN larger than of MCP-STN	The RN is no reliable marker for STN position
Pollo et al. 2003 [247]	31	AC-PC, RN, IC, thalamus, SN	3D MPAGE and coronal IR, 1.5 T	Schaltenbrand-Wahren atlas	Mean target coordinates located in inferior STN	A combination of different landmarks yields a visual procedure to find the STN
Giller et al. 2005 [118]	29	nigrocapsular angle (IC, SN)	Sagittal FSE IR, 1.5 T	No quantitative comparison done	IC detected in 97% of slices, SN in 95%, STN in 73%	The indirect sagittal method using the nigro-capsular angle can refine STN localization
Lee et al. 2006 [181]	6	SMC	Coronal MPAGE, FSE, 1.5 T	RN-based targeting	RN-based matches atlas (12, -3, -4 mm), SMC-based errors in X (14.25) and Z (-5.0)	The method of this paper is sensitive to ventricular enlargement, but the top of the SMC is a reliable landmark
Toda et al. 2009 [303]	26	PMC, RN, mamillothalamic tract	Axial and coronal TSE, 1.5 and 3 T	RN-based and AC-PC-based targeting, MER	The central track was selected in 81% of 3-T cases, in 31% of 1.5-T cases	The composite targeting method on 3 T offers reliable STN targeting

Table 4.2 Table summarizing indirect studies based on brain atlases.

Study	Subjects	Atlas information	Registration method	Validation method	Outcome	Conclusion
Ortega et al. 2008 [227]	10	Digitized Talairach-Tournoux atlas	Nonlinear registration	Final microelectrode position	Difference in coordinates: 1.89 ± 1.00 mm	System matching the atlas to T_1 -weighted MRI offers good targeting results
Sánchez-Castro et al. 2005 [265]	8	MRI of subject with best visible STN	Nonrigid registration (affine and nonlinear)	Direct STN targeting by expert	Smallest difference in coordinates: 1.80 ± 0.62 mm	Automatic STN location using nonrigid atlas registration is possible and accurate
Bardinet et al. 2005 [21]	16	Postmortem MRI and histology data	Rigid and affine registration	Electrophysiological recordings (6) and final electrode position (10)	81.5% of recordings and 70% of electrodes within STN as defined by atlas	Atlas/MRI coregistration could be used as a standard method for targeting of deep brain structures
Nowinski et al. 2007 [224]	184	Ventriculography, MER, neurological assessment	Linear scaling along AC-PC line	STN in Schaltenbrand-Wahren atlas	The functional STN (probability ≥ 0.5) is completely inside the anatomical STN	The functional STN can be used for identification of the STN on images
D'Haese et al. 2005 [84]	21	MER, stimulation parameters, final electrode positions	Nonlinear registration	Preoperative AC-PC and retrospective automatic targeting	Average distance: 3.66 mm for AC-PC, 2.71 mm for automatic targeting (right STN)	Automatic prediction of the STN target from previous targets and electrophysiology data is an achievable goal
Guo et al. 2007 [125]	28	Atlas, MER, optimal contacts, MRI-based methods	Nonrigid registration	Actual surgical target location	Average distance smallest for combination of all atlas data: 1.7 ± 0.7 mm	The method with both anatomical and functional data provides the most reliable STN target

Table 4.3 Table summarizing direct studies using T_2 -weighted MRI and relaxation time maps.

Study	Subjects	MRI protocol	Validation method	Outcome	Conclusion
Starr et al. 1999 [285]	6	Coronal T_2 -weighted FSE MRI, 1.5 T	MER	Coordinates were close to AC-PC-based values and initial MER track passed through the STN in every case	Direct visualization facilitates reliable targeting of the STN but MER mapping remains necessary
Starr 2002 [283]	44	Coronal T_2 -weighted FSE MRI, 1.5 T	MER and postoperative MRI	The STN was directly visualized on MRI in 92% of cases; MER was used to adapt the target intraoperatively	The combined approach leads to consistent electrode placement in the dorsolateral STN
Bejjani et al. 2000 [32]	12	Coronal T_2 -weighted spin-echo MRI, 1.5 T	MER and optimal contact position	The central track was selected for 19 of 24 electrodes	MRI targeting is useful for STN stimulation but should be combined with MER
Egidi et al. 2002 [95]	13	Axial T_2 -weighted spin-echo MRI, 1.5 T	MER and postoperative MRI	The targeted track was chosen for 22 of 26 electrodes	1.5-T MR images are highly effective for STN targeting
Littlechild et al. 2003 [193]	25	Axial T_2 -weighted MRI, 1.5 T	MER and optimal contact position	Significant variation in target position (4–5 mm); mean distance between target and electrode 1.7 mm	The STN varies in position and can be accurately targeted from MRI alone
Slavin et al. 2006 [276]	13	T_2 -weighted FSE MRI in three directions, 3.0 T	MER	Variation in target position around 2 mm; all tracks pass through STN	3-T MRI enables accurate direct visualization of the STN
Patel et al. 2002 [237]	26; 19	Axial and coronal T_2 -weighted MRI, 1.5 T	Macrostimulation; intraoperative MRI	Mean target error of 0.3 mm medially and 0.4 mm anteroposteriorly	MRI-directed targeting of the STN through guide tubes is accurate, and allows direct verification and corrections as necessary
Guo et al. 2005 [127]	15	T_1 and T_2 maps, 1.5 T	Atlas coordinates, actual surgical targets	Mean displacement 3.21 ± 0.80 mm	The results indicate the potential capability of this system to accurately identify the STN

Table 4.4 Table summarizing studies comparing indirect and direct methods.

Study	Subjects	Methods	Validation method	Outcome	Conclusion
Zonenshajn et al. 2000 [340]	15	Coronal MRI (T_2 -weighted/IR), atlas, AC-PC, combination	Final target based on MER	Distance between MRI and target: 2.6 ± 1.3 mm; between composite and target: 1.3 ± 1.1 mm	Combination of three targeting methods offers best correlation with the final target
Cuny et al. 2002 [71]	14	T_2 -weighted MRI, AC-PC with ventriculography, AC-PC with MRI	Most effective contact	Distance between AC-PC (MRI)/best contact: 2.6 ± 1.2 mm; between direct/best contact: 3.9 ± 1.9 mm	Indirect targeting based on MR works best, direct targeting gives worst outcome
Andrade-Souza et al. 2005 [11]	14	Coronal MRI, AC-PC, RN-based targeting	Optimal contact (MER and postoperative MRI)	Distances to optimal contact: MRI: 4.7 mm; AC-PC: 3.4 mm; RN: 3.2 mm	RN is a reliable marker to approximate the optimal contact position
Breit et al. 2006 [45]	30	Coronal T_2 -weighted MRI, AC-PC based on ventriculography	Most effective contact	Mean targeting error 4.1 ± 1.7 mm for MRI and 2.4 ± 1.1 mm for AC-PC	AC-PC using ventriculography is more accurate than direct targeting on MRI
Sánchez-Castro et al. 2006 [264]	39	Coronal T_2 -weighted MRI, anatomical atlas based on direct targets	Comparison of STN coordinates in MRI	Best atlas registration method (B-splines): average error 1.72 ± 0.48 mm	Automatic STN targeting is possible and as accurate as current expert methods
Andrade-Souza et al. 2005 [12]	14	Axial T_2 -weighted MRI, 3D reconstruction (both direct and indirect)	Optimal contact (MER and postoperative MRI)	Distances to optimum: 2D MRI direct: 4.7 mm; 3D reco direct: 3.5 mm; 2D MRI indirect: 3.4 mm; 3D reco indirect: 2.6 mm	3D reconstruction leads to better approximation of optimal contact; indirect methods are better than direct targets
Starr et al. 2002 [283]	44	Coronal T_2 -weighted FSE MRI, AC-PC	Comparison in atlas coordinate system	In 34% the STN lies >1 mm more lateral than 12 mm and in 40% the STN lies >1 mm more inferior than 4 mm	Direct targeting accounts better for interpatient variability than indirect targeting
Schlaier et al. 2005 [267]	14	Axial/coronal T_2 -weighted MRI and atlas, AC-PC	Comparison in atlas coordinate system	All STN coordinates displayed a range of 4 to 5 mm	Direct targeting seemed more reliable due to large interpatient variability
Ashkan et al. 2007 [17]	29	Axial T_2 -weighted MRI, AC-PC	Comparison in atlas coordinate system	Direct: 1.7 mm more medial, 0.7 mm more anterior, 0.7 mm more ventral	Direct targeting more accurate due to variability in STN position
Koike et al. 2008 [167]	44	T_2 -weighted MRI (using RN), AC-PC	MER and clinical parameters	Direct group: longer track through STN and larger clinical improvement	Direct targeting with single-track recording can be standard for DBS
Acar et al. 2007 [2]	20	Axial T_2 -weighted FSE MRI (3.0 T), AC-PC (1.5 T)	Comparison in atlas coordinate system	Mean distances were 0.45 mm, 0.72 mm and 0.98 mm in X, Y, Z directions	Direct targeting is no longer imprecise
Caire et al. 2009 [55]	22	Coronal T_2 -weighted TSE MRI, AC-PC	Comparison of STN center coordinates	Significant differences in coordinates in all three directions	MRI-based and AC-PC-based targets do not coincide



Science never solves a problem without creating ten more.

George Bernard Shaw

This chapter is based on:

“Untangling a fiber bundle knot - Preliminary results on STN connectivity using DTI and HARDI on rat brains.” Ellen Brunenberg, Vesna Prčkovska, Bram Platel, Gustav Strijkers, and Bart ter Haar Romeny. In *Proceedings of Seventeenth Annual Meeting of the International Society for Magnetic Resonance in Medicine (ISMRM) 2009*, pp. 740.

“K-means and graph cuts clustering of diffusion MRI in rat STN.” Ellen Brunenberg, Erik Pelgrim, Bart ter Haar Romeny, and Bram Platel. In *Proceedings of Eighteenth Annual Meeting of the International Society for Magnetic Resonance in Medicine (ISMRM) 2010*, pp. 4045.

“A Sobolev norm based distance measure for HARDI clustering - A feasibility study on phantom and real data.” Ellen Brunenberg, Remco Duits, Bart ter Haar Romeny and Bram Platel. In *Proceedings of Medical Image Computation and Computer-Assisted Intervention (MICCAI) 2010, Lecture Notes in Computer Science 6361*, pp. 175–182.

5.1 Introduction

5.1.1 Background

Deep brain stimulation in Parkinson’s disease patients can be improved by enhancing the motor effect and minimizing cognitive and emotional side effects. In this study, we wanted to investigate the added value of noninvasive diffusion MR imaging for this purpose. We hypothesized that the underlying axonal connectivity is different for distinct functional parts of the STN, for example, that the STN motor part is connected to the motor cortex, but the associative and limbic parts are not [136]. This principle enables a segmentation based on either the local fiber orientation and thus the local diffusion information or on the contextual information given by fiber bundles departing from or arriving in the STN.

5.1.2 Related work

Recently, many studies have been published on segmentation of gray matter nuclei from brain diffusion MRI data. A rich variety of classification and clustering algorithms has been employed, together with a multitude of dissimilarity measures, mainly focusing on diffusion tensor imaging (DTI).

Wiegell et al. [325] clustered DTI tensors in the thalamus, using k-means and the Frobenius norm. Ziyan et al. used graph cuts [338] and consistency clustering [339] on the same data set to investigate other metrics, namely the angular difference and the K-L (Kullback-Leibler) divergence. Duan et al. [91] classified diffusion within the thalamus using mean-shift clustering and the Frobenius norm, while Jonasson et al.

[161] investigated a level set approach. Apart from the thalamus, researchers have tried to segment other structures as well. Lenglet et al. [188] addressed the segmentation of cerebral white matter structures from DTI and proved that the dissimilarity measure has a deep impact on tensor statistics and thus also on achieved results. They presented a statistical surface evolution framework and implemented this with the Euclidean distance, K-L divergence and a Riemannian geodesic distance.

For high angular resolution diffusion imaging or HARDI [310], fewer choices for the dissimilarity measure are available. The \mathbb{L}_2 norm has been used most often to compare ODFs, possibly represented by spherical harmonics (SH) coefficients. Grassi et al. [121] published a similar study as Wiegell et al. [325], performing k-medoids clustering of HARDI data in the thalamus using the \mathbb{L}_2 norm on the ODFs. Similarly, Descoteaux [81] and Wassermann et al. [320] used the \mathbb{L}_2 norm on SH coefficient vectors. According to Descoteaux [81], one could use K-L divergence between 2 ODFs. However, this problem would quickly become too computationally expensive, because all N points on the sphere (~ 200) are used, instead of only n_{SH} SH coefficients (~ 15).

Apart from a clustering using SH coefficient vectors, there are other ways to represent the ODF and segment the data. Some studies have modeled the ODF by mixtures of von Mises-Fisher distributions [202] or other directional functions and mixture models [252]. Others have used a model-free representation of the ODF [60, 119], the latter proposing the geometric anisotropy as a scalar measure.

5.1.3 Aim

We started with a visual inspection of the local diffusion profiles within the rat STN ROI, to investigate the feasibility of this approach by determining whether HARDI glyphs can distinguish between the rat STN motor part on the one hand, and the cognitive and emotional part on the other hand. The first part of this chapter (Section 5.2) presents the results of our feasibility study on the added value of HARDI in comparison to DTI.

Afterwards, in Section 5.3, we discuss the clustering experiments that we performed on the rat STN ROI using k-means and graph cuts algorithms. Rats were used for these tests because postmortem rat measurements enable very high-resolution imaging. In addition, neural tract tracing studies have provided us with considerable knowledge on rat neuroanatomy and connectivity.

Subsequently, after experiencing some difficulties with respect to the weighing of different orders of diffusion information in the distance measure for clustering, we aimed to improve upon the commonly used \mathbb{L}_2 norm. To this end, we developed the so-called Sobolev norm, that incorporates all orders of spherical harmonics intuitively.

5.2. Exploration of the rat STN

More importantly, this norm does not only take into account the amplitudes of the glyphs under comparison, but also the coincidence of extrema. In Section 5.4, we elaborate on our new dissimilarity measure for HARDI clustering.

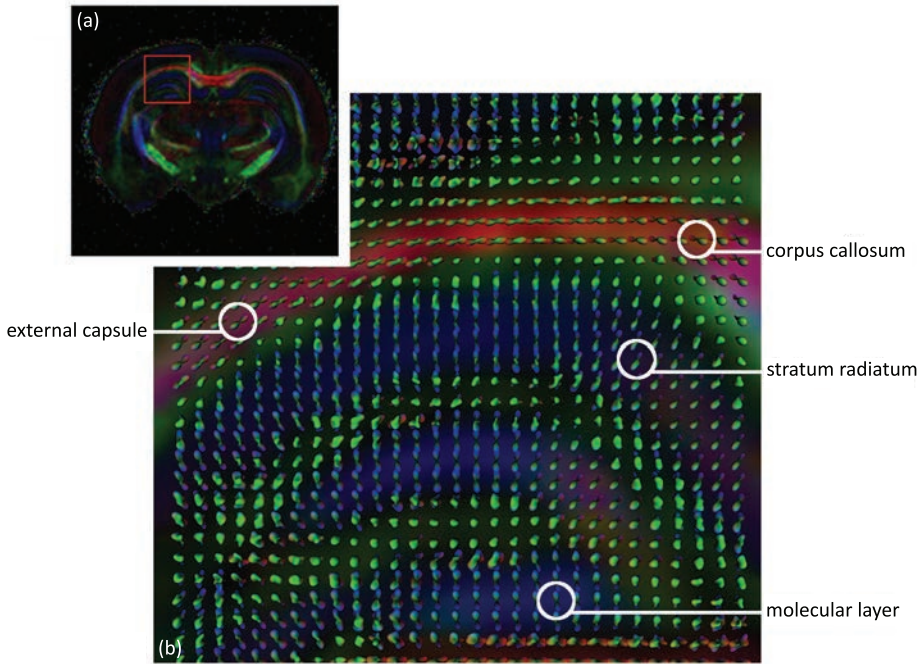


Figure 5.1 R_0 parameter tuning using linear diffusion profiles. (a) Weighted FA map of a rat brain slice, with red square indicating the ROI. Color coding: red: left-right, green: anterior-posterior, blue: inferior-superior. (b) Enlarged region of interest. The DOT parameters should be tuned in such a way that the diffusion profile is linear in the corpus callosum, external capsule, and hippocampus (stratum radiatum and molecular layer).

5.2 Exploration of the rat STN

5.2.1 Methods

Data acquisition

Rat brains (17-week old male Wistar rats) were extracted after transcardiac perfusion with 4% paraformaldehyde in phosphate buffered saline (PBS). The brains were stored in the fixation solution for 14 weeks, subsequently rinsed and put in pure PBS for 48 hours. Afterwards, the brains were immersed in Fomblin (Fens Chemicals,

Goes, The Netherlands) for magnetic susceptibility matching.

Imaging was performed on a 9.4-T Bruker Biospec AVANCE-III system. Anatomical T_2 -weighted images were recorded using a RARE sequence (RARE-factor 8, TE 36 ms, TR 2500 ms, NA 16, total time 32 minutes). Fifteen coronal slices with matrix size 384x384 were measured. The FOV was 25.6x25.6 mm, leading to an in-plane pixel dimension of 67 μm . Slice thickness was 500 μm and the interslice gap 50 μm . HARDI was acquired using a diffusion-weighted spin-echo sequence with two unipolar pulsed field gradients placed symmetrically around the 180 degree pulse (TE 27 ms, TR 4000 ms, NA 1, total time 19 hours). Some parameters (number of slices, slice thickness, and FOV) were identical to the RARE acquisition. For HARDI, the matrix was 128x128, zero-filled to 256x256, leading to an in-plane pixel dimension of 100 μm . A series of 132 images with different gradient directions and b -value 3000 s/mm^2 , together with an unweighted image, was measured.

Data processing

Processing of the diffusion MRI data was done in the DTITool developed at Eindhoven University of Technology [90]. Three of the available HARDI techniques (as elaborated on in Section 3.2.3) were implemented in this tool: analytical Q-ball imaging [82] and parametric and non-parametric DOT [228]. DOT has two extra parameters that require tuning: the effective diffusion time τ and the radius of a shell of the reconstructed probability profile R_0 .

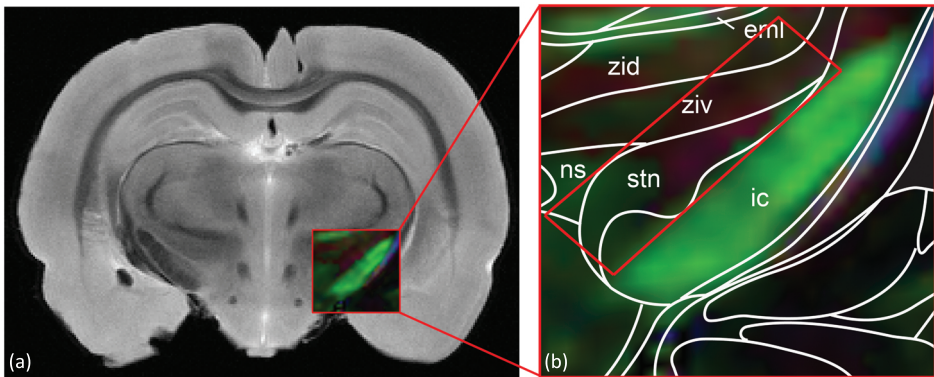


Figure 5.2 Anatomical MRI and FA map of a rat brain slice. (a) Anatomical RARE image, with the inlay representing a weighted FA map around the STN. Color coding as in Figure 5.1. (b) Enlarged STN region with part of the Paxinos rat atlas [240] as overlay (eml = external medullary lamina, ic = internal capsule, ns = nigrostriatal bundle, stn = subthalamic nucleus, zid = dorsal zona incerta, ziv = ventral zona incerta) and a smaller ROI in red.

Using the imaging parameters, we determined $\tau = \Delta - \delta/3 = 12$ ms, with Δ representing the time between two complementary diffusion gradients and δ the gradient duration. The R_0 parameter was varied, such that the correct probability profile would be reconstructed. This parameter tuning was validated using the elongated fibers in the corpus callosum, analogous to Özarslan et al. [228], as can be seen in Figure 5.1. The order of the spherical harmonics was varied between 4 and 8. Fiber bundle crossings in the area around the STN could be observed even at fourth order. As a preprocessing step, we included Laplace-Beltrami smoothing for both methods, with smoothing parameter $\lambda = 0.00005$ as an empirical optimal value for our data with a signal-to-noise ratio (SNR) of 30. We assumed that the fiber directions are given by the local maxima of the probability profile.

5.2.2 Results

Anatomical MRI and FA map

The RARE MRI protocol resulted in detailed anatomical images, as shown in Figure 5.2(a). In this coronal slice, the STN is visible as a middle-gray nucleus, lying along the dorsal border of the internal capsule. The image inlay represents the FA (fractional anisotropy) map that was calculated from the HARDI data for this slice. The map is colored according to maximum eigenvector direction (red: left-right, green: anterior-posterior, and blue: inferior-superior). In Figure 5.2(b), this inlay is enlarged and overlaid with the corresponding slice from the Paxinos rat brain atlas [240]. The STN and several neighboring areas, such as the internal capsule, are indicated. A smaller region of interest (ROI) aligned with the STN is drawn in red.

Different diffusion glyphs

Three different types of glyphs, visualizing the diffusion in a voxel, were rendered for the ROI shown in Figure 5.2(b). The rectangle was rotated approximately 50 degrees clockwise to enable a better view. Figure 5.3(a) displays superquadrics based on the second-order diffusion tensor, as derived from the HARDI data. Figures 5.3(b) and (c) show more advanced HARDI-based models, namely Q-ball and DOT glyphs.

Comparing the images of Figure 5.3(a), (b), and (c), it is clear that DTI superquadrics are unable to resolve the diffusion in the STN region. Figure 5.3(a) shows linear (anteroposterior) diffusion in the internal capsule (IC), but oblate tensors in the rest of the ROI. The linearity in the internal capsule is preserved in the Q-ball and DOT glyphs (Figure 5.3(b) and (c)). Moreover, the rest of the ROI shows more heterogeneity compared to the superquadrics.

Figure 5.4(a) provides us with the anatomical context of the diffusion glyphs, by means of an atlas overlay. We clearly observe crossings in the lateral part of the STN and the ventral zona incerta. A more linear configuration can again be seen in the upper left corner of the ROI. This area corresponds with the medial part of the STN and the nigrostriatal bundle. Based on this difference in diffusion profiles, we might be able to distinguish the two subterritories of the rat STN, the lateral motor part and the medial cognitive/emotional part (see Figure 5.4(b)).

5.3 Preliminary clustering experiments

5.3.1 Methods

Atlas registration

We used the anatomical (RARE, 67- μm pixel, 500- μm slice) and HARDI data (b -value 3000 s/mm^2 , 132 directions, 100- μm pixel) of a fixed rat brain measured at 9.4 T, acquired as described in Section 5.2.1. Instead of identifying the STN region using the RARE images (which do not always provide sufficient contrast) or manual registration with slices from the Paxinos rat brain atlas [240], for this experiment we registered a digitized version of that atlas, reconstructed by the Institute of Basic Medical Sciences in Oslo, Norway [145, 241]. A slice of this 3D rat brain atlas can be seen in Figure 5.5.

Because of the differences in contrast between the HARDI data and rat atlas labels, registration was performed using a T_2 -weighted MRI template matching the atlas as an intermediate [272]. Since Hjørnevik et al. [145] used another version of the Paxinos atlas [240, 241] than Schweinhardt et al. [272], the template developed by the latter did not exactly match with the atlas anymore. Therefore, we adapted the deformation matrix between the atlas and template by manual scaling and translation.

Nonlinear registration between the T_2 -weighted rat brain MRI template and our T_2 -weighted RARE data was done using FSL's FNIRT [10]. Subsequently, the deformation between the T_2 -weighted RARE data and the HARDI data was resolved with a rigid 2D method implementing the intensity-gradient-based registration by Haber et al. [128]. An ROI of 21 by 21 pixels around the right STN was extracted from the slice on which the STN was largest (see Figure 5.6).

5.3. Preliminary clustering experiments

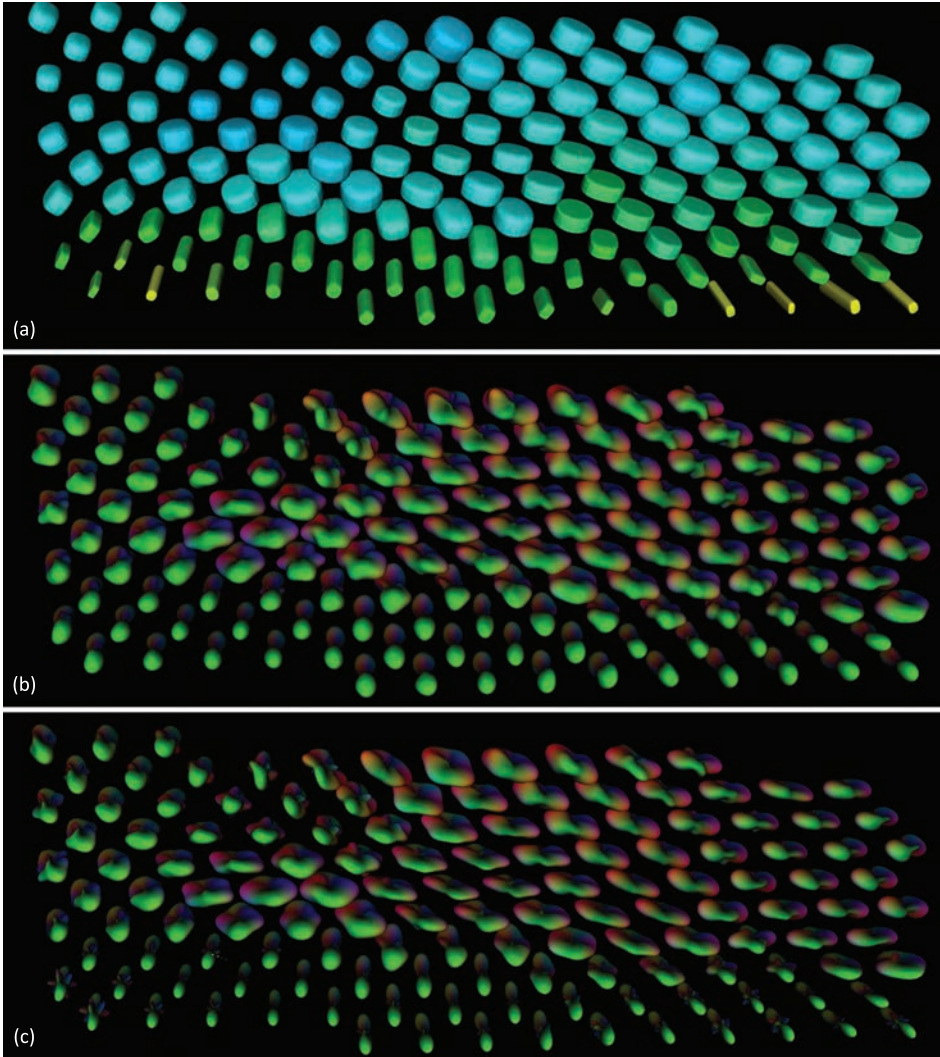


Figure 5.3 Different types of diffusion glyphs in the STN region (corresponding to the rectangular ROI shown in Figure 5.2(b)). (a) Second-order diffusion tensor superquadrics, color-coded according to FA (blue: low FA ~ 0.25 , yellow: high FA ~ 0.75). (b) Normalized Q-ball glyphs represented by 6th-order spherical harmonics. (c) DOT glyphs with the same order spherical harmonics.

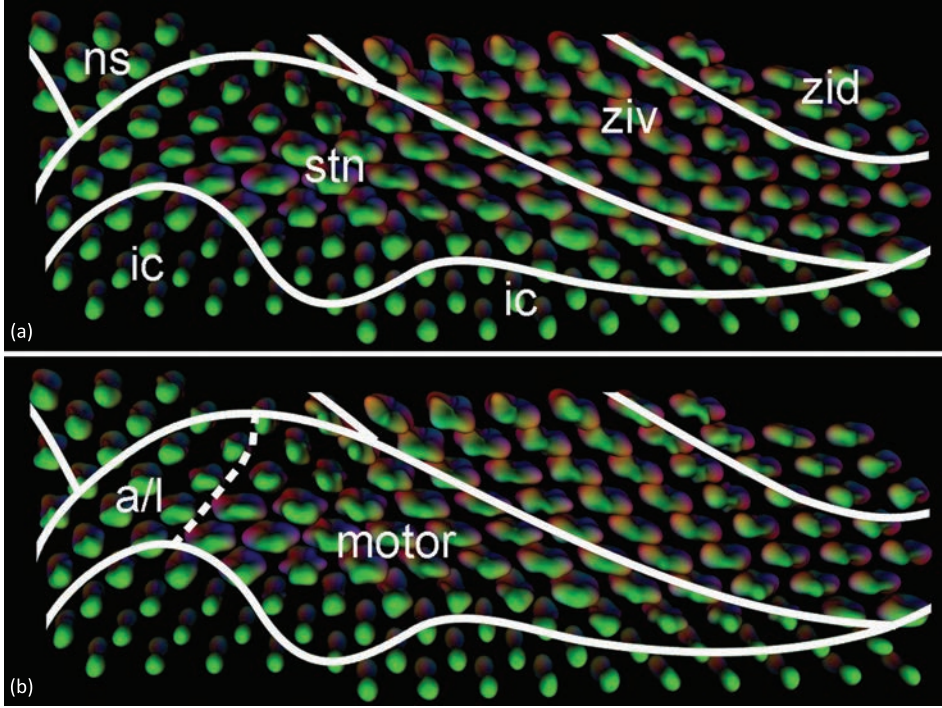


Figure 5.4 Diffusion glyphs in the STN region with anatomical context. (a) Normalized Q-ball glyphs in the STN region (from Figure 5.3(b)), with atlas overlay based on [240] (ic = internal capsule, ns = nigrostriatal bundle, stn = subthalamic nucleus, zid = dorsal zona incerta, ziv = ventral zona incerta). (b) Supposed subdivision of rat STN into the large lateral motor part (motor) and the smaller medial associative and limbic part (a/l), indicated by the dashed line.

Clustering

Clustering was done using two algorithms that have proven useful for classifying diffusion MRI data of the thalamus, namely k-means [121, 325] and spectral clustering involving graph cuts [338]. In Section 5.2, we already showed that HARDI results in more heterogeneous diffusion glyphs than DTI, which provides mainly isotropic profiles. Therefore, we performed clustering with the \mathbb{L}_2 norm on the spherical harmonics coefficients as a distance measure, analogous to Wassermann et al. [320]. Each diffusion profile was reconstructed using spherical harmonics basis functions of even orders, up to 8th order.

To investigate the influence of different orders on the clustering results, we experi-

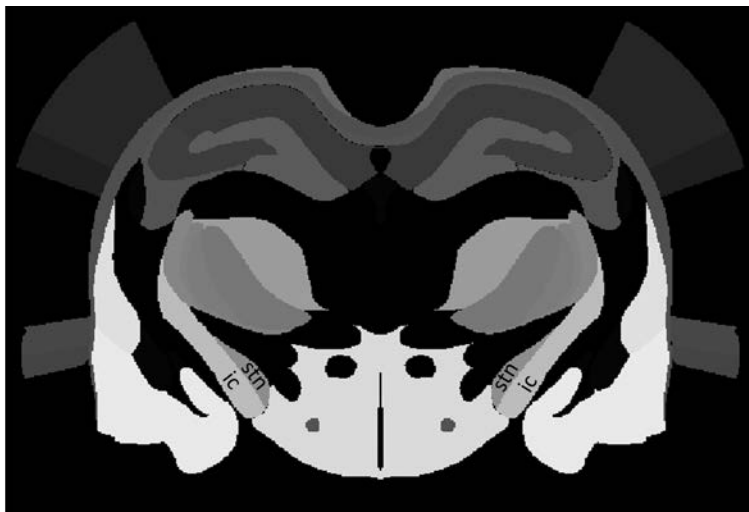


Figure 5.5 Coronal slice of 3D digital rat brain atlas [145]. Each gray value represents another anatomical structure. Labeled here are the subthalamic nucleus (stn) and the internal capsule (ic).

mented with several weighting factors denoted in a 5-element vector. Each element represents one of the even orders (0^{th} , 2^{nd} , 4^{th} , 6^{th} , or 8^{th}) and can have value 0 or 1. The vector $\{1,1,0,0,0\}$ means that the distance measure contains no information of 4^{th} , 6^{th} , and 8^{th} order, but is the result of the \mathbb{L}_2 norm on 0^{th} and 2^{nd} -order coefficients only.

Prior to the k-means clustering, we selected four seed points. One seed point was located within the STN, one in the IC (internal capsule) and two in the surrounding (background) structures. With regard to the graph cuts clustering, we chose to execute 10 clustering steps, yielding 11 clusters.

5.3.2 Results

The clustering results of the right STN ROI, processed with k-means and graph cuts algorithms and different weighting vectors, are presented in Figure 5.7. The k-means clustering finds one IC cluster, the best result being generated without 0^{th} -order information (Figure 5.7(d)). However, this technique is apparently unable to distinguish the STN from surrounding structures. In three cases of graph cuts results, the medial STN is separated (Figures 5.7(b), (c), and (f)). This might correspond to the cognitive/emotional part of the rat STN. The STN motor part would still be connected to the environment.

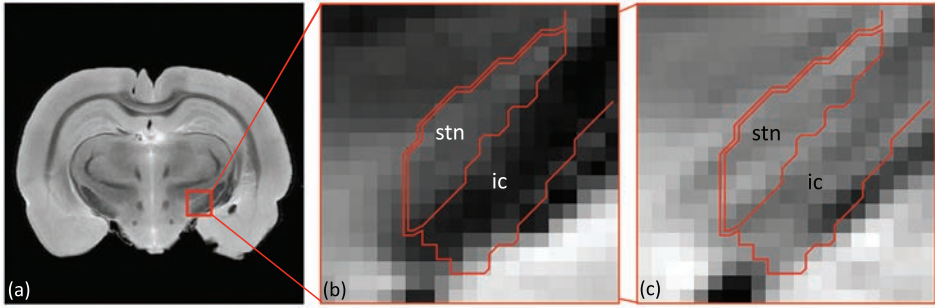


Figure 5.6 Selection of ROI around the right STN. (a) ROI indicated as a red square on T_2 -weighted RARE anatomical image. (b) Selected ROI of 21 by 21 pixels around the right STN in the resampled T_2 -weighted RARE data, with contours of the rat brain atlas [145] overlaid in red (ic = internal capsule, stn = subthalamic nucleus). (c) Contours of the rat brain atlas in red, overlaying the HARDI data that were averaged over all directions.

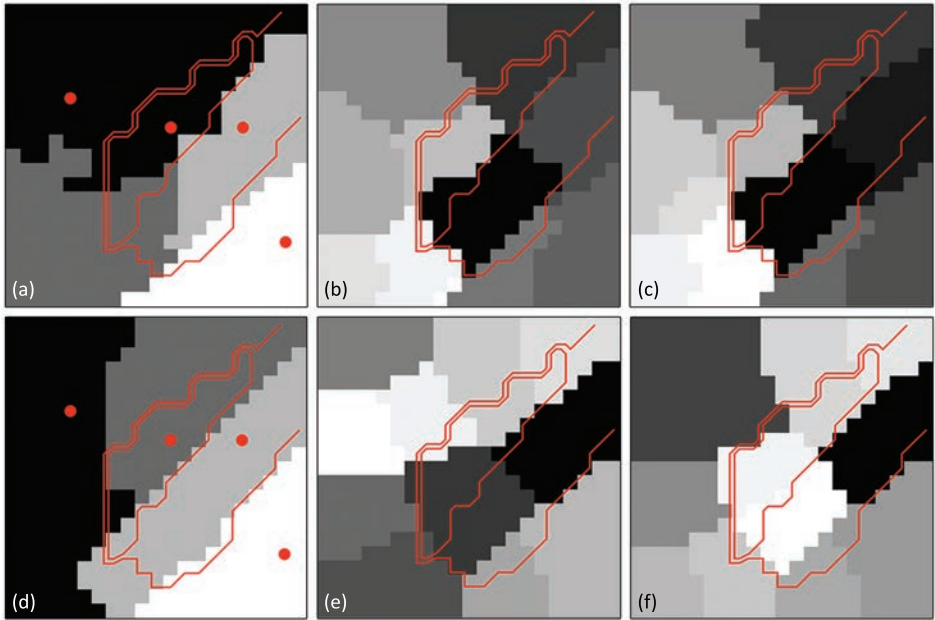


Figure 5.7 Preliminary clustering results for the right STN ROI (see Figure 5.6). (a) K-means result for weighting vector $\{1,1,0,0,0\}$ (identical for $\{1,1,1,1,1\}$). (b) Graph cuts result for weighting vector $\{1,1,0,0,0\}$. (c) Graph cuts result for weighting vector $\{1,1,1,1,1\}$. (d) K-means result for weighting vector $\{0,1,0,0,0\}$ (identical for $\{0,1,1,1,1\}$). (e) Graph cuts result for weighting vector $\{0,1,0,0,0\}$. (f) Graph cuts result for weighting vector $\{0,1,1,1,1\}$.

5.4 A specialized distance measure: the Sobolev norm

Because of the difficulties with respect to the weighing of different orders of diffusion information in the previous section, we attempted to improve upon the \mathbb{L}_2 norm. To this end, we developed the so-called Sobolev norm, which will be explained below.

5.4.1 Theory

Consider HARDI-image¹ $U : \mathbb{R}^3 \times S^2 \rightarrow \mathbb{R}^+$ and assume it is square integrable, i.e., $U \in \mathbb{L}_2(\mathbb{R}^3 \times S^2)$. By restricting this HARDI-image to two fixed points, say $\mathbf{x}_1, \mathbf{x}_2$ in \mathbb{R}^3 we obtain two functions on the 2-sphere:

$$S^2 \ni \mathbf{n} \mapsto U(\mathbf{x}_1, \mathbf{n}) \in \mathbb{R}^+$$

and

$$S^2 \ni \mathbf{n} \mapsto U(\mathbf{x}_2, \mathbf{n}) \in \mathbb{R}^+,$$

which we from now on denote by $U(\mathbf{x}_1, \cdot)$ and $U(\mathbf{x}_2, \cdot)$. These functions can be represented by a so-called glyph $\mathcal{S}_\mu(U)(\mathbf{x}_1)$ and $\mathcal{S}_\mu(U)(\mathbf{x}_2)$ as defined below.

Definition 1 A glyph of a distribution $U : \mathbb{R}^3 \times S^2 \rightarrow \mathbb{R}^+$ on positions and orientations is a surface $\mathcal{S}_\mu(U)(\mathbf{x}) = \{\mathbf{x} + \mu U(\mathbf{x}, \mathbf{n}) \mathbf{n} \mid \mathbf{n} \in S^2\} \subset \mathbb{R}^3$ for some $\mathbf{x} \in \mathbb{R}^3$, $\mu > 0$. A glyph visualization of distribution $U : \mathbb{R}^3 \times S^2 \rightarrow \mathbb{R}^+$ is a visualization of a field $\mathbf{x} \mapsto \mathcal{S}_\mu(U)(\mathbf{x})$ of glyphs, where $\mu > 0$ is a suitable constant.

A common approach to compare two glyphs $\mathcal{S}_\mu(U)(\mathbf{x}_1)$ and $\mathcal{S}_\mu(U)(\mathbf{x}_2)$ is to compute the \mathbb{L}_2 distance between $U(\mathbf{x}_1, \cdot) : S^2 \rightarrow \mathbb{R}^+$ and $U(\mathbf{x}_2, \cdot) : S^2 \rightarrow \mathbb{R}^+$, i.e.,

$$d(U(\mathbf{x}_1, \cdot), U(\mathbf{x}_2, \cdot)) = \sqrt{\int_{S^2} |U(\mathbf{x}_1, \mathbf{n}) - U(\mathbf{x}_2, \mathbf{n})|^2 d\sigma(\mathbf{n})},$$

where σ denotes the surface measure on S^2 .

However, this distance only compares glyph amplitudes (using the same $\mu > 0$ in both cases). It does not take into account robust regularization and more importantly, it does not consider whether the extrema of the glyphs coincide. Therefore we

¹In case a DTI image is given, set $U(\mathbf{x}, \mathbf{n}) = \mathbf{n}^T D(\mathbf{x}) \mathbf{n}$, analogous to Equation (3.9).

include a blob-detector [192] in our distance. We do not use higher-order derivatives because they hinder damping before the Nyquist frequency and are more ill-posed due to a higher operator norm.

We have defined the (squared) Sobolev distance between two glyphs as

$$\begin{aligned}
 (d_{\alpha, \gamma, t}(U(\mathbf{x}_1, \cdot), U(\mathbf{x}_2, \cdot)))^2 &= \\
 &\int_{S^2} \left| (e^{-t|\Delta_{S^2}|^\alpha} U)(\mathbf{x}_1, \mathbf{n}) - (e^{-t|\Delta_{S^2}|^\alpha} U)(\mathbf{x}_2, \mathbf{n}) \right|^2 d\sigma(\mathbf{n}) + \\
 &\gamma^{2\alpha} \int_{S^2} \left| |\Delta_{S^2}|^\alpha (e^{-t|\Delta_{S^2}|^\alpha} U)(\mathbf{x}_1, \mathbf{n}) - |\Delta_{S^2}|^\alpha (e^{-t|\Delta_{S^2}|^\alpha} U)(\mathbf{x}_2, \mathbf{n}) \right|^2 d\sigma(\mathbf{n}) \\
 &=: \|U(\mathbf{x}_1, \cdot) - U(\mathbf{x}_2, \cdot)\|_{\mathbb{H}_t^{2\alpha}(S^2)}^2. \quad (5.1)
 \end{aligned}$$

This Sobolev distance basically is a sum of a (smoothed) standard intensity-sensitive \mathbb{L}_2 part (first integral) and a (smoothed) blob-sensitive second part (second integral). Next we provide a brief explanation on the involved parameters:

- The parameter $\alpha \in [\frac{1}{2}, 1]$ denotes the α -scale space regularization on a sphere [93], applied at time $t \geq 0$ (or scale $t^{\frac{1}{2\alpha}}$). Note that $e^{-t|\Delta_{S^2}|^\alpha}$ denotes a smoothing operator generated by a fractional power of the Laplace-Beltrami operator Δ_{S^2} , i.e., $W_U(\mathbf{x}, \mathbf{n}, t) = e^{-t|\Delta_{S^2}|^\alpha} U(\mathbf{x}, \mathbf{n})$ is the solution of

$$\frac{\partial W_U}{\partial t}(\mathbf{x}, \mathbf{n}, t) = -|\Delta_{S^2}|^\alpha W_U(\mathbf{x}, \mathbf{n}, t), \quad (5.2)$$

with $\mathbf{x} \in \mathbb{R}^3$, $\mathbf{n} \in S^2$, $t \geq 0$, and

$$W_U(\mathbf{x}, \mathbf{n}, 0) = U(\mathbf{x}, \mathbf{n}). \quad (5.3)$$

- The parameter $t \geq 0$ determines the stopping time of the spherical α -scale space regularization.
- The parameter γ (physical dimension $[\text{Length}]^2$) determines the influence of the blob-sensitive and the standard intensity-sensitive \mathbb{L}_2 part of the Sobolev norm.

The blob-sensitive part is the same as the total difference of all scale space dynamics of the glyphs². This follows from the fact that (5.1) can be rewritten as

²Local extrema are typically preserved over certain ranges of scale, until annihilation between extrema and saddles takes place in so-called top-points, [73].

5.4. A specialized distance measure: the Sobolev norm

$$\int_{S^2} |W(\mathbf{x}_1, \mathbf{n}, t) - W(\mathbf{x}_2, \mathbf{n}, t)|^2 + \gamma^{2\alpha} \left| \frac{\partial W}{\partial t}(\mathbf{x}_1, \mathbf{n}, t) - \frac{\partial W}{\partial t}(\mathbf{x}_2, \mathbf{n}, t) \right|^2 d\sigma(\mathbf{n}) =$$

$$\int_{S^2} |W(\mathbf{x}_1, \mathbf{n}, t) - W(\mathbf{x}_2, \mathbf{n}, t)|^2 + \gamma^{2\alpha} \|\Delta_{S^2}\|^\alpha W(\mathbf{x}_1, \mathbf{n}, t) - \|\Delta_{S^2}\|^\alpha W(\mathbf{x}_2, \mathbf{n}, t)|^2 d\sigma(\mathbf{n}) ,$$

where we use short notation $W = W_U$. Roughly speaking, $\gamma > 0$ balances the similarity of the scale space extrema (blobs) and the similarity of the amplitudes of $\mathcal{S}_\mu(U)(\mathbf{x}_1)$ and $\mathcal{S}_\mu(U)(\mathbf{x}_2)$.

Recall that the spherical harmonics $\{Y_{lm}\}_{l=0, \dots, \infty}^{m=-l, \dots, l}$ form an orthonormal basis of $\mathbb{L}_2(S^2)$, i.e.,

$$(Y_{lm}, Y_{l'm'})_{\mathbb{L}_2(S^2)} = \delta_{ll'} \delta_{mm'}$$

and

$$\forall_{l=0, \dots, \infty} \forall_{m=-l, \dots, l} : (f, Y_{lm})_{\mathbb{L}_2(S^2)} = 0 \Rightarrow f = 0 ,$$

and that the Y_{lm} are eigenvalues of the negative semi-definite, fractional Laplacian operator:

$$-\|\Delta_{S^2}\|^\alpha Y_{lm} = -l^\alpha(l+1)^\alpha Y_{lm}.$$

Thereby the solution of (5.2) and (5.3) is given by

$$W(\mathbf{x}, \mathbf{n}(\theta, \phi), t) = \sum_{l=0}^{\infty} \sum_{m=-l}^l (Y_{lm}, U(\mathbf{x}, \cdot)) e^{-t\|\Delta_{S^2}\|^\alpha} Y_{lm}(\theta, \phi) =$$

$$\sum_{l=0}^{\infty} \sum_{m=-l}^l (Y_{lm}, U(\mathbf{x}, \cdot)) e^{-t(l(l+1))^\alpha} Y_{lm}(\theta, \phi) . \quad (5.4)$$

In particular for $\alpha = \frac{1}{2}$ (Poisson scale space [93, 100, 101]) the solution of (5.2) and (5.3) is nearly equivalent to outward harmonic extension of the initial distribution $\mathbf{n} \mapsto U(\mathbf{n})$ on the 2-sphere, where one must set the radius $\rho = e^{-t}$, since

$$\rho \mathbf{n}(\theta, \phi) = (\rho \cos \phi \sin \theta, \rho \sin \phi \sin \theta, \rho \cos \theta) \mapsto \rho^l Y_{lm}(\theta, \phi)$$

is a harmonic function on \mathbb{R}^3 and $\rho^l = e^{-tl} \approx e^{-t\sqrt{l(l+1)}}$ for l sufficiently large. So intuitively one may consider a radial scale axis for scale spaces on glyphs.

We can expand $U(\mathbf{x}_1, \cdot)$ and $U(\mathbf{x}_2, \cdot)$ into the orthonormal basis of spherical harmonics:

$$U(\mathbf{x}_i, \mathbf{n}(\theta, \phi)) = \sum_{l=0}^{\infty} \sum_{m=-l}^l c_i^{lm} Y_{lm}(\mathbf{n}(\theta, \phi)) , \quad i = 1, 2,$$

with

$$Y_{lm}(\theta, \phi) = \sqrt{\frac{(2l+1)(l-|m|)!}{4\pi(l+|m|)!}} P_{lm}(\cos \theta) e^{im\phi},$$

with P_{lm} the associated Legendre polynomial of degree l and order m , and with $c_i^{lm} = (Y_{lm}, U(\mathbf{x}_i, \cdot))_{\mathbb{L}_2(S^2)}$, $i = 1, 2$. The squared Sobolev distance (5.1) then simply reads:

$$(d_{\alpha, \gamma, t}(U(\mathbf{x}_1, \cdot), U(\mathbf{x}_2, \cdot)))^2 = \sum_{l=0}^{\infty} \sum_{m=-l}^l |c_1^{lm} - c_2^{lm}|^2 \tilde{m}_l^{\alpha, \gamma, t},$$

which is a weighted ℓ_2 inner product on the coefficients so we only have to study the multiplier

$$\tilde{m}_l^{\alpha, \gamma, t} = (1 + (\gamma l(l+1))^{2\alpha}) e^{-2t(l(l+1))^\alpha},$$

to see how the different spherical harmonics are weighted in the Sobolev distance. Note that if $\gamma = t = 0$, the Sobolev norm is equivalent to the \mathbb{L}_2 norm.

Analytical example

To qualify the behavior of the Sobolev norm in comparison to the \mathbb{L}_2 norm, we investigated several diffusion profiles. The basis for each profile is a single fiber distribution

$$U(\mathbf{n}) = (\mathbf{n}^T M \mathbf{n})^4,$$

with M the diagonal diffusion matrix with $\{1, \epsilon, \epsilon\}$ as diagonal elements and $\mathbf{n} \in S^2$ describing the tessellation orientations. The fourth power is taken to sharpen the result. To this static part, a second single fiber profile is added, that is rotated over angle ϕ with respect to the first profile. The total profile then amounts to

$$U(\mathbf{n}) = (\mathbf{n}^T M \mathbf{n})^4 + (\mathbf{n}^T R_\phi M R_\phi^T \mathbf{n})^4,$$

with R_ϕ a transformation matrix resulting in a clockwise rotation over angle ϕ . We compare the default diffusion profile f ($\phi = 0$, $f = U(\mathbf{x}_1, \cdot)$) with a set of profiles g with ϕ varying between 0 and $\pi/2$ ($g = U(\mathbf{x}_2, \cdot)$).

Figure 5.8 shows the results for both the Sobolev and \mathbb{L}_2 norm, normalized by their maximum response:

$$d_{\text{normalized}}(f, g) = \frac{\|f - g\|}{\max_g \|f - g\|}.$$

It can be seen that for $\phi = \pi/4$, the diffusion profile has maxima that do not overlap with those at $\phi = 0$, while two of the four maxima at $\phi = \pi/2$ do coincide. The Sobolev norm clearly punishes the deviations in extrema. For small differences in angle ϕ , the Sobolev norm gives a larger response, but in the case of partly overlapping extrema, towards $\phi = \pi/2$, the Sobolev norm is again lower than its \mathbb{L}_2 counterpart. The latter yields its maximum at $\phi = \pi/2$, because the amplitudes of the diffusion profiles differ most at that point.

Implementation

In practice, a discretization of the continuous spherical harmonics transform is used. There are two options, namely the discrete spherical harmonic transform, or the pseudo-inverse of the inverse spherical harmonic transform (DISHT), see for example [94]. Similar to Descoteaux [81], we use only even orders of spherical harmonics to represent our HARDI data, i.e., order $l = 0, 2, 4, \dots, L_{\max}$. As m still has range $-l, \dots, 0, \dots, l$, the total number of SH coefficients is defined as $n_{SH} = \frac{1}{2}(L_{\max} + 1)(L_{\max} + 2)$. Since n_{SH} should be smaller than the number N of samples in a spherical sampling, but as large as possible within these boundaries, the DISHT approach is more suited for our application.

We define a single index j in terms of l and m such that $j(l, m) = (l^2 + l + 2)/2 + m$ and compute the spherical harmonic coefficients $\mathbf{s} \in \mathbb{C}^{n_{SH}}$ from the values $\mathbf{f} \in (\mathbb{R}^+)^N$ by means of

$$\mathbf{s} = (\text{DISHT})^+[\mathbf{f}] = (\overline{\mathbf{M}}\mathbf{M}^T)^{-1}\overline{\mathbf{M}}\mathbf{f},$$

with $\mathbf{M} = [M_k^j] = [\frac{1}{\sqrt{C}} Y_{l(j)m(j)}(\mathbf{n}_k)]$ and $C = \sum_{j=1}^{n_{SH}} |Y_{l(j)m(j)}(0,0)|^2$, such that $\mathbf{M}^\dagger \mathbf{M}$ has a diagonal of ones. If $\mathbf{f}_i \in (\mathbb{R}^+)^N$ denotes the discrete data on glyph $U(\mathbf{x}_i, \cdot)$, $i = 1, 2$, i.e., $(\mathbf{f}_i)_k = U(\mathbf{x}_i, \mathbf{n}_k)$, $k = 1, \dots, N$ then the discrete Sobolev norm is computed as

$$d_{\alpha, \gamma, t}^{\text{discrete}}(\mathbf{f}_1, \mathbf{f}_2) = \sqrt{\sum_{j=1}^{n_{SH}} |(DISHT)^+[\mathbf{f}_2][j] - (DISHT)^+[\mathbf{f}_1][j]|^2 \tilde{m}_{l[j]}^{\alpha, \gamma, t}}.$$

5.4.2 Methods

Phantom and real brain data

Using the DTI and HARDI modeling part of the Mathematica package MathVision-Tools, developed at our university, we computer-generated a HARDI phantom. For signal generation, a multi-tensor model was employed [280], using a gradient table of 121 different directions and a simulated b -value of 3000 s/mm^2 . The phantom consists of 18 columns with different diffusion profiles. The collection of diffusion profiles consists of single fiber profiles at angles $\{0, 1, 3, 6, 10, 15, 21, 28, 36, 45\}$ degrees, two fibers crossing in-plane at angles $\{40, 45, 55, 70, 90\}$ degrees, and three fibers crossing in-plane at angles $\{30, 40, 60\}$ degrees. Each column of the phantom contains the original diffusion profile as its first element, followed by ten times this profile with random noise added. This noise is Rician, meaning that we applied the transformation

$$((\mathbf{y}, \mathbf{n}) \mapsto U(\mathbf{y}, \mathbf{n})) \mapsto ((\mathbf{y}, \mathbf{n}) \mapsto \sqrt{(U(\mathbf{y}, \mathbf{n}) \cos \eta_1 + \eta_2)^2 + (U(\mathbf{y}, \mathbf{n}) \sin \eta_1 + \eta_3)^2}),$$

with $\eta_2, \eta_3 \sim \mathcal{N}(0, \sigma)$ normally distributed and η_1 uniformly distributed over $[0, 2\pi)$. To obtain data with SNR 30, comparable with real data, σ was chosen to be 0.1. Using the Funk-Radon transform as described by Descoteaux [81], the simulated signal was converted to a representation in spherical harmonic coefficients, with $L_{\max} = 12$. Comparing the ℓ_2 norm of the SH coefficients, the noise was shown to lead to a disturbance of approximately 10%.

We also tested our algorithm on real data, analogous to other HARDI clustering experiments, for example that of Grassi et al. [121]. Human brain diffusion MRI data were acquired at 3 T, measuring 52 slices of 128×128 2-mm isotropic voxels, using TE 85 ms, 128 unique gradient directions and b -value 2000 s/mm^2 .

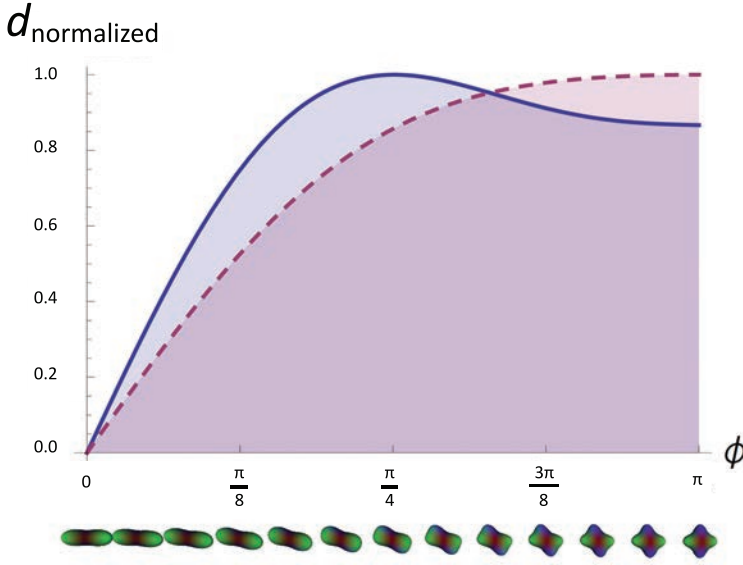


Figure 5.8 Results of the analytic example: normalized response of the Sobolev norm (blue, solid line) and the \mathbb{L}_2 norm (red, dashed line) for a combination of two single fiber profiles generated with angle ϕ in between.

The data were registered onto the MNI152 template and the accompanying Talairach atlas, using an affine transformation within FSL [157]. Subsequently, an ROI of 30 pixels wide and 39 pixels high, containing the subject's right thalamus, was selected on an axial slice. The data were again transformed to spherical harmonic coefficients ($L_{max} = 12$).

Parameter tuning

The Sobolev norm contains three parameters – α , γ , t – that needed tuning, in order to yield the desired behavior. Equivalent to Lindeberg [192], α was set to 1, the value for Gaussian regularization. We chose t to be 0, as our data were sufficiently smooth. In addition, the \mathbb{L}_2 norm lacks regularization, so setting $t = 0$ enables a fair comparison. To assess the optimal value for γ , we performed a 1-nearest-neighbor classification, using the 18 original profiles of the phantom (i.e., without noise) as training and the whole phantom as test set, while γ was varied from 0 to 0.8 in steps of 0.01. The performance of the \mathbb{L}_2 norm for this phantom is 71.2%. However, using the Sobolev norm with $\gamma \geq 0.69$, the phantom classification reached a performance of 100%.

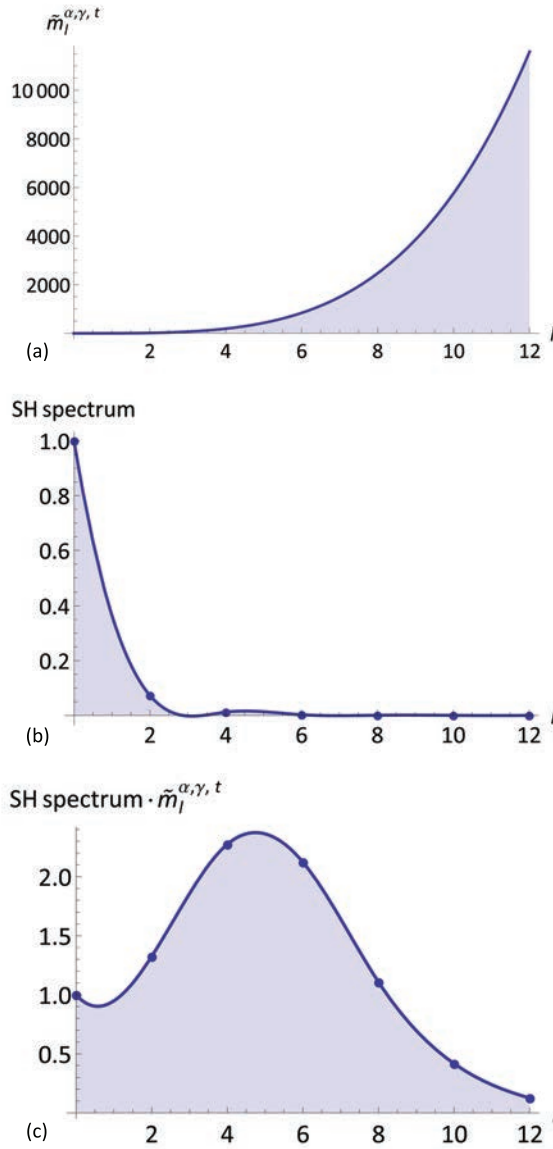


Figure 5.9 Plots of Sobolev multiplier, SH coefficients spectrum, and the product of these two terms. (a) Behavior of the Sobolev multiplier $\tilde{m}_l^{\alpha, \gamma, t}$ for $\{\alpha = 1, \gamma = 0.69, t = 0\}$. (b) Normalized mean spectrum of spherical harmonic coefficients of the phantom diffusion profiles. (c) Product of multiplier and spectrum.

The behavior of the multiplier $\tilde{m}_l^{\alpha, \gamma, t}$ for $\{\alpha = 1, \gamma = 0.69, t = 0\}$ is plotted in

Figure 5.9(a). It can be seen that the function exponentially rises towards higher values of l . However, the spherical harmonic coefficients of the used diffusion profiles at higher orders are quite small, as can be seen in Figure 5.9(b). This means that the product of the multiplier and the spectrum is damped well enough to be truncated at $l = 12$ and avoid Gibbs artifacts (see Figure 5.9(c)).

K-means clustering

Following the example set by Wiegell et al. [325], we performed k-means clustering. For both the synthetic phantom and the real brain data, a set of seed points to serve as initial centroids was determined manually. The seed point placement for the phantom was straightforward, with a seed point in the middle of each column.

The real brain ROI was masked using the Talairach atlas' thalamus segmentation, while the seven seed points for this ROI were chosen to lie in the different nuclei of the thalamus, as defined by the atlas (see Figure 5.11 (b)). To associate each point of the data sets with a cluster, we used both the \mathbb{L}_2 norm and the Sobolev norm with the parameters calculated in Section 5.4.2: $\{\alpha = 1, \gamma = 0.69, t = 0\}$. The new centroids of each cluster were calculated as the mean of the voxel positions of all connected points. Since our dissimilarity measures only concerned diffusion information, we calculated the distance between each data point and the mean diffusion profile of all points associated with each cluster.

5.4.3 Results

The results of the k-means clustering for the phantom can be seen in Figure 5.10. The \mathbb{L}_2 norm yields only a 20.7% correct classification (Figure 5.10(a)). Clearly, the Sobolev norm has performed much better, obtaining 73.7% correctly classified diffusion profiles, as shown in Figure 5.10(b)).

With respect to the thalamus ROI, in Figure 5.11 we can see that the k-means clustering succeeds to classify the thalamus nuclei reasonably well. The pulvinar and ventral posterior medial nucleus are segmented but cannot be separated. The results of the Sobolev norm seem more stable, i.e., less dependent on the weight factor between diffusion and spatial information, introduced to the clustering as defined by Wiegell et al. [325], than the results of the \mathbb{L}_2 norm.

5.5 Discussion

5.5.1 Current findings

In this chapter, we began with visually comparing DTI superquadrics and HARDI Q-ball and DOT glyphs within the rat STN, to see whether HARDI could help to identify the two STN parts. The results showed that the more heterogeneous HARDI glyphs indeed provide more information on the neuroanatomy of the subthalamic nucleus and its surroundings than the oblate traditional DTI glyphs. The HARDI glyphs in the STN have different characteristics and it seems possible to distinguish two parts of the STN. These parts could correspond with the two subterritories of the rat STN, the lateral motor part and the medial associative and limbic parts [298].

Subsequently, we tried to automate and validate the separation obtained visually by clustering experiments. We performed k-means and graph cuts clustering on the right STN ROI, and found that while k-means clustering can segment the IC, it is unable to separate the STN from its environment. Some weighting vectors facilitate the graph cuts algorithm to find a cluster in the medial STN, which might correspond to the cognitive/emotional part of the rat STN. The fact that the motor part was connected to the background cluster, and the similarity of the medial part to the nigrostriatal bundle and of the lateral part to the zona incerta in the feasibility study, could be explained by the fact that the rat STN is not a closed nucleus, i.e., dendrites cross the STN borders into surrounding areas.

Finally, we introduced a new dissimilarity measure that can be employed for clustering of HARDI data. Instead of comparing only the amplitudes of the diffusion profiles, the Sobolev norm also takes into account whether the extrema of the profiles coincide. We illustrated the behavior of our norm for some simple synthetic glyphs and then built a more difficult phantom. The optimal parameters were found using 1-nearest-neighbor clustering of this phantom, and these parameters were used for the subsequent k-means clustering. The Sobolev norm consistently performed better than the \mathbb{L}_2 norm, for both the phantom and the real brain data.

5.5.2 Future work

For the feasibility experiment, we used manual registration of a slice of the Paxinos atlas [240] with the HARDI data. In the clustering experiment, we aimed to improve upon this by using the digitized rat brain atlas [145]. However, the matching of that atlas with the MRI template is done by manual scaling and translation. Therefore, the identification of the STN ROI in the rat HARDI data is still subject to registration errors.

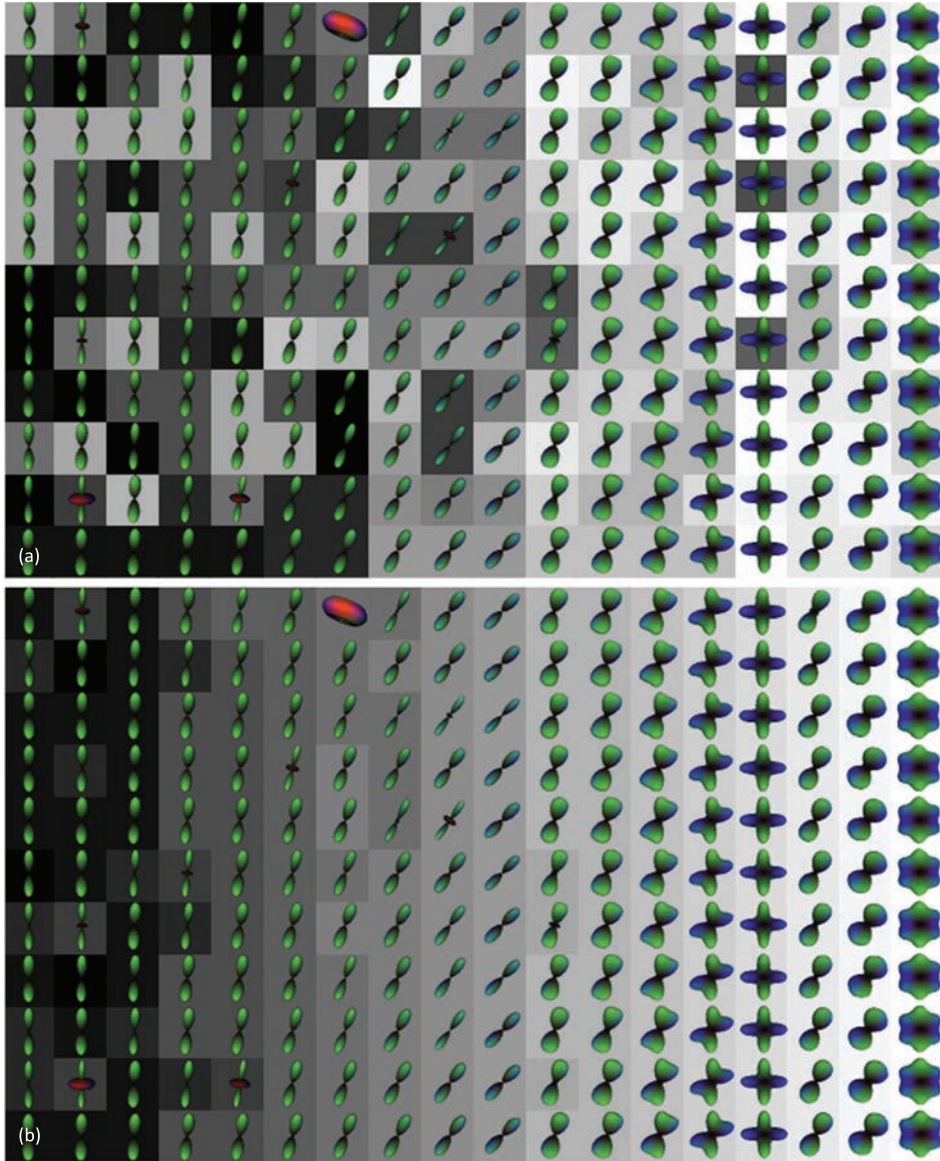


Figure 5.10 K-means clustering results for computer-generated phantom. (a) K-means clustering result of \mathbb{L}_2 norm (20.7% correctly classified). (b) K-means clustering result of Sobolev norm with $\{\alpha = 1, \gamma = 0.69, t = 0\}$ (73.7% correctly classified). The diffusion profiles, visualized as min-max normalized Q-ball glyphs using SH coefficients up to $l = 8$, are overlayed on the resulting clustering maps. Each gray value represents one cluster.

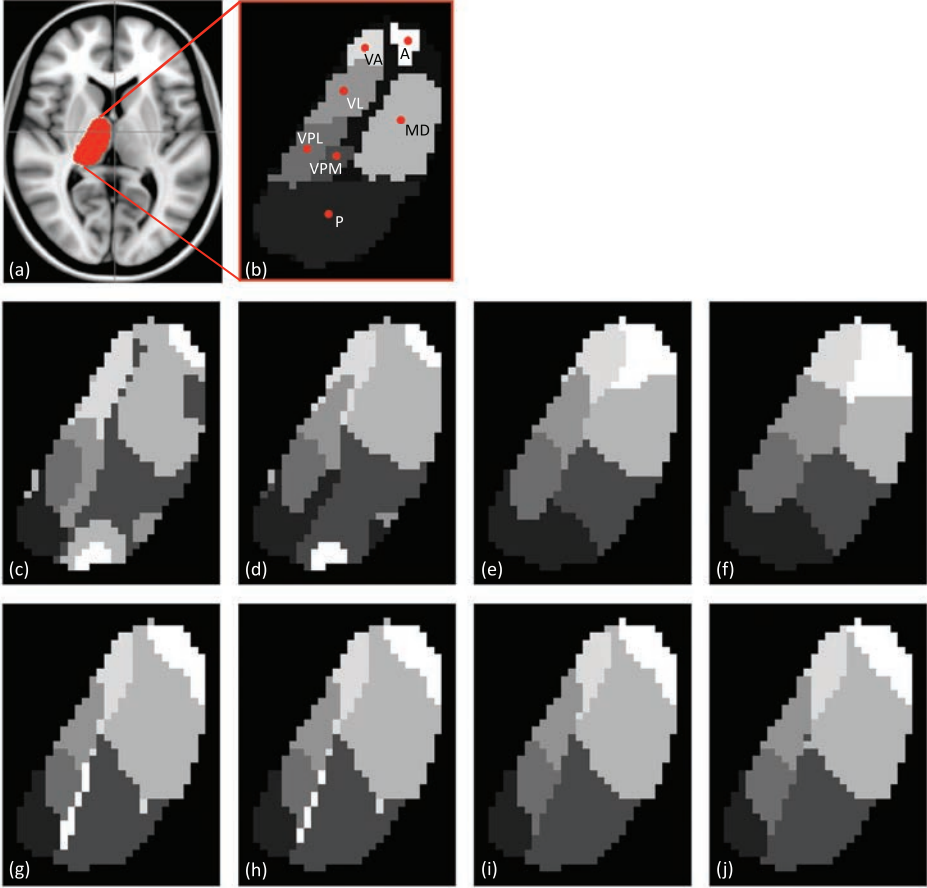


Figure 5.11 K-means clustering results for real brain data. (a) Thalamus ROI shown in red on an axial slice of the MNI152 template. (b) Talairach atlas labels of thalamus nuclei and seed points for k-means clustering. (c) to (f) Clustering results using \mathbb{L}_2 norm. (g) to (j) Clustering results using Sobolev norm ($\{\alpha = 1, \gamma = 0.69, t = 0\}$). The ratio between diffusion and spatial information was varied, from left to right: (g) ratio 1:1; (h) $\frac{1}{5}$ -weight factor (as defined in [325]); (i) 1-weight factor; (j) 5-weight factor.

Regarding the preliminary clustering study, the tuning of the parameters for the clustering should be simplified. The first disadvantage with respect to parameters is the seed point selection that is necessary for k-means clustering. This algorithm needs manual or atlas-based points and will find clusters around these points by definition. Although the graph cuts method does not have this bias, this method requires other arbitrary parameters, e.g., the number of splitting and merging steps. Another issue concerning the parameters of this clustering experiment is the incorporation of the

different orders of diffusion information into the distance measure. For k-means, the results showed that the use of 2nd-order information is important, while the 0th order can be excluded. Graph cuts showed a medial STN cluster for weightings including 2nd-order information. However, using only this order did not give satisfactory results. The IC was split, probably because too much spatial information is embedded in the affinity matrix for the graph cuts clustering.

We developed the Sobolev norm to deal with these weighting issues. During the first tests using this norm, we set the regularization parameter t to zero, as this gave the best results for our apparently sufficiently smooth data. This might indicate that the Sobolev norm comprises too much regularization. We would like to test a negative value for t and adapt the Sobolev norm and its parameters according to the results. Furthermore, it would be nice to use the Sobolev norm in combination with a graph cuts method instead of the easily biased k-means clustering.

Besides improvements on the methodological side, such as using clustering methods that are not biased by seed point selection, and more intuitive regularization in the Sobolev norm, a lot of work can be done in the future. Naturally, the Sobolev norm still has to be tried on the STN ROI in rats and also humans. However, clustering the diffusion profiles within the STN ROI is one thing, but there is more information to be gained.

On a larger scale, the many crossings that were found during the explorative study indicate that an entangled network of fibers can be found around the STN. From literature, we know that this network includes the internal capsule, the ansa lenticularis, the thalamic fasciculus or H1 Field of Forel, and the lenticular fasciculus or H2 Field of Forel [136]. Future work could include visualization of these specific bundles around the STN. This complex network could then be used as a contextual guide to localize the STN more accurately.

Assessing the projections of the different STN parts, i.e., the connectivity of each part with other brain areas, could help us to get insight into the level of separation of the motor part. We could then judge the feasibility to identify this part with greater certainty and minimize the cognitive and emotional side effects due to DBS. The fiber tracking needed for these objectives should take into account information on crossing fibers. The connectivity values for each STN voxel could then be used as input for clustering, in addition to the information on the diffusion profile within the voxel. If we would have more data, we could incorporate these into a classifier and train this to segment the STN and its different parts for new cases.

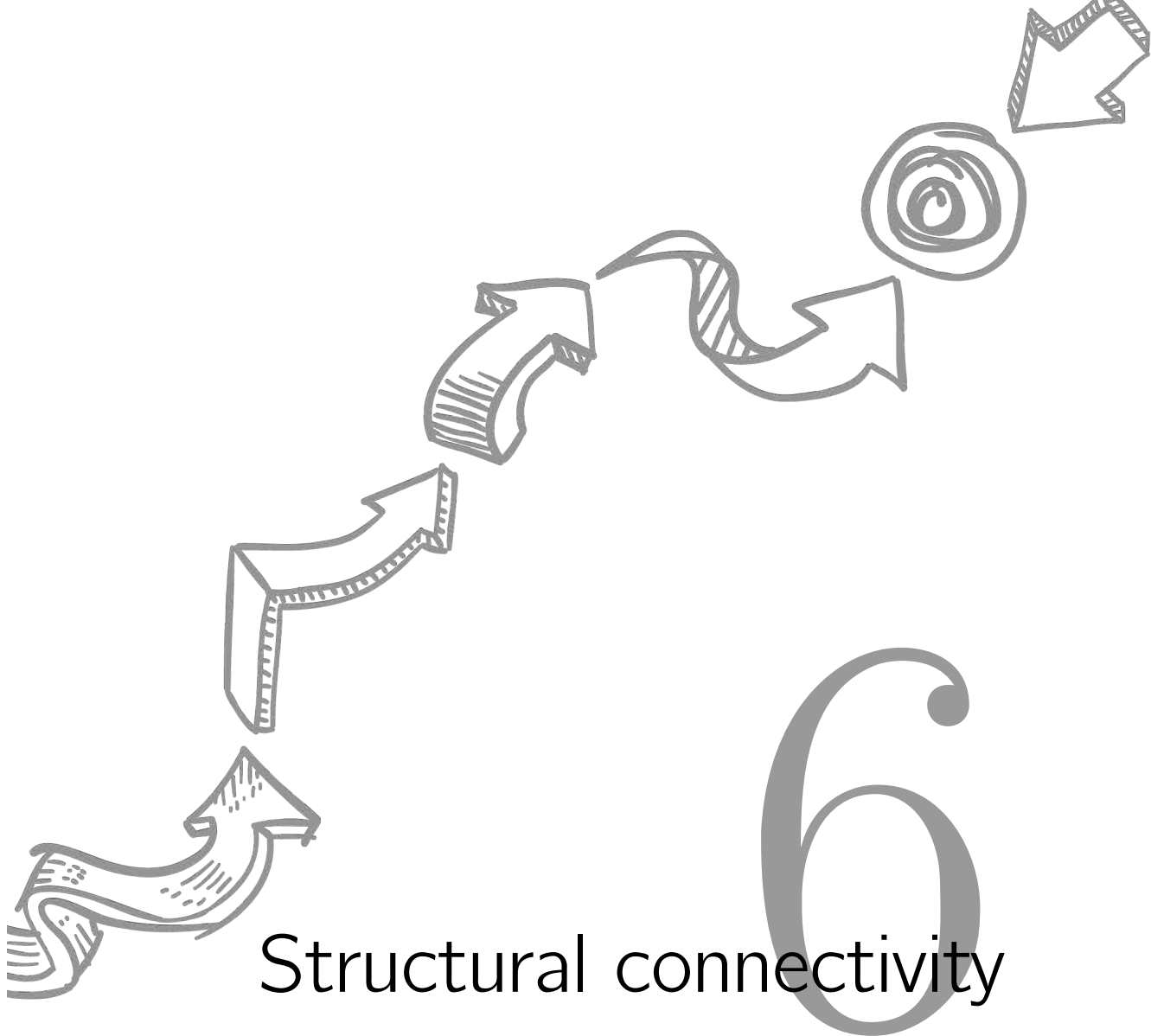
However, we need proper ground truth for such a training process. Although results could be compared with the literature on STN neuroanatomy and circuitry, it will remain a challenge to interpret the results of the STN data and obtain a golden standard. Histological experiments could provide a solution for this issue.

5.5.3 Conclusion

In conclusion, in this chapter we showed that HARDI data provide us with enough information to distinguish two parts in the rat STN. The preliminary clustering experiments showed that it is also possible to automatically segment the IC and the medial STN part from the surrounding structures. We developed a new distance measure to deal with the problem of weighing different orders of diffusion information and showed that this new Sobolev measure outperforms the traditional \mathbb{L}_2 norm for phantom and real brain diffusion data. Future work should include the application of the Sobolev norm to the STN region.

5.6 Acknowledgments

We are grateful to Jan Bjaalie and colleagues from the Institute of Basic Medical Sciences, Oslo, Norway, for providing the digitized rat brain atlas. In addition, we would like to thank Bart Spronck, Vesna Prčkovska and Markus van Almsick for their help on the HARDI processing and visualization.



Structural connectivity

The modern geography of the brain has a deliciously antiquated feel to it - rather like a medieval map with the known world encircled by terra incognita where monsters roam.

David Bainbridge

This chapter is based on:

“Structural connectivity of the human subthalamic nucleus: identification of the “hyperdirect” pathway and segregation of motor and non-motor STN parts.” Ellen Brunenberg, Pim Moeskops, Anna Vilanova, Walter Backes, Mark Janssen, Veerle Visser-Vandewalle, Bart ter Haar Romeny, and Bram Platel. Submitted.

6.1 Introduction

6.1.1 Background

Based on current literature, the STN is divided into three functionally different parts [136]. The largest part is the sensorimotor area, which forms the dorsolateral two-thirds of the STN. The associative area is located in the ventrolateral STN, while the smallest part, namely the limbic area, lies in the medial tip of the STN [136, 233, 298]. Although the literature presents the motor, associative, and limbic cortico-basal-ganglia loops as parallel circuits, it is still not obvious to what extent these functional circuits are integrated within the STN. The possibility of selective stimulation of the motor STN, without affecting the associative and limbic circuits, is strongly influenced by the level of integration of these loops within the STN. To resolve these issues, we looked into the use of MRI methods providing functional information for the identification of the different functional STN areas. In the study described in this chapter, we investigated the structural connectivity of the STN based on diffusion-weighted MRI. The results of this analysis provide us with more insight on the level of segregation of the motor and non-motor cortico-basal-ganglia loops at the level of the STN. Moreover, they support the existence of the “hyperdirect” pathway (from motor cortex to STN) in humans.

6.1.2 Related work

Structural connectivity analysis of whole-brain networks based on probabilistic tracking in diffusion-weighted MRI has been performed for about 8 years [120, 130, 131, 132, 152, 153]. In their 2005 review article [30], Behrens and Johansen-Berg discussed three methods for parcellation of gray matter nuclei based on diffusion-weighted MRI data. First, parcellation can be done without any prior knowledge about projections of the nuclei, using changes in connectivity profiles per voxel [160]. Second, local diffusion profiles can be clustered in order to separate different regions without the use of contextual information [47, 320, 325]. Third and most common, prior knowledge about projections (from atlases or functional MRI) can be used to obtain a parcellation. This method has been practiced for the thalamus [29],

striatum (caudate nucleus and putamen) [182, 183, 184], and the combination of thalamus, striatum and globus pallidus [89, 201].

As for the STN, to our knowledge, no studies have been published that analyze the full structural connectivity of the STN. Aron et al. analyzed solely the pathways between the STN and the inferior frontal cortex and pre-supplementary motor area [16], while Forstmann et al. considered only the connectivity of the STN with the pre-supplementary motor area, primary motor cortex, anterior cingulate cortex, inferior frontal gyrus, and the striatum [106].

6.1.3 Aim

As a complement to the literature described above, a complete description of the structural connectivity of the STN based on high angular resolution diffusion imaging (HARDI) is useful. In addition, segmentation of the STN motor part based on structural connectivity has not been attempted before. The aim of this study was to assess the structural connectivity of the STN in healthy subjects based on HARDI data. We hypothesize that the structural connectivity results offer insight into the level of segregation of the motor area with respect to the limbic and associative areas and the feasibility of selective stimulation of the STN motor part. In addition, we assume that the results provide evidence for the existence of the “hyperdirect” pathway in humans.

To test this, we reconstructed diffusion profiles using Q-ball imaging [312] and performed probabilistic fiber tracking using the probabilistic index of connectivity (PICO) algorithm [273]. Connectivity measures for each atlas region of interest were derived from streamline counts and tested for significance. The results were compared with existing literature on STN circuitry based on invasive neural tract tracing or electrophysiology studies. Moreover, we studied the level of segregation of the motor part of the STN, based on its connectivity. For this purpose, we analyzed the connectivity to the motor cortical areas per STN voxel and indeed found different values in medial and lateral STN parts.

6.2 Methods

6.2.1 Data acquisition

A group of 8 healthy adult subjects (4 males, 4 females, age 24–49 years, mean age = 31.5) was scanned. Written informed consent was obtained from all volunteers prior to participation, and the study was approved by the Medical Ethics Committee of Maastricht University Medical Center.

Data acquisition was done on a Philips Achieva 3-T system. Structural images were scanned using two protocols, namely a three-dimensional inversion recovery (IR) T_1 -weighted sequence including 60 coronal slices and a three-dimensional turbo spin-echo (TSE) T_2 -weighted sequence of 50 coronal slices. The latter involved only part of the brain, situated around the midbrain region of interest, parallel to the brain stem. High angular resolution diffusion imaging (HARDI) was performed using a diffusion-weighted EPI protocol, acquiring a series of 128 diffusion-weighted images with different gradient directions and b -value 2000 s/mm², together with an unweighted b_0 image. Detailed scanning parameters can be found in Table 6.1.

Table 6.1 Parameters of MRI sequences.

Parameter	Inversion recovery	Turbo spin-echo	Diffusion-weighted
TE (ms)	15	110	85
TR (ms)	5441	2500	6370
EPI factor	-	-	55
Direction	coronal	coronal	axial
Number of slices	60	50	52
Slice thickness (mm)	3.0	1.0	2.0
Number of voxels	640x640	256x256	128x128
Voxel size (mm)	0.359x0.359	1.0x1.0	2.0x2.0
Scan duration	7 min 26 s	7 min 43 s	14 min 39 s

6.2.2 Data preprocessing

A flowchart representing the data analysis pipeline used for this study is shown in Figure 6.1. To enable parcellation of the brain into regions of interest for the connectivity calculation, all data were registered to match the (skull-stripped) MNI152 template and the accompanying Talairach atlas labels [293] (at 2 mm resolution), as provided by FSL [115]. The HARDI images were transformed to match this atlas with the T_1 -weighted IR data as intermediate step.

The registration pipeline can be seen in Figure 6.2. The process involved the affine registration of the MNI152 template to the T_1 -weighted IR images by FSL's FLIRT [157] as a first step, employing an affine transformation with 9 degrees of freedom and mutual information as the cost function. This affine transformation was used as the starting point for a subsequent nonlinear transformation using FSL's FNIRT [10]. Second, intersubject matching of the IR data to the unweighted (b_0) HARDI image was done using affine transformation in the same way as described above. Third, FSL's eddy current correction (involving affine registration) was applied to the remaining 128 diffusion-weighted volumes, in order to correct for distortions and head motion. Finally, all transformations were sequentially applied to the MNI152

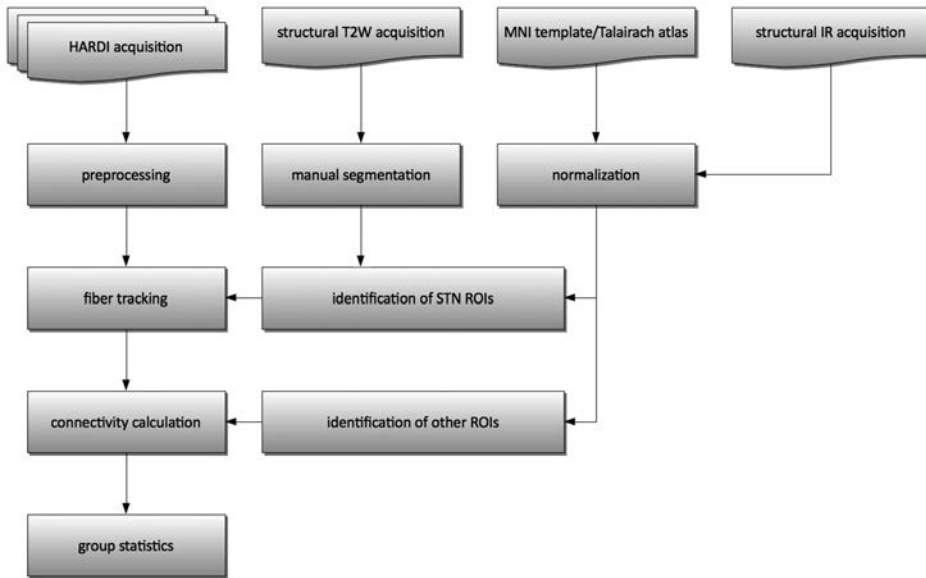


Figure 6.1 Flowchart of data analysis steps for structural connectivity.

template and the accompanying Talairach atlas labels, interpolating the latter in a nearest neighbor fashion.

We chose to apply the transformations to the atlas images to avoid deformation of the HARDI data and the involved correction of gradient direction. After the analysis, scalar output maps of each subject can be inversely transformed to the MNI152 space in order to enable group analysis.

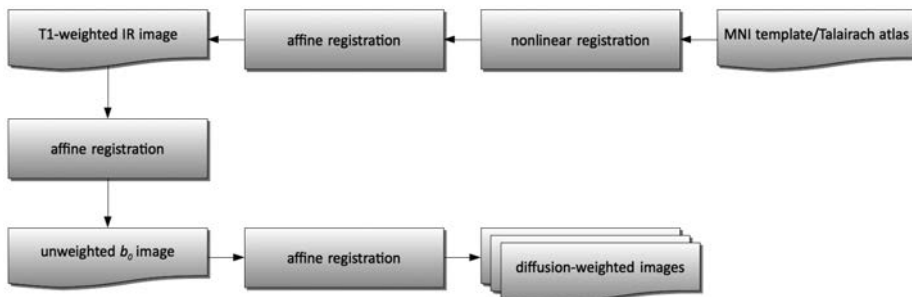


Figure 6.2 Flowchart of data registration steps for structural connectivity.

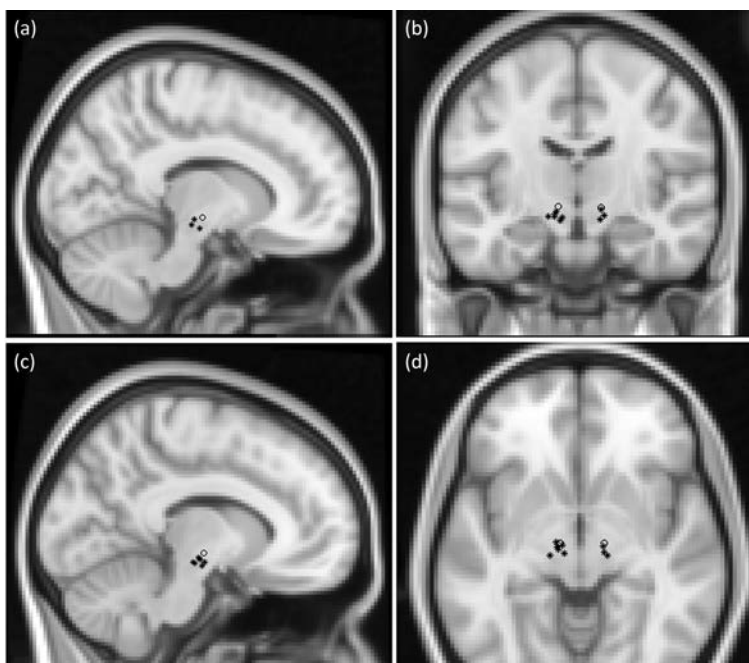


Figure 6.3 STN centers of mass in MNI152 atlas space. (a) Projections of right STN ROIs in sagittal plane. (b) Projections of right and left STN ROIs in coronal plane. (c) Projections of left STN ROIs in sagittal plane. (d) Projections of right and left STN ROIs in axial plane. Legend: circles: centers of mass of atlas-based STN ROIs; stars: centers of mass of manually segmented STNs.

6.2.3 Identification of the subthalamic nucleus ROIs

To identify the STN ROIs in the MRI data, two methods were used. First, the Talairach labels accompanying the MNI152 template were used to mask the right and left STN. In addition, the STNs that were visible on the structural turbo spin-echo images were segmented by an experienced neurosurgeon (Claudio Pollo), using ITK-SNAP, a software application that facilitates 3D segmentation of medical images [336]. This manual procedure led to 3 right STNs and 6 left STNs, segmented in 6 subjects.

To compare the two segmentation methods, the centers of mass of the labeled STNs were projected onto planes in the MNI152 atlas space, as can be seen in Figure 6.3. From this figure, it is apparent that the manually segmented STNs as seen on the structural images differ from the atlas-based STNs. The directly visualized STNs seem to lie more posterior and more ventral than the atlas-based structures. While

papers that compare direct and atlas-based targeting of the STN do not agree on the difference in anteroposterior and mediolateral directions [17, 75, 255], they do concur on the fact that the MRI-based STN seems to lie more ventral than the atlas-based STN [17, 75], as can be seen in Figure 6.3 as well. The discrepancy between atlas-based and MRI-based STN centers might be caused by the fact that the Talairach atlas is based on only one brain specimen [255].

In the near future, the use of 7-T MRI will facilitate direct identification of the STN [1, 61, 62]. For this study, however, we used the atlas-based segmentation because it is available for all volunteers.

6.2.4 Probabilistic tractography

To enable analysis of the connectivity between different regions of interest from the Talairach atlas, fibers estimating the trajectories of the white matter axonal bundles were calculated using Camino [66]. We performed fiber tracking using Camino's probabilistic tractography method, a refined version [273] of the streamline-based probabilistic index of connectivity (PICO) algorithm [67, 235].

As a first step, the diffusion profile in each voxel is reconstructed from the preprocessed diffusion-weighted data. A threshold on the b_0 images ensures that profiles are only generated within the brain. Subsequently, the directions of principal diffusion are detected as the peaks in the calculated orientation distribution functions (ODFs). The shape of the peaks of the ODFs is used to estimate a probability distribution function that describes the uncertainty of the principal diffusion directions. The actual probabilistic tracking procedure starts multiple streamlines from the center of each seed voxel. Each of these streamlines can follow a unique trajectory because the principal diffusion directions are perturbed by the randomly sampled uncertainties. The repeated tracking yields maps that estimate the structural connectivity of the selected seed voxel to other regions of interest in the brain, by means of the number of fibers passing through or ending in a region. If the seed region contains 16 voxels, the output of the tracking will thus consist of 16 distinct connectivity maps.

In this study, we employed Q-ball imaging [309] based on 6th-order spherical harmonics for the reconstruction of the orientation distribution functions. As a seed region, we used the STN mask from the Talairach atlas, matched to the subject's diffusion-weighted data. Concerning the tracking parameters, we generated 5000 different streamlines per seed voxel. These were terminated if curvature over a single voxel exceeded 80 degrees, while no threshold was set on anisotropy values and fiber length. The output of the tracking algorithm was saved as both raw streamline data in VTK format, and connection probability maps in Analyze format.

6.2.5 Connectivity measures

One of the aims of this study was to determine the connectivity between the STN and other gray matter regions in the brain (called target ROIs in the rest of this section). We calculated the connectivity based on the output of the fiber tracking in Camino, which normally consists of as many probability maps as there were seed voxels within the STN. Each of these probability maps contains the amount of streamlines passing through every voxel in the brain. This amount is expressed as a ratio of the total amount of streamlines starting from the given seed voxel in the STN. A value of 0.5 would therefore mean that 2500 of the 5000 streamlines starting in the STN seed voxel pass through the given brain voxel.

However, this could lead to multiple counts of a single streamline in a target ROI that consists of more than one voxel. For example, a target ROI where a streamline ends in a voxel on the boundary would then be seen as “less connected” than a target ROI where the streamline ends in the middle of the region. Therefore, we also generated streamline data as output of the fiber tracking algorithm. For each STN seed voxel, a set of 5000 streamlines was tracked. We summed these streamline sets for all distinct seed voxels of each subject in one volume.

To calculate the structural connectivity, we followed each streamline in the total set from beginning to end, meanwhile checking the Talairach atlas labels of the voxels that were traversed by the streamline. We considered all voxels with the same Talairach atlas labels to belong to one target ROI and ensured that each of these regions was counted only once per streamline.

Thus, for every target ROI, we obtained $N_{\text{target ROI}}$, the total number of streamlines passing through or ending in this region. From this number, we calculated two connectivity measures. The first measure C_1 was defined as:

$$C_1(\text{STN}, \text{target ROI}) = \frac{1}{V_{\text{STN}} V_{\text{target ROI}}} N_{\text{target ROI}}.$$

The number of streamlines $N_{\text{target ROI}}$ is normalized by V_{STN} and $V_{\text{target ROI}}$. V_{STN} is the size in voxels of the STN region derived from the registered atlas (i.e., the number of seed voxels). V_{STN} varied between subjects, from 12 to 22 for the left STN (mean size = 16 voxels), and from 13 to 18 for the right STN (mean size = 15 voxels). $V_{\text{target ROI}}$ represents the size in voxels of the target region of interest.

The second measure C_2 is a variation on C_1 . As streamlines are less likely to reach a target ROI that is far away from the seed region than an ROI that is nearby, we tried to avoid a bias of the tracking algorithm with respect to the streamline length, by adding a term representing this property:

.....

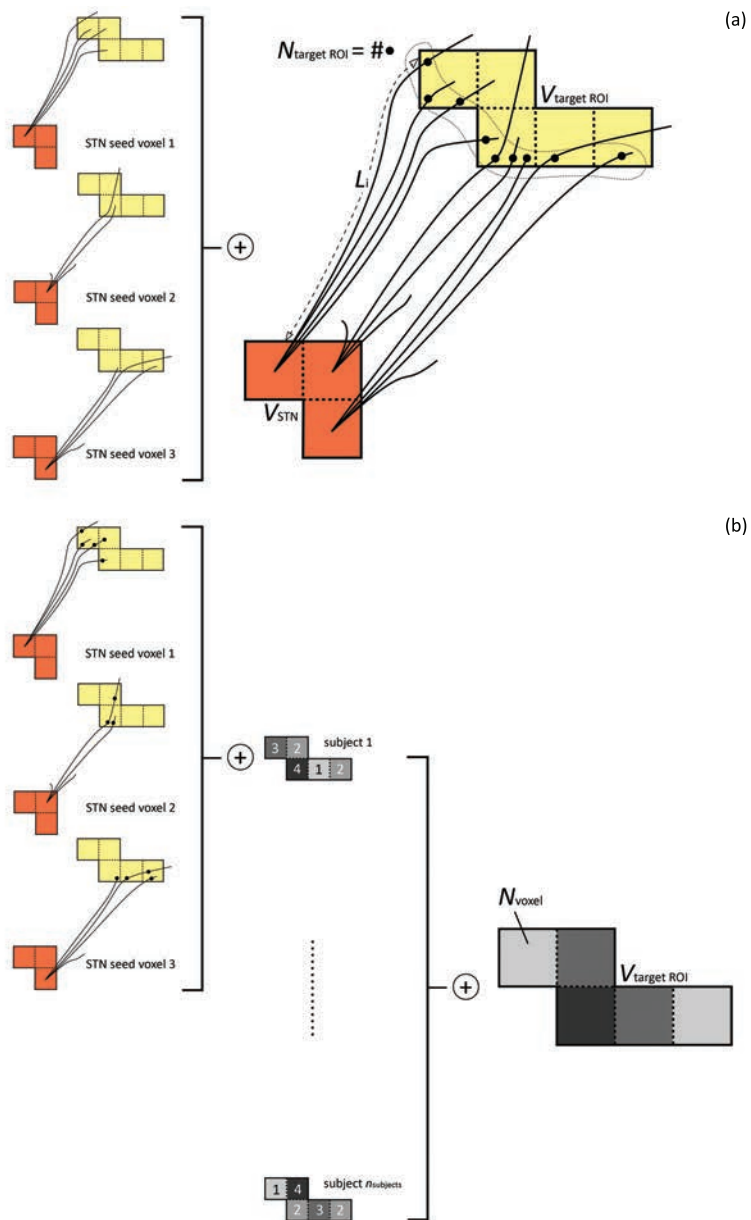


Figure 6.4 Illustration of the streamline counting involved in the calculation of the connectivity measures C_1 , C_2 , and C_3 . (a) Streamline counting per region of interest for C_1 and C_2 . (b) Streamline counting per voxel for C_3 .

$$C_2(\text{STN, target ROI}) = \frac{1}{V_{\text{STN}} V_{\text{target ROI}}} \sum_{i=1}^{N_{\text{target ROI}}} L_i$$

with L_i the distance along the i^{th} streamline between the STN and the first voxel of the target region of interest. The calculation of C_1 and C_2 is illustrated in Figure 6.4(a).

The connectivity measures C_1 and C_2 were calculated for the target regions of interest of all 8 subjects. To test the statistical significance over this group of subjects, we performed a one-sided Student t -test (test if $C_i > 0$) with significance level $\alpha = 0.05$. The results of the two defined connectivity measures will be compared in Section 6.3.

We also wanted to visualize the structural connectivity of the STN as a total probability map instead of streamlines. For this purpose, we needed another connectivity measure, as we could not use the streamline information. Instead, we converted the individual probability maps for each seed voxel into streamline counts (again, a probability of 0.5 in a selected voxel means that 2500 of the 5000 streamlines leaving the seed voxel pass through the given voxel) and cumulated these streamline count maps for all STN seed voxels and all different subjects (n_{subjects}) after registration with the MNI152 template.

As mentioned above, this procedure did not provide us with individual streamline information, but with a total streamline count per voxel N_{voxel} . Therefore, we defined a third connectivity measure C_3 (illustrated in Figure 6.4(b)):

$$C_3(\text{STN, target ROI}) = \frac{1}{n_{\text{subjects}} V_{\text{STN}} V_{\text{target ROI}}} \sum_{j=1}^{V_{\text{target ROI}}} (N_{\text{voxel}})_j$$

C_3 already incorporates all subjects, hence no t -test was performed for this connectivity measure.

6.2.6 Segregation of motor and non-motor regions of the STN

To examine the possibility to distinguish the STN motor part from the associative and limbic territories, we looked at the motor connectivity for each STN voxel separately. In order to evaluate streamlines per target region and take into account streamline length, C_2 was chosen as connectivity measure. We assessed C_2 between the STN and four different motor cortical regions of interest: the primary motor cortex (Brodmann area 4), the pre- and supplementary motor areas (Brodmann area 6), the precentral gyrus, and these three regions together. After registration to the MNI152 template (using linear interpolation), the resulting maps were cumulated over all subjects and masked by the atlas STN.

6.3 Results

6.3.1 Probabilistic tractography

After probabilistic tracking, the resulting streamlines were visualized in ParaView [3], an open-source data analysis and visualization application, which allows for interactive data exploration in 3D. For an example, see Figure 6.5.

Figure 6.6 shows a comparison between fibers tracked from an atlas-based STN ROI and fibers tracked from a manually segmented STN ROI. Because the fibers overlap quite extensively, and manual segmentations were only available for a limited number of volunteers, we proceeded the structural connectivity analysis with just the atlas-based STN ROIs. The normalized total probability map is presented in Figure 6.7. Both the fiber visualization and the probability map indicated connections of the right STN to motor regions of the cortex, to the temporal lobe, and the anterior cingulate cortex, amongst others.

In addition to the visualization of the results, we also assessed whether the streamlines that were found to be going from the STN to motor regions of the cortex supported the existence of the so-called “hyperdirect” pathway that directly connects the motor cortex to the STN. For this purpose, we analyzed all streamlines ending in the premotor and supplementary motor cortex, the primary motor cortex and the precentral gyrus. We calculated the percentage of the streamlines that do not pass through the thalamus, caudate, putamen or globus pallidus and thus can be said to form a monosynaptic connection between the motor cortex and the STN. Of the 16 analyzed STNs, 10 exhibited direct streamlines to the motor cortical areas. For 3 STNs, the results showed streamlines that seemed to be collaterals of the internal capsule, as expected from literature on primate circuits [136, 233]. These streamlines are shown for subject 1 in Figure 6.8. A non-existing medial pathway including the corpus callosum was found in 4 cases, while both the correct lateral and the incorrect medial trajectories were found in 3 cases.

6.3.2 STN connectivity

The significant results of the calculated connectivity based on streamline tracking in different subjects are shown in Table 6.2 for C_1 (without normalization for length) and in Table 6.3 for C_2 (with normalization for streamline length). In these tables, only the most significantly connected regions (p values ≤ 0.010) are shown, the full data (also for the left STN) can be found in Tables A.1 to A.4 of Appendix A.

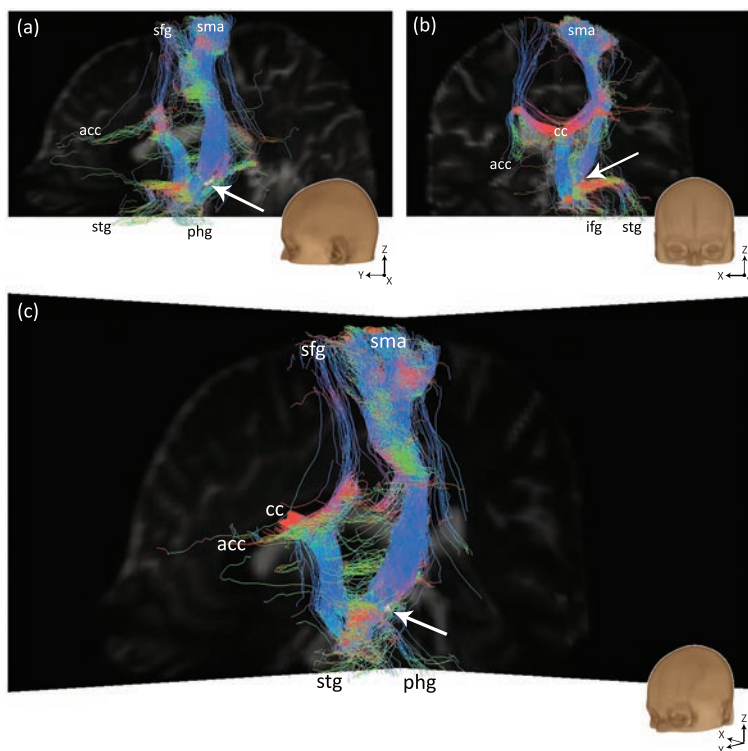


Figure 6.5 Visualizations of probabilistic fiber tracking results. (a) Sagittal view from the left. (b) Coronal view from the front. (c) Oblique view. The images show 500 streamlines per seed voxel in the right STN of one subject, color-coded for streamline direction (red = left-right, green = anterior-posterior, blue = inferior-superior). The right STN seed is represented by the white surface, indicated by the white arrow. Abbreviations: acc = anterior cingulate cortex, cc = corpus callosum, ifg = inferior frontal gyrus, phg = parahippocampal gyrus, sfg = superior frontal gyrus, sma = supplementary motor area, stg = superior temporal gyrus.

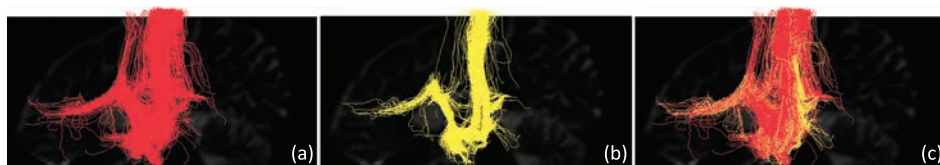


Figure 6.6 Comparison of fiber tracking results for the atlas-based and manual right STN ROI of one volunteer. (a) Fibers tracked from atlas-based right STN ROI. (b) Fibers tracked from manually segmented right STN ROI. (c) Both bundles overlaid (red: atlas-based STN ROI, yellow: manual STN ROI). All images show sagittal views from the left.

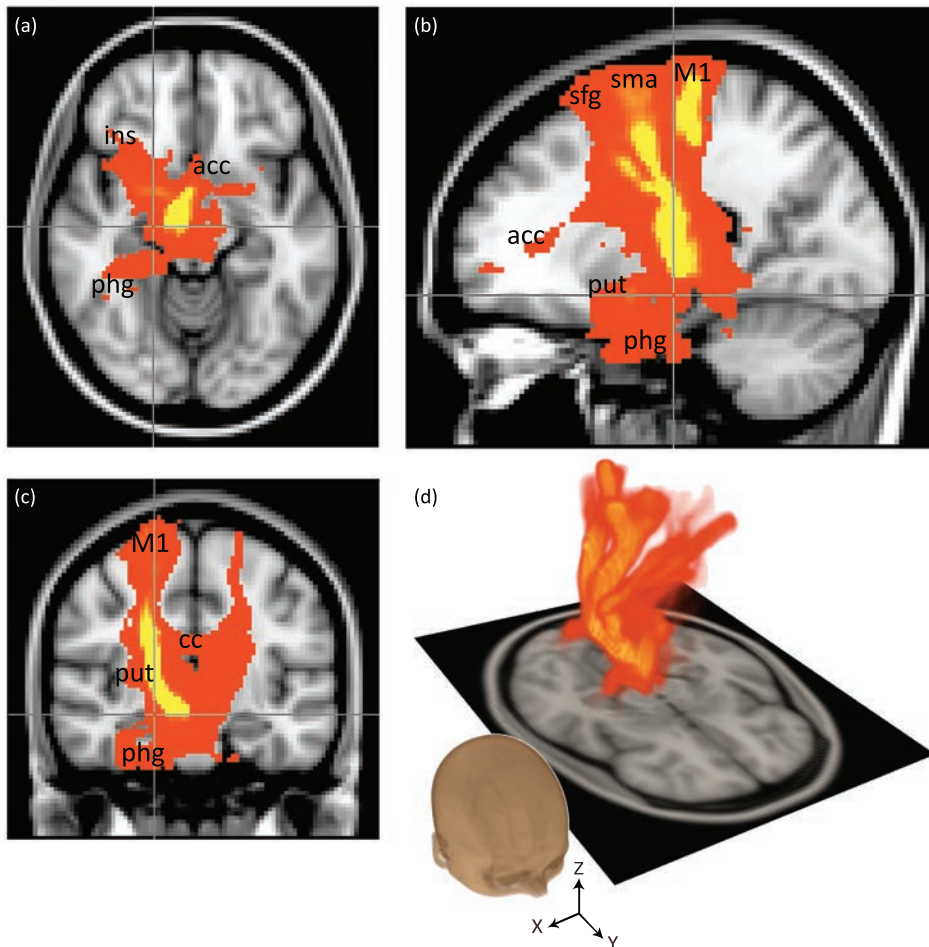


Figure 6.7 Total probability map of right STN connectivity in MNI152 space, using color coding from red (low streamline count, ~ 5) to yellow (high streamline count, ~ 6000). (a) Axial view. (b) Sagittal view. (c) Coronal view. (d) Volume rendering in 3D. In the 2D images, the crosshairs indicate the plane positions. Abbreviations: acc = anterior cingulate cortex, cc = corpus callosum, ins = insular cortex, M1 = precentral gyrus/primary motor cortex, phg = parahippocampal gyrus, put = putamen, sfg = superior frontal gyrus, sma = supplementary motor area.

Tables 6.2 and 6.3 indicate that the right STN exhibits significant connections with gray matter nuclei such as the thalamus, substantia nigra, caudate nucleus, red nucleus, putamen, and globus pallidus. Furthermore, projections to cortical areas with different functions were found, for example to the pre- and supplementary motor area (motor function), and the medial frontal and anterior cingulate cortex (limbic). The difference between the two connectivity measures C_1 and C_2 (without

and with normalization for streamline length) is small, as most connected structures were found in both tables. Deviations occurred mostly in structures that lie next to regions of interest that were detected in both cases. For instance, the medial globus pallidus (GPi) can be found in Table 6.3, while the neighboring lateral globus pallidus (GPe) is present in both Table 6.2 and Table 6.3.

We also calculated the connectivity based on the total probability map in MNI152 space (as shown in Figure 6.7), using connectivity measure C_3 . The results are presented in brief in Table 6.4, arbitrarily thresholded at $C_3 \geq 1.00$, while the complete data (also for left STN) can again be found in Appendix A (Tables A.5 and A.6). Many regions that were found using C_1 and C_2 were again reported here, such as the gray matter nuclei (thalamus, substantia nigra, red nucleus, caudate nucleus, globus pallidus) and cortical areas like the pre- and supplementary motor area, the cingulate cortex, and the medial frontal gyrus. However, this procedure also resulted in connected regions that were not retrieved earlier, such as the primary motor cortex/precentral gyrus (motor function), and the amygdala (limbic).

6.3.3 Segregation of motor and non-motor regions of the STN

The normalized maps of C_2 (STN, motor cortical areas), cumulated over all subjects, are visualized in Figure 6.9, for both the left and right STN. The images show high connectivity to the motor cortical areas in the lateral STN regions, especially for the total motor cortical areas (Figure 6.9(a)) and Brodmann area 6 (Figure 6.9(c)), while low connectivity is found medially.

6.4 Discussion

6.4.1 Current findings

In this chapter, we aimed to determine the full structural connectivity of the STN based on streamline counts derived from probabilistic HARDI tractography. Streamline visualizations and probability maps revealed direct (“hyperdirect” pathway) and indirect connections to motor, cingulate, and temporal cortical areas. We tested the connectivity measures derived from streamline counts for significance over the group of 8 subjects, which yielded a more specific description of connected areas. These areas could be classified as belonging to a few major groups, such as the gray matter nuclei, motor cortical areas (premotor and supplementary motor area), and limbic cortex (medial frontal and cingulate cortex). The connectivity based on the total probability map showed the same trends, while adding the primary motor cortex to the motor cortical group, and the amygdala to the limbic system. Regarding

the subdivision of the STN, based on connectivity between the distinct STN voxels and the motor cortical areas, we found high connectivity in the lateral STN and low connectivity in the medial STN parts.

In the following sections, the correspondence of these findings with the existing literature on STN circuitry will be elaborated on, as well as the consequent implications on the clinical practice of DBS procedures and possible future work.

6.4.2 Correspondence of findings with existing literature

The “hyperdirect” pathway

The first evidence of the presence of the so-called “hyperdirect” pathway in the non-human primate was already provided in 1940 [221], and subsequent tracer studies extensively described the cortico-subthalamic projections in the non-human primate [57, 140, 169, 216, 218]. Later, an electrophysiological study by Nambu et al. [217] confirmed the existence of “hyperdirect” pathway in non-human primates. To our knowledge, our study is the first study which gives an indication for the existence of the “hyperdirect” pathway in humans. In 7 out of 10 STNs that exhibited a direct connection to the motor cortical areas, the “hyperdirect” pathway could be seen as a small bundle traveling along the internal capsule, a route that corresponds with the existing primate literature [136, 233]. With respect to the medial trajectory found in some volunteers, the probabilistic fiber tracking method seems to be inclined to follow anisotropic diffusion profiles from the fornix to the corpus callosum, via the dural ligaments.

STN connectivity with motor areas

According to tracer studies in non-human primates, within the motor circuit, the STN should exhibit connections with the following cortical areas: the primary motor cortex, premotor and supplementary motor cortex, and the somatosensory cortex [140, 216, 218, 232]. With respect to the deep brain nuclei, we expected to find strong connectivity with the striatum, the central and ventrolateral part of the lateral globus pallidus (GPe), the ventrolateral part of the medial globus pallidus (GPi), and the thalamus [57, 158, 233, 262, 274]. In our results, considering the motor cortical areas, the pre- and supplementary motor area is most significant, though the primary motor cortex and somatosensory areas do appear in the C_3 results and also significantly in the C_1 and C_2 tables (also as pre- and postcentral gyrus, respectively). All expected gray matter nuclei present in the atlas are reported as highly significantly connected to the STN.

That the premotor and supplementary motor area is more significantly connected to the STN than the primary motor cortex might seem odd, but this finding is supported by electrophysiological studies on frequency-specific functional connectivity [172, 194]. These studies also support the rather medial location on the motor cortex that we found to be connected [144, 194]. Furthermore, we discovered significant connectivity measures for the lingual gyrus in the occipital lobe. This gyrus was not mentioned in the reviewed literature, however, more recent imaging studies using PET and fMRI considered the lingual gyrus to be involved in movement velocity, together with the basal ganglia [313, 329].

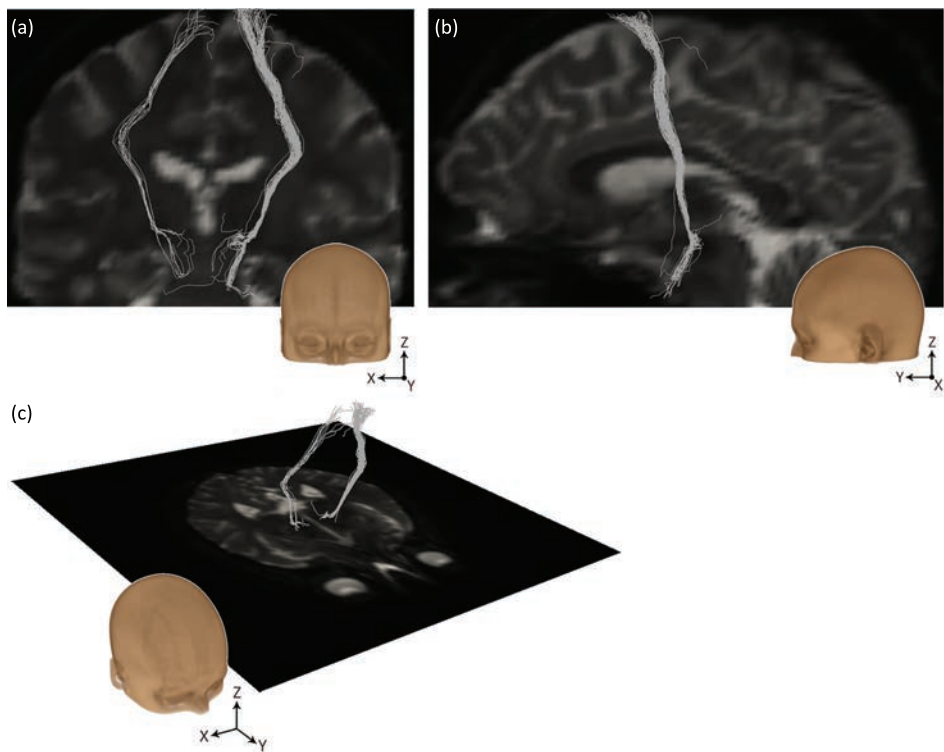


Figure 6.8 Streamlines from the right and left STN in subject 1, ending in the motor cortex, that do not pass through thalamus, caudate, putamen or globus pallidus. These streamlines are therefore an indication for the existence of the “hyperdirect” pathway. (a) Coronal view. (b) Sagittal view on streamlines from the right STN. (c) Streamline rendering in 3D, showing an axial plane of the unweighted diffusion image.

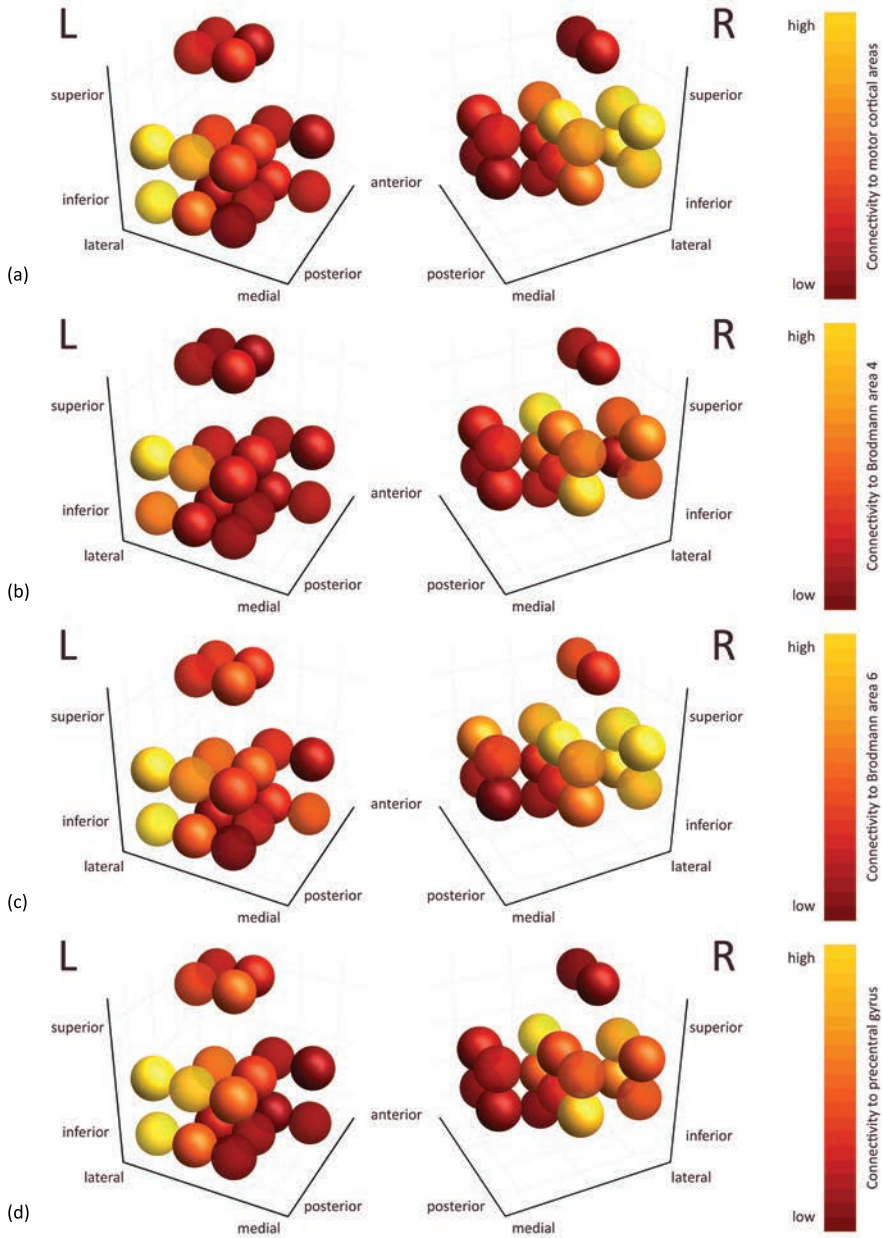


Figure 6.9 Structural connectivity to the motor cortical areas per STN voxel, cumulated over all subjects, in MNI152 atlas space. Each sphere represents one voxel in atlas space (voxel size 2x2x2 mm) and is color-coded by the C_2 connectivity: dark red means low connectivity, while yellow means high connectivity.

STN connectivity with associative and limbic areas

Concerning the associative loop, we expected the STN to be connected to the orbitofrontal and dorsolateral prefrontal cortex, as well as the CM-Pf nucleus of the thalamus, the nucleus accumbens, the ventral part of the putamen and caudate nucleus, the ventral pallidum, the ventral tegmental area, and the medial part of the substantia nigra reticulata [5, 6, 7, 57, 140, 215, 233]. As reported above, the gray matter nuclei present in the atlas were all found to be structurally connected to the STN. With regard to the cortical areas, we found the superior temporal gyrus to be highly significant. Other connected associative cortical areas include the temporal fusiform, inferior temporal, and middle temporal gyri, as well as the orbitofrontal cortex.

For the limbic circuit, the literature reported on connections with the (para)limbic cortical areas such as the anterior cingulate and the medial orbitofrontal cortex [6]. Subcortically, the limbic loop comprises the nucleus accumbens, ventral pallidum, ventral tegmental area, substantia nigra pars reticulata, globus pallidus, thalamus, hippocampus and amygdala [6, 129]. The most significantly connected regions we found included the medial frontal gyrus, the cingulate cortex, and the amygdala. Other expected limbic areas such as the substantia nigra, globus pallidus, thalamus and hippocampus, were also present in our resulting tables.

Segregation of motor and non-motor regions of the STN

According to the review articles on STN anatomy and function [136, 298], the tripartite functional subdivision of the STN is organized as follows: the medial tip of the nucleus is devoted to the limbic circuit, the associative part is situated ventrolaterally, and the motor subterritory is located at the dorsolateral side of the STN. The subdivision results based on our experiments with connectivity to the motor cortical areas indeed show a mediolateral gradient, yielding the highest connectivity at lateral positions, where we expect the STN motor part, while connectivity in the supposed medial tip is lowest. A clear segregation of motor and non-motor regions was not found. Therefore, our data support the idea of open circuits, in which motor and non-motor pathways are partially integrated within the STN.

6.4.3 Clinical perspective

The correspondence with the existing literature on anatomical tracer and electrophysiological studies validates the performed structural connectivity measurements based on diffusion-weighted MRI. Thus, our study indicates that it might be possible to assess the STN connectivity in a noninvasive way. The voxel-wise connectivity

assessment of the motor cortical areas shows that the lateral part of the STN exhibits the highest connectivity. This again emphasizes that the therapeutic target for DBS is located in the dorsolateral STN part. To compensate for interindividual variations, diffusion-weighted MRI may assist in optimization of the patient-specific target.

In addition, our results support the existence of the “hyperdirect” pathway, running between the motor cortical areas and the STN. The presence of the “hyperdirect” pathway in humans validates current models on cortico-basal ganglia circuits. This pathway could be used in electrophysiological studies to target the STN motor part during DBS procedures, or might be subject to research as a new treatment target for stimulation.

6.4.4 Future work

The pipeline that we used for the calculation of structural connectivity can still be improved in multiple ways. First of all, for a clinically feasible MRI measurement, we would need to reduce the acquisition time for the diffusion-weighted data. It might be that 60 (or less) gradient directions are sufficient, thereby halving the scan duration. On the other hand, if the spatial resolution could be increased, we could probably improve the separation of the STN motor and non-motor parts. Second, inaccuracies are inherent to image acquisition (i.e., EPI deformation, spatial resolution) and registration. This influences the precision of for example the STN segmentation and thus also the results of the experiment on the level of segregation of the different STN parts.

The atlas-based STN segmentation which serves as the seed region for the probabilistic tracking is sensitive to registration inaccuracies. We could probably perform a better image registration if we were to acquire an isotropic structural (T_1 -weighted) image of the brain, besides the currently used data with limited field-of-view or thick slices. In addition, we could question the inherent precision of this ROI for the left STN, as it contains two parts that only have a corner point of their voxels in common, instead of an edge or face. Although we showed that fibers based on manual and atlas-based STN ROIs overlap extensively, the use of the atlas-based STN could be avoided by using 7-T MRI for the localization of the STN [1, 61, 62]. The evidence for the “hyperdirect” pathway is also susceptible to registration inaccuracies, via the atlas segmentations of gray matter nuclei that should be bypassed by this pathway.

Furthermore, validation of diffusion-weighted data is a well-known issue. We can only compare the found projections with the results of electrophysiological studies in humans, or tract tracing experiments in animals, but a ground truth for all white matter tracts (also smaller bundles) in humans is not readily available. The

structural connectivity results, based on a probabilistic fiber tracking method that inherently finds all possible pathways, could be corrected for non-existing anatomical connections using such a ground truth. We did not perform such a correction in this study and for instance found multiple contralateral connections of the STN. However, according to literature on STN circuitry [232, 233], no direct contralateral cortico-subthalamic pathways are to be expected. Although weaker than their ipsilateral equivalents, indirect connections to the contralateral side do exist, via the cortex, globus pallidus, substantia nigra, and brain stem. In addition, probabilistic fiber tracking in some volunteers showed a non-existing medial trajectory for the “hyperdirect” pathway from motor cortical areas to STN.

Future work could include a comparison of the structural connectivity found in this study with STN functional connectivity based on resting state functional MRI data [50]. In addition, all available information per voxel of the STN (structural connectivity, functional connectivity, local diffusion information) could be joined to obtain a more robust conclusion on the level of segregation of the motor, limbic, and associative regions of the STN. To this end, the connectivity of each STN voxel to the different functional parts of the globus pallidus and striatum could also be taken into account [22]. Another way to achieve more robust results would involve the inclusion of more subjects.

6.4.5 Conclusions

By calculating the structural connectivity of the STN based on HARDI data, we were able to confirm the STN’s connections to motor, associative, and limbic areas that have been found before by means of neuronal tract tracing and electrophysiological studies. Furthermore, we produced evidence for the existence of the “hyperdirect” pathway from motor cortex to STN in humans. We also reported that the connectivity of distinct STN voxels to the motor cortical areas increased when going from the medial to the lateral STN, though a clear segregation was not seen. This gradient in connectivity might indicate that the STN motor part and therefore the therapeutic target for STN DBS is located dorsolaterally. While improvements could be made on the amount of data and the registration and validation steps, this work is a promising step towards the use of diffusion-weighted MRI for the segmentation of STN functional parts and subsequent DBS planning.

6.5 Acknowledgments

We thank Maarten Vaessen and Marc Geerlings for technical support.

Table 6.2 Regions significantly connected to the *right* STN after a *t*-test on C_1 , using $n_{\text{subjects}} = 8$. Here only the most important regions are shown, thresholded at $p \leq 0.010$. Full information (also on left STN) is presented in Tables A.1 and A.2 of Appendix A.

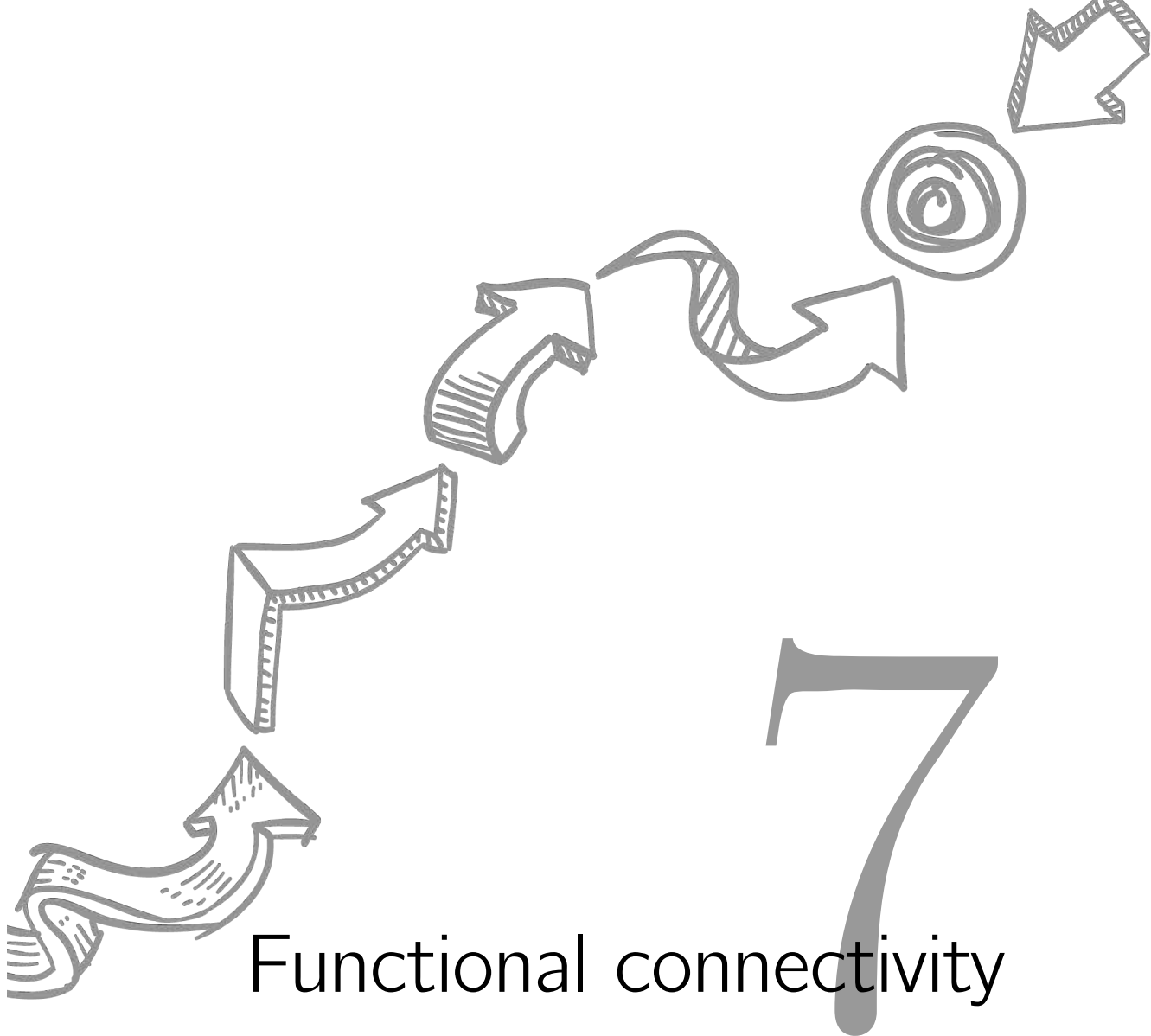
Hemisphere	Region of interest	<i>p</i> value
Subcortical		
Right	Thalamus	0.000
Right	Thalamus, Ventral Posterior Lateral Nucleus	0.002
Right	Thalamus, Ventral Posterior Medial Nucleus	0.004
Right	Thalamus, Ventral Anterior Nucleus	0.005
Right	Thalamus, Ventral Lateral Nucleus	0.007
Right	Thalamus, Lateral Posterior Nucleus	0.007
Right	Caudate	0.003
Right	Putamen	0.004
Right	Lateral Globus Pallidus (GPe)	0.007
Right	Red Nucleus	0.004
Right	Substantia Nigra	0.001
Right	Clastrum	0.007
Right	Hypothalamus	0.006
Right	Brainstem, Midbrain	0.000
Frontal		
Right	Pre- & Supplementary Motor Area	0.006
Right	Medial Frontal Gyrus	0.010
Right	Cingulate Gyrus	0.000
Left	Anterior Cingulate, Brodmann area 24 (limbic lobe)	0.008
Right	Anterior Cingulate, Brodmann area 25 (limbic lobe)	0.010
Temporal		
Right	Superior Temporal Gyrus	0.007
Occipital		
Right	Lingual Gyrus, Brodmann area 18	0.009

Table 6.3 Regions significantly connected to the *right* STN after a *t*-test on C_2 , using $n_{\text{subjects}} = 8$. Here only the most important regions are shown, thresholded at $p \leq 0.010$. Full information (also on left STN) is presented in Table A.3 and A.4 of Appendix A.

Hemisphere	Region of interest	<i>p</i> value
Subcortical		
Right	Thalamus	0.000
Right	Thalamus, Ventral Posterior Lateral Nucleus	0.001
Right	Thalamus, Ventral Anterior Nucleus	0.003
Right	Thalamus, Medial Dorsal Nucleus	0.004
Right	Thalamus, Ventral Posterior Medial Nucleus	0.004
Right	Thalamus, Lateral Posterior Nucleus	0.008
Right	Thalamus, Ventral Lateral Nucleus	0.009
Right	Caudate	0.003
Right	Putamen	0.004
Right	Lateral Globus Pallidus (GPe)	0.010
Right	Medial Globus Pallidus (GPi)	0.009
Right	Red Nucleus	0.003
Right	Substantia Nigra	0.001
Right	Clastrum	0.007
Right	Hypothalamus	0.004
Right	Brainstem, Midbrain	0.000
Frontal		
Right	Pre- & Supplementary Motor Area	0.006
Right	Medial Frontal Gyrus	0.010
Right	Cingulate Gyrus	0.001
Left	Anterior Cingulate, Brodmann area 24 (limbic lobe)	0.010
Left	Limbic Lobe	0.010
Temporal		
Right	Superior Temporal Gyrus	0.005
Occipital		
Right	Lingual Gyrus, Brodmann area 18	0.008
Cerebellar		
	Cerebellum	0.007

Table 6.4 Regions connected to the *right* STN derived from the total probability map (C_3). Here only the most important regions are shown, thresholded at $C_3 \geq 1.00$. Full information (also on left STN) is presented in Tables A.5 and A.6 of Appendix A.

Hemisphere	Region of interest	Connectivity
Subcortical		
Right	Thalamus	42.09
Right	Thalamus, Ventral Posterior Lateral Nucleus	246.77
Right	Thalamus, Ventral Posterior Medial Nucleus	161.61
Right	Thalamus, Lateral Posterior Nucleus	130.62
Right	Thalamus, Ventral Lateral Nucleus	63.19
Right	Thalamus, Mammillary Body	61.56
Right	Thalamus, Pulvinar	14.44
Right	Thalamus, Medial Geniculum Body	4.40
Right	Caudate	2.82
Right	Medial Globus Pallidus (GPi)	1.57
Right	Red Nucleus	68.39
Right	Substantia Nigra	76.47
Right	Amygdala	1.53
Right	Mammillary Body	58.67
Left	Mammillary Body	1.87
Right	Hypothalamus	103.55
	Hypothalamus	1.48
Right	Midbrain	7.14
Right	Brainstem, Midbrain	23.23
Right	Brainstem, Midbrain, Medial Geniculum Body	23.89
Frontal		
Right	Precentral Gyrus	1.09
Right	Primary Motor Cortex	5.87
Right	Pre- & Supplementary Motor Area	1.47
Right	Medial Frontal Gyrus	1.79
Right	Cingulate Gyrus	2.83
Right	Anterior Cingulate (limbic lobe)	1.63
Right	Anterior Cingulate, Brodmann area 24 (limbic lobe)	26.86
Left	Anterior Cingulate, Brodmann area 25 (limbic lobe)	1.62
Right	Subcallosal Gyrus	9.41
Left	Subcallosal Gyrus	1.20
Right	Subcallosal Gyrus (limbic lobe)	2.50
Right	Subcallosal Gyrus, Brodmann area 34	3.31
Right	Subcallosal Gyrus, Brodmann area 34 (limbic lobe)	3.34



Functional connectivity

Humor is by far the most significant activity of the human brain.

Edward de Bono

This chapter is based on:

“Resting state functional connectivity of the motor and non-motor areas of the human subthalamic nucleus.” Ellen Brunenberg, Walter Backes, Claudio Pollo, Leila Cammoun, Mark Janssen, Veerle Visser-Vandewalle, Bart ter Haar Romeny, Jean-Philippe Thiran, and Bram Platel. Submitted.

7.1 Introduction

7.1.1 Background

As we saw before, in topical literature, the STN has been divided into three functionally different parts, which were distinguished by their afferent and efferent connections in the non-human primate. The largest part is the sensorimotor area, which encompasses the dorsolateral two-thirds of the STN. The associative area is located ventrolaterally, while the limbic area is positioned at the medial tip of the STN [136, 233, 298]. To what extent these functional areas overlap within the STN is not clear yet. The level of segregation determines the possibility of selective stimulation of the motor STN, without affecting the associative and limbic circuits. Resting state BOLD functional MRI enables us to examine correlations in resting state activity between the STN and other brain regions. The resulting functional information can be used to investigate the spatial organization of the different functional STN parts and the consequent possibilities for specific identification of the STN.

7.1.2 Related work

A number of studies have already applied fMRI-based functional connectivity analysis to basal ganglia nuclei. Some have investigated the motor network in healthy subjects [257] or patients with PD [332], without looking at the STN specifically. Others have examined the resting state functional connectivity of specific nuclei such as the red nucleus [220] or the striatum [85]. Barnes et al. [22] identified subdivisions in the caudate and putamen based on the functional connectivity data.

To our knowledge, the only resting state functional connectivity study concentrating on the STN was reported by Baudrexel et al. [26, 27]. However, they reported only on alterations in the functional connectivity pattern caused by PD and did not discuss the “normative” functional connectivity of the STN with the rest of the brain. Other studies concerning STN connectivity make use of more invasive techniques, such as PET [179, 242, 287] and electrophysiological recordings in humans [8, 287, 326] and in the mouse brain [200]. The functional connectivity of the STN and the

implications for the subdivision of the STN have not yet been investigated in a noninvasive way.

7.1.3 Aim

Accordingly, the aim of the present study was to investigate the functional connectivity of the STN with cortical and subcortical structures in healthy subjects based on resting state BOLD fMRI. We hypothesized that the functional connectivity information clarifies the level of segregation of the motor area from the limbic and associative areas of the STN. This level of segregation indicates to what extent selective stimulation of the STN motor part is feasible.

For this purpose, we conducted a resting state BOLD fMRI experiment on healthy volunteers and postprocessed the data using linear regression analysis. This approach calculates the correspondence of the resting state fMRI signal in an arbitrary voxel of the brain with the signal in the STN ROIs (based on both manual and atlas-based segmentations) and other explanatory variables such as the motion correction parameters and the global mean signal.

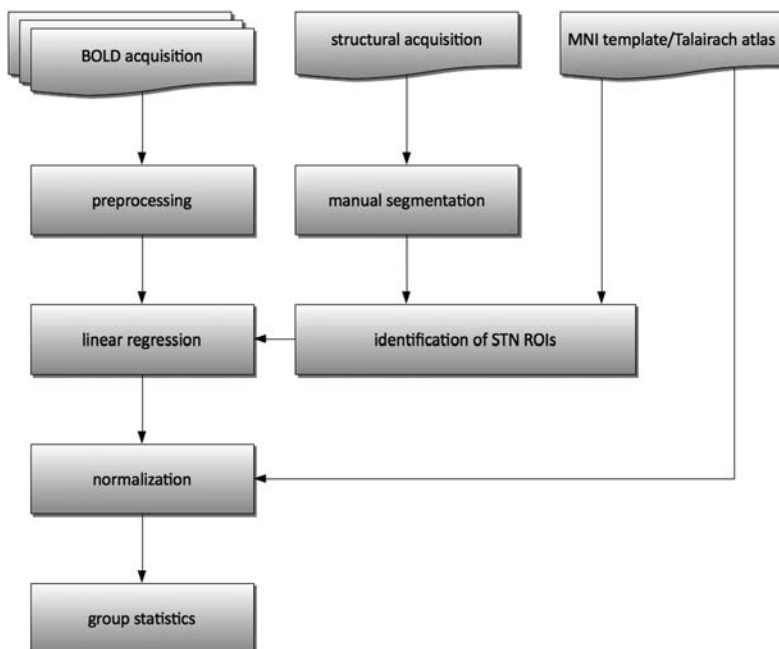


Figure 7.1 Flowchart of data analysis steps for functional connectivity.

7.2 Methods

7.2.1 Data acquisition

A group of 10 healthy adult subjects (4 males, 6 females, age 24–35 years, mean age = 27.5 years) was recruited from the Eindhoven University of Technology and Maastricht University Medical Center. Written informed consent was obtained from all subjects prior to participation, and the study was approved by the Medical Ethics Committee of Maastricht University Medical Center.

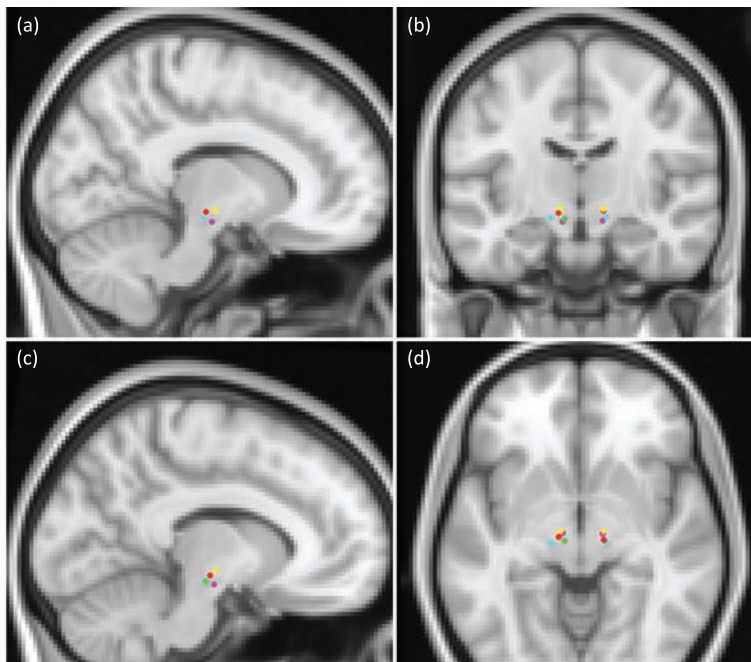


Figure 7.2 STN centers of mass in MNI152 atlas space. Top left: right STN in sagittal plane. Bottom left: left STN in sagittal plane. Top right: right and left STN in coronal plane. Bottom right: right and left STN in axial plane. Color legend: yellow dots: average coordinates of atlas-based STNs; red, green, cyan, and magenta dots: average coordinates of manually segmented STNs (different color for each subject).

MRI data were acquired on a Philips Achieva 3-T system. Structural images were obtained using a multi-slice turbo spin-echo (TSE) T_2 -weighted sequence (TE = 110 ms, TR = 2.5 s, 50 1-mm thick coronal slices with 256x256 matrix, pixel size 1x1 mm).

Functional imaging was performed using a blood-oxygen-level-dependent (BOLD) contrast sensitive gradient-echo echo-planar imaging protocol (TE = 35 ms, TR = 2.2 s, flip angle = 90°, 25 3-mm thick coronal slices with 128x128 matrix, pixel size 1.563x1.563 mm). One dynamic run of 200 time points was acquired. Both acquisitions covered only part of the brain (coronal FOV of 50 mm for structural and 75 mm for functional imaging), situated around the midbrain region of interest, parallel to the brain stem. The total acquisition time for the two scans was about 15 minutes.

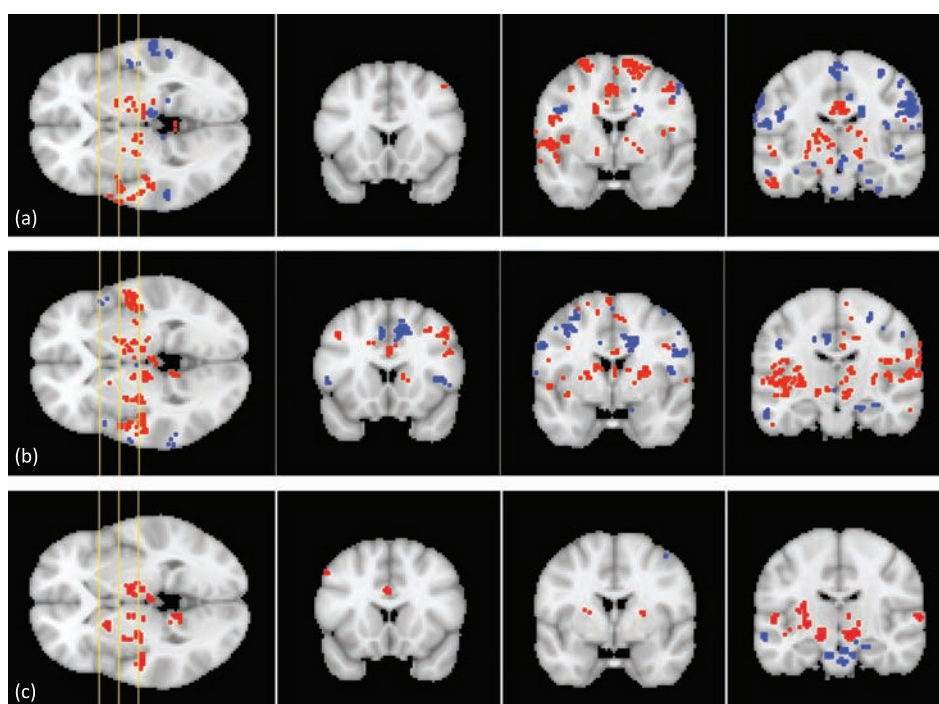


Figure 7.3 Significant clusters for the right STN ROI, shown on three coronal slices of the MNI152 template. (a) 3 manually segmented right STN ROIs. (b) 3 atlas-based right STN ROIs (same volunteers). (c) All 10 atlas-based right STN ROIs. The yellow lines on the axial image on the left-hand side show the position of the coronal slices. Red clusters exhibit positive regression coefficients, while blue clusters yield negative coefficients.

7.2.2 Data preprocessing

A flowchart of all the data analysis steps performed for this study is represented in Figure 7.1. First, the functional data were preprocessed to reduce image artifacts and signal variance due to factors other than neuronal activation. Preprocessing steps included (i) correction for head movement using MCFLIRT [156] in FSL [115], (ii) brain extraction with FSL's BET [278], (iii) removal of the first 5 time points to correct for T_1 -saturation effects, (iv) slice timing correction, (v) spatial smoothing (3 mm FWHM) (both in SPM5), (vi) linear detrending, (vii) temporal bandpass filtering ($0.01 \text{ Hz} < f < 0.1 \text{ Hz}$) (both using the REST toolbox for MATLAB [333]).

The structural images were registered to the functional image data using FSL's FLIRT [157], employing a rigid body transformation (6 degrees of freedom). The data from different subjects were spatially normalized by means of registration with the MNI152 template [64] and the accompanying Talairach atlas labels [173, 293] using an affine transformation, also in FSL's FLIRT.

7.2.3 Identification of the subthalamic nucleus ROIs

Two methods were used to identify the STN ROIs in the subjects. First, the STNs that were visible on the structural images were segmented by an experienced neurosurgeon (Claudio Pollo), using ITK-SNAP, a software application that facilitates 3D segmentation of medical images [336]. This manual procedure led to 3 right STNs and 4 left STNs, segmented in 4 subjects. Furthermore, the Talairach labels indicating the left and right STN were used to determine the ROIs.

To compare the two segmentation methods, the centers of mass of the labeled STNs were projected into the MNI152 atlas space, as can be seen in Figure 7.2. For each orientation, the slice on which the atlas-based STN lies is shown, whereas the manually segmented STNs are projected onto this slice. From this figure, it is apparent that the manually segmented STNs as seen on the structural images differ from the atlas-based STNs. The directly visualized STNs seem to lie more posterior and more ventral than the atlas-based structures.

While papers that compare direct and atlas-based targeting of the STN do not agree on the difference in anteroposterior and mediolateral directions [17, 75, 255], they do concur on the fact that the MRI-based STN seems to lie more ventral than the atlas-based STN [17, 75], as can be seen in Figure 7.2 as well. The discrepancy between atlas-based and MRI-based STN centers might be caused by the fact that the Talairach atlas is based on only one brain specimen [255].

7.2.4 Linear regression analysis

For all STN ROIs (left, right, atlas-based and manually segmented), whole-brain correlation maps were generated by linear regression. Let $y(t)$ be the resting state signal over time in an arbitrary voxel within the brain mask. This $y(t)$ can be expressed as a linear combination of the signal in the STN ROI and some confounds.

The BOLD fMRI signal at time t , averaged over all voxels of our STN ROI, is denoted by $r(t)$. This signal can be standardized according to $\hat{r}(t) = \frac{r(t) - \mu}{\sigma}$, where μ is the mean and σ the standard deviation of the signal. So, $y(t) = \beta \cdot \hat{r}(t) + \text{confounds}$, with β the “goodness of fit” and thus an estimate of functional connectivity. The confounds include an offset ($\alpha \cdot \mathbf{1}$), the motion correction parameters from our preprocessing ($\gamma \cdot \mathbf{M}(t)$), and the global mean signal over all brain voxels ($\delta \cdot \bar{s}(t)$). We did not include a regressor for low frequency drift, because we already detrended the functional data during the preprocessing. Taken together, we performed linear regression using the following system for each STN ROI:

$$y(t) = \alpha \cdot \mathbf{1} + \beta \cdot \hat{r}(t) + \gamma \cdot \mathbf{M}(t) + \delta \cdot \bar{s}(t).$$

We implemented this linear regression system in the MATLAB programming environment. After performing the regression algorithm, we saved the estimated $\hat{\beta}$ maps for further (statistical) analysis.

7.2.5 Statistical analysis

For each voxel within the atlas’ brain mask, and not labeled as white matter or cerebrospinal fluid, we performed a Student t -test on the $\hat{\beta}$ maps for the same STN ROI across subjects. The regression coefficients were normalized first, using the Fisher z -transform.

The resulting test statistic T for each voxel was corrected for multiple comparisons using the cluster thresholding method based on random field theory (implemented in the fmristat toolbox for Matlab [330]). A critical cluster size was calculated for test statistics larger than a given threshold, for a given significance level. We used threshold $T = 2.7$ at $p < 0.05$, resulting in a critical cluster size of 14 voxels.

We separated the thresholding procedure for voxels with negative regression coefficients ($T < 2.7$) and voxels with positive regression coefficients ($T > 2.7$). This procedure resulted in significant clusters of voxels with negative and positive regression coefficients, respectively, instead of clusters with mixed responses. The locations of the significant clusters were compared with Talairach atlas labels to generate lists of functionally connected regions.

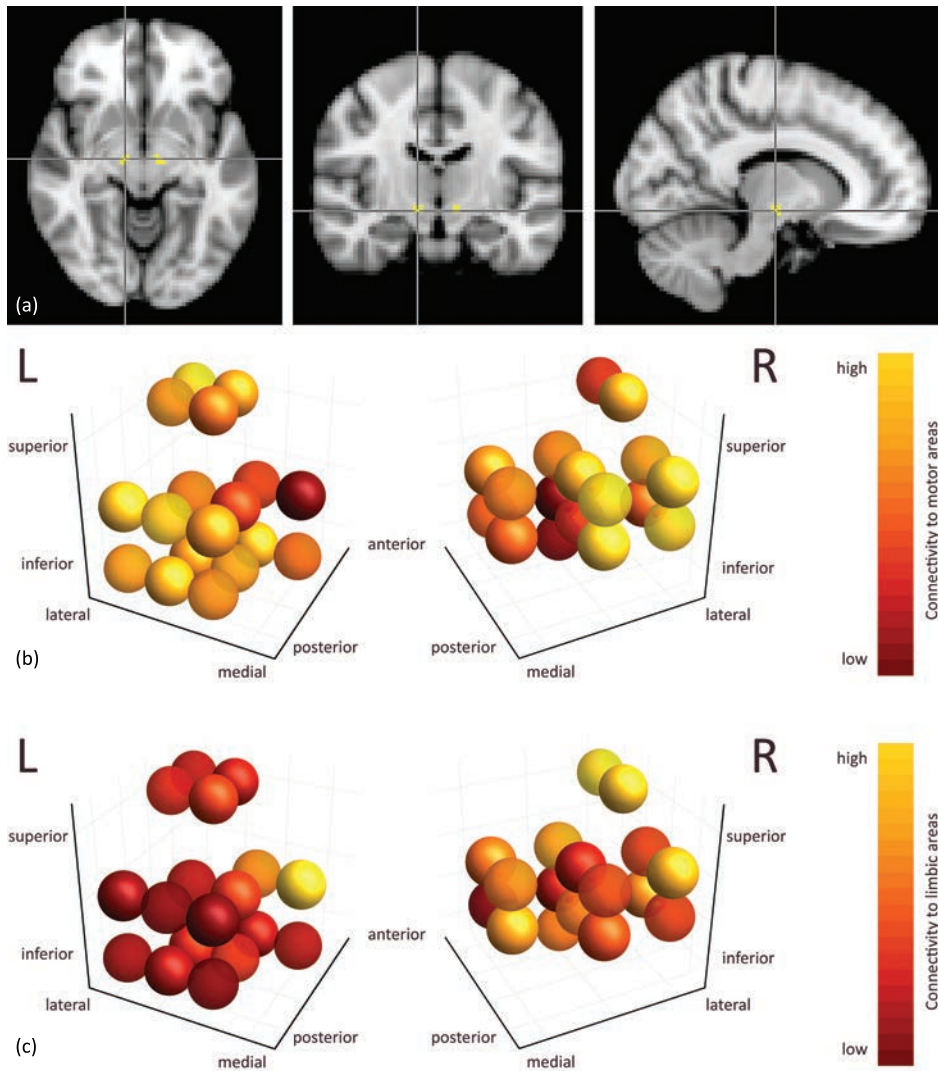


Figure 7.4 Functional connectivity per STN voxel in atlas space (see (a)) after applying the reverse-regression procedure. (a) STN masks (yellow) derived from the Talairach atlas, overlaid on MNI152 template. From left to right: axial, coronal and sagittal images. Crosshair is positioned at the right STN. (b) Connectivity to motor areas per voxel of the left and right STN, cumulated over all subjects. (c) Connectivity to limbic areas per voxel of the left and right STN, cumulated over all subjects. Each sphere in (b) and (c) represents one voxel and is color-coded by functional connectivity: dark red means low connectivity, while yellow means high connectivity.

7.2.6 Reverse regression for segregation of STN regions

To get more insight in the level of segregation of the motor area from the other STN areas, and thus to what extent selective stimulation of the STN motor part is feasible, we performed a reverse-regression procedure. We chose the primary motor cortex, precentral gyrus, and premotor and supplementary motor area as ROIs representing the motor loop, while the hippocampus, amygdala, parahippocampal gyrus, anterior cingulate, and cingulate gyrus formed the ROIs for the limbic group. These ROIs were taken from the MNI152/Talairach atlas in FSL, and transformed into individual subject space using the inverse of the affine transformations calculated in Subsection 7.2.2.

Linear regression was performed in the same way as in Subsection 7.2.4, using the average signals of both groups of ROIs as principal regressors (the right motor and limbic ROIs for the right STN voxels, and the left ROIs for the left STN voxels, respectively). This procedure yielded two regression coefficient maps, $\hat{\beta}_{motor}$ and $\hat{\beta}_{limbic}$ for both the right and left STNs. These maps were registered back towards the MNI152 template (using linear interpolation), masked by the atlas STN ROIs, and summed over all subjects.

7.3 Results

7.3.1 Whole-brain STN connectivity

The significant clusters were visualized onto the MNI152 template within MATLAB, as can be seen in Figure 7.3 for the right STN. The left STN results can be found in Figure B.1 of Appendix B. The figures indicate that clusters that are significantly correlated to the STN ROIs were found in various cortical and subcortical structures. Figures 7.3(a), 7.3(b), B.1(a) and B.1(b), based on only the subjects for which manual segmentation of the STN was feasible, show a larger number of significant clusters than Figures 7.3(c) and B.1(c), based on the atlas-based STNs of all 10 subjects.

For each significant cluster, the voxel with the maximum response (maximum absolute value of test statistic T) was selected. The characteristics of these voxels are specified in Tables 7.1 to 7.4 for the right and left atlas-based STN ROIs. X , Y and Z represent the coordinates (in atlas space) of the maximum response for each cluster. The related value for T and the cluster extent (in voxels) are given, as well as the other structures belonging to the cluster. The same was done for the manually segmented STN ROIs. Those results are presented in Appendix B, in Tables B.1 and B.2 for the right and in Tables B.3 and B.4 for the left STN ROIs.

Tables 7.1 to 7.4 and B.1 to B.4 report functional connectivity of the STN ROIs with a multitude of other brain areas. The most significantly correlated structures include a group of subcortical areas such as the thalamus, caudate, putamen, globus pallidus, and midbrain. The cerebellum is functionally connected to the STN ROIs as well. Furthermore, connected structures in the frontal cortex encompass the pre- and supplementary motor area, the medial and middle frontal gyri, and the cingulate gyrus, while correlations to the temporal cortex incorporate the superior temporal gyrus and the fusiform gyrus.

We can further classify the results in several ways, for example by looking at the differences between automatic (atlas-based) and manual STN segmentation. According to Tables 7.1 to 7.4, the atlas-based STN ROIs are functionally connected to subcortical structures including the thalamus, caudate, putamen, and the midbrain in general. With respect to the frontal cortex, the premotor and supplementary motor area, medial frontal gyrus, and cingulate gyrus, insula are found to be correlated to the STN ROIs. Connected temporal cortex areas include the parahippocampal gyrus, superior temporal gyrus, and the fusiform gyrus. The cerebellum shows functional connectivity as well.

Tables B.1 to B.4, containing the results of the manually segmented STN ROIs, show more connected structures in subcortical, frontal, temporal, and cerebellar areas, but also in the parietal cortex. In Figures 7.3(b) and B.1(b), we show the significantly correlated clusters for the atlas-based STN ROIs of only the subjects for whom manual segmentation of the STN was possible. It can be seen that this test yielded more significant clusters than the test over all 10 subjects, of which the results are presented in Figures 7.3(c) and B.1(c).

With regard to laterality, many functional connections are found bilaterally (i.e., the right STN ROI is correlated with both left and right putamen) and show up in the results of both the right and the left STN ROIs. The only exceptions are the anterior cingulate and the supramarginal gyrus, which are found only in relation to the right STN.

Finally, we can evaluate the similarities and differences of the results for positive and negative correlation coefficients. Many structures exhibit both positive and negative clusters, such as the thalamus, midbrain, pons, precentral gyrus, pre- and supplementary motor area, cingulate gyrus, parahippocampal gyrus, and cerebellum. The basal ganglia structures (caudate, putamen, globus pallidus) only show a positive correlation with the STN ROIs, while for example the postcentral gyrus yields only negative clusters. In general, the subcortical structures, give rise to more positive than negative correlation, while the parietal and temporal cortex show more negative than positive correlation.

Table 7.1 Brain regions showing significant *positive* correlations with the 10 atlas-based *right* STN ROIs. X, Y, and Z represent the coordinates (in atlas space) of the maximum response for each cluster. The related test statistic T and the cluster extent (in voxels) are given, as well as the other structures belonging to the cluster.

X	Y	Z	Hemisphere	Anatomical landmark	Extent	T	Other structures in cluster
Subcortical							
8	-20	4	Right	Thalamus	171	7.73	Midbrain, Substantia Nigra, Red Nucleus, Subthalamic Nucleus
-26	-12	4	Left	Putamen	86	6.78	Lateral Globus Pallidus, Claustrum, Insula
-20	8	-6	Left	Putamen	24	4.81	-
-22	4	8	Left	Putamen	23	5.12	-
24	-2	8	Right	Putamen	22	5.70	Lateral Globus Pallidus
-14	-12	-12	Left	Midbrain	122	5.90	Thalamus, Substantia Nigra, Subthalamic Nucleus
Frontal							
-48	10	46	Left	Pre- & Supplementary Motor Area	85	6.31	Precentral Gyrus, Middle Frontal Gyrus, Inferior Frontal Gyrus
-12	34	38	Left	Medial Frontal Gyrus	19	5.18	Superior Frontal Gyrus
-2	24	28	Left	Cingulate Gyrus	34	3.74	-
Temporal							
24	-36	-12	Right	Parahippocampal Gyrus	15	4.13	-
-46	-20	0	Left	Superior Temporal Gyrus	145	7.04	Precentral Gyrus, Insula, Postcentral Gyrus, Transverse Temporal Gyrus
66	-14	6	Right	Superior Temporal Gyrus	37	3.95	Postcentral Gyrus, Transverse Temporal Gyrus
-36	-50	-20	Left	Fusiform Gyrus	16	5.25	Cerebellum
Occipital							
-12	-50	0	Left	Lingual Gyrus	34	4.45	Parahippocampal Gyrus
Cerebellar							
-34	-54	-28	Left	Cerebellum	28	3.74	-
-22	-50	-30	Left	Cerebellum	21	5.15	-
14	-48	-16	Right	Cerebellum	15	3.58	-

Table 7.2 Brain regions showing significant *negative* correlations with the 10 atlas-based *right* STN ROIs. X, Y, and Z represent the coordinates (in atlas space) of the maximum response for each cluster. The related test statistic T and the cluster extent (in voxels) are given, as well as the other structures belonging to the cluster.

X	Y	Z	Hemisphere	Anatomical landmark	Extent	T	Other structures in cluster
Subcortical							
16	-26	-18	Right	Midbrain	22	-2.73	Substantia Nigra
2	-14	-28	Right	Pons	65	-2.70	Midbrain
Frontal							
42	-10	46	Right	Precentral Gyrus	31	-2.70	Primary Motor Cortex, Pre- & Supplementary Motor Area, Middle Frontal Gyrus
16	44	16	Right	Medial Frontal Gyrus	17	-2.72	Anterior Cingulate
Parietal							
-52	-12	22	Left	Postcentral Gyrus	22	-2.72	Precentral Gyrus
Temporal							
28	-12	-16	Right	Parahippocampal Gyrus	35	-2.72	Amygdala
48	6	-28	Right	Superior Temporal Gyrus	19	-2.75	Middle Temporal Gyrus
-60	-20	-10	Left	Middle Temporal Gyrus	15	-2.75	-

7.3. Results

Table 7.3 Brain regions showing significant *positive* correlations with the 10 atlas-based *left* STN ROIs. X, Y, and Z represent the coordinates (in atlas space) of the maximum response for each cluster. The related test statistic *T* and the cluster extent (in voxels) are given, as well as the other structures belonging to the cluster.

X	Y	Z	Hemisphere	Anatomical landmark	Extent	<i>T</i>	Other structures in cluster
Subcortical							
-12	-14	2	Left	Thalamus	39	7.78	Midbrain, Substantia Nigra, Subthalamic Nucleus
12	8	6	Right	Caudate	44	5.71	Putamen
-18	2	10	Left	Putamen	41	4.57	-
30	-10	10	Right	Putamen	81	5.44	Lateral Globus Pallidus, Claustrum, Insula, Superior Temporal Gyrus, Transverse Temporal Gyrus
26	0	0	Right	Putamen	76	7.51	Lateral Globus Pallidus
6	-14	-6	Right	Midbrain	94	4.90	Thalamus, Substantia Nigra, Red Nucleus, Subthalamic Nucleus
Frontal							
12	4	64	Right	Medial Frontal Gyrus	16	3.97	Pre- & Supplementary Motor Area
Parietal							
-44	-36	26	Left	Inferior Parietal Lobule	21	4.13	-
Temporal							
-50	-18	2	Left	Superior Temporal Gyrus	16	3.82	-
Cerebellar							
-36	-50	-28	Left	Cerebellum	51	5.59	-
4	-64	-40	Right	Cerebellum	41	4.47	-

Table 7.4 Brain regions showing significant *negative* correlations with the 10 atlas-based *left* STN ROIs. X, Y, and Z represent the coordinates (in atlas space) of the maximum response for each cluster. The related test statistic *T* and the cluster extent (in voxels) are given, as well as the other structures belonging to the cluster.

X	Y	Z	Hemisphere	Anatomical landmark	Extent	<i>T</i>	Other structures in cluster
Subcortical							
18	-20	-14	Right	Midbrain	22	-2.71	Parahippocampal Gyrus
Frontal							
20	18	48	Right	Superior Frontal Gyrus	29	-2.71	Pre- & Supplementary Motor Area, Medial Frontal Gyrus, Cingulate Gyrus
22	34	46	Right	Superior Frontal Gyrus	23	-2.70	-
Temporal							
-18	-16	-16	Left	Parahippocampal Gyrus	18	-2.70	Hippocampus
-22	-26	-18	Left	Parahippocampal Gyrus	15	-2.72	-
18	-6	-20	Right	Parahippocampal Gyrus	15	-2.72	Midbrain, Amygdala

7.3.2 Segregation of STN regions

The results of the reverse-regression procedure for the right and left STN of all subjects can be seen in Figure 7.4. The masks of the STN ROIs in the atlas are depicted in Figure 7.4(a).

Figure 7.4(b) represents the functional connectivity of the STN voxels to the motor cortical areas (precentral cortex, primary motor cortex, premotor and supplementary motor area). The posterior lateral part of the STN shows the highest functional connectivity to the motor areas, while the anterior medial part yields the lowest values. Figure 7.4(c) shows the functional connectivity of the STN voxels to the limbic areas (amygdala, hippocampus, parahippocampal gyrus, anterior cingulate, cingulate cortex). Especially for the left STN, the posterior lateral part reveals the lowest functional connectivity to the limbic areas, while the anterior medial part returns higher values.

7.4 Discussion

7.4.1 Current findings

In this study, we investigated the functional connectivity of the STN, based on correlations in resting state BOLD-signal time series between the STN ROIs and other brain structures. Cluster maps displayed connections to various cortical and subcortical structures. The resulting significant clusters for the atlas-based STN ROIs predominantly belonged to a few major groups of structures, such as subcortical structures, the frontal cortex, temporal cortex, and cerebellum.

The results of the manually segmented STN ROIs in general exhibited more clusters in subcortical and cerebellar areas, frontal and temporal cortex, but also showed significant clusters in the parietal cortex. Because the atlas-based analysis involved 10 STNs on both sides, instead of 3 right STNs or 4 left STNs (for which manual segmentation was possible), the decrease in the number of significant clusters is probably due to an increasingly strict Student t test with an increasing number of subjects. This is supported by the cluster map for the atlas-based STN of only the subjects for whom manual segmentation was possible, which yielded more significant clusters than the test over all 10 subjects. There was no evidence for an asymmetrical distribution of functional connectivity of the STN, as many connections were found bilaterally and showed up in the results of both right and left STN ROIs.

With respect to the level of segregation of the functional parts of the STN, the posterior lateral part of the STN shows the highest functional connectivity to the motor areas, while the anterior medial part yields the lowest values. For the connectivity of the STN voxels to the limbic areas, it is the other way around: the posterior lateral part reveals the lowest functional connectivity to the limbic areas, while the anterior medial part returns higher values.

Below, we will discuss the correspondence of these connectivity results with existing literature, consequent implications for DBS procedures, and possible future work.

7.4.2 Correspondence of findings with existing literature

Motor circuit

With respect to the motor circuit, tracer studies in non-human primates reported on connections between the STN and the primary motor cortex, premotor and supplementary motor area, and the somatosensory cortex [140, 216, 218, 232]. Deeper in the brain, we would expect to find connectivity with the striatum, the central and ventrolateral GPe, the ventrolateral GPI, and the thalamus [57, 158, 233, 262, 274].

Our functional connectivity analysis indeed yielded significant clusters for primary motor cortex (precentral gyrus), pre- and supplementary motor area, and somatosensory cortex (postcentral gyrus). In addition, the expected gray matter nuclei were also discovered to be strongly connected to the STN.

Associative and limbic circuits

Concerning the associative loop, we expected correlations in activity between the STN and the orbitofrontal and dorsolateral prefrontal cortex, as well as the thalamus, the nucleus accumbens, the ventral part of the putamen and caudate nucleus, the ventral pallidum, the ventral tegmental area, and the medial part of the substantia nigra pars reticulata [5, 6, 7, 57, 140, 215, 233]. Again, the gray matter nuclei present in the atlas were all found to be functionally connected to the STN. Cortically, the analysis resulted in significant clusters in the frontal, temporal, and parietal cortex.

With regard to the limbic function, the literature reported on connections with the (para)limbic cortical areas such as the anterior cingulate and the medial orbitofrontal cortex [6]. Subcortically, the limbic circuit includes the nucleus accumbens, ventral pallidum, ventral tegmental area, substantia nigra pars reticulata, globus pallidus, thalamus, hippocampus and amygdala [6, 129]. Cortical areas such as the anterior cingulate, the medial frontal, and the parahippocampal gyrus indeed showed significant regression coefficients. The same holds for all gray matter nuclei present in the atlas that belong to the limbic loop.

Segregation of motor and non-motor regions of the STN

Review articles on STN anatomy, circuitry and function [136, 298] have reported on a tripartite functional subdivision of the STN. The medial tip of the STN is devoted to the limbic circuit and an associative part is located ventrolaterally, while the motor subterritory is positioned at the dorsolateral side of the STN.

The subdivision results based on our reverse-regression experiment (Figure 7.4) display a mediolateral gradient in motor and limbic connectivity. The highest connectivity to the motor regions is obtained in the posterior lateral STN part, where we expect the STN motor part, while the anterior medial part (the supposed limbic tip) contains voxels that are more connected to the limbic ROIs. The gradient indicates some level of separation between the functional parts of the STN, though no complete segregation of motor and non-motor regions was found. The latter supports the idea of open circuits, in which all pathways are partially integrated within the STN.

7.4.3 Clinical perspective

The reported consistency between the existing literature on anatomical tracing and electrophysiological studies validates the performed functional connectivity measurements based on resting state BOLD fMRI. Our study thus indicates that it might be feasible to determine STN functional connectivity in a noninvasive way. The voxel-wise assessment of motor and limbic connectivity per STN voxel proves that there is some separation between the different functional STN parts. The high motor connectivity found in the dorsolateral STN part underlines that the therapeutic target for STN DBS is located in this dorsolateral part. To compensate for interindividual variations in motor connectivity, functional connectivity analysis based on resting state BOLD fMRI may assist in optimization of the patient-specific planning of the DBS procedure.

7.4.4 Future work

There are multiple ways in which the functional connectivity pipeline employed in this study can still be improved. First, we found some atlas regions to be correlated that have not been reported in previous literature, such as the red nucleus, midbrain in general, pons, medulla, insula, claustrum, paracentral lobule, parietal lobules, supramarginal gyrus, lingual gyrus, and cerebellum. Some of the structures may be considered as the output of the motor circuit, for example the midbrain, while the insula might to some extent be associated with the limbic loop. However, most of these areas are located close to brain parts that are known to be connected to the STN, so the connectivity found in this study might be due to small shifts in the data.

These inaccuracies could be caused by BOLD image deformation, a too coarse spatial resolution, spatial smoothing, the inherent physiologic nature (i.e., point-spread function of the neurovascular coupling mechanism) of the spatial response, or registration errors. The image registration would benefit from the acquisition of whole-brain three-dimensional T_1 -weighted data, besides the currently used data

with limited field-of-view or thick slices. The STN segmentations are sensitive to registration inaccuracies and we could also question the inherent precision of the atlas-based STN ROI, as it contains two parts for the left STN that are only connected by a corner point. The use of atlas-based STN segmentations could be avoided by using 7-T MRI for the localization of the STN [1, 61, 62].

Future work should include a larger number of healthy subjects to increase the robustness of the analysis. Data acquisition should include a whole-brain three-dimensional structural scan with isotropic voxels to facilitate image registration and preferably also susceptibility-weighted image data at high field-strength, to enable high-resolution manual segmentations of the STN for all subjects. Ultimately, similar work remains to be done on PD patients to be able to validate the direct and reverse-regression procedure for DBS planning.

Moreover, it would be useful to compare the functional connectivity found in this study with STN structural connectivity based on diffusion-weighted MRI data and probabilistic fiber tracking [51]. In addition, all available information per voxel of the STN (functional connectivity, structural connectivity, local diffusion profile) could be collected in order to achieve more robust results on the level of segregation of the motor, associative, and limbic STN parts. To this end, the connectivity of each STN voxel to the different functional parts of other gray matter nuclei such as the globus pallidus and striatum could also be considered [22].

7.4.5 Conclusions

We have shown that the resting state functional connectivity of the STN in healthy subjects corresponds with the anatomical connectivity that has been described in literature. Areas that have been described in relation to all three STN circuits, namely motor, associative and limbic, were found to be correlated in activity. In addition, functional connectivity measures per STN voxel, based on the correlation with motor and limbic areas, showed promising results with respect to segregation in functional STN parts. Although improvements could be made on the amount of data and the segmentation and registration steps, this work is an important step towards the use of functional connectivity analysis for segmentation of the STN motor part, which in turn could optimize patient-specific STN DBS planning.

7.5 Acknowledgments

We thank Maarten Vaessen, Marc Geerlings, and Alia Lemkaddem for technical support.



General discussion

*When one does a thing, it appears good, otherwise one would not write it.
Only later comes reflection, and one discards or accepts the thing.
Time is the best censor, and patience a most excellent teacher.*

Frédéric Chopin

8.1 Contributions

In this section, we will summarize the studies presented in this thesis. Subsequently, a non-exhaustive list of methodological considerations and possible areas of future research will be provided, to put our experiments into a broader perspective.

The context and outline of our research was sketched in **Chapter 1**. We investigated whether it is possible to distinguish the different functional STN parts based on three types of connectivity information, inferred from noninvasive MRI protocols. First, clustering of local diffusion information, derived from diffusion MRI, was examined. The second experiment involved an analysis of the structural connectivity of the STN, based on probabilistic fiber tracking using diffusion MRI data. The third and last feature we studied was functional connectivity based on resting state BOLD fMRI.

To understand the clinical context of this thesis, some basic knowledge on Parkinson's disease and its mechanism, symptoms and possible therapies is necessary. We provided this medical and anatomical background information in **Chapter 2**. In addition, in **Chapter 3**, we explained the technical concepts necessary to understand our experiments, such as diffusion and functional MRI, and brain connectivity modes. In **Chapter 4**, we gave a systematic overview of noninvasive methods already available to target the STN, together with their benefits and drawbacks. The review did not lead to a straightforward conclusion on which targeting technique to use; identification of the dorsolateral and motor part of the STN remained an open question.

In an attempt to answer this question, the research presented in this thesis has led to more insight in the possibilities of noninvasive imaging to identify the STN and its functional parts. The main contributions of the remaining chapters can be summarized as follows:

- **Chapter 5** addressed the feasibility studies that were done on clustering of local diffusion profiles within the STN region, in order to segment the different functional parts of the STN. For the first experiments, post mortem rat brain diffusion MRI data were acquired using a 9.4-T system and a long acquisition time. We began with a visual inspection of these data, which perfectly illustrated the added value of complex HARDI ODFs as compared to second-order DTI glyphs, in order to distinguish different kinds of diffusion profiles within the STN region. To expand upon this manual segmentation method, we implemented k-means and graph cuts clustering, using the traditional \mathbb{L}_2 norm on the ODFs as a distance measure. Because the weighing of different orders of diffusion information in this distance measure was not trivial, we developed a specialized distance measure, the so-called Sobolev norm. This norm does not

only take into account the amplitudes of the diffusion profiles, but also their extrema. We illustrated the principle of this norm with an analytical example, and tuned the parameters using 1-nearest neighbor classification on synthetic diffusion MRI data. During a k-means experiment on the same synthetic and also real thalamus diffusion MRI data, our Sobolev norm outperformed the \mathbb{L}_2 norm in both cases. In the synthetic data, the percentage of correctly classified voxels was much higher for the Sobolev norm than for the \mathbb{L}_2 norm. With respect to the thalamus data, the results of the Sobolev norm were less dependent on the weight factor between diffusion and spatial information, which alleviates the issue of the tuning of this parameter. In conclusion, in this chapter we introduced a specialized distance measure for HARDI clustering which enables better clustering of gray matter structures in the brain.

- In **Chapter 6**, we were the first to investigate the full structural connectivity of the STN based on diffusion MRI data of healthy volunteers. We performed probabilistic fiber tracking with the STN as a seed region. The resulting streamline counts were used in three different connectivity measures. The first and second measure counted the streamlines per target region, with the second measure normalized for streamline length whereas the first was not. These measures were calculated per subject and subsequently tested for significance over all subjects. The third measure was calculated from the streamline count per voxel, cumulated for all volunteers. From these results, we obtained a complete description of the structural connectivity of the STN, corresponding well to topical literature on STN projections. Furthermore, assessing the results per voxel of the STN seed region, we discovered a gradient in motor connectivity within the STN. While going from the medial to the lateral STN, the connectivity to the motor cortical areas increases, confirming the expected lateral location of the STN motor part. Finally, the connectivity analysis produced the first evidence for the existence of the “hyperdirect” pathway from the motor cortex to the STN in humans, which is very useful for future research into stimulation targets. The results of this chapter indicated that it is possible to localize the STN motor part as target for deep brain stimulation using structural connectivity information based on noninvasive diffusion MRI measurements. However, further evaluation is necessary before specific stimulation of this motor part, which would increase motor effects and reduce side effects, can be tested.
- **Chapter 7** showed the results of another brain connectivity mode, namely functional connectivity. We were the first to analyze the full functional connectivity of the STN based on resting state BOLD fMRI. For this experiment, data from the same group of healthy volunteers were used. We defined the STN, both manually segmented and based on the Talairach atlas, as a seed region for correlation analysis. Specifically, we performed linear regression with

the time-series signal, averaged over the STN, as the principal regressor. As such, for each voxel in the brain, we obtained the “goodness-of-fit”, a measure for how well the fMRI time-series signal in that voxel resembled the average STN signal. This measure was statistically tested over all subjects and thresholded on cluster size. The resulting significantly correlated clusters provided us with a complete description of the STN’s resting state functional connectivity, which again corresponded with the expectations based on available literature. Moreover, we performed two reverse regressions, with the average time-series signals in motor and limbic areas as principal regressors, respectively. The results were analyzed for each STN voxel separately and also showed medio-lateral gradients in functional connectivity within the STN. The lateral STN part exhibited more motor connectivity, while the medial part seemed to be more functionally connected to limbic brain areas, as was to be expected from literature. In summary, this chapter showed that functional connectivity analysis is another noninvasive method to find the motor part of the STN. This knowledge can also be applied to enhance deep brain stimulation procedures after thorough evaluation.

8.2 Methodological considerations

As described by Jones and Cercignani [162], it is a challenge to obtain reliable and robust results from diffusion MRI. The methods described in this thesis can certainly be improved upon, to avoid some of the pitfalls that were described. Naturally, this also holds for the functional MRI processing. In this section, we will discuss some of the issues and possible enhancements.

8.2.1 Localization and registration

Accurate localization of the STN is of great importance for the definition of the ROI for clustering of diffusion profiles, the starting points for fiber tracking, and the seed region for functional connectivity analysis. In the first case, small errors can result in imprecise seed point definition for clustering and incorrect clusters. Regarding the fibers, starting the tracking from erroneous points can give rise to wrong streamlines and therefore false positives and negatives in structural connectivity measurements. Finally, an inaccurate seed region definition for the correlation analysis could lead to less strong true correlations, or yield false correlations.

With respect to the localization, manual segmentation on T_2 -weighted images acquired at 3 T is very dependent on the observer that performed the segmentation, and hindered by the low image contrast in the region under consideration. High-

field-strength images, for example at 7 T, which display the STN and its boundaries in a more conspicuous manner, could help to resolve this issue [1, 61, 62], although not yet in a clinical setting.

The other method used to identify the STN ROI, employing a digitized brain atlas, is very sensitive to the used atlas to begin with. Furthermore, the registration procedure undoubtedly introduces inaccuracies. The image registration would benefit from an additional measurement, namely a whole-brain three-dimensional T_1 -weighted scan, in addition to the limited FOV or thick slices of the current data. We did not include such a measurement in the healthy volunteer acquisitions because of the already long scanning time. However, the isotropic voxels of such a scan and coverage of the whole brain would facilitate the registration procedure.

Moreover, the affine registration procedure that was used to match the different diffusion-weighted images to the b_0 data could be replaced by a nonlinear method, including correction of the gradient direction. We used available software from FSL to do this registration, but nonlinear transformations and corrections of the gradients would probably lead to a more accurate registration and therefore more reliable fiber tracking.

In addition, errors are not only caused by the registration procedure, but they are also inherent to image acquisition, such as deformation caused by the MRI sequence (for example EPI), the selected spatial resolution, and spatial smoothing (either during image processing or due to the intrinsic point-spread function of the data).

8.2.2 Diffusion MRI and structural connectivity

As for the reconstruction of the diffusion profiles used for this research, we used the Q-ball reconstruction method that was commonly used a couple of years ago. Meanwhile, HARDI research has progressed rapidly and new modeling techniques have appeared. As we acquired data on a single spherical shell, we could not use techniques that require a dense sampling of \mathbf{q} -space, such as diffusion spectrum imaging (DSI). With our acquisition, we could have used spherical deconvolution (SD), but the drawback of this method is that it is rather sensitive to noise. However, in the past years, multiple constrained SD methods that impose regularization have been developed [79, 304, 306], so this method would now be a serious option, because it directly recovers the fiber orientation (fODF), instead of an estimate of the dODF as in Q-ball.

With respect to the clustering of the diffusion profiles, even though we introduced the new Sobolev norm to get rid of the weighting parameters for the different SH orders, we still experience problems with parameter tuning. The parameters γ and t in the Sobolev norm seem to have opposite effects on the resulting norm: while γ

determines to what extent details on the sphere are taken into account, resulting in more details at higher orders of SH, t on the other hand results in more smoothing of the data at higher orders. Furthermore, because the Sobolev norm and the \mathbb{L}_2 norm (with $\gamma = 0$) are not scaled to operate in the same range, the weight factor between spatial and diffusion information does not have exactly the same influence in these two cases.

Regarding the structural connectivity, some improvements would be possible as well. We could improve our connectivity measurements by introducing quantitative dimensionless measures. In addition, we should check the sensitivity to the STN seed region of our fiber tracking and structural connectivity algorithm. However, the most important issue is the validation of the probabilistic fiber tracking. How do we know which connections are “real” and how can we detect outliers? In general, neuronal tracing or electrophysiological studies have described projections, but not the trajectories along which the projections run.

8.2.3 Functional MRI and functional connectivity

Considering the functional MRI experiments and the resulting functional connectivity data, it would be wise to investigate the sensitivity of the method to the STN seed region used for the correlation analysis. In addition, the results of such an analysis are very much dependent on the general linear model that was used. Therefore, the influence of the regressors included in (for example the global mean) or excluded from (for example low-frequency drift) our GLM should be subject to research. The results could then also be compared with a model-free method such as ICA (independent component analysis) [203].

Furthermore, the BOLD fMRI mechanism itself has some shortcomings. The contrast between activated and resting states is small and the temporal resolution poor. Because of the nature of the hemodynamic response, the position of the detected signal might not correspond to the actual activation site. Another interpretation issue is that of clusters displaying negative correlation with the seed region. Are they mainly introduced by the regression with the global mean, as suggested by Murphy et al. [214], and if not, what does the negative correlation mean?

8.2.4 Ethical considerations

In most experiments described in Chapter 5 we made use of animal data. The necessary brains were excised from rats that had been perfused transcardially after cardiovascular research, approved by the Institutional Ethical Review Committee for animal experiments of Maastricht University. We considered it justifiable to use the

brains of sacrificed rats that would otherwise be disposed of.

For a small part of Chapter 5 and for Chapter 6 and 7, we used MRI data of healthy volunteers. Written informed consent was obtained from all volunteers prior to participation, and the study was approved by the Medical Ethics Committee of Maastricht University Medical Center. Because the conventional MRI acquisition did not involve any safety risks for the subjects (only the risk of coincidental findings), we considered it justifiable to use healthy volunteers for these experiments. Healthy volunteers can better endure the long scanning time than Parkinson's patients, and are less likely to cause motion artifacts.

8.3 Future work

As a final objective for this research we foresee a patient-specific MRI scan of the brain, including a visible STN, with a segmentation of the three different functional STN parts as an overlay. The steps necessary to bridge the gap between this ultimate goal and the preliminary results presented in this thesis will be discussed in this section.

8.3.1 Imaging for deep brain stimulation

First of all, we need to validate the robustness of our results with respect to the STN subdivision. This could be realized by acquiring and processing more volunteer data, in order to test the reproducibility of our results. Moreover, it is possible to combine the structural connectivity data, functional connectivity information, and local diffusion profiles within the STN into one feature vector for clustering, in order to achieve a more robust estimate of the different functional STN parts.

When sufficiently robust results are obtained in healthy volunteers, this research should find its way to the clinic. We started this project using rat data and performed subsequent studies on human volunteer data. However, to assess the added value for deep brain stimulation operations, it is necessary to conduct experiments on data from Parkinson's disease patients that are eligible for DBS as well. Initially, we should examine the clinical requirements for the necessary MRI acquisitions. Of course, the scanning procedure for Parkinson's patients should be as short as possible, to reduce both the burden for the patient and the occurrence of (movement) artifacts. However, the scans should also provide us with useful and complete MR data. To search for the right compromise between these two objectives, we should first answer some questions on the accuracy and reproducibility of the volunteer data used in this thesis.

With respect to the diffusion-weighted imaging, we could for example ask ourselves whether we really should consider 128 unique gradient directions. Would less directions, for example 54 or 80, also be enough for the probabilistic fiber tracking and structural connectivity calculation, as suggested by Prčkovska et al. [250]? The required number of gradient directions could be tested by subsampling the set of diffusion-weighted measurements from our healthy volunteers. Furthermore, new techniques to reconstruct fiber crossings for a sparse diffusion MRI acquisition are being developed [174, 175, 249]. In addition, is the one b_0 measurement that was used for the structural connectivity study good enough or should we use an average of multiple unweighted images? As we did acquire five b_0 measurements for each volunteer, we could examine this issue as well. Also for the fMRI experiments, we can wonder whether the time series of 200 time points with TR 2.2s could be shortened while still yielding reliable functional connectivity maps [307]. This claim could be tested by dividing each series into two (or more) parts and assessing the reproducibility of the functional connectivity results based on the separate parts.

In contrast to adaptations in the image acquisition, we could also consider other processing techniques for our data. For fiber tracking maps based on diffusion MRI, track-density imaging (TDI) seems to be very promising [56]. With this post-processing procedure, spatial resolution can be gained, in order to reveal fiber structures beyond the resolution of the acquired imaging voxel.

Besides, the issues with respect to diffusion and functional MRI described above could possibly be bypassed by state-of-the-art anatomical imaging techniques such as very-high-field-strength imaging. Abosch et al. combined a 7-T scanner with multiple acquisition schemes and images contrast, which enabled them to clearly separate the STN from the SN and distinguish internal thalamic nuclei at 7 T [1]. Cho et al. also showed that 7-T MRI is superior to 1.5 and 3 T for visualization of DBS targeting structures such as STN and GPi [61]. In addition, these authors visualized the SN at 7 T in 10 PD patients and 9 control subjects and identified morphological changes that could be used as a diagnostic marker for PD [62]. However, thus far, 7-T MR imaging is not applicable in a clinical setting.

When the image acquisition is optimized for clinical practice, we will be able to investigate the structural and functional connectivity properties of the STN and its functional parts in PD patients. Naturally, the first thing to examine is whether these properties of the STN are the same in patients with Parkinson's. Hopefully, the results, whether the same or different, will support our hypothesis that noninvasive MR imaging techniques such as dMRI and fMRI facilitate patient-specific mapping of the STN parts with high motor connectivity and/or low limbic connectivity. Subsequently, this knowledge can be used to optimize motor effects and reduce side effects involved with DBS, and to decrease the time necessary for the planning and implantation phases of this operation.

8.3.2 Deep brain stimulation and other therapies for Parkinson's

On top of studies focusing on enhanced imaging for deep brain stimulation, other, complementary, lines of research exist. For instance, McIntyre's group modeled the voltage distribution generated by deep brain stimulation and the consequent volume of activated tissue after stimulation [54, 208]. This knowledge could be used to produce electrodes that facilitate an asymmetric stimulation volume, adapted to patient-specific conditions.

Besides the STN, the medial globus pallidus (GPi) is also a possible target for deep brain stimulation in Parkinson's disease. A recent study by Follett et al. reported similar motor improvement after GPi and STN stimulation [105]. The same study also showed an argument against switching to pallidal instead of subthalamic stimulation in order to reduce side effects, namely that patients after GPi stimulation remain more dependent on medication than after STN DBS. However, the GPi is successfully used for deep brain stimulation procedures in patients with dystonia [205] and Huntington's disease [212]. For the latter, the lateral globus pallidus (GPe) is a possible target as well [190]. In addition, different thalamic nuclei have been identified as effective stimulation sites: the anterior nucleus for epilepsy [104], the centromedian-parafascicular nuclear complex (CM-Pf) for Tourette syndrome [324], and the ventral intermediate nucleus (Vim) for tremor [191]. The imaging methods described in this thesis could also be applied to enhance identification of the stimulation targets within the globus pallidus and thalamus.

Other researchers zoom in on the underlying anatomical and physiological mechanisms of deep brain stimulation of the STN. For example, Temel et al. found that STN DBS inhibits 5-HT (serotonine) neurons in the limbic system, which in turn evokes the depression-related behavioral changes after DBS [299]. Recently, Tan et al. proposed that the mechanism behind the vulnerability to depressions in PD in general and after STN DBS is probably a combination of alterations to the 5-HT system and altered network activity within the basal ganglia [294]. On the other hand, Janssen et al. concentrated on the motor circuit and investigated the feasibility of motor cortex stimulation to evoke a spatially specific response within the motor part of the STN [155].

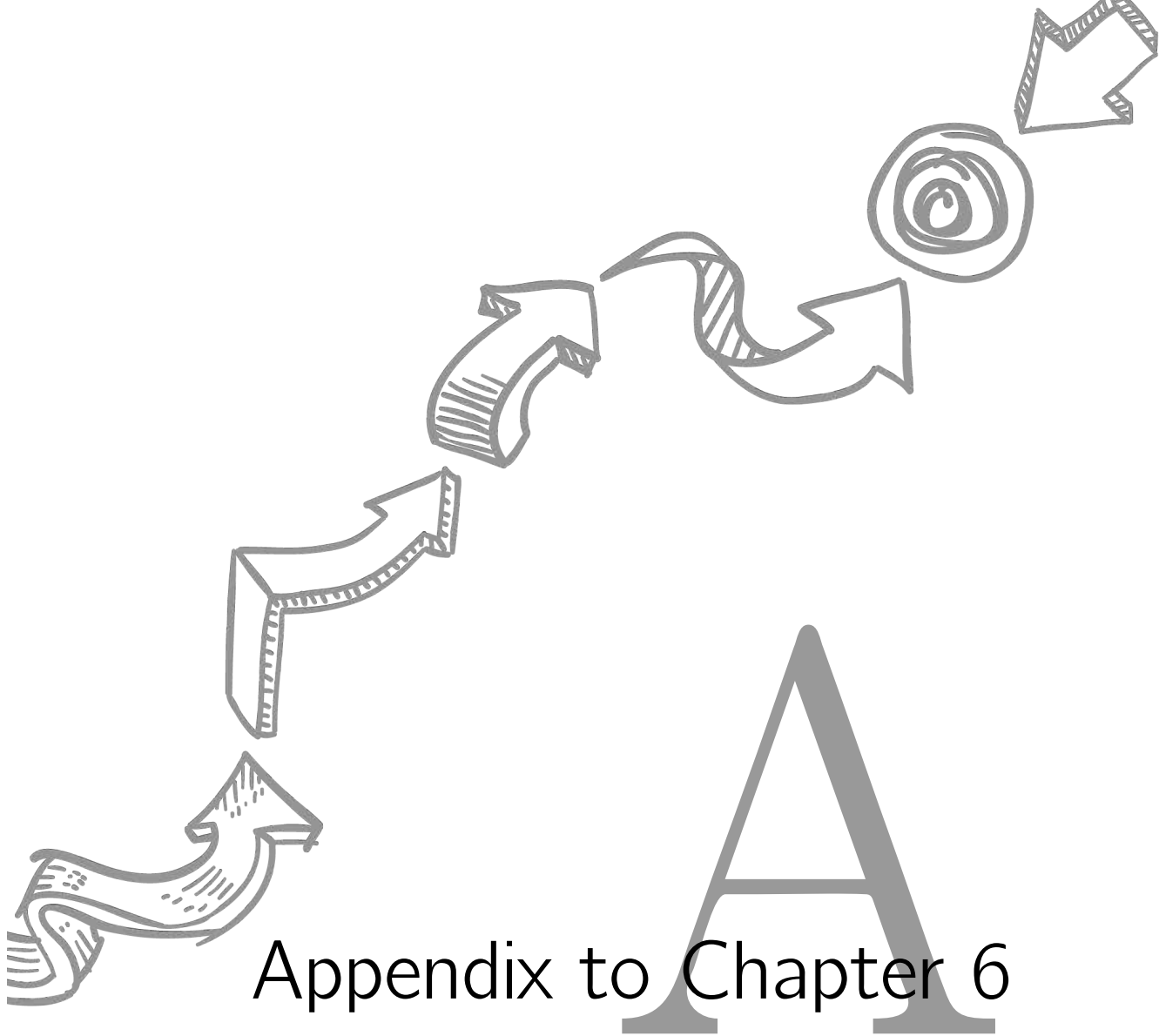
However, in the long term, transcranial magnetic stimulation (TMS) instead of deep brain stimulation might be a treatment option for Parkinson's disease. In 2008 already, Arias-Carrión considered rTMS (repetitive TMS) to play a role in the neurogenesis of dopaminergic neurons to replace degenerated neurons in PD [15]. Maybe replacing neurons as a whole is not even necessary. A recent study by LeWitt et al. reported on a successful clinical trial applying gene therapy to Parkinson's disease [189]. PD patients exhibit a shortage of the neurotransmitter GABA in their subthalamic nucleus. LeWitt et al. used a virus to infect neurons with

a gene to increase the GABA production, resulting in a mild reduction of symptoms in half of the cases.

In any case, taking into account the rapid current and future developments with respect to imaging and other improvements for deep brain stimulation in Parkinson's disease, which hopefully result in more effective and less burdensome treatment options for PD patients, it is unavoidable that this thesis will be outdated relatively soon.

8.4 Conclusion

The aim of the research presented in this thesis was to determine the possibility to distinguish the different functional parts of the STN based on noninvasive MR imaging. We experimented with three modes of connectivity information for the STN region. First, we clustered local diffusion profiles and found that although HARDI shows diffusion profiles with different complexities within the STN, parameter tuning for the clustering remains rather difficult. Second, we analyzed the structural connectivity of the STN, based on fiber tracking derived from diffusion MRI. This experiment confirmed the connections expected from literature, and showed high structural connectivity to the motor cortical areas in the lateral STN, which is useful information for targeting of the STN motor part. Finally, we also studied the functional connectivity of the STN based on resting state BOLD fMRI. This study again verified the expected connections of the STN and also showed high motor connectivity in the lateral STN, while the medial part exhibited higher functional connectivity to the limbic system. In spite of the fact that many methodological improvements can be thought of, this research has brought us one step closer to specific stimulation of the motor part of the STN in patients with Parkinson's disease.



Appendix to Chapter 6

Table A.1 Regions significantly connected to the *right* STN after a *t*-test on C_1 , using $n_{\text{subjects}} = 8$ and $\alpha = 0.05$.

Region of interest	<i>p</i> value	Region of interest	<i>p</i> value
Right Brainstem, Midbrain	0.000	Left Uncus, Brodmann area 28	0.021
Right Thalamus	0.000	Right Medial Globus Pallidus (GPi)	0.022
Right Cingulate Gyrus	0.000	Right Transverse Temporal Gyrus	0.023
Right Substantia Nigra	0.001	Right Brodmann area 11 (orbitofrontal cortex)	0.023
Right Thalamus Ventral Posterior Lateral Nucleus	0.002	Right Anterior Cingulate	0.024
Right Caudate	0.003	Left Brainstem, Pons	0.025
Right Red Nucleus	0.004	Right Brodmann area 47 (orbitofrontal cortex)	0.025
Right Putamen	0.004	Right Rectal Gyrus	0.026
Right Thalamus Ventral Posterior Medial Nucleus	0.004	Right Posterior Cingulate, Brodmann area 30	0.026
Right Thalamus Ventral Anterior Nucleus	0.005	Left Posterior Cingulate, Brodmann area 29	0.027
Right Brodmann area 6 (pre- & supplementary motor area)	0.006	Right Inferior Temporal Gyrus	0.027
Right Hypothalamus	0.006	Left Medial Frontal Gyrus	0.028
Right Thalamus Ventral Lateral Nucleus	0.007	Left Thalamus Ventral Anterior Nucleus	0.030
Right Lateral Globus Pallidus (GPe)	0.007	Right Insula	0.030
Right Superior Temporal Gyrus	0.007	Left Anterior Cingulate, Brodmann area 24	0.030
Right Claustrum	0.007	Right Mammillary Body	0.030
Right Thalamus Lateral Posterior Nucleus	0.007	Left Fusiform Gyrus	0.031
Left Limbic Lobe, Brodmann area 24	0.008	Left Red Nucleus	0.031
Right Occipital Lobe, Lingual Gyrus, Brodmann area 18	0.009	Right Limbic Lobe, Brodmann area 24	0.032
Right Anterior Cingulate, Brodmann area 25	0.010	Right Posterior Cingulate, Brodmann area 29	0.033
Right Medial Frontal Gyrus	0.010	Left Subcallosal Gyrus	0.035
Left Hippocampus	0.011	Left Thalamus, Pulvinar	0.036
Left Brainstem, Midbrain	0.011	Left Brodmann area 6 (pre- & supplementary motor area)	0.037
Limbic Lobe, Parahippocampal Gyrus	0.012	Right Hippocampus	0.037
Left Brodmann area 47 (orbitofrontal cortex)	0.013	Left Inferior Frontal Gyrus	0.039
Cerebellum	0.013	Right Limbic Lobe	0.039
Left Insula	0.013	Right Thalamus	0.039
Right Inferior Frontal Gyrus	0.014	Left Thalamus	0.039
Left Thalamus Medial Dorsal Nucleus	0.014	Right Anterior Cingulate, Brodmann area 24	0.040
Left Mammillary Body	0.014	Right Subcallosal Gyrus, Brodmann area 34	0.041
Left Putamen	0.015	Left Posterior Cingulate, Brodmann area 30	0.042
Right Brainstem	0.015	Right Brodmann area 13	0.044
Right Superior Frontal Gyrus	0.016	Right Middle Temporal Gyrus	0.044
Right Thalamus, Mammillary Body	0.017	Left Cingulate Gyrus	0.045
Right Thalamus, Medial Dorsal Nucleus	0.019	Inter-Hemispheric Precuneus	0.045
Right Anterior Cingulate, Brodmann area 33	0.019	Right Occipital Lobe, Lingual Gyrus	0.046
Left Limbic Lobe	0.019	Left Parietal Lobe, Precuneus	0.047
Left Posterior Cingulate	0.020	Left Anterior Cingulate, Brodmann area 25	0.048
Right Parahippocampal Gyrus	0.020	Right Fusiform Gyrus	0.049
Left Middle Frontal Gyrus	0.020	Right Thalamus, Anterior Nucleus	0.049
Right Occipital Lobe, Lingual Gyrus, Brodmann area 19	0.021	Right Brodmann area 2 (primary somatosensory)	0.050
Left Claustrum	0.021		

Table A.2 Regions significantly connected to the *left* STN after a *t*-test on C_1 , using $n_{\text{subjects}} = 8$ and $\alpha = 0.05$.

Region of interest	<i>p</i> value	Region of interest	<i>p</i> value
Left Brainstem, Midbrain	0.000	Left Occipital Lobe, Lingual Gyrus, Brodmann area 19	0.024
Left Thalamus	0.000	Left Thalamus, Medial Dorsal Nucleus	0.024
Left Substantia Nigra	0.000	Limbic Lobe, Parahippocampal Gyrus	0.024
Left Thalamus, Mammillary Body	0.001	Left Brodmann area 10 (orbitofrontal cortex)	0.025
Left Mammillary Body	0.001	Left Superior Temporal Gyrus	0.026
Left Red Nucleus	0.001	Left Cingulate Gyrus	0.030
Left Thalamus Ventral Anterior Nucleus	0.001	Right Thalamus Lateral Dorsal Nucleus	0.031
Left Thalamus Pulvinar	0.002	Left Anterior Cingulate, Brodmann area 32	0.033
Left Thalamus Ventral Posterior Lateral Nucleus	0.002	Left Subcallosal Gyrus	0.033
Right Thalamus Anterior Nucleus	0.003	Right Occipital Lobe, Lingual Gyrus, Brodmann area 19	0.034
Left Posterior Cingulate	0.003	Right Posterior Cingulate, Brodmann area 29	0.034
Left Thalamus Ventral Posterior Medial Nucleus	0.003	Right Precentral Gyrus	0.034
Left Thalamus Ventral Lateral Nucleus	0.004	Right Uncus	0.035
Right Red Nucleus	0.004	Right Anterior Cingulate, Brodmann area 32	0.036
Right Brainstem, Midbrain	0.005	Right Anterior Cingulate	0.037
Right Thalamus Medial Dorsal Nucleus	0.005	Left Medial Frontal Gyrus	0.037
Left Posterior Cingulate, Brodmann area 29	0.005	Left Uncus, Brodmann area 34	0.037
Right Thalamus Midline Nucleus	0.006	Right Lateral Globus Pallidus (GPe)	0.037
Right Parahippocampal Gyrus	0.007	Left Uncus, Brodmann area 28	0.038
Left Hypothalamus	0.007	Left Inferior Frontal Gyrus	0.039
Left Thalamus Lateral Posterior Nucleus	0.007	Left Parahippocampal Gyrus	0.039
Left Putamen	0.008	Left Claustrum	0.039
Right Insula	0.009	Left Brodmann area 13	0.040
Right Subcallosal Gyrus, Brodmann area 34	0.010	Left Precentral Gyrus	0.040
Right Posterior Cingulate	0.011	Right Thalamus, Mammillary Body	0.041
Left Medial Globus Pallidus (GPI)	0.012	Left Sub-lobar Gray Matter, Lateral Geniculum Body	0.041
Hypothalamus	0.015	Left Amygdala	0.041
Right Caudate	0.015	Right Limbic Lobe	0.041
Right Limbic Lobe, Brodmann area 30	0.017	Left Brodmann area 11 (orbitofrontal cortex)	0.042
Left Caudate	0.017	Right Posterior Cingulate, Brodmann area 30	0.043
Cerebellum	0.018	Left Superior Frontal Gyrus	0.044
Right Anterior Cingulate, Brodmann area 24	0.018	Left Uncus	0.045
Right Fusiform Gyrus	0.019	Right Brodmann area 3 (primary somatosensory)	0.045
Left Frontal Lobe	0.020	Left Limbic Lobe	0.045
Left Insula	0.020	Right Anterior Cingulate, Brodmann area 33	0.046
Right Claustrum	0.020	Left Occipital Lobe, Lingual Gyrus	0.046
Left Lateral Globus Pallidus (GPe)	0.021	Left Anterior Cingulate, Brodmann area 24	0.047
Right Thalamus Pulvinar	0.023	Left Inferior Temporal Gyrus	0.047
Left Subcallosal Gyrus, Brodmann area 34	0.023	Right Hippocampus	0.048
Right Thalamus	0.023	Right Posterior Cingulate, Brodmann area 23	0.049
Right Mammillary Body	0.024		

Table A.3 Regions significantly connected to the *right* STN after a *t*-test on C_2 , using $n_{\text{subjects}} = 8$ and $\alpha = 0.05$.

Region of interest	p value	Region of interest	p value
Right Brainstem, Midbrain	0.000	Right Anterior Cingulate	0.019
Right Thalamus	0.000	Left Thalamus, Medial Dorsal Nucleus	0.019
Right Cingulate Gyrus	0.001	Right Middle Temporal Gyrus	0.019
Right Substantia Nigra	0.001	Right Transverse Temporal Gyrus	0.019
Right Thalamus Ventral Posterior Lateral Nucleus	0.001	Left Posterior Cingulate	0.019
Right Red Nucleus	0.003	Left Parahippocampal Gyrus	0.019
Right Caudate	0.003	Left Fusiform Gyrus	0.021
Right Thalamus Ventral Anterior Nucleus	0.003	Right Thalamus Anterior Nucleus	0.022
Right Thalamus Medial Dorsal Nucleus	0.004	Left Middle Frontal Gyrus	0.026
Right Thalamus Ventral Posterior Medial Nucleus	0.004	Left Medial Frontal Gyrus	0.028
Right Hypothalamus	0.004	Right Posterior Cingulate, Brodmann area 30	0.028
Right Putamen	0.004	Right Limbic Lobe, Brodmann area 24	0.029
Right Superior Temporal Gyrus	0.005	Left Anterior Cingulate, Brodmann area 24	0.030
Right Brodmann area 6 (pre- & supplementary motor area)	0.006	Right Rectal Gyrus	0.030
Right Claustrum	0.007	Left Thalamus Ventral Anterior Nucleus	0.030
Cerebellum	0.007	Right Mammillary Body	0.030
Right Thalamus Lateral Posterior Nucleus	0.008	Right Brodmann area 47 (orbitofrontal cortex)	0.031
Right Occipital Lobe, Lingual Gyrus, Brodmann area 18	0.008	Right Insula	0.031
Right Medial Globus Pallidus (GPI)	0.009	Left Subcallosal Gyrus	0.031
Right Thalamus Ventral Lateral Nucleus	0.009	Left Brodmann area 6 (pre- & supplementary motor area)	0.036
Right Medial Frontal Gyrus	0.010	Left Posterior Cingulate, Brodmann area 29	0.036
Left Limbic Lobe, Brodmann area 24	0.010	Left Uncus, Brodmann area 28	0.038
Right Lateral Globus Pallidus (GPe)	0.010	Right Occipital Lobe, Lingual Gyrus, Brodmann area 30	0.040
Left Limbic Lobe	0.010	Left Parietal Lobe, Precuneus	0.040
Left Insula	0.011	Right Subcallosal Gyrus, Brodmann area 34	0.041
Right Parahippocampal Gyrus	0.011	Left Brodmann area 47 (orbitofrontal cortex)	0.041
Left Hippocampus	0.012	Right Subcallosal Gyrus	0.041
Right Hippocampus	0.012	Left Anterior Cingulate, Brodmann area 25	0.042
Right Limbic Lobe	0.012	Right Uncus	0.043
Right Brodmann area 11 (orbitofrontal cortex)	0.013	Right Thalamus	0.043
Right Thalamus, Mammillary Body	0.014	Left Posterior Cingulate, Brodmann area 30	0.044
Left Mammillary Body	0.014	Left Cingulate Gyrus	0.045
Right Anterior Cingulate, Brodmann area 25	0.015	Left Caudate	0.045
Right Occipital Lobe, Lingual Gyrus, Brodmann area 19	0.015	Left Subcallosal Gyrus, Brodmann area 34	0.046
Right Superior Frontal Gyrus	0.016	Right Thalamus Pulvinar	0.047
Right Inferior Frontal Gyrus	0.016	Right Brodmann area 13	0.047
Left Inferior Frontal Gyrus	0.016	Inter-Hemispheric Precuneus	0.047
Right Inferior Temporal Gyrus	0.017	Right Sub-lobar Gray Matter, Lateral Geniculum Body	0.047
Left Putamen	0.017	Right Anterior Cingulate, Brodmann area 24	0.048
Right Anterior Cingulate, Brodmann area 33	0.017	Right Thalamus, Medial Geniculum Body	0.050
Right Fusiform Gyrus	0.018	Right Uncus, Brodmann area 28	0.050
Left Claustrum	0.018		

Table A.4 Regions significantly connected to the *left* STN after a *t*-test on C_2 , using $n_{\text{subjects}} = 8$ and $\alpha = 0.05$.

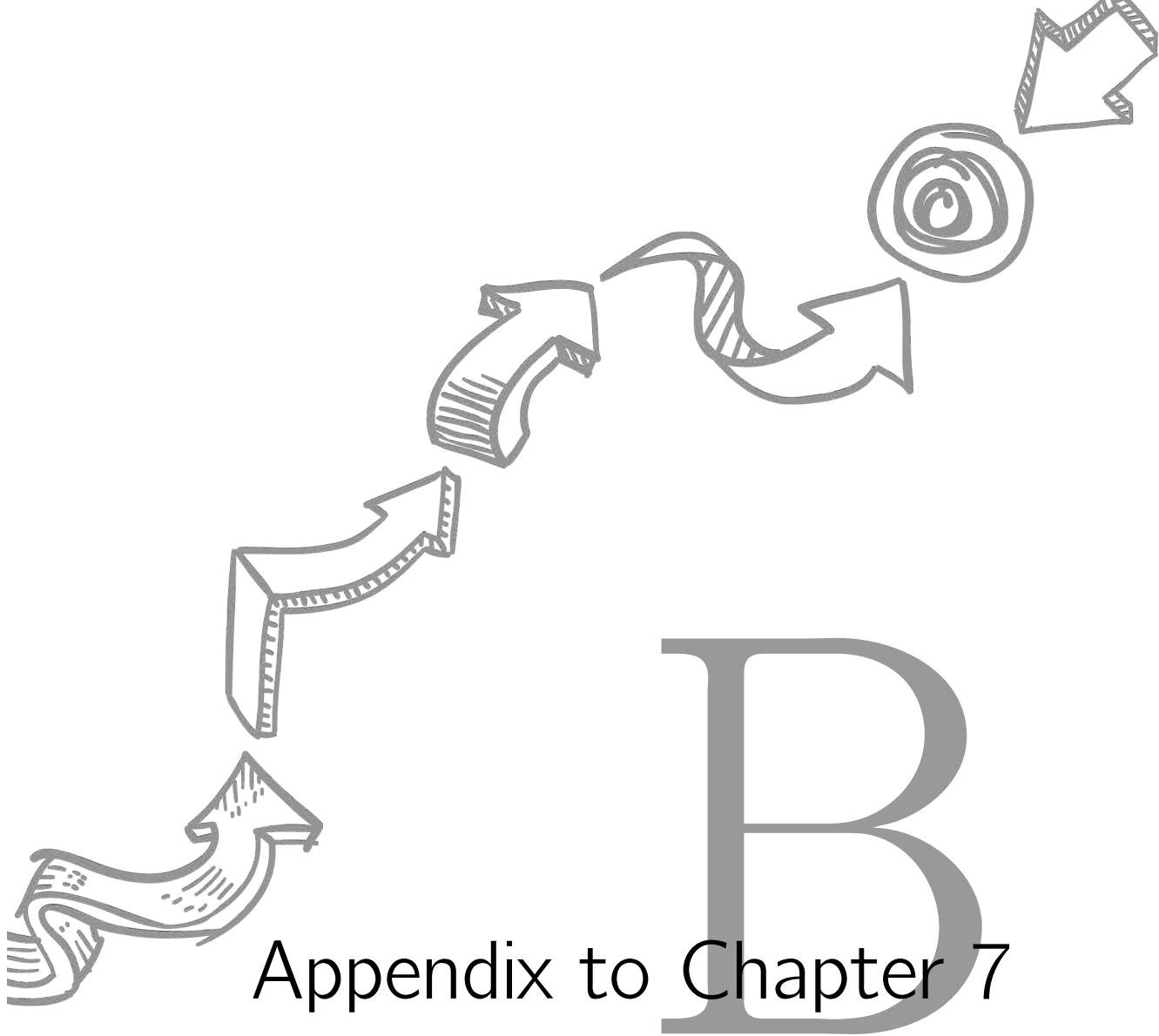
Region of interest	<i>p</i> value	Region of interest	<i>p</i> value
Left Brainstem, Midbrain	0.000	Right Mammillary Body	0.024
Left Thalamus	0.000	Right Thalamus Pulvinar	0.025
Left Substantia Nigra	0.000	Right Limbic Lobe	0.025
Left Thalamus, Mammillary Body	0.001	Left Brodmann area 10 (orbitofrontal cortex)	0.026
Left Mammillary Body	0.001	Right Posterior Cingulate, Brodmann area 23	0.026
Left Thalamus Ventral Posterior Lateral Nucleus	0.001	Left Subcallosal Gyrus	0.026
Left Thalamus Medial Dorsal Nucleus	0.002	Left Cingulate Gyrus	0.027
Left Red Nucleus	0.002	Right Fusiform Gyrus	0.028
Left Posterior Cingulate, Brodmann area 29	0.002	Left Posterior Cingulate, Brodmann area 30	0.028
Left Thalamus Ventral Posterior Medial Nucleus	0.002	Left Superior Temporal Gyrus	0.028
Left Thalamus Pulvinar	0.002	Right Thalamus Lateral Dorsal Nucleus	0.029
Left Posterior Cingulate	0.003	Right Precentral Gyrus	0.030
Left Medial Globus Pallidus (GPI)	0.004	Right Occipital Lobe, Lingual Gyrus, Brodmann area 19	0.030
Right Thalamus Anterior Nucleus	0.005	Right Anterior Cingulate	0.030
Right Red Nucleus	0.005	Left Uncus	0.032
Left Thalamus Ventral Anterior Nucleus	0.006	Left Occipital Lobe, Lingual Gyrus	0.032
Right Brainstem Midbrain	0.006	Right Claustrum	0.033
Right Parahippocampal Gyrus	0.007	Left Inferior Frontal Gyrus	0.033
Right Thalamus Medial Dorsal Nucleus	0.007	Left Parahippocampal Gyrus	0.035
Left Thalamus Ventral Lateral Nucleus	0.007	Left Brodmann area 13	0.035
Left Putamen	0.007	Left Limbic Lobe	0.036
Right Thalamus Midline Nucleus	0.007	Left Uncus, Brodmann area 28	0.036
Left Thalamus Lateral Posterior Nucleus	0.008	Left Anterior Cingulate, Brodmann area 32	0.036
Left Hypothalamus	0.008	Left Medial Frontal Gyrus	0.037
Right Subcallosal Gyrus, Brodmann area 34	0.009	Left Brainstem, Midbrain, Medial Geniculum Body	0.037
Right Posterior Cingulate	0.010	Left Precentral Gyrus	0.037
Cerebellum	0.011	Right Anterior Cingulate, Brodmann area 32	0.038
Right Anterior Cingulate, Brodmann area 33	0.011	Right Posterior Cingulate, Brodmann area 29	0.040
Left Insula	0.012	Left Superior Frontal Gyrus	0.042
Left Frontal Lobe	0.013	Left Anterior Cingulate, Brodmann area 24	0.042
Hypothalamus	0.013	Left Occipital Lobe, Lingual Gyrus	0.042
Left Caudate	0.013	Right Thalamus	0.043
Right Insula	0.015	Right Brainstem, Pons	0.043
Left Occipital Lobe, Lingual Gyrus, Brodmann area 19	0.015	Left Occipital Lobe, Lingual Gyrus, Brodmann area 18	0.044
Left Uncus, Brodmann area 34	0.017	Right Thalamus, Mammillary Body	0.044
Right Caudate	0.017	Right Uncus	0.044
Left Lateral Globus Pallidus (GPe)	0.018	Right Limbic Lobe, Sub-Gyral	0.045
Left Subcallosal Gyrus, Brodmann area 34	0.018	Right Hippocampus	0.046
Right Limbic Lobe, Brodmann area 30	0.018	Right Limbic Lobe, Brodmann area 24	0.046
Right Anterior Cingulate, Brodmann area 24	0.020	Left Amygdala	0.048
Limbic Lobe, Parahippocampal Gyrus	0.022	Right Brodmann area 3 (primary somatosensory)	0.048
Left Sub-lobar Gray Matter, Lateral Geniculum Body	0.022	Left Middle Temporal Gyrus	0.049
Left Claustrum	0.023		

Table A.5 Regions connected to the *right* STN based on the total probability map, thresholded at $C_3 \geq 0.10$.

Region of interest	Connectivity	Region of interest	Connectivity
Right Thalamus Ventral Posterior Lateral Nucleus	246.77	Right Brodmann area 3 (primary somatosensory)	0.60
Right Thalamus Ventral Posterior Medial Nucleus	161.61	Right Lateral Globus Pallidus (GPe)	0.60
Right Thalamus Lateral Posterior Nucleus	130.62	Right Anterior Cingulate, Brodmann area 25	0.57
Right Hypothalamus	103.55	Right Sub-lobar Gray Matter, Lateral Geniculum Body	0.54
Right Substantia Nigra	76.47	Left Thalamus Pulvinar	0.54
Right Red Nucleus	68.39	Right Thalamus	0.52
Right Thalamus Ventral Lateral Nucleus	63.19	Right Subcallosal Gyrus, Brodmann area 25	0.50
Right Thalamus, Mammillary Body	61.56	Right Thalamus, Anterior Nucleus	0.49
Right Mammillary Body	58.67	Left Thalamus, Ventral Posterior Medial Nucleus	0.49
Right Thalamus	42.09	Left Subcallosal Gyrus, Brodmann area 25	0.45
Right Limbic Lobe, Brodmann area 24	26.86	Right Frontal Lobe	0.42
Right Brainstem, Midbrain, Medial Geniculum Body	23.89	Left Thalamus Lateral Posterior Nucleus	0.42
Right Brainstem, Midbrain	23.23	Left Thalamus Anterior Nucleus	0.40
Right Thalamus Pulvinar	14.44	Left Thalamus	0.36
Right Subcallosal Gyrus	9.41	Right Parahippocampal Gyrus	0.35
Right Midbrain	7.14	Right Limbic Lobe	0.34
Right Brodmann area 4 (primary motor)	5.87	Left Thalamus Midline Nucleus	0.33
Right Thalamus, Medial Geniculum Body	4.40	Left Red Nucleus	0.33
Right Subcallosal Gyrus, Brodmann area 34	3.34	Left Thalamus Mammillary Body	0.32
Right Subcallosal Gyrus, Brodmann area 34	3.31	Right Putamen	0.32
Right Cingulate Gyrus	2.83	Left Limbic Lobe, Brodmann area 24	0.30
Right Caudate	2.82	Left Anterior Cingulate	0.29
Right Subcallosal Gyrus	2.50	Left Thalamus, Ventral Lateral Nucleus	0.27
Left Mammillary Body	1.87	Left Thalamus, Medial Dorsal Nucleus	0.27
Right Medial Frontal Gyrus	1.79	Right Uncus, Brodmann area 28	0.26
Right Anterior Cingulate	1.63	Left Subthalamic Nucleus	0.26
Left Anterior Cingulate, Brodmann area 25	1.62	Left Brainstem, Midbrain	0.25
Right Medial Globus Pallidus (GPi)	1.57	Right Brodmann area 13	0.25
Right Amygdala	1.53	Right Middle Frontal Gyrus	0.24
Hypothalamus	1.48	Limbic Lobe, Uncus	0.24
Right Brodmann area 6 (pre- & supplementary motor area)	1.47	Right Postcentral Gyrus	0.24
Left Subcallosal Gyrus	1.20	Left Caudate	0.24
Right Precentral Gyrus	1.09	Left Thalamus, Lateral Dorsal Nucleus	0.24
Right Paracentral Lobule	0.94	Right Hippocampus	0.23
Superior Frontal Gyrus	0.90	Right Uncus	0.22
Right Thalamus Ventral Anterior Nucleus	0.85	Right Thalamus Lateral Dorsal Nucleus	0.18
Left Hypothalamus	0.85	Left Cingulate Gyrus	0.18
Right Uncus, Brodmann area 34	0.69	Right Limbic Lobe, Brodmann area 35	0.17
Right Subcallosal Gyrus, Brodmann area 13	0.68	Left Substantia Nigra	0.12
Right Superior Frontal Gyrus	0.64	Right Brainstem, Pons	0.10
Right Brainstem	0.63	Left Thalamus Ventral Anterior Nucleus	0.10
Right Thalamus, Medial Dorsal Nucleus	0.62	Right Thalamus, Midline Nucleus	0.10
Left Thalamus, Ventral Posterior Lateral Nucleus	0.60	Right Uncus, Brodmann area 36	0.10
Right Limbic Lobe	0.60		

Table A.6 Regions connected to the *left* STN based on the total probability map, thresholded at $C_3 \geq 0.10$.

Region of interest	Connectivity	Region of interest	Connectivity
Left Thalamus Ventral Posterior Lateral Nucleus	217.57	Right Thalamus Pulvinar	0.54
Left Thalamus Ventral Posterior Medial Nucleus	130.56	Left Brainstem, Pons	0.51
Left Hypothalamus	126.33	Left Thalamus Lateral Dorsal Nucleus	0.48
Left Mammillary Body	120.62	Right Cingulate Gyrus	0.46
Left Red Nucleus	99.85	Left Superior Frontal Gyrus	0.44
Left Thalamus Lateral Posterior Nucleus	95.79	Right Subcallosal Gyrus	0.41
Left Substantia Nigra	78.85	Left Anterior Cingulate	0.40
Left Thalamus, Mammillary Body	73.32	Right Thalamus Lateral Posterior Nucleus	0.37
Hypothalamus	59.96	Left Limbic Lobe	0.33
Left Thalamus	39.55	Left Hippocampus	0.32
Left Limbic Lobe, Brodmann area 24	38.68	Right Thalamus, Mammillary Body	0.29
Left Thalamus Ventral Lateral Nucleus	37.34	Right Thalamus Ventral Posterior Medial Nucleus	0.29
Left Brainstem Midbrain	29.94	Left Frontal Lobe	0.29
Left Thalamus Pulvinar	8.32	Right Substantia Nigra	0.29
Left Thalamus Anterior Nucleus	5.01	Left Brodmann area 13	0.29
Left Paracentral Lobule	4.50	Right Thalamus Ventral Posterior Lateral Nucleus	0.28
Left Brainstem, Midbrain, Medial Geniculum Body	4.34	Left Lateral Globus Pallidus (GPe)	0.28
Right Limbic Lobe, Brodmann area 24	4.09	Left Middle Frontal Gyrus	0.26
Right Mammillary Body	3.95	Right Occipital Lobe, Lingual Gyrus, Brodmann area 30	0.25
Left Subcallosal Gyrus	2.73	Right Thalamus	0.25
Left Brodmann area 4 (primary motor)	2.65	Left Parahippocampal Gyrus	0.22
Left Brodmann area 3 (primary somatosensory)	2.16	Left Putamen	0.21
Left Caudate	1.95	Right Limbic Lobe, Brodmann area 30	0.19
Left Brodmann area 6 (pre- & supplementary motor area)	1.80	Left Postcentral Gyrus	0.19
Left Thalamus Ventral Anterior Nucleus	1.54	Right Thalamus Medial Dorsal Nucleus	0.18
Left Thalamus Medial Dorsal Nucleus	1.48	Right Thalamus Lateral Dorsal Nucleus	0.15
Right Red Nucleus	1.41	Right Hypothalamus	0.15
Right Thalamus	1.26	Parahippocampal Gyrus	0.13
Left Limbic Lobe, Brodmann area 25	1.22	Left Amygdala	0.13
Left Cingulate Gyrus	1.12	Right Brainstem, Midbrain, Medial Geniculum Body	0.13
Right Brainstem	1.06	Right Thalamus Ventral Lateral Nucleus	0.12
Left Brodmann area 5 (somatosensory association)	0.99	Left Precentral Gyrus	0.12
Left Thalamus, Medial Geniculum Body	0.97	Right Subthalamic Nucleus	0.11
Left Sub-lobar Gray Matter, Lateral Geniculum Body	0.92	Right Caudate	0.11
Left Subcallosal Gyrus, Brodmann area 25	0.89	Right Medial Frontal Gyrus	0.11
Left Subcallosal Gyrus, Brodmann area 34	0.89	Right Brainstem, Pons	0.10
Left Medial Frontal Gyrus	0.85	Right Thalamus, Anterior Nucleus	0.10
Left Claustrum	0.83	Left Occipital Lobe, Lingual Gyrus, Brodmann area 30	0.10
Right Limbic Lobe	0.73	Left Limbic Lobe	0.10
Left Medial Globus Pallidus (GPI)	0.66	Left Parietal Lobe, Brodmann area 40	0.10
Right Brainstem, Midbrain	0.65		



Appendix to Chapter 7

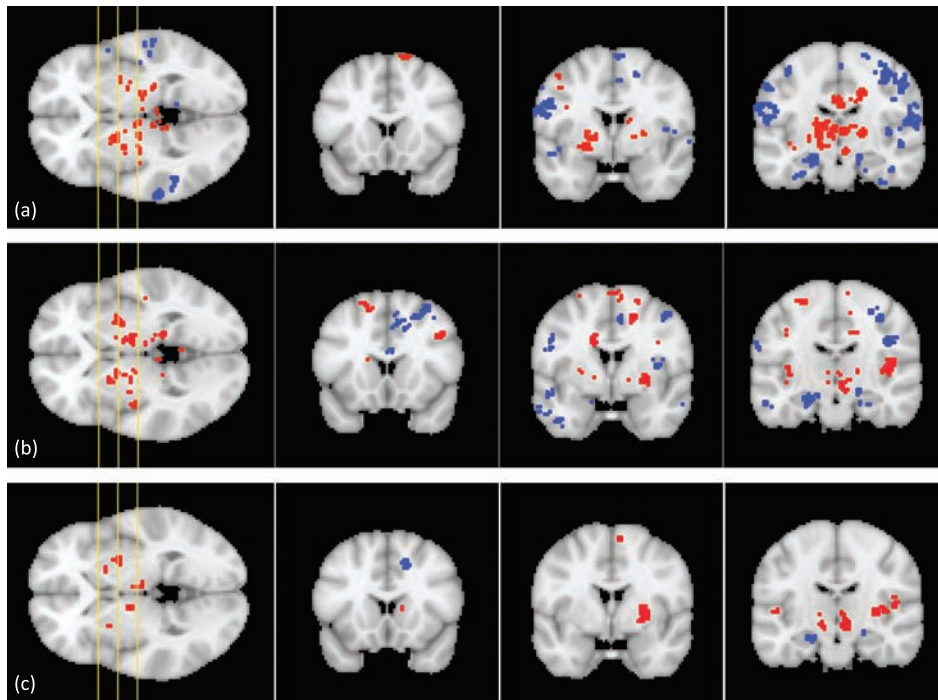


Figure B.1 Significant clusters for the left STN ROI, shown on three coronal slices of the MNI152 template. (a) 4 manually segmented left STN ROIs. (b) 4 atlas-based left STN ROIs (same volunteers). (c) All 10 atlas-based left STN ROIs. The yellow lines on the axial image on the left-hand side show the position of the coronal slices. Red clusters exhibit positive regression coefficients, while blue clusters yield negative coefficients.

Table B.1 Brain regions showing significant *positive* correlation with the manually segmented *right* STN ROIs. X, Y, and Z represent the coordinates (in atlas space) of the maximum response for each cluster. The related test statistic *T* and the cluster extent (in voxels) are given, as well as the other structures belonging to the cluster.

X	Y	Z	Hemisphere	Anatomical landmark	Extent	<i>T</i>	Other structures in cluster
Subcortical							
-8	-14	-2	Left	Thalamus	201	70.80	Midbrain, Substantia Nigra, Subthalamic Nucleus, Parahippocampal Gyrus
24	-30	12	Right	Thalamus	304	88.18	Caudate, Midbrain, Substantia Nigra, Red Nucleus, Pons
-24	-14	-2	Left	Lateral Globus Pallidus (GPe)	24	17.33	Putamen
22	-2	-8	Right	Lateral Globus Pallidus (GPe)	30	911.33	Putamen, Medial Globus Pallidus
-16	-4	-4	Left	Medial Globus Pallidus (GPi)	20	49.44	Lateral Globus Pallidus
-36	-4	6	Left	Clastrum	190	33.13	Precentral Gyrus, Primary Motor Cortex, Pre- & Supplementary Motor Area, Inferior Frontal Gyrus, Insula, Superior Temporal Gyrus, Middle Temporal Gyrus
-18	-34	-34	Left	Pons	44	22.34	Cerebellum
-16	-28	-30	Left	Pons	17	9.55	-
6	-28	-34	Right	Pons	82	30.06	Midbrain
Frontal							
-42	-12	42	Left	Precentral Gyrus	33	32.04	-
-34	-6	50	Left	Precentral Gyrus	21	15.38	Pre- & Supplementary Motor Area, Middle Frontal Gyrus
-50	0	22	Left	Pre- & Supplementary Motor Area	26	11.03	Precentral Gyrus, Inferior Frontal Gyrus
62	4	26	Right	Pre- & Supplementary Motor Area	270	91.04	Precentral Gyrus, Middle Frontal Gyrus, Inferior Frontal Gyrus
18	-4	70	Right	Pre- & Supplementary Motor Area	111	20.95	Precentral Gyrus, Superior Frontal Gyrus, Middle Frontal Gyrus, Medial Frontal Gyrus
-22	2	68	Left	Superior Frontal Gyrus	50	44.03	Precentral Gyrus, Pre- & Supplementary Motor Area, Middle Frontal Gyrus
-10	-6	58	Left	Medial Frontal Gyrus	38	50.96	Pre- & Supplementary Motor Area, Superior Frontal Gyrus
0	-2	44	Left	Cingulate Gyrus	442	65.18	Pre- & Supplementary Motor Area, Superior Frontal Gyrus, Middle Frontal Gyrus, Medial Frontal Gyrus
-2	-32	32	Left	Cingulate Gyrus	244	51.75	Posterior Cingulate
-42	-22	2	Left	Insula	379	65.64	Postcentral Gyrus, Primary Somatosensory Cortex, Inferior Parietal Lobule, Superior Temporal Gyrus, Middle Temporal Gyrus, Transverse Temporal Gyrus
-36	-28	14	Left	Insula	22	10.34	Transverse Temporal Gyrus
40	2	14	Right	Insula	21	15.13	-
Parietal							
58	-28	32	Right	Inferior Parietal Lobule	169	25.76	Insula, Postcentral Gyrus, Primary Somatosensory Cortex, Supramarginal Gyrus, Superior Temporal Gyrus, Transverse Temporal Gyrus
Temporal							
-38	-24	-28	Left	Parahippocampal Gyrus	29	25.53	Fusiform Gyrus
-64	-4	-4	Left	Superior Temporal Gyrus	15	14.93	Middle Temporal Gyrus
46	-24	6	Right	Superior Temporal Gyrus	33	98.80	Insula, Transverse Temporal Gyrus
54	-10	-16	Right	Middle Temporal Gyrus	15	20.93	Superior Temporal Gyrus
-58	-16	-28	Left	Fusiform Gyrus	19	9.77	Inferior Temporal Gyrus
44	-38	-18	Right	Fusiform Gyrus	21	10.01	Parahippocampal Gyrus, Cerebellum
Cerebellar							
-2	-46	2	Left	Cerebellum	56	18.80	Posterior Cingulate, Parahippocampal Gyrus
-14	-46	-44	Left	Cerebellum	18	14.74	-
8	-56	-30	Right	Cerebellum	29	17.84	-
44	-48	-38	Right	Cerebellum	22	38.45	-

Table B.2 Brain regions showing significant *negative* correlation with the manually segmented *right* STN ROIs. X, Y, and Z represent the coordinates (in atlas space) of the maximum response for each cluster. The related test statistic *T* and the cluster extent (in voxels) are given, as well as the other structures belonging to the cluster.

X	Y	Z	Hemisphere	Anatomical landmark	Extent	<i>T</i>	Other structures in cluster
Subcortical							
-12	-32	4	Left	Thalamus	39	-2.73	Parahippocampal Gyrus
12	-24	-2	Right	Thalamus	24	-2.77	Midbrain
2	-16	-12	Right	Midbrain	16	-2.81	-
-8	-48	-38	Left	Pons	31	-2.73	Medulla, Cerebellum
-8	-24	-36	Left	Pons	20	-2.72	-
10	-38	-38	Right	Pons	31	-2.93	Cerebellum
Frontal							
42	-12	66	Right	Precentral Gyrus	65	-2.70	Primary Motor Cortex, Postcentral Gyrus, Primary Somatosensory Cortex
-62	-16	42	Left	Primary Motor Cortex	272	-2.70	Precentral Gyrus, Pre- & Supplementary Motor Area, Postcentral Gyrus, Primary Somatosensory Cortex, Inferior Parietal Lobule
56	-2	48	Right	Primary Motor Cortex	21	-2.76	Precentral Gyrus, Pre- & Supplementary Motor Area
-50	4	36	Left	Pre- & Supplementary Motor Area	88	-2.72	Precentral Gyrus, Middle Frontal Gyrus, Inferior Frontal Gyrus
-24	-6	50	Left	Pre- & Supplementary Motor Area	41	-2.79	Precentral Gyrus, Primary Motor Cortex, Middle Frontal Gyrus
-34	10	48	Left	Pre- & Supplementary Motor Area	18	-2.71	Precentral Gyrus, Middle Frontal Gyrus
40	10	32	Right	Inferior Frontal Gyrus	15	-2.74	Precentral Gyrus
-12	-14	26	Left	Cingulate Gyrus	19	-2.74	-
22	-8	40	Right	Cingulate Gyrus	151	-2.71	Caudate, Pre- & Supplementary Motor Area, Medial Frontal Gyrus, Cingulate Gyrus, Paracentral Lobule
12	6	46	Right	Cingulate Gyrus	30	-2.74	-
40	-18	18	Right	Insula	28	-2.74	Clastrum
Parietal							
46	-24	32	Right	Postcentral Gyrus	376	-2.70	Precentral Gyrus, Primary Motor Cortex, Primary Somatosensory Cortex, Inferior Parietal Lobule
58	-12	22	Right	Postcentral Gyrus	31	-2.74	Transverse Temporal Gyrus
-2	-30	56	Left	Somatosensory Association Cortex	112	-2.72	Pre- & Supplementary Motor Area, Medial Frontal Gyrus, Paracentral Lobule
-56	-30	36	Left	Inferior Parietal Lobule	27	-2.70	Postcentral Gyrus, Primary Somatosensory Cortex
-38	-32	46	Left	Inferior Parietal Lobule	15	-2.80	-
Temporal							
-16	-10	-16	Left	Parahippocampal Gyrus	27	-2.95	Amygdala
-30	-8	-26	Left	Parahippocampal Gyrus	21	-2.78	Hippocampus
-20	-22	-16	Left	Parahippocampal Gyrus	18	-2.75	-
22	-20	-14	Right	Parahippocampal Gyrus	83	-2.71	Midbrain, Amygdala
36	-26	-16	Right	Parahippocampal Gyrus	44	-2.74	Hippocampus
38	-28	-28	Right	Parahippocampal Gyrus	20	-2.71	Inferior Temporal Gyrus
34	-16	-34	Right	Parahippocampal Gyrus	17	-2.73	Inferior Temporal Gyrus
64	-38	16	Right	Superior Temporal Gyrus	65	-2.73	Middle Temporal Gyrus
52	-8	0	Right	Superior Temporal Gyrus	40	-2.71	Precentral Gyrus, Insula
-56	-38	-16	Left	Middle Temporal Gyrus	99	-2.73	Inferior Temporal Gyrus
-56	-10	-18	Left	Middle Temporal Gyrus	36	-2.70	Inferior Temporal Gyrus
-58	-38	0	Left	Middle Temporal Gyrus	19	-2.80	-
-58	-8	-10	Left	Middle Temporal Gyrus	18	-2.80	Superior Temporal Gyrus
66	-28	0	Right	Middle Temporal Gyrus	83	-2.73	Superior Temporal Gyrus
-38	-50	-12	Left	Fusiform Gyrus	53	-2.70	Hippocampus, Parahippocampal Gyrus
54	-40	-14	Right	Fusiform Gyrus	15	-3.43	Middle Temporal Gyrus, Inferior Temporal Gyrus
Cerebellar							
-34	-42	-24	Left	Cerebellum	71	-2.70	Parahippocampal Gyrus, Fusiform Gyrus
-20	-52	-28	Left	Cerebellum	70	-2.72	-
-18	-46	-14	Left	Cerebellum	27	-2.74	Parahippocampal Gyrus
-44	-52	-32	Left	Cerebellum	24	-2.91	-
24	-38	-20	Right	Cerebellum	211	-2.71	Hippocampus, Parahippocampal Gyrus, Fusiform Gyrus
24	-50	-40	Right	Cerebellum	74	-2.75	-
36	-44	-30	Right	Cerebellum	15	-3.00	-

Table B.3 Brain regions showing significant *positive* correlation with the manually segmented *left* STN ROIs. X, Y, and Z represent the coordinates (in atlas space) of the maximum response for each cluster. The related test statistic *T* and the cluster extent (in voxels) are given, as well as the other structures belonging to the cluster.

X	Y	Z	Hemisphere	Anatomical landmark	Extent	<i>T</i>	Other structures in cluster
Subcortical							
-8	-6	6	Left	Thalamus	582	49.67	Caudate, Putamen, Lateral Globus Pallidus, Medial Globus Pallidus, Midbrain, Red Nucleus, Subthalamic Nucleus
26	-30	0	Right	Thalamus	23	28.54	Midbrain, Parahippocampal Gyrus
-24	-2	4	Left	Putamen	146	22.64	Lateral Globus Pallidus, Medial Globus Pallidus
-28	-18	0	Left	Putamen	21	13.92	Lateral Globus Pallidus
-36	-20	4	Left	Clastrum	47	6.95	Insula, Superior Temporal Gyrus
-2	-38	-6	Left	Midbrain	36	6.28	-
4	-18	-10	Right	Midbrain	17	12.49	Red Nucleus
12	-38	-38	Right	Pons	18	10.98	Medulla
-28	-22	-10	Left	Hippocampus	23	11.69	Parahippocampal Gyrus
Frontal							
50	6	46	Right	Pre- & Supplementary Motor Area	20	6.66	Middle Frontal Gyrus
12	16	68	Right	Pre- & Supplementary Motor Area	15	5.45	Superior Frontal Gyrus, Middle Frontal Gyrus
-16	14	68	Left	Superior Frontal Gyrus	16	4.84	Pre- & Supplementary Motor Area, Middle Frontal Gyrus
-40	8	38	Left	Middle Frontal Gyrus	174	28.60	Precentral Gyrus, Pre- & Supplementary Motor Area, Inferior Frontal Gyrus
-16	4	52	Left	Medial Frontal Gyrus	36	9.34	Pre- & Supplementary Motor Area, Cingulate Gyrus
-14	-8	30	Left	Cingulate Gyrus	36	8.44	Thalamus, Caudate
-4	14	42	Left	Cingulate Gyrus	17	6.63	Medial Frontal Gyrus
16	-26	32	Right	Cingulate Gyrus	330	31.31	Posterior Cingulate
Temporal							
-6	-38	2	Left	Parahippocampal Gyrus	18	11.72	-
16	-34	-2	Right	Parahippocampal Gyrus	47	10.19	Midbrain
-48	-38	18	Left	Superior Temporal Gyrus	38	13.34	Insula
Cerebellar							
-8	-50	-22	Left	Cerebellum	302	17.02	Midbrain, Pons, Medulla
-38	-56	-40	Left	Cerebellum	69	8.50	-
26	-56	-40	Right	Cerebellum	33	10.50	-
42	-54	-32	Right	Cerebellum	18	5.91	-

Table B.4 Brain regions showing significant *negative* correlation with the manually segmented *left* STN ROIs. X, Y, and Z represent the coordinates (in atlas space) of the maximum response for each cluster. The related test statistic *T* and the cluster extent (in voxels) are given, as well as the other structures belonging to the cluster.

X	Y	Z	Hemisphere	Anatomical landmark	Extent	<i>T</i>	Other structures in cluster
Subcortical							
38	2	6	Right	Clastrum	21	-2.72	Insula
2	-24	-32	Right	Pons	27	-2.70	-
Frontal							
-28	-12	60	Left	Precentral Gyrus	67	-2.70	Primary Motor Cortex, Pre- & Supplementary Motor Area, Middle Frontal Gyrus, Postcentral Gyrus, Primary Somatosensory Cortex
-54	6	36	Left	Precentral Gyrus	18	-2.73	Pre- & Supplementary Motor Area, Middle Frontal Gyrus
32	-22	64	Right	Precentral Gyrus	542	-2.70	Primary Motor Cortex, Pre- & Supplementary Motor Area, Postcentral Gyrus, Primary Somatosensory Cortex, Inferior Parietal Lobule
60	-10	34	Right	Precentral Gyrus	263	-2.71	Primary Motor Cortex, Pre- & Supplementary Motor Area, Insula, Postcentral Gyrus, Primary Somatosensory Cortex, Inferior Parietal Lobule, Superior Temporal Gyrus, Transverse Temporal Gyrus
-6	-10	52	Left	Pre- & Supplementary Motor Area	42	-2.72	Medial Frontal Gyrus
8	-22	58	Right	Pre- & Supplementary Motor Area	74	-2.72	Medial Frontal Gyrus, Somatosensory Association Cortex, Paracentral Lobule
16	6	52	Right	Medial Frontal Gyrus	38	-2.75	Pre- & Supplementary Motor Area, Cingulate Gyrus
-46	-6	12	Left	Insula	18	-2.84	-
38	-4	8	Right	Insula	29	-2.71	Putamen, Claustrum
Parietal							
-54	-24	32	Left	Inferior Parietal Lobule	507	-2.71	Precentral Gyrus, Primary Motor Cortex, Pre- & Supplementary Motor Area, Inferior Frontal Gyrus, Postcentral Gyrus, Primary Somatosensory Cortex, Superior Temporal Gyrus, Transverse Temporal Gyrus
-52	-24	46	Left	Inferior Parietal Lobule	61	-2.71	Postcentral Gyrus, Primary Somatosensory Cortex
Temporal							
-22	-16	-22	Left	Parahippocampal Gyrus	40	-2.76	Hippocampus, Amygdala
-22	-40	-8	Left	Parahippocampal Gyrus	22	-2.72	-
-32	-12	-36	Left	Parahippocampal Gyrus	21	-2.75	Hippocampus, Inferior Temporal Gyrus
34	-24	-20	Right	Parahippocampal Gyrus	47	-2.71	-
28	-12	-22	Right	Parahippocampal Gyrus	30	-2.73	Lateral Globus Palidus, Amygdala
2	2	70	Right	Parahippocampal Gyrus	27	-2.74	Pre- & Supplementary Motor Area, Superior Frontal Gyrus, Medial Frontal Gyrus
34	-16	-34	Right	Parahippocampal Gyrus	26	-2.72	Inferior Temporal Gyrus
24	-28	-18	Right	Parahippocampal Gyrus	19	-2.75	Cerebellum
24	-22	-16	Right	Parahippocampal Gyrus	18	-2.73	Midbrain
40	-32	-24	Right	Parahippocampal Gyrus	17	-2.71	Cerebellum
-66	-32	10	Left	Superior Temporal Gyrus	306	-2.70	Middle Temporal Gyrus, Inferior Temporal Gyrus, Fusiform Gyrus, Cerebellum
-50	-2	-6	Left	Superior Temporal Gyrus	27	-2.71	Insula
-52	-12	-4	Left	Superior Temporal Gyrus	20	-2.75	Middle Temporal Gyrus
54	-26	-4	Right	Superior Temporal Gyrus	106	-2.75	Insula, Middle Temporal Gyrus, Transverse Temporal Gyrus
60	-38	14	Right	Superior Temporal Gyrus	27	-2.72	Middle Temporal Gyrus
54	-6	-6	Right	Superior Temporal Gyrus	26	-2.71	Middle Temporal Gyrus
-44	-28	12	Left	Transverse Temporal Gyrus	15	-2.77	Superior Temporal Gyrus
32	-36	-18	Right	Fusiform Gyrus	45	-2.70	Cerebellum
Cerebellar							
-28	-36	-22	Left	Cerebellum	24	-2.74	Parahippocampal Gyrus
10	-44	-10	Right	Cerebellum	195	-2.71	Parahippocampal Gyrus, Lingual Gyrus
50	-48	-26	Right	Cerebellum	29	-2.76	-

References

- [1] A. Abosch, E. Yacoub, K. Ugurbil, and N. Harel. An assessment of current brain targets for deep brain stimulation surgery with susceptibility-weighted imaging at 7 Tesla. *Neurosurgery*, 67(6):1745–1756, 2010. *Cited on pages 48, 89, 101, 122, 127, and 130.*
- [2] F. Acar, J. P. Miller, M. C. Berk, G. Anderson, and K. J. Burchiel. Safety of anterior commissure-posterior commissure-based target calculation of the subthalamic nucleus in functional stereotactic procedures. *Stereotactic and Functional Neurosurgery*, 85(6):287–291, 2007. *Cited on pages 50 and 56.*
- [3] J. Ahrens, B. Geveci, and C. Law. ParaView: An end-user tool for large data visualization. In C. Hansen and C. Johnson, editors, *The Visualization Handbook*. Elsevier, Amsterdam, 2005. *Cited on page 93.*
- [4] R. A. Alderden, M. D. Hall, and T. W. Hambley. The discovery and development of cisplatin. *Journal of Chemical Education*, 83(5):728, 2006. *Cited on page 2.*
- [5] G. E. Alexander and M. D. Crutcher. Functional architecture of basal ganglia circuits: neural substrates of parallel processing. *Trends in Neuroscience*, 13(7):266–271, 1990. *Cited on pages 9, 14, 100, and 120.*
- [6] G. E. Alexander, M. D. Crutcher, and M. R. DeLong. Basal ganglia-thalamocortical circuits: parallel substrates for motor, oculomotor, “prefrontal” and “limbic” functions. *Progress in Brain Research*, 85:119–146, 1990. *Cited on pages 14, 100, and 120.*
- [7] G. E. Alexander, M. R. DeLong, and P. L. Strick. Parallel organization of functionally segregated circuits linking basal ganglia and cortex. *Annual Review of Neuroscience*, 9(1):357–381, 1986. *Cited on pages 14, 100, and 120.*
- [8] F. Amtage, K. Henschel, B. Schelter, J. Vesper, J. Timmer, C. H. Lücking, and B. Hellwig. High functional connectivity of tremor related subthalamic neurons in Parkinson’s disease. *Clinical Neurophysiology*, 120(9):1755–1761, 2009. *Cited on page 108.*
- [9] A. Anderson and Z. Ding. Sub-voxel measurement of fiber orientation using high angular resolution diffusion tensor imaging. In *Proceedings of International Society for Magnetic Resonance in Medicine (ISMRM)*, volume 10, page 440, 2002. *Cited on page 27.*
- [10] J. Andersson, S. Smith, and M. Jenkinson. FNIRT - FMRIB’s non-linear image registration tool. In *Proceedings of Human Brain Mapping*, volume 14, 2008. *Cited on pages 63 and 86.*
- [11] Y. M. Andrade-Souza, J. M. Schwalb, C. Hamani, H. Eltahawy, T. Hoque, J. Saint-Cyr, and A. M. Lozano. Comparison of three methods of targeting the subthalamic nucleus for chronic stimulation in Parkinson’s disease. *Neurosurgery*, 56(Suppl 2):360–368, 2005. *Cited on pages 49, 51, and 56.*
- [12] Y. M. Andrade-Souza, J. M. Schwalb, C. Hamani, T. Hoque, J. Saint-Cyr, and A. M. Lozano. Comparison of 2-dimensional magnetic resonance imaging and 3-planar reconstruction methods for targeting the subthalamic nucleus in Parkinson disease. *Surgical Neurology*, 63(4):357–363, 2005. *Cited on pages 49, 51, and 56.*
- [13] O. J. Andy, M. F. Jurko, and F. R. Sias Jr. Subthalamotomy in treatment of parkinsonian tremor. *Journal of Neurosurgery*, 20:860–870, 1963. *Cited on page 13.*

References

- [14] B. A. Ardekani and A. H. Bachman. Model-based automatic detection of the anterior and posterior commissures on MRI scans. *NeuroImage*, 46(3):677–682, 2009. *Cited on pages 42 and 53.*
- [15] O. Arias-Carrión. Basic mechanisms of rTMS: implications in Parkinson’s disease. *International Archives of Medicine*, 1:2, 2008. *Cited on page 131.*
- [16] A. R. Aron, T. E. Behrens, S. Smith, M. J. Frank, and R. A. Poldrack. Triangulating a cognitive control network using diffusion-weighted magnetic resonance imaging (MRI) and functional MRI. *Journal of Neuroscience*, 27(14):3743–3752, 2007. *Cited on page 85.*
- [17] K. Ashkan, P. Blomstedt, L. Zrinzo, S. Tisch, T. Yousry, P. Limousin-Dowsey, and M. I. Hariz. Variability of the subthalamic nucleus: the case for direct MRI guided targeting. *British Journal of Neurosurgery*, 21(2):197–200, 2007. *Cited on pages 46, 47, 50, 51, 56, 89, and 112.*
- [18] T. Z. Aziz, D. Nandi, S. Parkin, X. Liu, N. Giladi, P. Bain, R. G. Gregory, C. Joint, R. B. Scott, and J. F. Stein. Targeting the subthalamic nucleus. *Stereotactic and Functional Neurosurgery*, 77(1–4):87–90, 2001. *Cited on pages 41, 42, and 50.*
- [19] T. Z. Aziz, D. Peggs, M. A. Sambrook, and A. R. Crossmann. Lesion of the subthalamic nucleus for the alleviation of 1-methyl-4-phenyl-1,2,3,6-tetrahydropyridine (MPTP)-induced parkinsonism in the primate. *Movement Disorders*, 6(4):288–292, 1991. *Cited on page 13.*
- [20] E. Bardinet, M. Bhattacharjee, D. Dormont, B. Pidoux, G. Malandain, M. Schüpbach, N. Ayache, P. Cornu, Y. Agid, and J. Yelnik. A three-dimensional histological atlas of the human basal ganglia. II. atlas deformation strategy and evaluation in deep brain stimulation for Parkinson disease. *Journal of Neurosurgery*, 110(2):208–219, 2009. *Cited on pages 45 and 50.*
- [21] E. Bardinet, D. Dormont, G. Malandain, M. Bhattacharjee, B. Pidoux, C. Saleh, P. Cornu, N. Ayache, Y. Agid, and J. Yelnik. Retrospective cross-evaluation of a histological and deformable 3D atlas of the basal ganglia on series of Parkinsonian patients treated by deep brain stimulation. In *Proceedings of Medical Image Computing and Computer-Assisted Intervention (MICCAI), LNCS*, volume 3750, pages 385–393, 2005. *Cited on pages 45, 50, and 54.*
- [22] K. A. Barnes, A. L. Cohen, J. D. Power, S. M. Nelson, Y. B. L. Dosenbach, F. M. Miezin, S. E. Petersen, and B. L. Schlaggar. Identifying basal ganglia divisions in individuals using resting-state functional connectivity MRI. *Frontiers in Systems Neuroscience*, 4(18):1–10, 2010. *Cited on pages 102, 108, and 122.*
- [23] R. Bartholow. *Medical electricity: a practical treatise on the applications of electricity to medicine and surgery*. Henry C. Lea’s Son & Co., Philadelphia, second edition, 1882. *Cited on page 8.*
- [24] P. J. Basser, J. Mattiello, and D. Le Bihan. MR diffusion tensor spectroscopy and imaging. *Biophysical Journal*, 66(1):259–267, 1994. *Cited on page 26.*
- [25] P. J. Basser and C. Pierpaoli. Microstructural and physiological features of tissues elucidated by quantitative-diffusion-tensor MRI. *Journal of Magnetic Resonance*, 111(3):209–219, 1996. *Cited on page 26.*

- [26] S. Baudrexel, T. Witte, C. Seifried, F. von Wegner, F. Beissner, J. C. Klein, H. Steinmetz, R. Deichmann, J. Roeper, and R. Hilker. Resting state fMRI reveals increased subthalamic nucleus - motor cortex connectivity in Parkinson's disease. *NeuroImage*, 55(4):1728–1738, 2011. *Cited on page 108.*
- [27] S. Baudrexel, T. Witte, C. Seifried, F. von Wegner, J. C. Klein, H. Steinmetz, R. Deichmann, and R. Hilker. Altered resting state functional connectivity in a subthalamic nucleus - motor cortex - cerebellar network in Parkinson's Disease. In *Proceedings of International Society for Magnetic Resonance in Medicine (ISMRM)*, volume 18, page 440, 2010. *Cited on page 108.*
- [28] C. F. Beckmann, M. DeLuca, J. T. Devlin, and S. M. Smith. Investigations into resting-state connectivity using independent component analysis. *Philosophical Transactions of the Royal Society B: Biological Sciences*, 360(1457):1001–1013, 2005. *Cited on page 34.*
- [29] T. Behrens, H. Johansen-Berg, M. Woolrich, S. Smith, C. Wheeler-Kingshott, P. Boulby, G. Barker, E. Sillery, K. Sheehan, O. Ciccarelli, A. Thompson, J. M. Brady, and P. Matthews. Non-invasive mapping of connections between human thalamus and cortex using diffusion imaging. *Nature Neuroscience*, 6(7):750–757, 2003. *Cited on pages 38 and 84.*
- [30] T. E. J. Behrens and H. Johansen-Berg. Relating connectional architecture to grey matter function using diffusion imaging. *Philosophical Transactions of the Royal Society B: Biological Sciences*, 360(1457):903–911, 2005. *Cited on pages 38 and 84.*
- [31] T. E. J. Behrens, H. Johansen-Berg, S. Jbabdi, M. F. S. Rushworth, and M. W. Woolrich. Probabilistic diffusion tractography with multiple fibre orientations. What can we gain? *NeuroImage*, 34(1):144–155, 2007. *Cited on page 26.*
- [32] B. P. Bejjani, D. Dormont, B. Pidoux, J. Yelnik, P. Damier, I. Arnulf, A. M. Bonnet, C. Marsault, Y. Agid, J. Philippon, and P. Cornu. Bilateral subthalamic stimulation for Parkinson's disease by using three-dimensional stereotactic magnetic resonance imaging and electrophysiological guidance. *Journal of Neurosurgery*, 92(4):615–625, 2000. *Cited on pages 41, 42, 46, 50, 51, 53, and 55.*
- [33] A. L. Benabid. Deep brain stimulation for Parkinson's disease. *Current Opinion in Neurobiology*, 13(6):696–706, 2003. *Cited on pages 16 and 17.*
- [34] A. L. Benabid, S. Chabardes, J. Mitrofanis, and P. Pollak. Deep brain stimulation of the subthalamic nucleus for the treatment of Parkinson's disease. *Lancet Neurology*, 8(1):67–81, 2009. *Cited on pages 3, 15, and 17.*
- [35] A. L. Benabid, A. Koudsie, A. Benazzouz, J.-F. Le Bas, and P. Pollak. Imaging of subthalamic nucleus and ventralis intermedius of the thalamus. *Movement Disorders*, 17(Suppl 3):S123–S129, 2002. *Cited on page 47.*
- [36] A. L. Benabid, P. Pollak, D. Hoffmann, C. Gervason, M. Hommel, J. E. Perret, J. de Rougemont, and D. M. Gao. Long-term suppression of tremor by chronic stimulation of the ventral intermediate thalamic nucleus. *Lancet*, 337(8738):403–406, 1991. *Cited on page 12.*
- [37] E. E. Benarroch. Subthalamic nucleus and its connections. *Neurology*, 70(21):1991–1995, 2008. *Cited on page 15.*
- [38] A. Benazzouz, C. Gross, J. Feger, T. Boraud, and B. Bioulac. Reversal of rigidity and improvement in motor performance by subthalamic high-frequency stimulation in MPTP-treated monkeys. *European Journal of Neuroscience*, 5(4):382–389, 1993. *Cited on page 13.*

References

- [39] A. Benazzouz, C. H. Tai, W. Meissner, B. Bioulac, E. Bezard, and C. Gross. High-frequency stimulation of both zona incerta and subthalamic nucleus induces a similar normalization of basal ganglia metabolic activity in experimental parkinsonism. *Journal of the Federation of American Societies for Experimental Biology (FASEB)*, 18(3):528–530, 2004. Cited on page 16.
- [40] H. Bergman, T. Wichmann, and M. R. DeLong. Reversal of experimental parkinsonism by lesions of the subthalamic nucleus. *Science*, 249(4975):1436–1438, 1990. Cited on page 13.
- [41] A. Berney, F. Vingerhoets, A. Perrin, P. Guex, J.-G. Villemure, P. R. Burkhard, C. Benkelfat, and J. Ghika. Effect on mood of subthalamic DBS for Parkinson’s disease: a consecutive series of 24 patients. *Neurology*, 59(9):1427–1429, 2002. Cited on pages 3 and 17.
- [42] C. Beurrier, B. Bioulac, J. Audin, and C. Hammond. High-frequency stimulation produces a transient blockade of voltage-gated currents in subthalamic neurons. *Journal of Neurophysiology*, 85(4):1351–1356, 2001. Cited on page 15.
- [43] S. Blond and J. Siegfried. Thalamic stimulation for the treatment of tremor and other movement disorders. *Acta Neurochirurgica Supplementum*, 52:109–111, 1991. Cited on page 12.
- [44] J. Bonny, F. Durif, J. E. Bazin, E. Touraille, J. Yelnik, and J. P. Renou. Contrast optimization of Macaca mulatta basal ganglia in magnetic resonance images at 4.7 Tesla. *Journal of Neuroscience Methods*, 107(1–2):25–30, 2001. Cited on pages 41, 47, and 48.
- [45] S. Breit, J.-F. LeBas, A. Koudsie, J. Schulz, A. Benazzouz, P. Pollak, and A.-L. Benabid. Pretargeting for the implantation of stimulation electrodes into the subthalamic nucleus: a comparative study of magnetic resonance imaging and ventriculography. *Neurosurgery*, 58(Suppl 1):ONS83–ONS95, 2006. Cited on pages 49, 51, and 56.
- [46] R. Brown. A brief account of microscopical observations made in the months of June, July, and August, 1827, on the particles contained in the pollen of plants; and on the general existence of active molecules in organic and inorganic bodies. *Philosophical Magazine*, 4:161–173, 1828. Cited on page 22.
- [47] E. Brunenberg, R. Duits, B. ter Haar Romeny, and B. Platel. A Sobolev norm based distance measure for HARDI clustering: A feasibility study on phantom and real data. In *Proceedings of Medical Image Computing and Computer-Assisted Intervention (MICCAI)*, LNCS, volume 6361, pages 175–182, 2010. Cited on pages 38 and 84.
- [48] E. Brunenberg, E. Pelgrim, B. ter Haar Romeny, and B. Platel. K-means and graph cuts clustering of diffusion MRI in rat STN. In *Proceedings of International Society for Magnetic Resonance in Medicine (ISMRM)*, volume 18, page 4045, 2010. Cited on page 52.
- [49] E. Brunenberg, V. Prčkovska, B. Platel, G. Strijkers, and B. ter Haar Romeny. Untangling a fiber bundle knot: Preliminary results on STN connectivity using DTI and HARDI on rat brains. In *Proceedings of International Society for Magnetic Resonance in Medicine (ISMRM)*, volume 17, page 740, 2009. Cited on page 52.
- [50] E. J. L. Brunenberg, W. H. Backes, C. Pollo, L. Cammoun, M. L. F. Janssen, V. E. R. M. Visser-Vandewalle, B. M. ter Haar Romeny, J.-P. Thiran, and B. Platel. Resting state functional connectivity of the motor and non-motor areas of the human subthalamic nucleus. Submitted. Cited on page 102.

- [51] E. J. L. Brunenberg, P. Moeskops, A. Vilanova, W. H. Backes, M. L. F. Janssen, V. E. R. M. Visser-Vandewalle, B. M. ter Haar Romeny, and B. Platel. Structural connectivity of the human subthalamic nucleus: identification of the "hyperdirect" pathway and segregation of motor and non-motor STN parts. Submitted. *Cited on page 122.*
- [52] E. J. L. Brunenberg, A. Vilanova, V. Visser-Vandewalle, Y. Temel, L. Ackermans, B. Platel, and B. M. ter Haar Romeny. Automatic trajectory planning for deep brain stimulation: a feasibility study. In *Proceedings of Medical Image Computing and Computer-Assisted Intervention (MICCAI), LNCS*, volume 4791, pages 584–592, 2007. *Cited on page 52.*
- [53] R. S. Burns, C. C. Chiueh, S. P. Markey, M. H. Ebert, D. M. Jacobowitz, and I. J. Kopin. A primate model of parkinsonism: selective destruction of dopaminergic neurons in the pars compacta of the substantia nigra by N-methyl-4-phenyl-1,2,3,6-tetrahydropyrene. *Proceedings of the National Academy of Sciences (PNAS)*, 80(14):4546–4550, 1983. *Cited on page 13.*
- [54] C. R. Butson, S. E. Cooper, J. M. Henderson, B. Wolgamuth, and C. C. McIntyre. Probabilistic analysis of activation volumes generated during deep brain stimulation. *NeuroImage*, 54(3):2096–2104, 2011. *Cited on page 131.*
- [55] F. Caire, L. Ouchchane, J. Coste, J. Gabrillargues, P. Derost, M. Ulla, F. Durif, and J. Lemaire. Subthalamic nucleus location: relationships between stereotactic AC-PC-based diagrams and MRI anatomy-based contours. *Stereotactic and Functional Neurosurgery*, 87(6):337–347, 2009. *Cited on pages 3, 40, 52, and 56.*
- [56] F. Calamante, J.-D. Tournier, G. D. Jackson, and A. Connelly. Track-density imaging (TDI): super-resolution white matter imaging using whole-brain track-density mapping. *NeuroImage*, 53(4):1233–1243, 2010. *Cited on page 130.*
- [57] M. B. Carpenter, S. C. Carleton, J. T. Keller, and P. Conte. Connections of the subthalamic nucleus in the monkey. *Brain Research*, 224(1):1–29, 1981. *Cited on pages 13, 14, 97, 100, and 120.*
- [58] H. Y. Carr and E. M. Purcell. Effects of diffusion on free precession in nuclear magnetic resonance experiments. *Physical Review*, 94(3):630–638, 1954. *Cited on page 23.*
- [59] W. M. Chardack, A. A. Gage, and W. Greatbatch. A transistorized, self-contained, implantable pacemaker for the long-term correction of complete heart block. *Surgery*, 48:643–654, 1960. *Cited on page 9.*
- [60] J. Cheng, A. Ghosh, T. Jiang, and R. Deriche. A Riemannian framework for orientation distribution function computing. In *Proceedings of Medical Image Computing and Computer-Assisted Intervention (MICCAI), LNCS*, volume 5761, pages 911–918, 2009. *Cited on page 59.*
- [61] Z.-H. Cho, H.-K. Min, S.-H. Oh, J.-Y. Han, C.-W. Park, J.-G. Chi, Y.-B. Kim, S. H. Paek, A. M. Lozano, and K. H. Lee. Direct visualization of deep brain stimulation targets in Parkinson disease with the use of 7-tesla magnetic resonance imaging. *Journal of Neurosurgery*, 113(3):639–647, 2010. *Cited on pages 48, 89, 101, 122, 127, and 130.*
- [62] Z.-H. Cho, S.-H. Oh, J.-M. Kim, S.-Y. Park, D.-H. Kwon, H.-J. Jeong, Y.-B. Kim, J.-G. Chi, C.-W. Park, J. Huston III, K. H. Lee, and B. S. Jeon. Direct visualization of Parkinson's disease by in vivo human brain imaging using 7.0T magnetic resonance imaging. *Movement Disorders*, preprint:DOI: 10.1002/mds.23465, 2011. *Cited on pages 49, 89, 101, 122, 127, and 130.*

- [63] V. A. Coenen, B. Mädler, H. Schiffbauer, H. Urbach, and N. Allert. Individual fiber anatomy of the subthalamic region revealed with DTI: a concept to identify the DBS target for tremor suppression. *Neurosurgery*, 68(4):1069–1076, 2011. *Cited on page 52.*
- [64] D. L. Collins, A. P. Zijdenbos, V. Kollokian, J. G. Sled, N. J. Kabani, C. J. Holmes, and A. C. Evans. Design and construction of a realistic digital brain phantom. *IEEE Transactions on Medical Imaging*, 17(3):463–468, 1998. *Cited on pages 41 and 112.*
- [65] P. A. Cook and D. C. Alexander. Modelling uncertainty in two fibre-orientation estimates within a voxel. In *Proceedings of International Society for Magnetic Resonance in Medicine (ISMRM)*, volume 14, page 1639, 2006. *Cited on page 30.*
- [66] P. A. Cook, Y. Bai, S. Nedjati-Gilani, K. K. Seunarine, M. G. Hall, G. J. Parker, and D. C. Alexander. Camino: Open-source diffusion-MRI reconstruction and processing. In *Proceedings of International Society for Magnetic Resonance in Medicine (ISMRM)*, volume 14, page 2759, 2006. *Cited on page 89.*
- [67] P. A. Cook, H. Zhang, B. B. Avants, P. Yushkevich, D. C. Alexander, J. C. Gee, O. Ciccarelli, and A. J. Thompson. An automated approach to connectivity-based partitioning of brain structures. In *Proceedings of Medical Image Computing and Computer-Assisted Intervention (MICCAI)*, LNCS, volume 3749, pages 164–171, 2005. *Cited on pages 30 and 89.*
- [68] D. Cordes, V. M. Haughton, K. Arfanakis, J. D. Carew, P. A. Turski, C. H. Moritz, M. A. Quigley, and M. E. Meyerand. Frequencies contributing to functional connectivity in the cerebral cortex in “resting-state” data. *American Journal of Neuroradiology (AJNR)*, 22(7):1326–1333, 2001. *Cited on page 34.*
- [69] D. Cordes, V. M. Haughton, K. Arfanakis, G. J. Wendt, P. A. Turski, C. H. Moritz, M. A. Quigley, and M. E. Meyerand. Mapping functionally related regions of brain with functionally connectivity MR imaging. *American Journal of Neuroradiology (AJNR)*, 21(9):1636–1644, 2000. *Cited on page 34.*
- [70] O. Corti, C. Hampe, F. Darios, P. Ibanez, M. Ruberg, and A. Brice. Parkinson’s disease: from causes to mechanisms. *Comptes Rendus Biologies*, 328(2):131–142, 2005. *Cited on page 12.*
- [71] E. Cuny, D. Guehl, P. Burbaud, C. Gross, V. Dousset, and A. Rougier. Lack of agreement between direct magnetic resonance imaging and statistical determination of a subthalamic target: the role of electrophysiological guidance. *Journal of Neurosurgery*, 97(3):591–597, 2002. *Cited on pages 42, 49, 50, 51, 53, and 56.*
- [72] J. S. Damoiseaux, S. A. Rombouts, F. Barkhof, P. Scheltens, C. J. Stam, S. M. Smith, and C. F. Beckmann. Consistent resting-state networks across healthy subjects. *Proceedings of the National Academy of Sciences (PNAS)*, 103(37):13848–13853, 2006. *Cited on page 34.*
- [73] J. Damon. Local Morse theory for solutions to the heat equation and Gaussian blurring. *Journal of Differential Equations*, 115(2):368–401, 1995. *Cited on page 69.*
- [74] S. Daniluk and K. Davies. Optimal stimulation site. *Journal of Neurosurgery*, 108(2):425–429, 2008. *Cited on page 46.*
- [75] S. Daniluk, K. G. Davies, S. A. Elias, P. Novak, and J. M. Nazzaro. Assessment of the variability in the anatomical position and size of the subthalamic nucleus among patients with advanced Parkinson’s disease using magnetic resonance imaging. *Acta Neurochirurgica*, 152:201–210, 2010. *Cited on pages 46, 51, 89, and 112.*

- [76] S. F. Danish, J. L. Jaggi, J. T. Moyer, L. Finkel, and G. H. Baltuch. Conventional MRI is inadequate to delineate the relationship between the red nucleus and subthalamic nucleus in Parkinson's disease. *Stereotactic and Functional Neurosurgery*, 84(1):12–18, 2006. *Cited on pages 42, 49, 50, and 53.*
- [77] W. Dauer and S. Przedborski. Parkinson's disease: mechanisms and models. *Neuron*, 39(6):889–909, 2003. *Cited on page 12.*
- [78] K. G. Davies and S. Daniluk. Stereotactic targeting of the subthalamic nucleus: relevance of magnetic resonance-based evaluation of interindividual variation in diencephalic anatomy. *Stereotactic and Functional Neurosurgery*, 86(5):330–331, 2008. *Cited on page 46.*
- [79] F. Dell'Acqua, P. Scifo, G. Rizzo, M. Catani, A. Simmons, G. Scotti, and F. Fazio. A modified damped Richardson-Lucy algorithm to reduce isotropic background effects in spherical deconvolution. *NeuroImage*, 49(2):1446–1458, 2010. *Cited on page 127.*
- [80] M. R. DeLong, A. P. Georgopoulos, M. D. Crutcher, S. J. Mitchell, R. T. Richardson, and G. E. Alexander. Functional organization of the basal ganglia: contributions of single-cell recording studies. *Ciba Foundation Symposium*, 107:64–82, 1984. *Cited on pages 12 and 13.*
- [81] M. Descoteaux. *High angular resolution diffusion MRI: from local estimation to segmentation and tractography*. PhD thesis, INRIA Sophia Antipolis, 2008. *Cited on pages 28, 59, 72, and 73.*
- [82] M. Descoteaux, E. Angelino, S. Fitzgibbons, and R. Deriche. Regularized, fast and robust analytical Q-ball imaging. *Magnetic Resonance in Medicine*, 58(3):497–510, 2007. *Cited on pages 28 and 61.*
- [83] G. Deuschl, W. Fogel, M. Hahne, A. Kupsch, D. Müller, M. Oechsner, U. Sommer, G. Ulm, T. Vogt, and J. Volkmann. Deep-brain stimulation for Parkinson's disease. *Journal of Neurology*, 249(Suppl 3):III/36–III/39, 2002. *Cited on page 16.*
- [84] P.-F. D'Haese, E. Cetinkaya, P. E. Konrad, C. Kao, and B. M. Dawant. Computer-aided placement of deep brain stimulators: from planning to intraoperative guidance. *IEEE Transactions on Medical Imaging*, 24(11):1469–1478, 2005. *Cited on pages 41, 46, 50, and 54.*
- [85] A. Di Martino, A. Scheres, D. S. Margulies, A. M. Kelly, L. Q. Uddin, Z. Shehzad, B. Biswal, J. R. Walters, F. X. Castellanos, and M. P. Milham. Functional connectivity of human striatum: a resting state fMRI study. *Cerebral Cortex*, 18(12):2735–2747, 2008. *Cited on page 108.*
- [86] D. Dormont, K. G. Ricciardi, D. Tandé, K. Parain, C. Menuel, D. Galanaud, S. Navarro, P. Cornu, Y. Agid, and J. Yelnik. Is the subthalamic nucleus hypointense on T2-weighted images? A correlation study using MR imaging and stereotactic atlas data. *American Journal of Neuroradiology (AJNR)*, 25(9):1516–1523, 2004. *Cited on pages 41, 46, 47, 50, and 51.*
- [87] D. Dormont, D. Seidenwurm, D. Galanaud, P. Cornu, J. Yelnik, and E. Bardinet. Neuroimaging and deep brain stimulation. *American Journal of Neuroradiology (AJNR)*, 31(1):15–23, 2010. *Cited on pages 3 and 40.*
- [88] E. R. Dorsey, R. Constantinescu, J. P. Thompson, K. M. Biglan, R. G. Holloway, K. Kieburtz, F. J. Marshall, B. M. Ravina, G. Schifitto, A. Siderowf, and C. M. Tanner. Projected number of people with Parkinson disease in the most populous nations, 2005 through 2030. *Neurology*, 68(5):384–386, 2007. *Cited on page 10.*

- [89] B. Draganski, F. Kherif, S. Klöppel, P. A. Cook, D. C. Alexander, G. J. M. Parker, R. Deichmann, J. Ashburner, and R. S. J. Frackowiak. Evidence for segregated and integrative connectivity patterns in the human basal ganglia. *Journal of Neuroscience*, 28(28):7143–7152, 2008. *Cited on pages 38 and 85.*
- [90] <http://bmia.bmt.tue.nl/software/dtitool/index.html>. *Cited on page 61.*
- [91] Y. Duan, X. Li, and Y. Xi. Thalamus segmentation from diffusion tensor magnetic resonance imaging. *International Journal of Biomedical Imaging*, 2007:90216, 2007. *Cited on page 58.*
- [92] V. Duay, X. Bresson, J. S. Castro, C. Pollo, M. Bach Cuadra, and J.-P. Thiran. An active contour-based atlas registration model applied to automatic subthalamic nucleus targeting on MRI: method and validation. In *Proceedings of Medical Image Computing and Computer-Assisted Intervention (MICCAI), LNCS*, volume 5242, pages 980–988, 2008. *Cited on pages 45 and 50.*
- [93] R. Duits, M. Felsberg, and L. M. J. Florack. α scale spaces on a bounded domain. In *Proceedings of Scale Space Conference, LNCS*, volume 2695, pages 494–510, 2003. *Cited on pages 69 and 70.*
- [94] R. Duits and E. Franken. Left-invariant diffusions on the space of positions and orientations and their application to crossing-preserving smoothing of HARDI images. *International Journal of Computer Vision*, 92(3):231–264, 2010. *Cited on page 72.*
- [95] M. Egidi, P. Rampini, M. Locatelli, M. Farabola, A. Priori, A. Pesenti, F. Tamma, E. Caputo, V. Chiesa, and R. M. Villani. Visualisation of the subthalamic nucleus: a multiple sequential image fusion (MuSIF) technique for direct stereotaxic localisation and postoperative control. *Neurological Sciences*, 23(Suppl 2):S71–S72, 2002. *Cited on pages 46, 50, and 55.*
- [96] A. Einstein. Über die von der molekularkinetischen Theorie der wärme geforderte Bewegung von in ruhenden Flüssigkeiten suspendierten Teilchen. *Annalen der Physik*, 322(8):549–560, 1905. *Cited on page 22.*
- [97] E. Eloff, V. Bockermann, T. Gringel, M. Knauth, P. Dechent, and G. Helms. Improved visibility of the subthalamic nucleus on high-resolution stereotactic MR imaging by added susceptibility ($T2^*$) contrast using multiple gradient echoes. *American Journal of Neuroradiology (AJNR)*, 28(6):1093–1094, 2007. *Cited on pages 48 and 51.*
- [98] F. R. Ervin and V. H. Mark. Stereotactic thalamotomy in the human. Part II, Physiologic observations on the human thalamus. *Archives of Neurology*, 3(4):368–380, 1960. *Cited on page 8.*
- [99] S. H. Faro and F. B. Mohamed. *Functional MRI: basic principles and clinical applications*. Springer Science+Business Media Inc., New York, first edition, 2006. *Cited on page 31.*
- [100] M. Felsberg, R. Duits, and L. M. J. Florack. The monogenic scale space on a bounded domain and its applications. *International Journal of Computer Vision*, 64(2–3):187–201, 2005. *Cited on page 70.*
- [101] M. Felsberg and G. Sommer. Scale adaptive filtering derived from the Laplace equation. In *Proceedings of the DAGM Symposium on Pattern Recognition, LNCS*, volume 2191, pages 124–131, 2001. *Cited on page 70.*
- [102] A. Fick. Concerns diffusion and concentration gradient. *Annalen der Physik*, 170(1):59–86, 1855. *Cited on page 22.*

- [103] M. Filali, W. D. Hutchison, V. N. Palter, A. M. Lozano, and J. O. Dostrovsky. Stimulation-induced inhibition of neuronal firing in human subthalamic nucleus. *Experimental Brain Research*, 156(3):274–281, 2004. *Cited on page 16.*
- [104] R. Fisher, V. Salanova, T. Witt, R. Worth, T. Henry, R. Gross, K. Oommen, I. Osorio, J. Nazzaro, D. Labar, M. Kaplitt, M. Sperling, E. Sandok, J. Neal, A. Handforth, J. Stern, A. DeSalles, S. Chung, A. Shetter, D. Bergen, R. Bakay, J. Henderson, J. French, G. Baltuch, W. Rosenfeld, A. Youkilis, W. Marks, P. Garcia, N. Barbaro, N. Fountain, C. Bazil, R. Goodman, G. McKhann, K. Babu Krishnamurthy, S. Papavassiliou, C. Epstein, J. Pollard, L. Tonder, J. Grebin, R. Coffey, and N. Graves. Electrical stimulation of the anterior nucleus of thalamus for treatment of refractory epilepsy. *Epilepsia*, 51(5):899–908, 2010. *Cited on page 131.*
- [105] K. A. Follett, F. M. Weaver, M. Stern, K. Hur, C. L. Harris, P. Luo, W. J. Marks Jr., J. Rothlind, O. Sagher, C. Moy, R. Pahwa, K. Burchiel, P. Hogarth, E. C. Lai, J. E. Duda, K. Holloway, A. Samii, S. Horn, J. M. Bronstein, G. Stoner, P. A. Starr, R. Simpson, G. Baltuch, A. D. Salles, G. D. Huang, and D. J. Reda. Pallidal versus subthalamic deep-brain stimulation for Parkinson's disease. *New England Journal of Medicine*, 362(22):2077–2091, 2010. *Cited on page 131.*
- [106] B. U. Forstmann, A. Anwander, A. Schäfer, J. Neumann, S. Brown, E.-J. Wagenmakers, R. Bogacz, , and R. Turner. Cortico-striatal connections predict control over speed and accuracy in perceptual decision making. *Proceedings of the National Academy of Sciences (PNAS)*, 107(36):15916–15920, 2010. *Cited on page 85.*
- [107] M. D. Fox and M. E. Raichle. Spontaneous fluctuations in brain activity observed with functional magnetic resonance imaging. *Nature Reviews Neuroscience*, 8(9):700–711, 2007. *Cited on pages 33 and 34.*
- [108] M. D. Fox, A. Z. Snyder, J. L. Vincent, M. Corbetta, D. C. Van Essen, and M. E. Raichle. The human brain is intrinsically organized into dynamic, anticorrelated functional networks. *Proceedings of the National Academy of Sciences (PNAS)*, 102(27):9673–9678, 2005. *Cited on page 34.*
- [109] P. T. Fox and M. E. Raichle. Focal physiological uncoupling of cerebral blood flow and oxidative metabolism during somatosensory stimulation in human subjects. *Proceedings of the National Academy of Sciences (PNAS)*, 83(4):1140–1144, 1986. *Cited on page 31.*
- [110] P. T. Fox, M. E. Raichle, M. A. Mintun, and C. Dence. Nonoxidative glucose consumption during focal physiologic neural activity. *Science*, 241(4864):462–464, 1988. *Cited on page 31.*
- [111] K. Friston, A. Holmes, K. Worsley, J.-P. Poline, C. Frith, and R. Frackowiak. Statistical parametric maps in functional imaging: a general linear approach. *Human Brain Mapping*, 2(4):189–210, 1995. *Cited on page 34.*
- [112] K. J. Friston. Functional connectivity: the principal-component analysis of large (PET) data sets. *Journal of Cerebral Blood Flow & Metabolism*, 13(1):5–14, 1993. *Cited on page 38.*
- [113] K. J. Friston. Functional and effective connectivity in neuroimaging: a synthesis. *Human Brain Mapping*, 2(1–2):56–78, 1994. *Cited on page 38.*
- [114] G. Fritsch and E. Hitzig. The electrical excitability of the cerebrum. In R. W. Wilkins, editor, *Neurosurgical classics*, pages 15–27. American Association of Neurological Surgeons, Rolling Meadows, first edition, 1992. *Cited on page 8.*

References

- [115] <http://www.fmrib.ox.ac.uk/fsl/>. Cited on pages 86 and 112.
- [116] P. L. Gildenberg. History of movement disorder surgery. In A. M. Lozano, editor, *Movement disorder surgery*, pages 1–20. Karger, Basel, first edition, 2000. Cited on page 12.
- [117] P. L. Gildenberg. Evolution of basal ganglia surgery for movement disorders. *Stereotactic and Functional Neurosurgery*, 84(4):131–135, 2006. Cited on page 12.
- [118] C. A. Giller, E. E. Babcock, and D. B. Mendelsohn. Use of sagittal images for localization of the subthalamic nucleus. Technical note. *Journal of Neurosurgery*, 102(3):571–575, 2005. Cited on pages 41, 42, 52, and 53.
- [119] A. Goh, C. Lenglet, P. M. Thompson, and R. Vidal. A nonparametric Riemannian framework for processing high angular diffusion images (HARDI). In *Proceedings of IEEE Conference on Computer Vision and Pattern Recognition (CVPR)*, pages 2496–2503, 2009. Cited on page 59.
- [120] G. Gong, Y. He, L. Concha, C. Lebel, D. W. Gross, A. C. Evans, and C. Beaulieu. Mapping anatomical connectivity patterns of human cerebral cortex using in vivo diffusion tensor imaging tractography. *Cerebral Cortex*, 19(3):524–536, 2008. Cited on pages 38 and 84.
- [121] A. Grassi, L. Cammoun, C. Pollo, P. Hagmann, R. Meuli, and J. P. Thiran. Thalamic nuclei clustering on high angular resolution diffusion images. In *Proceedings of International Society for Magnetic Resonance in Medicine (ISMRM)*, volume 16, page 1777, 2008. Cited on pages 59, 65, and 73.
- [122] A. M. Graybiel. The basal ganglia. *Current Biology*, 10(14):R509–R511, 2000. Cited on pages 9 and 10.
- [123] D. Guehl, R. Edwards, E. Cuny, P. Burbaud, A. Rougier, J. Modolo, and A. Beuter. Statistical determination of the optimal subthalamic nucleus stimulation site in patients with Parkinson disease. *Journal of Neurosurgery*, 106(1):101–110, 2007. Cited on pages 3, 17, and 40.
- [124] T. Guo, K. W. Finnis, S. C. L. Deoni, A. G. Parrent, and T. M. Peters. Comparison of different targeting methods for subthalamic nucleus deep brain stimulation. In *Proceedings of Medical Image Computing and Computer-Assisted Intervention (MICCAI)*, LNCS, volume 4190, pages 768–775, 2006. Cited on pages 41, 46, 48, and 50.
- [125] T. Guo, A. G. Parrent, and T. M. Peters. Automatic target and trajectory identification for deep brain stimulation (DBS) procedures. In *Proceedings of Medical Image Computing and Computer-Assisted Intervention (MICCAI)*, LNCS, volume 4791, pages 483–490, 2007. Cited on pages 46 and 54.
- [126] T. Guo, A. G. Parrent, and T. M. Peters. Surgical targeting accuracy analysis of six methods for subthalamic nucleus deep brain stimulation. *Computer Aided Surgery*, 12(6):325–334, 2007. Cited on pages 41, 46, 48, and 50.
- [127] T. Guo, T. Peters, S. L. Deoni, A. Parrent, and K. Finnis. Application of T1 and T2 maps for stereotactic deep-brain neurosurgery planning. In *Proceedings of the Conference of the IEEE Engineering in Medicine and Biology Society (IEEE-EMBS)*, volume 5, pages 5416–5419, 2005. Cited on pages 48 and 55.
- [128] E. Haber and J. Modersitzki. Intensity gradient based registration and fusion of multi-modal images. Technical Report TR-2004-027-A, Department of Mathematics and Computer Science, Emory University, Atlanta, 2004. Cited on page 63.

- [129] C. Haegelen, T. Rouaud, P. Darnault, and X. Morandia. The subthalamic nucleus is a key-structure of limbic basal ganglia functions. *Medical Hypotheses*, 72(4):421–426, 2009. *Cited on pages 14, 100, and 120.*
- [130] P. Hagmann, L. Cammoun, X. Gigandet, R. Meuli, C. J. Honey, V. J. Wedeen, and O. Sporns. Mapping the structural core of human cerebral cortex. *PLoS Biology*, 6:e159, 2008. *Cited on pages 38 and 84.*
- [131] P. Hagmann, M. Kurant, X. Gigandet, P. Thiran, V. J. Wedeen, R. Meuli, and J.-P. Thiran. Mapping human whole-brain structural networks with diffusion MRI. *PLoS One*, 2:e597, 2007. *Cited on pages 30, 38, and 84.*
- [132] P. Hagmann, J.-P. Thiran, L. Jonasson, P. Vandergheynst, S. Clarke, P. Maeder, and R. Meuli. DTI mapping of human brain connectivity: statistical fibre tracking and virtual dissection. *NeuroImage*, 19(3):545–554, 2003. *Cited on pages 38 and 84.*
- [133] E. L. Hahn. Spin echoes. *Physical Review*, 80(4):580–594, 1950. *Cited on page 21.*
- [134] C. Hamani, E. Richter, J. M. Schwalb, and A. M. Lozano. Bilateral subthalamic nucleus stimulation for Parkinson’s disease: a systemic review of the clinical literature. *Neurosurgery*, 56(6):1313–1321, 2005. *Cited on page 15.*
- [135] C. Hamani, E. O. Richter, Y. Andrade-Souza, W. Hutchison, J. A. Saint-Cyr, and A. M. Lozano. Correspondence of microelectrode mapping with magnetic resonance imaging for subthalamic nucleus procedures. *Surgical Neurology*, 63(3):249–253, 2005. *Cited on page 51.*
- [136] C. Hamani, J. A. Saint-Cyr, J. Fraser, M. Kaplitt, and A. M. Lozano. The subthalamic nucleus in the context of movement disorders. *Brain*, 127(Pt 1):4–20, 2004. *Cited on pages 3, 14, 58, 80, 84, 93, 97, 100, 108, and 120.*
- [137] W. Hamel, U. Fietzek, A. Morsnowski, B. Schrader, J. Herzog, D. Weinert, G. Pfister, D. Müller, J. Volkmann, G. Deuschl, and H. Mehdorn. Deep brain stimulation of the subthalamic nucleus in Parkinson’s disease: evaluation of active electrode contacts. *Journal of Neurology, Neurosurgery & Psychiatry*, 74(8):1036–1046, 2003. *Cited on page 52.*
- [138] N. A. Hamid, R. D. Mitchell, P. Moccoft, G. W. M. Westby, J. Milner, and H. Pall. Targeting the subthalamic nucleus for deep brain stimulation: technical approach and fusion of pre- and postoperative MR images to define accuracy of lead placement. *Journal of Neurology, Neurosurgery & Psychiatry*, 76(3):409–414, 2005. *Cited on page 51.*
- [139] M. I. Hariz, P. Krack, R. Melvill, J. V. Jorgensen, W. Hamel, H. Hirabayashi, M. Lenders, N. Wesslen, M. Tengvar, and T. A. Yousry. A quick and universal method for stereotactic visualization of the subthalamic nucleus before and after implantation of deep brain stimulation electrodes. *Stereotactic and Functional Neurosurgery*, 80(1–4):96–101, 2003. *Cited on page 51.*
- [140] K. Hartmann-von Monakow, K. Akert, and H. Künzle. Projections of the precentral motor cortex and other cortical areas of the frontal lobe to the subthalamic nucleus in the monkey. *Experimental Brain Research*, 33(3–4):395–403, 1978. *Cited on pages 13, 14, 97, 100, and 120.*
- [141] T. Hashimoto, C. M. Elder, M. S. Okun, S. K. Patrick, and J. L. Vitek. Stimulation of the subthalamic nucleus changes the firing pattern of pallidal neurons. *Journal of Neuroscience*, 23(5):1916–1923, 2003. *Cited on page 16.*

References

- [142] R. Hassler and T. Reichert. Indikationen und Localizations-Methode der gezielten Hirnoperationen. *Nervenarzt*, 25:441, 1954. *Cited on page 8.*
- [143] G. Helms, T. Gringel, M. Knauth, P. Dechent, and E. Elolf. Delineation of the subthalamic nucleus (STN) on high-resolution maps of R2*. In *Proceedings of International Society for Magnetic Resonance in Medicine (ISMRM)*, volume 16, page 880, 2008. *Cited on pages 48, 51, and 52.*
- [144] J. Hirschmann, T. E. Özkurt, M. Butz, M. Homburger, S. Elben, C. J. Hartmann, J. Vesper, L. Wojtecki, and A. Schnitzler. Distinct oscillatory STN-cortical loops revealed by simultaneous MEG and local field potential recordings in patients with Parkinson's disease. *NeuroImage*, 55(3):1159–1168, 2010. *Cited on page 98.*
- [145] T. Hjørnevik, T. B. Leergaard, D. Darine, O. Moldestad, A. M. Dale, F. Willoch, and J. G. Bjaalie. Three-dimensional atlas system for mouse and rat brain imaging data. *Frontiers in Neuroinformatics*, 1:4, 2007. *Cited on pages 63, 66, 67, and 77.*
- [146] C. J. Honey, R. Koetter, M. Breakspear, and O. Sporns. Network structure of cerebral cortex shapes functional connectivity on multiple time scales. *Proceedings of the National Academy of Sciences (PNAS)*, 104(24):10240–10245, 2007. *Cited on page 37.*
- [147] M. Hornyak, R. L. Rovit, A. Stolper Simon, and W. T. Couldwell. Irving S. Cooper and the early surgical management of movement disorders. *Neurosurgical Focus*, 11(2):E6, 2001. *Cited on page 2.*
- [148] V. Horsley. Case of occipital encephalocele in which a correct diagnosis was obtained by means of the induced current. *Brain*, 7(2):228–243, 1884. *Cited on page 8.*
- [149] V. Horsley. Remarks on the surgery of the central nervous system. *British Medical Journal*, 2(1562):1286–1292, 1890. *Cited on page 8.*
- [150] S. Hunsche, D. Sauner, M. Maarouf, J. Poggenborg, K. Lackner, V. Sturm, and H. Treuer. Intraoperative X-ray detection and MRI-based quantification of brain shift effects subsequent to implantation of the first electrode in bilateral implantation of deep brain stimulation electrodes. *Stereotactic and Functional Neurosurgery*, 87(5):322–329, 2009. *Cited on page 52.*
- [151] T. Ishimori, S. Nakano, Y. Mori, R. Seo, T. Togami, T. Masada, T. Kusahara, M. Ohkawa, S. Nagao, Y. Yamashita, and S. Sugiura. Preoperative identification of subthalamic nucleus for deep brain stimulation using three-dimensional phase sensitive inversion recovery technique. *Magnetic Resonance in Medical Sciences*, 6(4):225–229, 2008. *Cited on pages 47 and 51.*
- [152] Y. Iturria-Medina, E. J. Canales-Rodríguez, L. Melie-García, P. A. Valdés-Hernández, E. Martínez-Montes, Y. Alemán-Gómez, and J. M. Sánchez-Bornot. Characterizing brain anatomical connections using diffusion weighted MRI and graph theory. *NeuroImage*, 36(3):645–660, 2007. *Cited on pages 38 and 84.*
- [153] Y. Iturria-Medina, R. C. Sotero, E. J. Canales-Rodríguez, Y. Alemán-Gómez, and L. Melie-García. Studying the human brain anatomical network via diffusion-weighted MRI and graph theory. *NeuroImage*, 40(3):1064–1076, 2008. *Cited on pages 38 and 84.*
- [154] K. M. Jansons and D. C. Alexander. Persistent angular structure: new insights from diffusion magnetic resonance imaging data. *Inverse Problems*, 19(5):1031–1046, 2003. *Cited on page 27.*

- [155] M. L. F. Janssen, D. G. M. Zwartjes, Y. Temel, V. Van Kranen-Mastenbroek, A. Duits, L. J. Bour, P. H. Veltink, T. Heida, and V. Visser-Vandewalle. Subthalamic nucleus neuronal responses to single cortical stimuli in a Parkinson's disease patient during stereotactic surgery. Submitted. *Cited on page 131.*
- [156] M. Jenkinson, P. R. Bannister, J. M. Brady, and S. M. Smith. Improved optimisation for the robust and accurate linear registration and motion correction of brain images. *NeuroImage*, 17(2):825–841, 2002. *Cited on page 112.*
- [157] M. Jenkinson and S. M. Smith. A global optimisation method for robust affine registration of brain images. *Medical Image Analysis*, 5(2):143–156, 2001. *Cited on pages 74, 86, and 112.*
- [158] D. Joel and I. Weiner. The connections of the primate subthalamic nucleus: indirect pathways and the open-interconnected scheme of basal ganglia thalamo-cortical circuitry. *Brain Research Reviews*, 23(1–2):62–78, 1997. *Cited on pages 13, 97, and 120.*
- [159] H. Johansen-Berg and T. E. Behrens. *Diffusion MRI: from quantitative measurement to in vivo neuroanatomy*. Academic Press, Elsevier Inc., London, first edition, 2009. *Cited on pages 20, 23, 26, 27, 28, 29, 30, and 38.*
- [160] H. Johansen-Berg, T. E. J. Behrens, M. D. Robson, I. Drobnjak, M. F. S. Rushworth, J. M. Brady, S. M. Smith, D. J. Higham, and P. M. Matthews. Changes in connectivity profiles define functionally distinct regions in human medial frontal cortex. *Proceedings of the National Academy of Sciences (PNAS)*, 101:13335–13340, 2004. *Cited on pages 38 and 84.*
- [161] L. Jonasson, P. Hagmann, C. Pollo, X. Bresson, C. R. Wilson, R. Meuli, and J.-P. Thiran. A level set method for segmentation of the thalamus and its nuclei in DT-MRI. *Signal Processing*, 87(2):309–321, 2007. *Cited on page 59.*
- [162] D. K. Jones and M. Cercignani. Twenty-five pitfalls in the analysis of diffusion MRI data. *NMR in Biomedicine*, 23(7):803–820, 2010. *Cited on page 126.*
- [163] K. Kane and A. Taub. A history of local electrical analgesia. *Pain*, 1(2):125–138, 1975. *Cited on page 8.*
- [164] P. Kellaway. The part played by electric fish in the early history of bioelectricity and electrotherapy. *Bulletin of the History of Medicine*, 20(2):112–137, 1946. *Cited on page 8.*
- [165] S. Kim, H. Ko, V. Dawson, and T. Dawson. Recent advances in our understanding of Parkinson's disease. *Drug Discovery Today: Disease Mechanisms*, 2(4):427–433, 2005. *Cited on page 12.*
- [166] M. Kitajima, S. Kakeda, J. Moriya, N. Ohnari, T. Sato, Y. Hayashida, T. Hirai, Y. Yamashita, M. Uike, and Y. Korogi. Direct visualization of normal subthalamic nucleus with high resolution MR imaging at 3.0 T: Comparison between FSE T2-WI and fast STIR image. In *Proceedings of International Society for Magnetic Resonance in Medicine (ISMRM)*, volume 15, page 780, 2007. *Cited on pages 41, 47, and 51.*
- [167] Y. Koike, F. Shima, A. Nakamizo, and Y. Miyagi. Direct localization of subthalamic nucleus supplemented by single-track electrophysiological guidance in deep brain stimulation lead implantation: techniques and clinical results. *Stereotactic and Functional Neurosurgery*, 86(3):173–178, 2008. *Cited on pages 50 and 56.*

References

- [168] B. H. Kopell and A. R. Rezai. Psychiatric neurosurgery: a historical perspective. In A. R. Rezai, S. A. Rasmussen, and B. D. Greenberg, editors, *Surgery for psychiatric disorders*, pages 181–198. W.B. Saunders Company, Philadelphia, 2003. *Cited on page 9.*
- [169] H. Künzle. An autoradiographic analysis of the efferent connections from premotor and adjacent prefrontal regions (areas 6 and 9) in *Macaca fascicularis*. *Brain, Behavior and Evolution*, 15(3):185–234, 1978. *Cited on page 97.*
- [170] L. V. Laitinen, A. T. Bergenheim, and M. I. Hariz. Leksell's posteroventral pallidotomy in the treatment of Parkinson's disease. *Journal of Neurosurgery*, 76(1):53–61, 1992. *Cited on page 12.*
- [171] L. V. Laitinen, A. T. Bergenheim, and M. I. Hariz. Ventroposterolateral pallidotomy can abolish all parkinsonian symptoms. *Stereotactic and Functional Neurosurgery*, 58(1–4):14–21, 1992. *Cited on page 12.*
- [172] E. Lalo, S. Thobois, A. Sharott, G. Polo, P. Mertens, A. Pogosyan, and P. Brown. Patterns of bidirectional communication between cortex and basal ganglia during movement in patients with Parkinson disease. *Journal of Neuroscience*, 28(12):3008–3016, 2008. *Cited on page 98.*
- [173] J. L. Lancaster, D. Tordesillas-Gutiérrez, M. Martínez, F. Salinas, A. Evans, K. Zilles, J. C. Mazziotta, and P. T. Fox. Bias between MNI and Talairach coordinates analyzed using the ICBM-152 brain template. *Human Brain Mapping*, 28(11):1194–1205, 2007. *Cited on page 112.*
- [174] B. Landman, J. Bogovic, and J. Prince. Compressed sensing of multiple intra-voxel orientations with traditional DTI. In *Proceedings of the MICCAI Workshop on Computational Diffusion MRI*, pages 175–182, 2008. *Cited on page 130.*
- [175] B. A. Landman, H. Wan, J. A. Bogovic, P. L. Bazin, and J. L. Prince. Resolution of crossing fibers with constrained compressed sensing using traditional diffusion tensor MRI. In *Proceedings of the SPIE Medical Imaging Conference*, volume 7623, pages 76231H–76231H–8, 2010. *Cited on page 130.*
- [176] J. W. Langston. The impact of MPTP on Parkinson's disease research: past, present, and future. In S. A. Factor and W. J. Weiner, editors, *Parkinson's Disease. Diagnosis and Clinical Management*. Demos Medical Publishing, New York, 2002. *Cited on page 2.*
- [177] M. M. Lanotte, M. Rizzone, B. Bergamasco, G. Faccani, A. Melcarne, and L. Lopiano. Deep brain stimulation of the subthalamic nucleus: anatomical, neurophysiological, and outcome correlations with the effects of stimulation. *Journal of Neurology, Neurosurgery & Psychiatry*, 72(1):53–58, 2002. *Cited on page 52.*
- [178] M. Lazar and A. L. Alexander. An error analysis of white matter tractography methods: synthetic diffusion tensor field simulations. *NeuroImage*, 20(2):1140–1153, 2003. *Cited on page 29.*
- [179] F. Le Jeune, J. Péron, D. Grandjean, S. Drapier, C. Haegelen, E. Garin, B. Millet, and M. Vérin. Subthalamic nucleus stimulation affects limbic and associative circuits: a PET study. *European Journal of Nuclear Medicine and Molecular Imaging*, 37(8):1512–1520, 2010. *Cited on page 108.*
- [180] R. Lebel, A. Eissa, M. Gee, M. Wieler, W. Martin, and A. Wilman. MRI methods at 4.7T for imaging Parkinson's Disease. In *Proceedings of International Society for Magnetic Resonance in Medicine (ISMRM)*, volume 16, page 2283, 2008. *Cited on pages 48 and 52.*

- [181] C. Lee, B. Young, and M. F. Sanders. The role of the supramammillary commissure in MR localization of the subthalamic nucleus. *Stereotactic and Functional Neurosurgery*, 84(5–6):193–204, 2006. *Cited on pages 41, 42, 52, and 53.*
- [182] S. E. Leh, A. Ptito, M. M. Chakravarty, and A. P. Strafella. Fronto-striatal connections in the human brain: a probabilistic diffusion tractography study. *Neuroscience Letters*, 419(2):113–118, 2007. *Cited on pages 38 and 85.*
- [183] S. Lehericy, M. Ducros, P.-F. V. de Moortele, C. Francois, L. Thivard, C. Poupon, N. Swindale, K. Ugurbil, and D.-S. Kim. Diffusion tensor fiber tracking shows distinct corticostriatal circuits in humans. *Annals of Neurology*, 55(4):522–529, 2004. *Cited on pages 38 and 85.*
- [184] S. Lehericy, M. Ducros, A. Krainik, C. Francois, P.-F. V. de Moortele, K. Ugurbil, and D.-S. Kim. 3-D diffusion tensor axonal tracking shows distinct SMA and pre-SMA projections to the human striatum. *Cerebral Cortex*, 14(12):1302–1309, 2004. *Cited on pages 38 and 85.*
- [185] J.-J. Lemaire, J. Coste, L. Ouchchane, F. Caire, C. Nuti, P. Derost, V. Cristini, J. Gabril-largues, S. Hemm, F. Durif, and J. Chazal. Brain mapping in stereotactic surgery: a brief overview from the probabilistic targeting to the patient-based anatomic mapping. *NeuroImage*, 37(Suppl 1):S109–S115, 2007. *Cited on pages 3 and 52.*
- [186] J.-J. Lemaire, J. Coste, L. Ouchchane, F. Caire, C. Nuti, P. Derost, V. Cristini, J. Gabril-largues, S. Hemm, F. Durif, and J. Chazal. Brain mapping in stereotactic surgery: a brief overview from the probabilistic targeting to the patient-based anatomic mapping. *NeuroImage*, 37(Suppl 1):S109–S115, 2007. *Cited on page 40.*
- [187] C. Lenglet, J. S. W. Campbell, M. Descoteaux, G. Haro, P. Savadjiev, D. Wassermann, A. Anwender, R. Deriche, G. B. Pike, G. Sapiro, K. Siddiqi, and P. Thompson. Mathematical methods for diffusion MRI processing. *NeuroImage*, 45(Suppl 1):S111–122, 2009. *Cited on pages 24, 27, 28, and 30.*
- [188] C. Lenglet, M. Rousson, and R. Deriche. DTI segmentation by statistical surface evolution. Technical Report 5843, INRIA Sophia-Antipolis, 2006. *Cited on page 59.*
- [189] P. A. LeWitt, A. R. Rezai, M. A. Leehey, S. G. Ojemann, A. W. Flaherty, E. N. Eskandar, S. K. Kostyk, K. Thomas, A. Sarkar, M. S. Siddiqui, S. B. Tatter, J. M. Schwalb, K. L. Poston, J. M. Henderson, R. M. Kurlan, I. H. Richard, L. V. Meter, C. V. Sapan, M. J. During, M. G. Kaplitt, and A. Feigin. AAV2-GAD gene therapy for advanced Parkinson’s disease: a double-blind, sham-surgery controlled, randomised trial. *Lancet Neurology*, 10(4):309–319, 2011. *Cited on page 131.*
- [190] N. Ligot, P. Krystkowiak, C. Simonin, S. Goldman, P. Peigneux, J. Van Naemen, M. Monclus, S. F. Lacroix, D. Devos, K. Dujardin, C. Delmaire, E. Bardinnet, A. Delval, M. Delliaux, L. Defebvre, J. Yelnik, S. Blond, A. Destée, and X. D. Tiège. External globus pallidus stimulation modulates brain connectivity in Huntington’s disease. *Journal of Cerebral Blood Flow & Metabolism*, 31(1):41–46, 2011. *Cited on page 131.*
- [191] P. Limousin, J. Speelman, F. Gielen, and M. Janssens. Multicentre European study of thalamic stimulation in parkinsonian and essential tremor. *Journal of Neurology, Neurosurgery & Psychiatry*, 66(3):289–296, 1999. *Cited on page 131.*
- [192] T. Lindeberg. Scale-space behaviour of local extrema and blobs. *Journal of Mathematical Imaging and Vision*, 1(1):65–99, 1992. *Cited on pages 69 and 74.*

- [193] P. Littlechild, T. R. K. Varma, P. R. Eldridge, S. Fox, A. Forster, N. Fletcher, M. Steiger, P. Byrne, K. Tyler, and S. Flinham. Variability in position of the subthalamic nucleus targeted by magnetic resonance imaging and microelectrode recordings as compared to atlas co-ordinates. *Stereotactic and Functional Neurosurgery*, 80(1–4):82–87, 2003. *Cited on pages 46, 51, and 55.*
- [194] V. Litvak, A. Jha, A. Eusebio, R. Oostenveld, T. Foltynie, P. Limousin, L. Zrinzo, M. I. Hariz, K. Friston, and P. Brown. Resting oscillatory cortico-subthalamic connectivity in patients with Parkinson's disease. *Brain*, 134(2):359–374, 2011. *Cited on page 98.*
- [195] X. Liu, J. Rowe, D. Nandi, G. Hayward, S. Parkin, J. Stein, and T. Aziz. Localisation of the subthalamic nucleus using Radionics Image Fusion and Stereoplan combined with field potential recording. A technical note. *Stereotactic and Functional Neurosurgery*, 76(2):63–73, 2001. *Cited on page 42.*
- [196] J. Livet, T. A. Weissman, H. Kang, R. W. Draft, J. Lu, R. A. Bennis, J. R. Sanes, and J. W. Lichtman. Transgenic strategies for combinatorial expression of fluorescent proteins in the nervous system. *Nature*, 450(7166):56–62, 2007. *Cited on page 36.*
- [197] N. K. Logothetis and J. Pfeuffer. On the nature of the BOLD fMRI contrast mechanism. *Magnetic Resonance Imaging*, 22(10):1517–1531, 2004. *Cited on page 31.*
- [198] N. K. Logothetis and B. A. Wandell. Interpreting the BOLD signal. *Annual Review of Physiology*, 66(1):735–769, 2004. *Cited on page 31.*
- [199] F. López-Muñoz, C. Alamo, E. Cuenca, W. W. Shen, P. Clervoy, and G. Rubio. History of the discovery and clinical introduction of chlorpromazine. *Annals of Clinical Psychiatry*, 17(3):113–135, 2005. *Cited on page 2.*
- [200] K. C. Loucif, C. L. Wilson, R. Baig, M. G. Lacey, and I. M. Stanford. Functional interconnectivity between the globus pallidus and the subthalamic nucleus in the mouse brain slice. *Journal of Physiology*, 567(Pt 3):977–987, 2005. *Cited on page 108.*
- [201] L. Marrakchi-Kacem, C. Delmaire, A. Tucholka, P. Roca, P. Guevara, F. Poupon, J. Yelnik, A. Durr, J.-F. Mangin, S. Lehericy, and C. Poupon. Analysis of the striato-thalamo-cortical connectivity on the cortical surface to infer biomarkers of Huntington's disease. In *Proceedings of Medical Image Computing and Computer-Assisted Intervention (MICCAI)*, LNCS, volume 6362, pages 217–224, 2010. *Cited on pages 38 and 85.*
- [202] T. McGraw, B. Vemuri, R. Yezierski, and T. Mareci. Segmentation of high angular resolution diffusion MRI modeled as a field of von Mises-Fisher mixtures. In *Proceedings of European Conference on Computer Vision (ECCV)*, LNCS, volume 3953, pages 463–475, 2006. *Cited on page 59.*
- [203] M. J. McKeown, S. Makeig, G. B. Brown, T.-B. Jung, S. S. Kindermann, A. J. Bell, and T. J. Sejnowski. Analysis of fMRI data by blind source separation into independent spatial components. *Human Brain Mapping*, 6(3):160–188, 1998. *Cited on pages 34 and 128.*
- [204] D. W. McRobbie, E. A. Moore, M. J. Graves, and M. R. Prince. *MRI: from picture to proton*. Cambridge University Press, Cambridge, second edition, 2007. *Cited on pages 20, 21, and 32.*
- [205] J. H. Mehrkens, K. Bötzel, U. Steude, K. Zeitler, A. Schnitzler, V. Sturm, and J. Voges. Long-term efficacy and safety of chronic globus pallidus internus stimulation in different types of primary dystonia. *Stereotactic and Functional Neurosurgery*, 87(1):8–17, 2009. *Cited on page 131.*

- [206] C. Menuel, L. Garnero, E. Bardinnet, F. Poupon, D. Phalippou, and D. Dormont. Characterization and correction of distortions in stereotactic magnetic resonance imaging for bilateral subthalamic stimulation in Parkinson disease. *Journal of Neurosurgery*, 103(2):256–266, 2005. *Cited on page 51.*
- [207] R. Meyers. The modification of alternating tremors, rigidity and festination by surgery of the basal ganglia. In T. J. Putnam, editor, *The Diseases of the Basal Ganglia*, pages 602–665. Hafner Publishing, New York, 1966. *Cited on page 8.*
- [208] S. Miocinovic, S. F. Lempka, G. S. Russo, C. B. Maks, C. R. Butson, K. E. Sakaie, J. L. Vitek, and C. C. McIntyre. Experimental and theoretical characterization of the voltage distribution generated by deep brain stimulation. *Experimental Neurology*, 216(1):166–176, 2009. *Cited on page 131.*
- [209] S. Mori. *Introduction to Diffusion Tensor Imaging*. Elsevier, Amsterdam, first edition, 2007. *Cited on page 23.*
- [210] S. Mori, B. Crain, V. Chacko, and P. van Zijl. Three dimensional tracking of axonal projections in the brain by magnetic resonance imaging. *Annals of Neurology*, 45(2):265–269, 1999. *Cited on page 29.*
- [211] S. Mori and J. Zhang. Principles of diffusion tensor imaging and its applications to basic neuroscience research. *Neuron*, 51(5):527–539, 2006. *Cited on pages 23, 24, and 52.*
- [212] E. Moro, A. E. Lang, A. P. Strafella, Y. Y. Poon, P. M. Arango, A. Dagher, W. D. Hutchison, and A. M. Lozano. Bilateral globus pallidus stimulation for Huntington’s disease. *Annals of Neurology*, 56(2):290–294, 2004. *Cited on page 131.*
- [213] A. Moser, A. Gieselberg, B. Ro, C. Keller, and F. Qadri. Deep brain stimulation: response to neuronal high frequency stimulation is mediated through GABA(A) receptor activation in rats. *Neuroscience Letters*, 341(1):57–60, 2003. *Cited on page 15.*
- [214] K. Murphy, R. M. Birn, D. A. Handwerker, T. B. Jones, and P. A. Bandettini. The impact of global signal regression on resting state correlations: Are anti-correlated networks introduced? *NeuroImage*, 44(3):893–905, 2009. *Cited on page 128.*
- [215] K. Nakano. Neural circuits and topographic organization of the basal ganglia and related regions. *Brain and Development*, 22(Suppl 1):S5–S16, 2000. *Cited on pages 14, 100, and 120.*
- [216] A. Nambu, M. Takada, M. Inase, and H. Tokuno. Dual somatotopical representations in the primate subthalamic nucleus: evidence for ordered but reversed body-map transformations from the primary motor cortex and the supplementary motor area. *Journal of Neuroscience*, 16(8):2671–2683, 1996. *Cited on pages 13, 97, and 120.*
- [217] A. Nambu, H. Tokuno, I. Hamada, H. Kita, M. Imanishi, T. Akazawa, Y. Ikeuchi, and N. Hasegawa. Excitatory cortical inputs to pallidal neurons via the subthalamic nucleus in the monkey. *Journal of Neurophysiology*, 84(1):289–300, 2000. *Cited on pages 9 and 97.*
- [218] A. Nambu, H. Tokuno, M. Inase, and M. Takada. Corticosubthalamic input zones from forelimb representations of the dorsal and ventral divisions of the premotor cortex in the macaque monkey: comparison with the input zones from the primary motor cortex and the supplementary motor area. *Neuroscience Letters*, 239(1):13–16, 1997. *Cited on pages 9, 13, 97, and 120.*

References

- [219] National Collaborating Centre for Chronic Conditions. Parkinson's disease: National clinical guideline for diagnosis and management in primary and secondary care. Technical report, Royal College of Physicians, London, 2006. <http://www.nice.org.uk/nicemedia/pdf/cg035fullguideline.pdf>. Cited on pages 10 and 12.
- [220] C. Nioche, E. A. Cabanis, and C. Habas. Functional connectivity of the human red nucleus in the brain resting state at 3T. *American Journal of Neuroradiology (AJNR)*, 30(2):396–403, 2009. Cited on page 108.
- [221] Y. Nisino. Faserverbindung der lateralen Fläche der Großhirnhemisphäre beim Affen, unter besonderer Berücksichtigung der corticalen extrapyramidalen Bahnen und der sogenannten Kleinhirnpiramide. *Zeitschrift für mikroskopisch-anatomische Forschung*, 47:401–440, 1940. Cited on page 97.
- [222] W. L. Nowinski, D. Belov, P. Pollak, and A. L. Benabid. A probabilistic functional atlas of the human subthalamic nucleus. *Neuroinformatics*, 2(4):381–398, 2004. Cited on pages 41, 45, and 50.
- [223] W. L. Nowinski, J. Liu, and A. Thirunavuukarasuu. Quantification and visualization of the three-dimensional inconsistency of the subthalamic nucleus in the Schaltenbrand-Wahren brain atlas. *Stereotactic and Functional Neurosurgery*, 84(1):46–55, 2006. Cited on page 45.
- [224] W. L. Nowinski, A. Thirunavuukarasuu, J. Liu, and A. L. Benabid. Correlation between the anatomical and functional human subthalamic nucleus. *Stereotactic and Functional Neurosurgery*, 85(2–3):88–93, 2007. Cited on pages 45 and 54.
- [225] J. A. Obeso, M. C. Rodríguez-Oroz, M. Rodríguez, J. Arbizu, and J. M. Giménez-Amaya. The basal ganglia and disorders of movement: pathophysiological mechanisms. *News in Physiological Sciences*, 17(2):51–55, 2002. Cited on page 11.
- [226] S. Ogawa, T.-M. Lee, A. S. Nayak, and P. Glynn. Oxygenation-sensitive contrast in magnetic resonance image of rodent brain at high magnetic fields. *Magnetic Resonance in Medicine*, 14(1):68–78, 1990. Cited on page 31.
- [227] M. Ortega, M. C. Juan, M. Alcañiz, J. A. Gil, and C. Monserrat. Deformable brain atlas validation of the location of subthalamic nucleus using T1-weighted MR images of patients operated on for Parkinson's. *Computerized Medical Imaging and Graphics*, 32(5):367–378, 2008. Cited on pages 41, 45, and 54.
- [228] E. Özarslan, T. M. Shepherd, B. C. Vemuri, S. J. Blackband, and T. H. Mareci. Resolution of complex tissue microarchitecture using the Diffusion Orientation Transform (DOT). *NeuroImage*, 36(3):1086–1103, 2006. Cited on pages 27, 61, and 62.
- [229] S. Pallavaram, B. M. Dawant, T. Koyama, H. Yu, J. Neimat, P. E. Konrad, and P.-F. D'Haese. Validation of a fully automatic method for the routine selection of the anterior and posterior commissures in magnetic resonance images. *Stereotactic and Functional Neurosurgery*, 87(3):148–154, 2009. Cited on pages 42 and 50.
- [230] S. Pallavaram, P.-F. D'Haese, C. Kao, H. Yu, M. Remple, J. Neimat, P. Konrad, and B. Dawant. A new method for creating electrophysiological maps for DBS surgery and their application to surgical guidance. In *Proceedings of Medical Image Computing and Computer-Assisted Intervention (MICCAI)*, LNCS, volume 5241, pages 670–677, 2008. Cited on pages 41, 46, 50, and 53.

- [231] S. Pallavaram, H. Yu, J. Spooner, P.-F. D'Haese, B. Bodenheimer, P. E. Konrad, and B. M. Dawant. Intersurgeon variability in the selection of anterior and posterior commissures and its potential effects on target localization. *Stereotactic and Functional Neurosurgery*, 86(2):113–119, 2008. *Cited on pages 42 and 50.*
- [232] A. Parent and L. N. Hazrati. Functional anatomy of the basal ganglia. I. The cortico-basal ganglia-thalamo-cortical loop. *Brain Research Reviews*, 20(1):91–127, 1995. *Cited on pages 13, 97, 102, and 120.*
- [233] A. Parent and L. N. Hazrati. Functional anatomy of the basal ganglia. II. The place of subthalamic nucleus and external pallidum in basal ganglia circuitry. *Brain Research Reviews*, 20(1):128–154, 1995. *Cited on pages 3, 13, 14, 84, 93, 97, 100, 102, 108, and 120.*
- [234] G. J. Parker and D. C. Alexander. Probabilistic anatomic connectivity derived from the microscopic persistent angular structure of cerebral tissue. *Philosophical Transactions of the Royal Society B: Biological Sciences*, 360(1457):893–902, 2005. *Cited on page 30.*
- [235] G. J. Parker, H. A. Haroon, and C. A. Wheeler-Kingshott. A framework for a streamline-based probabilistic index of connectivity (PICO) using a structural interpretation of MRI diffusion measurements. *Journal of Magnetic Resonance Imaging*, 18(2):242–254, 2003. *Cited on pages 30 and 89.*
- [236] J. Parkinson. *Essay on the shaking palsy*. Sherwood, Neely, and Jones, London, 1817. *Cited on page 10.*
- [237] N. K. Patel, P. Heywood, K. O'Sullivan, S. Love, and S. S. Gill. MRI-directed subthalamic nucleus surgery for Parkinson's disease. *Stereotactic and Functional Neurosurgery*, 78(3–4):132–145, 2002. *Cited on pages 47, 51, and 55.*
- [238] N. K. Patel, S. Khan, and S. S. Gill. Comparison of atlas- and magnetic-resonance-imaging-based stereotactic targeting of the subthalamic nucleus in the surgical treatment of Parkinson's disease. *Stereotactic and Functional Neurosurgery*, 86(3):153–161, 2008. *Cited on pages 46 and 51.*
- [239] N. K. Patel, P. Plaha, K. O'Sullivan, R. McCarter, P. Heywood, and S. S. Gill. MRI directed bilateral stimulation of the subthalamic nucleus in patients with Parkinson's disease. *Journal of Neurology, Neurosurgery & Psychiatry*, 74(12):1631–1637, 2003. *Cited on page 47.*
- [240] G. Paxinos and C. Watson. *The Rat Brain in Stereotaxic Coordinates*. Academic Press, New York, fourth edition, 1998. *Cited on pages 61, 62, 63, 65, and 77.*
- [241] G. Paxinos and C. Watson. *The Rat Brain in Stereotaxic Coordinates*. Elsevier Academic Press, San Diego, 2005. *Cited on page 63.*
- [242] J. Péron, F. Le Jeune, C. Haegelen, T. Dondaine, D. Drapier, P. Sauleau, J.-M. Reymann, S. Drapier, T. Rouaud, B. Millet, and M. Vérin. Subthalamic nucleus stimulation affects theory of mind network: a PET study in Parkinson's Disease. *PLoS ONE*, 5(3):e9919, 2010. *Cited on page 108.*
- [243] M. Perrin, C. Poupon, Y. Cointepas, B. Rieul, N. Golestani, C. Pallier, D. Riviere, A. Constantinesco, D. LeBihan, and J.-F. Mangin. Fiber tracking in q-ball fields using regularized particle trajectories. In *Proceedings of Information Processing in Medical Imaging*, volume 19, pages 52–63, 2005. *Cited on page 30.*

References

- [244] M. Perrin, C. Poupon, B. Rieul, P. Leroux, A. Constantinesco, J.-F. Mangin, and D. LeBihan. Validation of q-ball imaging with a diffusion fibre-crossing phantom on a clinical scanner. *Philosophical Transactions of the Royal Society B: Biological Sciences*, 360(1457):881–891, 2005. *Cited on page 28.*
- [245] S. D. Piasecki and J. W. Jefferson. Psychiatric complications of deep brain stimulation for Parkinson's disease. *Journal of Clinical Psychiatry*, 65(6):845–849, 2004. *Cited on pages 3 and 17.*
- [246] P. Pollak, A. L. Benabid, and C. Gross. [Effects of the stimulation of the subthalamic nucleus in Parkinson disease]. *Revue Neurologique (Paris)*, 149:175–176, 1993. *Cited on pages 3, 13, and 15.*
- [247] C. Pollo, R. Meuli, P. Maeder, F. Vingerhoets, J. Ghika, and J.-G. Villemure. Subthalamic nucleus deep brain stimulation for Parkinson's disease: magnetic resonance imaging targeting using visible anatomical landmarks. *Stereotactic and Functional Neurosurgery*, 80(1–4):76–81, 2003. *Cited on pages 42 and 53.*
- [248] T. J. Prescott, K. Gurney, and P. Redgrave. Basal ganglia. In M. A. Arbib, editor, *The Handbook of Brain Theory and Neural Networks*, pages 147–151. MIT Press, Cambridge, second edition, 2002. *Cited on page 9.*
- [249] V. Prčkovska, P. Rodrigues, R. Duits, A. Vilanova, and B. ter Haar Romeny. Extrapolating fiber crossings from DTI data. can we infer similar fiber crossings as in HARDI? In *Proceedings of the MICCAI Workshop on Computational Diffusion MRI*, 2010. *Cited on pages 25 and 130.*
- [250] V. Prčkovska, A. F. Roebroek, W. Pullens, A. Vilanova, and B. M. ter Haar Romeny. Optimal acquisition schemes in high angular resolution diffusion weighted imaging. In *Proceedings of Medical Image Computing and Computer-Assisted Intervention (MICCAI)*, LNCS, volume 5242, pages 9–17, 2008. *Cited on page 130.*
- [251] M. E. Raichle. Circulatory and metabolic correlates of brain function in normal humans. In V. Bethesda, editor, *Handbook of physiology: the nervous system*, pages 643–674. American Physiological Society, 1987. *Cited on page 31.*
- [252] Y. Rathi, O. Michailovich, M. E. Shenton, and S. Bouix. Directional functions for orientation distribution estimation. *Medical Image Analysis*, 13(3):432–444, 2009. *Cited on page 59.*
- [253] A. Rauscher, S. Witoszynskyj, S. Kolind, V. Coenen, and D. Li. Visualization of the subthalamic nuclei at high spatial resolution and high contrast with susceptibility weighted phase imaging. In *Proceedings of International Society for Magnetic Resonance in Medicine (ISMRM)*, volume 16, page 879, 2008. *Cited on page 48.*
- [254] A. R. Rezaei and A. M. Lozano. Deep brain stimulation for chronic pain. In K. J. Burchiel, editor, *Surgical management of pain*, pages 565–576. Thieme, New York, first edition, 2002. *Cited on page 12.*
- [255] E. O. Richter, T. Hoque, W. Halliday, A. M. Lozano, and J. A. Saint-Cyr. Determining the position and size of the subthalamic nucleus based on magnetic resonance imaging results in patients with advanced Parkinson disease. *Journal of Neurosurgery*, 100(3):541–546, 2004. *Cited on pages 46, 89, and 112.*

- [256] K. Rijkers, Y. Temel, V. Visser-Vandewalle, L. Vanormelingen, M. Vandersteen, P. Adriaensen, J. Gelan, and E. A. M. Beuls. The microanatomical environment of the subthalamic nucleus. Technical note. *Journal of Neurosurgery*, 107(1):198–201, 2007. *Cited on pages 41, 42, and 52.*
- [257] S. Robinson, G. Basso, N. Soldati, U. Sailer, J. Jovicich, L. Bruzzone, I. Kryspin-Exner, H. Bauer, and E. Moser. A resting state network in the motor control circuit of the basal ganglia. *BMC Neuroscience*, 10:137, 2009. *Cited on page 108.*
- [258] M. C. Rodriguez-Oroz, J. A. Obeso, A. E. Lang, J. L. Houeto, P. Pollak, S. Rehncrona, J. Kulisevsky, A. Albanese, J. Volkmann, M. I. Hariz, N. P. Quinn, J. D. Speelman, J. Guridi, I. Zamarbide, A. Gironell, J. Molet, B. Pascual-Sedano, B. Pidoux, A. M. Bonnet, Y. Agid, J. Xie, A. L. Benabid, A. M. Lozano, J. Saint-Cyr, L. Romito, M. F. Contarino, M. Scerrati, V. Fraix, and N. van Blercom. Bilateral deep brain stimulation in Parkinson's disease: a multicentre study with 4 years follow-up. *Brain*, 128(Pt 10):2240–2249, 2005. *Cited on pages 3 and 17.*
- [259] M. C. Rodriguez-Oroz, I. Zamarbide, J. Guridi, M. R. Palmero, and J. A. Obeso. Efficacy of deep brain stimulation of the subthalamic nucleus in Parkinson's disease 4 years after surgery: double blind and open label evaluation. *Journal of Neurology, Neurosurgery & Psychiatry*, 75(10):1382–1385, 2004. *Cited on pages 3, 15, and 17.*
- [260] U. Rossi. The history of electrical stimulation of the nervous system for the control of pain. In B. Simpson, editor, *Electrical stimulation and the relief of pain*, pages 5–16. Elsevier, Amsterdam, first edition, 2003. *Cited on pages 8 and 9.*
- [261] C. S. Roy and C. S. Sherrington. On the regulation of the blood supply of the brain. *Journal of Physiology*, 11(1–2):85–108, 1890. *Cited on page 31.*
- [262] A. F. Sadikot, A. Parent, and C. François. Efferent connections of the centromedian and parafascicular thalamic nuclei in the squirrel monkey: a PHA-L study of subcortical projections. *Journal of Comparative Neurology*, 315(2):137–159, 1992. *Cited on pages 13, 97, and 120.*
- [263] J. A. Saint-Cyr, T. Hoque, L. C. M. Pereira, J. O. Dostrovsky, W. D. Hutchison, D. J. Mikulis, A. Abosch, E. Sime, A. E. Lang, and A. M. Lozano. Localization of clinically effective stimulating electrodes in the human subthalamic nucleus on magnetic resonance imaging. *Journal of Neurosurgery*, 97(5):1152–1166, 2002. *Cited on page 52.*
- [264] F. J. Sánchez Castro, C. Pollo, R. Meuli, P. Maeder, O. Cuisenaire, M. B. Cuadra, J.-G. Villemure, and J.-P. Thiran. A cross validation study of deep brain stimulation targeting: from experts to atlas-based, segmentation-based and automatic registration algorithms. *IEEE Transactions on Medical Imaging*, 25(11):1440–1450, 2006. *Cited on pages 45, 49, 50, and 56.*
- [265] F. J. Sánchez Castro, C. Pollo, J.-G. Villemure, and J.-P. Thiran. Automatic subthalamic nucleus targeting for deep brain stimulation. A validation study. In *Proceedings of Computer Assisted Radiology and Surgery (CARS), International Congress Series*, volume 1281, pages 804–809, 2005. *Cited on pages 41, 45, 50, and 54.*
- [266] G. Schaltenbrand and W. Wahren. *Atlas for Stereotaxy of the Human Brain*. Thieme, Stuttgart, 1977. *Cited on pages 41 and 45.*
- [267] J. Schlaier, P. Schoedel, M. Lange, J. Winkler, J. Warnat, U. Dorenbeck, and A. Brawanski. Reliability of atlas-derived coordinates in deep brain stimulation. *Acta Neurochirurgica*, 147(11):1175–1180, 2005. *Cited on pages 50 and 56.*

- [268] C. E. Schoonover. *Portraits of the mind: visualizing the brain from antiquity to the 21st century*. Abrams, New York, first edition, 2010. *Cited on pages 35, 36, and 37.*
- [269] P. R. Schuurman, R. M. de Bie, C. B. Majoie, J. D. Speelman, and D. A. Bosch. A prospective comparison between three-dimensional magnetic resonance imaging and ventriculography for target-coordinate determination in frame-based functional stereotactic neurosurgery. *Journal of Neurosurgery*, 91(6):911–914, 1999. *Cited on pages 42 and 53.*
- [270] J. Schwalb and C. Hamani. The history and future of deep brain stimulation. *Neurotherapeutics*, 5(1):3–13, 2008. *Cited on pages 8 and 12.*
- [271] J. M. Schwalb and A. M. Lozano. Surgical management of tremor. *Neurosurgery Quarterly*, 14(1):60–68, 2004. *Cited on page 13.*
- [272] P. Schweinhardt, P. Fransson, L. Olson, C. Spenger, and J. L. R. Andersson. A template for spatial normalisation of MR images of the rat brain. *Journal of Neuroscience Methods*, 129(2):105–113, 2003. *Cited on page 63.*
- [273] K. K. Seunarine, P. A. Cook, M. G. Hall, K. V. Embleton, G. J. M. Parker, and D. C. Alexander. Exploiting peak anisotropy for tracking through complex structures. In *Proceedings of the ICCV Workshop on MMBIA*, pages 1–8, 2007. *Cited on pages 30, 85, and 89.*
- [274] E. Shink, M. Bevan, J. Bolam, and Y. Smith. The subthalamic nucleus and the external pallidum: two tightly interconnected structures that control the output of the basal ganglia in the monkey. *Neuroscience*, 73(2):335–357, 1996. *Cited on pages 13, 97, and 120.*
- [275] J. Siegfried and B. Lippitz. Bilateral chronic electrostimulation of ventroposterolateral pallidum: a new therapeutic approach for alleviating all parkinsonian symptoms. *Neurosurgery*, 35(6):1126–1129, 1994. *Cited on page 13.*
- [276] K. V. Slavin, K. R. Thulborn, C. Wess, and H. Nersesyan. Direct visualization of the human subthalamic nucleus with 3T MR imaging. *American Journal of Neuroradiology (AJNR)*, 27(1):80–84, 2006. *Cited on pages 46, 47, 51, and 55.*
- [277] H. M. Smeding, J. D. Speelman, M. Koning-Haanstra, P. R. Schuurman, P. Nijssen, T. van Laar, and B. Schmand. Neuropsychological effects of bilateral STN stimulation in Parkinson disease: a controlled study. *Neurology*, 66(12):1830–1836, 2006. *Cited on pages 3 and 17.*
- [278] S. M. Smith. Fast robust automated brain extraction. *Human Brain Mapping*, 17(3):143–155, 2002. *Cited on page 112.*
- [279] S. M. Smith. Overview of fMRI analysis. *The British Journal of Radiology*, 77(Suppl 2):S167–S175, 2004. *Cited on page 34.*
- [280] O. Söderman and B. Jönsson. Restricted diffusion in cylindrical geometry. *Journal of Magnetic Resonance, Series A*, 117(1):94–97, 1995. *Cited on page 73.*
- [281] E. A. Spiegel, H. T. Wycis, M. Marks, and A. S. Lee. Stereotactic apparatus for operations on the human brain. *Science*, 106(2754):349–350, 1947. *Cited on page 8.*
- [282] O. Sporns. *Networks of the brain*. The MIT Press, Cambridge, first edition, 2011. *Cited on pages 34, 37, and 38.*
- [283] P. A. Starr. Placement of deep brain stimulators into the subthalamic nucleus or globus pallidus internus: technical approach. *Stereotactic and Functional Neurosurgery*, 79(3–4):118–145, 2002. *Cited on pages 41, 46, 47, 53, 55, and 56.*

- [284] P. A. Starr, C. W. Christine, P. V. Theodosopoulos, N. Lindsey, D. Byrd, A. Mosley, and W. J. Marks. Implantation of deep brain stimulators into the subthalamic nucleus: technical approach and magnetic resonance imaging-verified lead locations. *Journal of Neurosurgery*, 97(2):370–387, 2002. *Cited on pages 41, 42, 50, and 51.*
- [285] P. A. Starr, J. L. Vitek, M. DeLong, and R. A. Bakay. Magnetic resonance imaging-based stereotactic localization of the globus pallidus and subthalamic nucleus. *Neurosurgery*, 44(2):303–314, 1999. *Cited on pages 41, 46, 50, and 55.*
- [286] E. O. Stejskal and J. E. Tanner. Spin diffusion measurements: spin echoes in the presence of a time-dependent field gradient. *Journal of Chemical Physics*, 42(1):288–292, 1965. *Cited on pages 23 and 24.*
- [287] A. P. Strafella. Cortico-basal ganglia functional connectivity investigated with transcranial magnetic stimulation. In *Proceedings of International Joint Conference on Neural Networks*, volume 3, pages 1525–1527, 2005. *Cited on page 108.*
- [288] M. Strupp. Spotlight on Parkinson's Disease: from a better understanding of fluctuating levodopa responses and the mechanisms of subthalamic nucleus stimulation to a better assessment of subcortical dementia. *Journal of Neurology*, 250(12):1513–1515, 2003. *Cited on page 12.*
- [289] D. Sun, H. Yu, J. Spooner, A. Tatsas, T. Davies, T. Abel, C. Kao, and P. Konrad. Post-mortem analysis following 71 months of deep brain stimulation of the subthalamic nucleus for Parkinson disease. *Journal of Neurosurgery*, 109(2):325–329, 2008. *Cited on page 52.*
- [290] R. Suri, C. Albani, and A. Glattfelder. A dynamic model of motor basal ganglia functions. *Biological Cybernetics*, 76(6):451–458, 1997. *Cited on pages 10 and 11.*
- [291] D. F. Swaab. *Wij zijn ons brein: van baarmoeder tot Alzheimer*. Uitgeverij Contact, Amsterdam Antwerpen, 2010. *Cited on page 2.*
- [292] C. H. Tai, T. Boraud, E. Bezard, B. Bioulac, C. Gross, and A. Benazzouz. Electrophysiological and metabolic evidence that high-frequency stimulation of the subthalamic nucleus bridges neuronal activity in the subthalamic nucleus and the substantia nigra reticulata. *Journal of the Federation of American Societies for Experimental Biology (FASEB)*, 17(13):1820–1830, 2003. *Cited on page 16.*
- [293] J. Talairach and P. Tournoux. *Co-planar stereotaxic atlas of the human brain: 3-dimensional proportional system - an approach to cerebral imaging*. Thieme Medical Publishers, New York, 1988. *Cited on pages 41, 86, and 112.*
- [294] S. K. H. Tan, H. Hartung, T. Sharp, and Y. Temel. Serotonin-dependent depression in Parkinson's disease: a role for the subthalamic nucleus? *Neuropharmacology*, preprint:DOI: 10.1016/j.neuropharm.2011.01.006, 2011. *Cited on page 131.*
- [295] T. Taoka, H. Hirabayashi, H. Nakagawa, M. Sakamoto, S. Kitano, J. Takahama, N. Marugami, K. Takayama, T. Akashi, T. Miyasaka, S. Iwasaki, N. Kurita, T. Sakaki, and K. Kichikawa. "sukeroku sign" and "dent internal-capsule sign" - identification guide for targeting the subthalamic nucleus for placement of deep brain stimulation electrodes. *Neuroradiology*, 51(1):11–16, 2009. *Cited on pages 47 and 51.*
- [296] T. Taoka, Y. Kubota, H. Hirabayashi, H. Nakagawa, M. Sakamoto, S. Iwasaki, S. Hirohashi, S. Nakanishi, and K. Kichikawa. Signal and shape of subthalamic nucleus on susceptibility-weighted image (SWI) -comparison with STIR image-. In *Proceedings of International Society for Magnetic Resonance in Medicine (ISMRM)*, volume 15, page 2175, 2007. *Cited on page 47.*

References

- [297] R. R. Tasker. One man's recollection of 50 years of functional and stereotactic neurosurgery. *Neurosurgery*, 55(4):968–974, 2004. *Cited on pages 9 and 12.*
- [298] Y. Temel, A. Blokland, H. W. M. Steinbusch, and V. Visser-Vandewalle. The functional role of the subthalamic nucleus in cognitive and limbic circuits. *Progress in Neurobiology*, 76(6):393–413, 2005. *Cited on pages 3, 9, 14, 15, 17, 77, 84, 100, 108, and 120.*
- [299] Y. Temel, L. J. Boothman, A. Blokland, P. J. Magill, H. W. M. Steinbusch, V. Visser-Vandewalle, and T. Sharp. Inhibition of 5-HT neuron activity and induction of depressive-like behavior by high-frequency stimulation of the subthalamic nucleus. *Proceedings of the National Academy of Sciences (PNAS)*, 104(43):17087–17092, 2007. *Cited on page 131.*
- [300] Y. Temel, A. Kessels, S. Tan, A. Topdag, P. Boon, and V. Visser-Vandewalle. Behavioural changes after bilateral subthalamic stimulation in advanced Parkinson disease: a systematic review. *Parkinsonism & Related Disorders*, 12(5):265–272, 2006. *Cited on pages 3 and 17.*
- [301] Y. Temel, T. Prinsenbergh, and V. Visser-Vandewalle. Imaging of the subthalamic nucleus for deep brain stimulation: a systematic review. *Neuromodulation*, 11(1):8–12, 2008. *Cited on page 40.*
- [302] W. Thevathasan and R. Gregory. Deep brain stimulation for movement disorders. *Practical Neurology*, 10(1):16–26, 2010. *Cited on page 16.*
- [303] H. Toda, N. Sawamoto, T. Hanakawa, H. Saiki, S. Matsumoto, R. Okumura, M. Ishikawa, H. Fukuyama, and N. Hashimoto. A novel composite targeting method using high-field magnetic resonance imaging for subthalamic nucleus deep brain stimulation. *Journal of Neurosurgery*, 111(4):737–745, 2009. *Cited on pages 41, 42, 52, and 53.*
- [304] J. D. Tournier, F. Calamante, and A. Connelly. Robust determination of the fibre orientation distribution in diffusion MRI: non-negativity constrained super-resolved spherical deconvolution. *NeuroImage*, 35(4):1459–1472, 2007. *Cited on page 127.*
- [305] J. D. Tournier, F. Calamante, D. G. Gadian, and A. Connelly. Direct estimation of the fiber orientation density function from diffusion-weighted MRI data using spherical deconvolution. *NeuroImage*, 23(3):1176–1185, 2004. *Cited on page 27.*
- [306] J. D. Tournier, C. H. Yeh, F. Calamante, K. H. Cho, A. Connelly, and C. P. Lin. Resolving crossing fibres using constrained spherical deconvolution: validation using diffusion-weighted imaging phantom data. *NeuroImage*, 42(2):617–625, 2008. *Cited on page 127.*
- [307] C. Triantafyllou, R. L. Buckner, S. Shannon, S. Arnold, and L. L. Wald. Temporal resolution in resting state time-series acquisitions for functional connectivity mapping. In *Proceedings of International Society for Magnetic Resonance in Medicine (ISMRM)*, volume 18, page 3427, 2010. *Cited on page 130.*
- [308] S. T. Tsai, S. H. Lin, S. Z. Lin, J. Y. Chen, C. W. Lee, and S. Y. Chen. Neuropsychological effects after chronic subthalamic stimulation and the topography of the nucleus in Parkinson's disease. *Neurosurgery*, 61(5):E1024–E1029, 2007. *Cited on pages 3, 17, and 40.*
- [309] D. Tuch. Q-ball imaging. *Magnetic Resonance in Medicine*, 52(6):1358–1372, 2004. *Cited on pages 27, 28, and 89.*
- [310] D. S. Tuch. *Diffusion MRI of complex tissue structure*. PhD thesis, Harvard, 2002. *Cited on page 59.*

- [311] D. S. Tuch, T. G. Reese, M. R. Wiegell, N. Makris, J. W. Belliveau, and V. J. Wedeen. High angular resolution diffusion imaging reveals intravoxel white matter fiber heterogeneity. *Magnetic Resonance in Medicine*, 48(4):577–582, 2002. Cited on pages 27 and 52.
- [312] D. S. Tuch, T. G. Reese, M. R. Wiegell, and V. J. Wedeen. Diffusion MRI of complex neural architecture. *Neuron*, 40(5):885–895, 2003. Cited on pages 27 and 85.
- [313] D. E. Vaillancourt, M. A. Mayka, K. R. Thulborn, and D. M. Corcos. Subthalamic nucleus and internal globus pallidus scale with the rate of change of force production in humans. *NeuroImage*, 23(1):175–186, 2004. Cited on page 98.
- [314] A. Vertinsky, V. Coenen, D. Lang, S. Kolind, C. Honey, D. Li, and A. Rauscher. Localization of the subthalamic nucleus: optimization with susceptibility-weighted phase MR imaging. *American Journal of Neuroradiology (AJNR)*, 30(9):1717–1724, 2009. Cited on pages 48 and 52.
- [315] V. Visser-Vandewalle, C. van der Linden, Y. Temel, H. Celik, L. Ackermans, G. Spince-maille, and J. Caemaert. Long-term effects of bilateral subthalamic nucleus stimulation in advanced Parkinson disease: a four year follow-up study. *Parkinsonism and Related Disorders*, 11(3):157–165, 2005. Cited on pages 12, 16, and 17.
- [316] M. T. Vlaardingerbroek and J. A. den Boer. *Magnetic Resonance Imaging*. Springer-Verlag, Berlin Heidelberg New York, first edition, 1996. Cited on page 20.
- [317] S. Volz, E. Hattingen, C. Preibisch, T. Gasser, and R. Deichmann. Reduction of susceptibility-induced signal losses in multi-gradient-echo images: application to improved visualization of the subthalamic nucleus. *NeuroImage*, 45(4):1135–1143, 2009. Cited on pages 48 and 52.
- [318] V. Voon, C. Kubu, P. Krack, J. L. Houeto, and A. I. Tröster. Deep brain stimulation: neuropsychological and neuropsychiatric issues. *Movement Disorders*, 21(S14):S305–S327, 2006. Cited on pages 3 and 17.
- [319] B. L. Walter and J. L. Vitek. Surgical treatment for Parkinson’s disease. *Lancet Neurology*, 3(12):719–728, 2004. Cited on page 2.
- [320] D. Wassermann, M. Descoteaux, and R. Deriche. Diffusion maps clustering for magnetic resonance q-ball imaging segmentation. *International Journal of Biomedical Imaging*, 2008:526906, 2008. Cited on pages 38, 59, 65, and 84.
- [321] F. M. Weaver, K. Follett, M. Stern, K. Hur, C. Harris, W. J. Marks Jr, J. Rothlind, O. Sagher, D. Reda, C. S. Moy, R. Pahwa, K. Burchiel, P. Hogarth, E. C. Lai, J. E. Duda, K. Holloway, A. Samii, S. Horn, J. Bronstein, G. Stoner, J. Heemskerk, and G. D. Huang. Bilateral deep brain stimulation vs best medical therapy for patients with advanced Parkinson disease: a randomized controlled trial. *Journal of the American Medical Association (JAMA)*, 301(6):63–73, 2009. Cited on pages 3, 15, and 17.
- [322] V. J. Wedeen, T. G. Reese, D. S. Tuch, J.-G. Dou, R. M. Weiskoff, and D. Chessler. Mapping fiber orientation spectra in cerebral white matter with Fourier-transform diffusion MRI. In *Proceedings of International Society for Magnetic Resonance in Medicine (ISMRM)*, volume 7, page 321, 1999. Cited on page 27.
- [323] D. Weishaupt, V. D. Köchli, and B. Marincek. *How does MRI work?* Springer-Verlag, Berlin Heidelberg New York, second edition, 2006. Cited on page 20.

References

- [324] M. L. Welter, L. Mallet, J. L. Houeto, C. Karachi, V. Czernecki, P. Cornu, S. Navarro, B. Pidoux, D. Dormont, E. Bardinet, J. Yelnik, P. Damier, and Y. Agid. Internal pallidal and thalamic stimulation in patients with Tourette syndrome. *Archives of Neurology*, 65(7):952–957, 2008. *Cited on page 131.*
- [325] M. R. Wiegell, D. S. Tuch, H. B. W. Larsson, and V. J. Wedeen. Automatic segmentation of thalamic nuclei from diffusion tensor magnetic resonance imaging. *NeuroImage*, 19(2):391–401, 2003. *Cited on pages 38, 58, 59, 65, 76, 79, and 84.*
- [326] D. Williams, M. Tijssen, G. van Bruggen, A. Bosch, A. Insola, V. Di Lazzaro, P. Mazzone, A. Oliviero, A. Quartarone, H. Speelman, and P. Brown. Dopamine-dependent changes in the functional connectivity between basal ganglia and cerebral cortex in humans. *Brain*, 125(Pt 7):1558–1569, 2002. *Cited on page 108.*
- [327] R. Williams. Alim-Louis Benabid: stimulation and serendipity. *Lancet Neurology*, 9(12):1152, 2010. *Cited on page 2.*
- [328] F. Windels, N. Bruet, A. Poupard, C. Feuerstein, A. Bertrand, and M. Savasta. Influence of the frequency parameter on extracellular glutamate and gamma-aminobutyric acid in substantia nigra and globus pallidus during electrical stimulation of subthalamic nucleus in rats. *Journal of Neuroscience Research*, 72(2):259–267, 2003. *Cited on page 16.*
- [329] C. Winstein, S. Grafton, and P. Pohl. Motor task difficulty and brain activity: investigation of goal-directed reciprocal aiming using positron emission tomography. *Journal of Neurophysiology*, 77(3):1581–1594, 1997. *Cited on page 98.*
- [330] K. J. Worsley, C. Liao, J. Aston, V. Petre, G. H. Duncan, F. Morales, and A. C. Evans. A general statistical analysis for fMRI data. *NeuroImage*, 15(1):1–15, 2002. *Cited on page 113.*
- [331] M. Wu, G. Young, and N. Chen. Midbrain nuclei visualization improved by susceptibility-enhanced 3D multi-echo SSFP for deep brain stimulation guidance. In *Proceedings of International Society for Magnetic Resonance in Medicine (ISMRM)*, volume 18, page 701, 2010. *Cited on pages 48 and 52.*
- [332] T. Wu, L. Wang, Y. Chen, C. Zhao, K. Li, and P. Chan. Changes of functional connectivity of the motor network in the resting state in Parkinson’s disease. *Neuroscience Letters*, 460(1):6–10, 2009. *Cited on page 108.*
- [333] C.-G. Yan and Y.-F. Zang. DPARSF: A MATLAB toolbox for “pipeline” data analysis of resting-state fMRI. *Frontiers in Systems Neuroscience*, 4:13, 2010. *Cited on page 112.*
- [334] J. Yelnik, E. Bardinet, D. Dormont, G. Malandain, S. Ourselin, D. Tandé, C. Karachi, N. Ayache, P. Cornu, and Y. Agid. A three-dimensional, histological and deformable atlas of the human basal ganglia. I. Atlas construction based on immunohistochemical and MRI data. *NeuroImage*, 34(2):618–638, 2007. *Cited on page 45.*
- [335] G. S. Young and N.-K. Chen. High contrast susceptibility weighted imaging: Reliable Unwrapping Susceptibility Technique (RUST SWI) improved visualization of midbrain nuclei for deep brain stimulation. In *Proceedings of International Society for Magnetic Resonance in Medicine (ISMRM)*, volume 15, page 937, 2007. *Cited on page 48.*
- [336] P. A. Yushkevich, J. Piven, H. Cody Hazlett, R. Gimpel Smith, S. Ho, J. C. Gee, and G. Gerig. User-guided 3D active contour segmentation of anatomical structures: significantly improved efficiency and reliability. *NeuroImage*, 31(3):1116–1128, 2006. *Cited on pages 88 and 112.*

- [337] X. L. Zhu, W. Hamel, B. Schrader, D. Weinert, J. Hedderich, J. Herzog, J. Volkmann, G. Deuschl, D. Müller, and H. M. Mehdorn. Magnetic resonance imaging-based morphometry and landmark correlation of basal ganglia nuclei. *Acta Neurochirurgica*, 144(10):959–969, 2002. *Cited on pages 46 and 51.*
- [338] U. Ziyen, D. Tuch, and C.-F. Westin. Segmentation of thalamic nuclei from DTI using spectral clustering. In *Proceedings of Medical Image Computing and Computer-Assisted Intervention (MICCAI)*, LNCS, volume 4191, pages 807–814, 2006. *Cited on pages 58 and 65.*
- [339] U. Ziyen and C.-F. Westin. Joint segmentation of thalamic nuclei from a population of diffusion tensor MR images. In *Proceedings of Medical Image Computing and Computer-Assisted Intervention (MICCAI)*, LNCS, volume 5241, pages 279–286, 2008. *Cited on page 58.*
- [340] M. Zonenshayn, A. R. Rezai, A. Y. Mogilner, A. Beric, D. Sterio, and P. J. Kelly. Comparison of anatomic and neurophysiological methods for subthalamic nucleus targeting. *Neurosurgery*, 47(2):282–94, 2000. *Cited on pages 49 and 56.*

List of figures

2.1	Pioneers of deep brain stimulation.	8
2.2	Basic anatomy of the basal ganglia.	10
2.3	Motor circuit in normal state and Parkinson's disease.	11
2.4	Structures and fiber tracts associated with the STN.	14
2.5	Functional subdivision of the STN.	15
2.6	Deep brain stimulation system.	16
3.1	Spin-echo MRI protocol.	21
3.2	Effect of diffusion in an MRI experiment.	24
3.3	Different DTI and HARDI glyphs in the centrum semiovale.	25
3.4	Various axon fiber configurations.	28
3.5	Funk-Radon transform.	28
3.6	Origin of the BOLD effect.	32
3.7	BOLD time course and stimulus function.	33
3.8	Relations of the soul by Robert Fludd.	35
3.9	Motor neuron axons colored by Brainbow.	36
3.10	Different types of brain connectivity.	37
4.1	AC-PC-based targeting in a sagittal plane.	43
4.2	RN-based targeting in an axial plane.	43
4.3	Targeting based on the nigrocapsular angle.	44
4.4	Indirect targeting based on atlas mapping.	44
4.5	Coronal and axial MRI slices visualizing the STN directly.	45
5.1	R_0 parameter tuning using linear diffusion profiles.	60
5.2	Anatomical MRI and FA map of a rat brain slice.	61
5.3	Different types of diffusion glyphs in the STN region.	64
5.4	Q-ball glyphs in the STN region with anatomical context.	65
5.5	Coronal slice of 3D digital rat brain atlas.	66
5.6	Selection of ROI around the right STN.	67
5.7	Preliminary clustering results for the right STN ROI.	67
5.8	Results of the analytic example.	74
5.9	Behavior of Sobolev multiplier.	75
5.10	K-means clustering results for computer-generated phantom.	78
5.11	K-means clustering results for real brain data.	79
6.1	Flowchart of data analysis steps for structural connectivity.	87
6.2	Flowchart of data registration steps for structural connectivity.	87
6.3	STN centers of mass in MNI152 atlas space.	88

List of figures

6.4	Streamline counting for the connectivity measures.	91
6.5	Visualizations of probabilistic fiber tracking results.	94
6.6	Fiber tracking results for atlas-based and manual STN ROI.	94
6.7	Total probability map of right STN connectivity.	95
6.8	Direct streamlines from STN to motor cortex.	98
6.9	Connectivity to the motor cortical areas per STN voxel.	99
7.1	Flowchart of data analysis steps for functional connectivity.	109
7.2	STN centers of mass in MNI152 atlas space.	110
7.3	Significant clusters for the right STN ROI.	111
7.4	Functional connectivity per STN voxel.	114
B.1	Significant clusters for the left STN ROI.	142

List of tables

4.1	Indirect studies based on anatomical landmarks visualized on MRI. . .	53
4.2	Indirect studies based on brain atlases.	54
4.3	Direct studies using T_2 -weighted MRI and relaxation time maps. . .	55
4.4	Studies comparing indirect and direct methods.	56
6.1	Parameters of MRI sequences.	86
6.2	Regions significantly connected to the <i>right</i> STN based on C_1	103
6.3	Regions significantly connected to the <i>right</i> STN based on C_2	104
6.4	Regions connected to the <i>right</i> STN based on C_3	105
7.1	Significant <i>positive</i> correlations with the atlas-based <i>right</i> STN ROIs.	117
7.2	Significant <i>negative</i> correlations with the atlas-based <i>right</i> STN ROIs.	117
7.3	Significant <i>positive</i> correlations with the atlas-based <i>left</i> STN ROIs.	118
7.4	Significant <i>negative</i> correlations with the atlas-based <i>left</i> STN ROIs.	118
A.1	Regions significantly connected to the <i>right</i> STN based on C_1	134
A.2	Regions significantly connected to the <i>left</i> STN based on C_1	135
A.3	Regions significantly connected to the <i>right</i> STN based on C_2	136
A.4	Regions significantly connected to the <i>left</i> STN based on C_2	137
A.5	Regions connected to the <i>right</i> STN based on C_3	138
A.6	Regions connected to the <i>left</i> STN based on C_3	139
B.1	Significant <i>positive</i> correlations with the manual <i>right</i> STN ROIs. .	143
B.2	Significant <i>negative</i> correlations with the manual <i>right</i> STN ROIs. .	144
B.3	Significant <i>positive</i> correlations with the manual <i>left</i> STN ROIs. . .	145
B.4	Significant <i>negative</i> correlations with the manual <i>left</i> STN ROIs. .	146

List of abbreviations

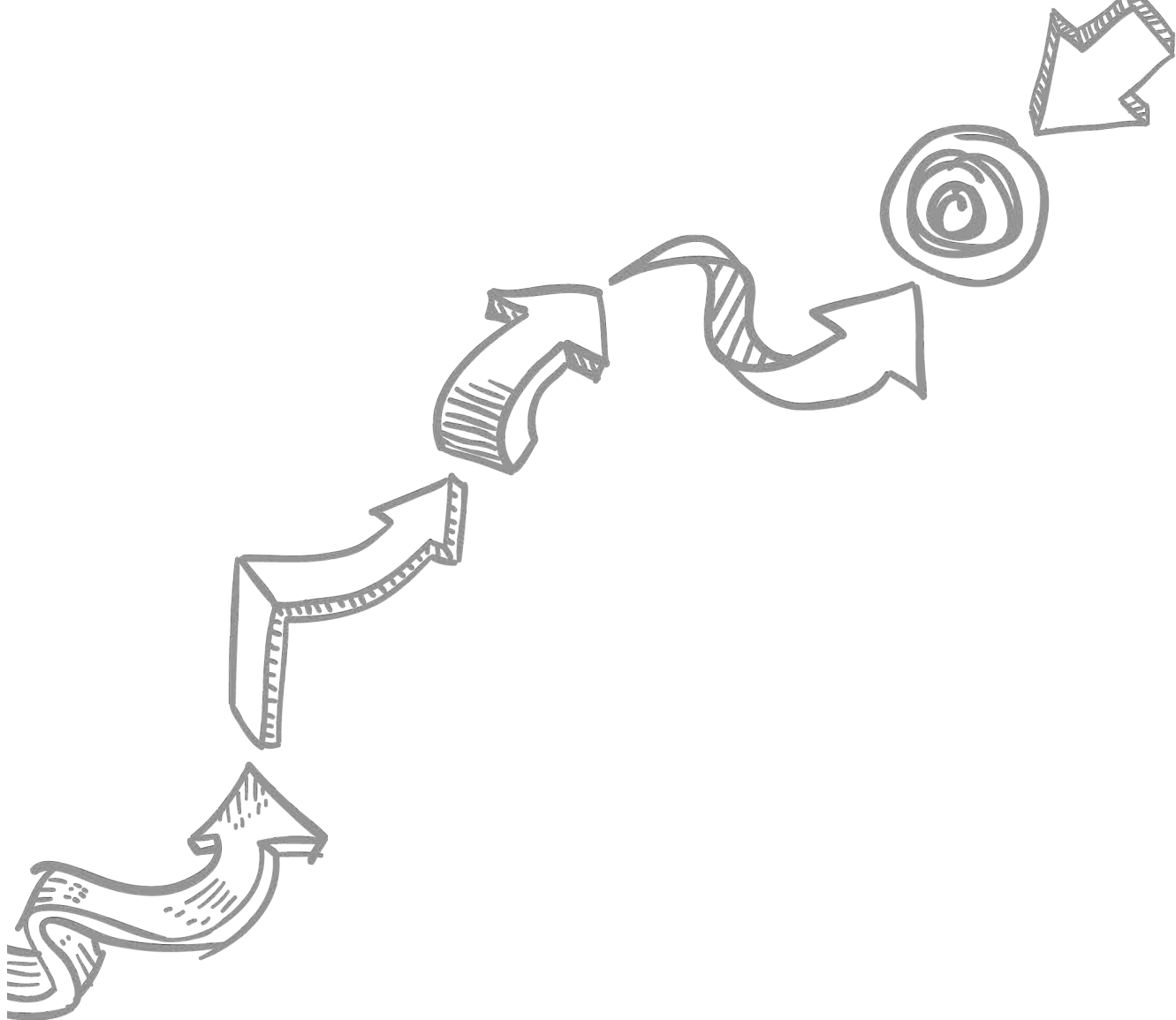
AC	anterior commissure
ADC	apparent diffusion coefficient
BOLD	blood-oxygen-level-dependent
CBF	cerebral blood flow
CBV	cerebral blood volume
CM-Pf	centromedian-parafascicular nuclear complex of the thalamus
CT	computed tomography
DBS	deep brain stimulation
DISHT	discrete inverse spherical harmonic transform
dMRI	diffusion-weighted MRI
dODF	diffusion orientation distribution function
DOT	diffusion orientation transform
DSI	diffusion spectrum imaging
DTI	diffusion tensor imaging
EEG	electroencephalography
EPI	echo-planar imaging
FA	fractional anisotropy
FACT	fiber assignment by continuous tracking
fMRI	functional MRI
fODF	fiber orientation distribution function
FOV	field of view
FRT	Funk-Radon transform
FSE	fast spin-echo
GLM	general linear model
GPe	globus pallidus externus; lateral globus pallidus
GPi	globus pallidus internus; medial globus pallidus
HARDI	high angular resolution diffusion imaging
IC	internal capsule
ICA	independent component analysis
IR	inversion recovery
MCP	midcommissural point
MEG	magnetoencephalography
MER	microelectrode recording
MNI	Montreal Neurological Institute
MPTP	1-methyl-4-phenyl-1,2,3,6-tetrahydropyridine
MR	magnetic resonance
MRI	magnetic resonance imaging
NA	number of averages
ODF	orientation distribution function (in this thesis the dODF)

List of abbreviations

PAS	persistent angular structure
PBS	phosphate buffered saline
PC	posterior commissure
PD	Parkinson's disease
PDF	probability density function
PET	positron emission tomography
PGSE	pulsed gradient spin-echo
PICo	probabilistic index of connectivity
PMC	postmammillary commissure
RARE	rapid acquisition with relaxation enhancement
RF	radiofrequency
RN	red nucleus
ROI	region of interest
SD	spherical deconvolution
SE	spin-echo
SH	spherical harmonics
SMC	supramammillary commissure
SN	substantia nigra
SNc	substantia nigra pars compacta
SNr	substantia nigra pars reticulata
SNR	signal-to-noise ratio
SSFP	steady-state free precession
STIR	short inversion time inversion recovery
STN	subthalamic nucleus
SWI	susceptibility-weighted imaging
TDI	track-density imaging
TE	echo time
TMS	transcranial magnetic stimulation
TR	repetition time
TSE	turbo spin-echo
uODF	uncertainty orientation distribution function
Vim	ventral intermediate nucleus of the thalamus

List of symbols

\mathbf{B}_0	main magnetic field
b_0	unweighted diffusion MRI image
b	summarizing influence of diffusion gradients ($b = \mathbf{q}^2\tau = \gamma^2\delta^2\mathbf{G}^2\tau$)
D	diffusion coefficient
\mathbf{D}	3x3 diffusion tensor
Δ	time between two complementary diffusion gradients
δ	gradient duration
$E(\mathbf{q}, \tau)$	signal attenuation in diffusion MRI
\mathbf{e}_i	eigenvectors of diffusion tensor \mathbf{D} ($i = 1, 2, 3$)
\mathbf{G}	gradient magnitude
γ	gyromagnetic ratio
j	single spherical harmonics index ($j = (l^2 + l + 2)/2 + m$)
L_{\max}	maximum (even) SH order used for signal reconstruction
l	order of spherical harmonics (in this thesis: $l = 0, 2, \dots, \infty$)
λ_i	eigenvalues of diffusion tensor \mathbf{D} ($i = 1, 2, 3$)
m	degree of spherical harmonics ($m = -l, \dots, l$)
N	number of samples on the sphere included in a HARDI signal
n_{SH}	number of SH coefficients that represent a HARDI signal
ρ	diffusion propagator
\mathbf{q}	gradient wavevector ($\mathbf{q} = \gamma\delta\mathbf{G}$)
R_0	shell radius of probability profile reconstructed by DOT
$S(\mathbf{q}, \tau)$	diffusion-weighted MRI signal
S_0	unweighted diffusion MRI signal
T_1	time constant of longitudinal relaxation
T_2	time constant of transverse relaxation
T_2^*	transverse relaxation time constant in inhomogeneous field
τ	effective diffusion time
Y_{lm}	spherical harmonics of order l and degree m



*Turn the light out, say goodnight, no thinking for a little while
Let's not try to figure out everything at once*

The National - Fake Empire

Dankwoord

Ondanks dat je als promovendus vrij solistisch aan je eigen project werkt, is input en feedback van anderen essentieel. Bruggen bouwen tussen de medische wereld en de techniek is één van de dingen die ik graag doe en ik heb dan ook met plezier samengewerkt met allerlei verschillende mensen. Hoewel één woord of een korte Brabantse uitdrukking eigenlijk genoeg is, en de meesten (ook degenen die ik ga vergeten) wel weten dat ik hun steun erg gewaardeerd heb, ga ik toch een aantal mensen persoonlijk bedanken.

Bart, bedankt voor je enthousiasme en het vertrouwen dat je als eerste promotor uitstraalde, en voor alle kansen die je me hebt gegeven om dingen te leren en te zien. Veerle, heel fijn dat je als tweede promotor de klinische kant van mijn werk in de gaten wilde houden, ik heb er heel veel van opgestoken. Bram, ontzettend bedankt voor het invullen van de rol van copromotor. Je hebt me heel veel vrijheid gegeven (hoewel het laatste jaar noodgewongen) maar je was er altijd als het nodig was. Kritische vragen stellen, samen “graph cutten”, of een peptalk geven, niks was je teveel. Voor een positieve bijdrage aan de sfeer had je ook altijd wel iets achter de hand, variërend van mooie foto's tot melige YouTube-filmpjes.

Ook de rest van de leden van de BMIA-groep wil ik hier bedanken. De bijzondere werksfeer in en rond het lab, de filmavonden en de Ardennenweekendjes hebben mijn promotie tot een onvergetelijke tijd gemaakt. Remco, bedankt voor al je wiskundige ideeën! Vesna, Paulo, and Tim, thanks for all the help on diffusion stuff and some really entertaining evenings. Alessandro, thanks for being a great story-teller and a wonderful cook. Marieke, bedankt voor de leuke ISMRM-trip en alle serieuze en minder serieuze gesprekken. Ralph, bedankt voor de geheel eigen wijze waarop je dingen ziet en het toelichten daarvan, al dan niet onder het genot van een biertje. Super dat je samen met Roy mijn paranimf wil zijn! Jorg, Patrick & Laura, Bas & Chantal, Juan, Erik en Pim, heel erg bedankt voor de bijdragen die jullie hebben geleverd aan mijn promotie. Ik heb jullie met veel plezier begeleid.

Gustav, heel erg bedankt voor alle brainstorms en rattendata de afgelopen jaren! Walter, Maarten en Marc, geweldig hoe jullie geholpen hebben bij de data-acquisitie en -analyse. Paul, bedankt voor je inzet voor het review paper. Mark en Sonny, fijn dat ik mijn neurochirurgische vragen aan jullie mocht stellen. Mark, ook bedankt

voor al je hulp bij mijn laatste papers. Arno en Paul, bedankt voor het meedenken over de post-mortem experimenten. Jammer dat we hier door tijdgebrek niks meer mee gedaan hebben. Alle mensen van de “oude” gang in het Provisorium en de nieuwe BMT-groep in Maastricht, bedankt voor de gezelligheid!

Of course, I'd also like to thank all people from the LTS5-lab at EPFL for the nice time I had in Lausanne! Jean-Philippe, Claudio, and Leila, thanks for the great help on the functional connectivity experiment. Alia, thanks for the practical support and (together with Meritxell) for taking me to the discofit. Verder wil ik graag Michel Decré, Luc Florack en Klaas Nicolaij hartelijk bedanken voor het plaatsnemen in, respectievelijk voorzitten van, mijn promotiecommissie. Ook mijn nieuwe collega's van de afdeling radiotherapie in het UMC St Radboud ben ik erg dankbaar voor het warme welkom dat ik heb gekregen. Ik kijk uit naar de komende jaren!

Naast het werk was er de afgelopen jaren gelukkig ook tijd om door te brengen met vrienden, tijdens borrels, etentjes, feestjes, concerten en festivals. Leonie, hoewel we elkaar vanaf de brugklas kennen werden we pas wat later vriendinnen. Fijn dat ik altijd bij je terecht kan voor wat dan ook. Bonny & Edwin, Anneke & Jeroen, Mieke & Gerard, Kristel & Sander en de rest van de groep, bedankt voor alle gezelligheid de afgelopen twaalf jaar en de steun de afgelopen tijd. Tessa, Leonie en Miriam, tien jaar na het begin van onze studie moeten we nog steeds regelmatig bijkletsen. Bedankt voor alles. Voor bijna iedereen geldt dat we elkaar niet altijd even frequent zien door afstand en drukte, maar ik ben erg blij met jullie!

Lieve (schoon)familieleden, bedankt voor het warme bad. In het bijzonder oma en Annemiek & Jan, wat fijn dat jullie altijd voor iedereen klaarstaan. Edith & Frans, ik vind het super dat jullie ook in mijn werk zoveel interesse tonen. Lieve Sanne & Jelmer, Inge & Ralf, bedankt voor jullie belangstelling en de gezelligheid als we weer eens met z'n allen thuis zijn. Lieve mama, bedankt voor je onvoorwaardelijke steun en liefde, en alle kansen die jij en papa ons gegeven hebben. Wat zou hij trots zijn geweest nu, maar wat ben ik ook blij met Jo, die ons allemaal op handen draagt en altijd bereid is een handje te helpen bij wat dan ook. Liefste Roy, soms zie je iemand hier beloven dat de rust nu zal terugkeren. Ik geloof niet dat ik je daar een plezier mee doe en weet ook niet of dat gaat gebeuren, voorlopig in elk geval niet met jouw promotie in zicht. Ik hoop dat we ook daarna nog vele uitdagingen aan zullen gaan samen, zowel in ons privéleven als op werkgebied. Bedankt dat je er altijd voor me bent en dat je me stimuleert om het beste in mezelf naar boven te halen.

Curriculum vitae



Ellen Brunenberg was born on November 4, 1983, in Weert, the Netherlands. She finished her pre-university education at the Bisschoppelijk College Weert in 2001. Subsequently, she started studying Biomedical Engineering at Eindhoven University of Technology, from which she obtained her Master of Science degree in 2007.

During her studies, she performed an internship at the Computer Vision Center of Universitat Autònoma de Barcelona (UAB), Barcelona, Spain, where she worked on automatic segmentation of soft and fibrous plaque from intravascular ultrasound images, using feature extraction and snakes. Her master's project was a collaboration between the Biomedical Image Analysis group at Eindhoven University of Technology and the department of Neurosurgery at Maastricht University Medical Center. The project focused on automatic electrode trajectory planning for deep brain stimulation in Parkinson's disease.

She was awarded an NWO TopTalent grant, enabling her to proceed with a PhD project at the same university, again in close collaboration with Maastricht University Medical Center. This project focused on noninvasive imaging methods for identification of the subthalamic nucleus and thus a more specific planning for deep brain stimulation. During her PhD, she visited the Signal Processing Lab at École Polytechnique Fédérale de Lausanne (EPFL), Lausanne, Switzerland, where she worked on functional connectivity analysis of the subthalamic nucleus. The result of the PhD project is this thesis entitled "Hitting the right target - Noninvasive localization of the subthalamic nucleus motor part for specific deep brain stimulation".

Since May 2011, she is working as a medical physicist trainee at the department of Radiotherapy of Radboud University Nijmegen Medical Center.

List of publications

Journal papers

- | | |
|------|---|
| 2011 | <p>E.J.L. Brunenberg, P. Moeskops, A. Vilanova, W.H. Backes, M.L.F. Janssen, V. Visser-Vandewalle, B.M. ter Haar Romeny, B. Platel. "Structural connectivity of the human subthalamic nucleus: identification of the "hyperdirect" pathway and segregation of motor and non-motor STN parts", submitted.</p> <p>E.J.L. Brunenberg, W.H. Backes, C. Pollo, L. Cammoun, M.L.F. Janssen, V. Visser-Vandewalle, B.M. ter Haar Romeny, J.-Ph. Thiran, B. Platel. "Resting state functional connectivity of the motor and non-motor areas of the human subthalamic nucleus", submitted.</p> <p>E.J.L. Brunenberg, B. Platel, P.A.M. Hofman, B.M. ter Haar Romeny, V. Visser-Vandewalle. "Magnetic resonance imaging techniques for visualization of the subthalamic nucleus: a review", in <i>Journal of Neurosurgery</i>, DOI:10.3171/2011.6.JNS101571, in press (accepted June 8, 2011).</p> |
| 2010 | <p>L.M.J. Florack, E. Balmashnova, L.J. Astola, E.J.L. Brunenberg. "A new tensorial framework for single-shell high angular resolution diffusion imaging", in <i>Journal of Mathematical Imaging and Vision</i>, 38(3):171–181.</p> <p>R.T.A. Megens, S. Reitsma, L. Prinzen, M.G. Oude Egbrink, W. Engels, P. Leenders, E.J.L. Brunenberg, K.D. Reesink, B.J.A. Janssen, B.M. ter Haar Romeny, D.W. Slaaf, M.A.M.J. van Zandvoort. "In vivo high-resolution structural imaging of large arteries in small rodents using two-photon laser scanning microscopy", in <i>Journal of Biomedical Optics</i>, 15(1):011108.</p> |

Conference papers

- | | |
|------|--|
| 2010 | <p>E.J.L. Brunenberg, R. Duits, B.M. ter Haar Romeny, B. Platel. "A Sobolev norm based distance measure for HARDI clustering: a feasibility study on phantom and real data", in <i>Proceedings of Medical Image Computation and Computer-Assisted Intervention (MICCAI)</i>, LNCS, volume 6361, pages 175–182.</p> <p>E.J.L. Brunenberg, R. Duits, B.M. ter Haar Romeny, B. Platel. "A Sobolev norm based distance measure for HARDI clustering: a feasibility study on phantom and real data", in <i>Proceedings of Advanced School for Computing and Imaging (ASCI)</i>.</p> |
| 2009 | <p>E.J.L. Brunenberg, V. Prčkovska, B. Platel, G.J. Strijkers, B.M. ter Haar Romeny. "A comparison of DTI and HARDI in rat subthalamic nucleus", in <i>Proceedings of Advanced School for Computing and Imaging (ASCI)</i>.</p> |
| 2007 | <p>E.J.L. Brunenberg, A. Vilanova, V. Visser-Vandewalle, Y. Temel, L. Ackermans, B. Platel, B.M. ter Haar Romeny. "Automatic trajectory planning for deep brain stimulation: a feasibility study", in <i>Proceedings of Medical Image Computation and Computer-Assisted Intervention (MICCAI)</i>, LNCS, volume 4791, pages 584–592.</p> |
| 2006 | <p>E.J.L. Brunenberg, O. Pujol, B.M. ter Haar Romeny, P. Radeva. "Automatic IVUS segmentation of atherosclerotic plaque with Stop & Go snake", in <i>Proceedings of Medical Image Computation and Computer-Assisted Intervention (MICCAI)</i>, LNCS, volume 4191, pages 9–16.</p> <p>E.J.L. Brunenberg, O. Pujol, B.M. ter Haar Romeny, P. Radeva. "Automatic IVUS segmentation of atherosclerotic plaque with Stop & Go snake", in <i>Proceedings of Advanced School for Computing and Imaging (ASCI)</i>.</p> |

Conference abstracts

- 2011 **E.J.L. Brunenberg**, R. Duits, B.M. ter Haar Romeny, B. Platel. "Taking extrema into account: a new distance measure for HARDI clustering", in *Proceedings of Dutch Biomedical Engineering Conference*, volume 3.
- 2010 **E.J.L. Brunenberg**, E. Pelgrim, B.M. ter Haar Romeny, B. Platel. "K-means and graph cuts clustering of diffusion MRI in rat STN", in *Proceedings of International Society for Magnetic Resonance in Medicine (ISMRM)*, volume 18, page 4045.
- E.J.L. Brunenberg**, E. Pelgrim, B.M. ter Haar Romeny, B. Platel. "K-means and graph cuts clustering of diffusion MRI in rat STN", in *Proceedings of ISMRM Benelux Meeting*, volume 2, page 118.
- 2009 **E.J.L. Brunenberg**, V. Prčkovska, B. Platel, G.J. Strijkers, B.M. ter Haar Romeny. "Untangling a fiber bundle knot: preliminary results on STN connectivity using DTI and HARDI on rat brains", in *Proceedings of International Society for Magnetic Resonance in Medicine (ISMRM)*, volume 17, page 740.
- E.J.L. Brunenberg**, B. Platel, B.M. ter Haar Romeny. "Finding the subthalamic nucleus for deep brain stimulation using diffusion-weighted MRI", in *Proceedings of Dutch Biomedical Engineering Conference*, volume 2.
- 2008 **E.J.L. Brunenberg**, V. Prčkovska, B. Platel, G.J. Strijkers, B.M. ter Haar Romeny. "Untangling a fiber bundle knot: preliminary results on STN connectivity using DTI and HARDI on rat brains", in *Proceedings of ISMRM Benelux Meeting*, volume 1, page 45.

PhD portfolio

Courses

2010	Masterclass Presenting using performance skills (TU/e)
2009	Workshop Neuroanatomy (UM) Course Fundamentals of biostatistics (TU/e) Course Presenting in English (TU/e)
2008	Course Writing articles and abstracts (TU/e) Summer school Mathematics in brain imaging (UCLA) Course Advanced pattern recognition (ASCI) Workshop 3rd M-Bic fMRI workshop (UM)
2007	Course Knowledge-driven image segmentation (ASCI)

International conferences

2010	MICCAI conference, Beijing (oral) ISMRM conference, Stockholm (poster)
2009	MICCAI conference, London (attending workshop) ISMRM conference, Honolulu (oral) ECR conference, Vienna (attending)
2007	MICCAI conference, Brisbane (poster)

Other meetings

2011	MISP symposium, Rotterdam (attending) Kempenhaeghe Epilepsy & Sleep update , Heeze (oral) Biomedical Engineering conference, Egmond aan Zee (oral)
------	---

- | | |
|------|--|
| 2010 | ASCI conference, Veldhoven (oral)
BME research day , Eindhoven (poster)
ISMRRM Benelux meeting, Utrecht (poster) |
| 2009 | ASCI conference, Zeewolde (oral)
BME research day , Eindhoven (poster)
Symposium Profiling Parkinson , Amsterdam (oral)
Biomedical Engineering conference, Egmond aan Zee (oral)
MISP symposium, Delft (oral) |
| 2008 | Symposium MIND unveiling itself , Maastricht (attending)
ISMRRM Benelux meeting, Antwerp (oral)
NVPHBV fall meeting, Eindhoven (organization)
BME research day , Eindhoven (oral) |

Educational activities

- | | |
|------|---|
| 2010 | Supervising Master's project (P. Moeskops)
Supervising Honors project (L. Neumann, P. Wijnings, J. Portegies)
Tutorial Clinical module neurology |
| 2009 | Supervising Master's project (E. Pelgrim)
Supervising Master's project (J. Escibano Navarro)
Supervising Medical Engineering project (B. v/d Velden, C. Tax)
Supervising Medical Engineering skills lab
Tutoring Medical Engineering case
Workshop Tutor training
Tutorial Clinical module neurology |
| 2008 | Workshop Supervising master students
Tutorial Clinical module neurology |